Planetary Surface Properties, Cratering Physics, and the Volcanic History of Mars from a New Global Martian Crater Database

by

Stuart James Robbins

B.S., Case Western Reserve University, 2005

M.S., University of Colorado, Boulder, 2008

A thesis submitted to the

Faculty of the Graduate School of the

University of Colorado in partial fulfillment

of the requirement for the degree of

Doctor of Philosophy

Department of Astrophysical and Planetary Sciences

2011

This thesis entitled:
Planetary Surface Properties, Cratering Physics, and the Volcanic History of Mars
from a New Global Martian Crater Database
written by Stuart James Robbins
has been approved for the Department of Astrophysical and Planetary Sciences

_____

Dr. Brian M. Hynek

_____

Dr. Frances Bagenal

_____

Dr. Nadine G. Barlow

_____

Dr. Bruce M. Jakosky

_____

Dr. Nicholas M. Schneider

Date: _____

The final copy of this thesis has been examined by the signatories, and we
Find that both the content and the form meet acceptable presentation standards
Of scholarly work in the above mentioned discipline.

Robbins, Stuart J. (Ph.D., Astrophysical and Planetary Sciences)

Planetary Surface Properties, Cratering Physics, and the Volcanic History of Mars from a New Global Martian Crater Database

Thesis directed by Assistant Professor Brian M. Hynek

Abstract

Impact craters are arguably the primary exogenic planetary process contributing to the surface evolution of solid bodies in the solar system. Craters appear across the entire surface of Mars, and they are vital to understanding its crustal properties as well as surface ages and modification events. They allow inferences into the ancient climate and hydrologic history, and they add a key data point for the understanding of impact physics. Previously available databases of Mars impact craters were created from now antiquated datasets, automated algorithms with biases and inaccuracies, were limited in scope, and/or complete only to multi-kilometer diameters. This work presents a new global database for Mars that contains 378,540 craters statistically complete for diameters $D \geq 1$ km. This detailed database includes location and size, ejecta morphology and morphometry, interior morphology and degradation state, and whether the crater is a secondary impact. This database allowed exploration of global crater type distributions, depth, and morphologies in unprecedented detail that were used to re-examine basic crater scaling laws for the planet. The inclusion of hundreds of thousands of small, approximately kilometer-sized impacts facilitated a detailed study of the properties of nearby fields of secondary craters in relation to their primary crater. It also allowed the discovery of vast distant clusters of secondary craters over 5000 km from their primary crater, Lyot. Finally, significantly smaller craters were used to age-date volcanic calderas on the planet to re-construct the timeline of the last primary eruption events from 20 of the major Martian volcanoes.

Dedication

I dedicate this thesis to four teachers I had in middle and high school. First, Mrs. Nancy Beauregard, my sixth grade English teacher, who taught me that completing reading assignments didn't need to be a chore, and who has since become a good friend. Second are my three high school science teachers: Dr. Beverly Fennell, Mrs. Naomi Horchak-Morris, and Mr. Pat Carroll. I thank them for nurturing an interest in the natural world and science. If all teachers could be as inspiring as these four, the world would be a much better place.

I also dedicate this to my parents who seemed to know the right amount of guidance, support, and distance to let me find my own way.

Acknowledgements

First and foremost, I want to thank my advisor, Brian Hynek, for his guidance over the past several years, *very* late-night input, and putting up with my verbosity. I also want to sincerely thank three undergraduate students who assisted in generating this database over the past four years: Rachel Haber, David McKenzie, and especially Danielle Russell. For my overall thesis, I also want to thank the several people who agreed to read various parts and provide input, feedback, corrections, and critiques: Brian Hynek, Pamela Gay, Brad Gisclair, Joe Boyce, Rich Orman, Tana Owens, and Dell Skinner. Finally, I want to thank all the music artists, podcasters, and radio hosts who kept me at least somewhat sane over the thousands of hours spent creating the crater database that formed the bulk of this dissertation. In particular, *The Skeptics Guide to the Universe* podcast helped to keep me entertained and informed, and it helped teach me to exercise a healthy amount of doubt about my own research conclusions.

Chapters in this thesis are published, submitted, or will soon be submitted papers. Acknowledgements for each section follow:

Sections 2 and 3: This paper benefited from discussions with N. Barlow, J. Boyce, and M. Mellon. This work benefited from the assistance of R. Haber, D. McKenzie, and D. Russell. Support for this work was through NASA NESSF Award NNX07AU85H and NASA Award NNX10AL65G.

Section 4.1: This paper benefited from useful discussions with J. Skinner and R.A. Nava, and from reviews by C. Chapman and an anonymous individual. This work was supported through NASA Award Number NNX10AL65G.

Section 4.2: Support for this work was through NASA Award Number NNX10AL65G.

Section 5: This paper benefited from useful discussions with E.B. Bierhaus and two anonymous reviewers. S.J. Robbins was supported through NASA NESSF Award NNX07AU85H. G. Di Achille was supported through NASA Grant Award NNX07AU41G. B.M. Hynek was supported through NASA Awards NNX07AU41G and NNX06AE08G.

Table of Contents

List of Tables

List of Figures

1. Introduction

When one looks at the Moon through binoculars or a small telescope, some of the most apparent features are the craters that dominate much of its landscape. Impact craters are prevalent across the surface of almost every solid body in the solar system; the notable exceptions are Earth, Titan, Io, and regions of Triton and Enceladus where rapid, ongoing resurfacing is caused by endogenic processes. Venus also presents an abbreviated crater pattern due to volcanic resurfacing and a thick atmosphere that prevents many smaller impactors from reaching the planet's surface. On bodies that lack active resurfacing, impact craters are the primary mode of surface modification, both in the present and even more so in the past. A single impact likely formed our Moon and gave Earth a disproportionately large iron core. Impacts deliver water, and they may also deliver organic compounds like amino acids to planets, helping life to begin. Conversely, a large impact can completely destroy life that has formed. Impacts on Earth have been tied to some of the greatest extinction events in our planet's history, and future impacts may repeat this.

Understanding impactor and crater populations is a key part of understanding the history of the solar system. From the initial collisions that formed the planets to the continued impacts today, knowing the impactor population and flux through time is integral to interpreting the geologic past and its processes. Because crater sizes relate to the object that formed them, comprehensive studies of crater populations inform impactor population censuses. Craters can be used to determine relative surface ages, resurfacing rates, and properties of the crust within which they form. Differences in impact crater morphology from an expected norm can be used to glean further information about the surface and near-surface properties that modified them. Studying actual impacts also puts constraints on models of crater formation. This is important for understanding the underlying physics of such destructive events, ranging from natural incidents by asteroids and comets to manmade affairs by bombs and missiles. Delving into these issues and questions forms the bulk of this dissertation, but in order to understand how

differences among craters inform these applications, one must first understand the basics of impactor populations, crater formation, and crater morphology.

1.1. Crater Production Throughout the Solar System's History

The cratering rate and number of craters of a given size on the solar system's bodies are dependent almost entirely upon the number of potential impactors. Projectiles in the inner solar system are, for the most part, asteroids disrupted from the asteroid belt. To a lesser extent, comets will also impact planets (*e.g.*, Comet Shoemaker-Levy 9's collision with Jupiter in 1994), though their role in cratering during the lifetime of the solar system has been debated (*e.g.*, Levison *et al.*, 2001; Ivanov, 2001). The discussions and calculations in this work are based upon asteroid-only models. The role of comets is contested, but if they play a role, it is believed they mainly follow the same trends seen in asteroids (see Melosh, 1989; Neukum *et al.*, 2001). Their inclusion would change the nature of the impactors, but in the inner solar system it should not significantly affect important variables such as the average size- and impact velocity-distributions. In the outer solar system, comets likely play a much more significant role and their population should not be averaged out.

Today, most asteroids lie between the orbits of Mars and Jupiter in the Main Asteroid Belt. Their size distribution is governed by collisions which yield the theoretical "production function" size-frequency distribution (Ivanov, 2001). This can be compared observationally with crater sizes on planets (Melosh, 1989). This distribution is such that when a histogram of diameters integrated from large to small sizes is graphed logarithmically, the slope is $b \approx -3$. A fit to the current data on asteroids yields a -3.3 slope (data for 547,100 asteroids, downloaded on March 14, 2011, from Lowell Observatory). Asteroids are also found in other parts of the solar system and can cross planetary orbits, but such asteroids are much fewer in number than the Main Belt asteroid population (~2% of identified asteroids).

Based upon the established lunar timescale (*e.g.* Neukum *et al.*, 2001) (see Fig. **1**), the cratering rate just after the solar system's formation ~4.5 Ga ago was up to 10^5 times today's rate,

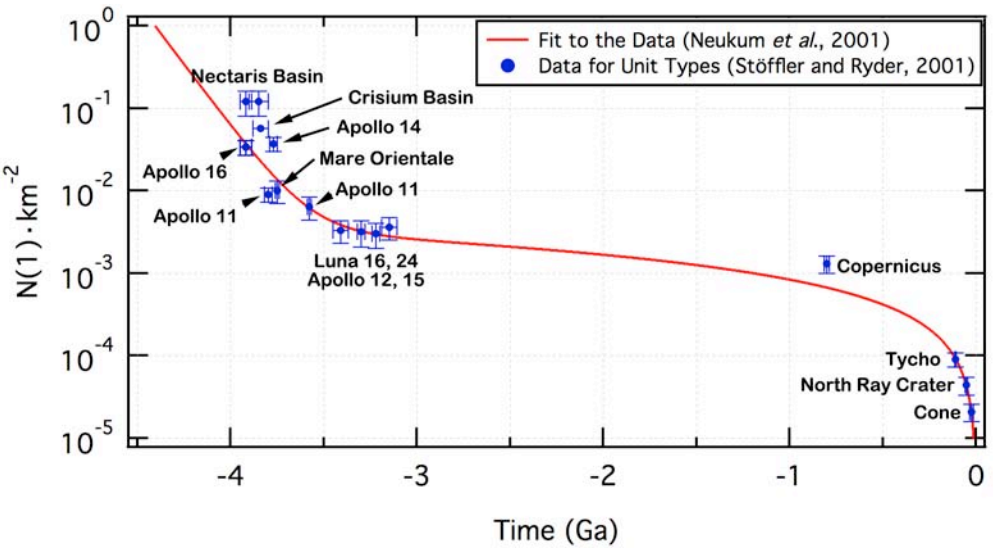

Figure 1: Cratering rate through the solar system's history. Vertical axis is the number of craters that are $D \geq 1$ km per km^2, and the horizontal axis is billions of years before the present. Function is Eq. 5 from Neukum *et al*. (2001) and data and uncertainties are from Table VI from Stöffler and Ryder (2001). An N(#) age is an age based upon the number of craters per unit area that are greater than or equal to the parenthetical number.

or up to 10^6 1-km craters per 10^6 km^2 per Ga. This rate exponentially decayed until ~3.5 Ga ago, at which time the cratering rate was $\sim 3 \times 10^2$ times greater than what it is today, or 3×10^3 1-km craters per 10^6 km^2 per Ga. From then until about the time Copernicus Crater was formed (~1 Ga ago on the Moon), the impactor flux decreased slowly to $\sim 10^2$ today's rate. Over the last billion years, the flux continued to decay dramatically, down to the current estimated rate of 10 1-km craters per 10^6 km^2 per Ga. With high-resolution imagery repeatedly gathered over several years for Mars and the Moon, directly measuring the present-day impact flux can now be estimated (*e.g.*, Malin *et al*., 2006; Daubar *et al*., 2010, 2011).

It has been argued lately (*e.g.*, Neukum, 2001) that the size distribution of asteroids has remained constant through time, or at least for the last 4 Ga. This certainly makes extrapolation of historic crater populations easier, but it also was not necessarily true during the very early part of the solar system's history (*e.g.*, Strom *et al*., 1992, 2008). The difference is that today's function is governed by collisional processes among the impactor population while, early in the solar system's history, potential impactors had not had time to break down via collisions to form the size distribution presently observed. Rather, according to some models, their size

distribution would be more closely linked to accretionary growth during the solar system's formation (*e.g.*, Strom *et al*., 1992, 2008). For simplicity, however, Hartmann and Neukum (2001) and Hartmann (2005) adopt the position of a consistent production function when establishing the Martian isochrons (isochrons are established crater frequencies as a function of diameter for a given surface age; see Sections 1.4.1, 5.2.4).

This earliest period of heavy cratering is aptly named the "Heavy Bombardment," while a subsequent period ~700 Ma later saw a pulse of increased cratering termed the "Late Heavy Bombardment" (LHB). This was possibly caused by dynamic interplay between the large gas and ice giant planets – Jupiter, Saturn, Uranus, and Neptune (*e.g.*, Gomes *et al.*, 2005) (described as the "Nice Model"). This period is significant for all terrestrial bodies in the inner solar system, not only because the relatively frequent impact rate pulverized their surfaces, but also because *most* of the craters that would ever be carved out of the landscape were formed during this period of time. The Heavy Bombardment was also an important time because most of the largest asteroid impacts in our solar system occurred during that period, forming the large lunar basins, Mercury's Caloris Basin, and basins such as Mars' Utopia, Isidis, Hellas, and Argyre (Nimmo and Tanaka, 2005). Post-LHB impactors may have originally been seeded from the asteroid belt, but their population derives from inner solar system –crossing asteroids and comets.

1.2. Crater Formation

Primary exogenic craters form during hypervelocity (10s of km/sec) impacts of a projectile into a planetary surface. Because of impactors' high velocities, the initial shape of the projectile and angle of impact (except for very low angles) will not significantly affect the final crater morphology. Velocities of asteroidal impactors are typically between 10-20 km/sec in the inner solar system (McEwen and Bierhaus, 2006), though these velocities increase closer to the Sun and so are less at Mars than Earth. The following discussion is primarily adapted from Melosh (1989).

There are three main stages of crater formation; the divisions are artificial but aid in the understanding the cratering process. The first stage is contact and compression, wherein the projectile physically contacts the target's surface. This compresses both the impactor and the surface as the impactor burrows into the target, moving material in the process. Most of the kinetic energy from the projectile is transferred into the target. Shock pressures typically reach hundreds of GPa (similar to the pressure of the metallic hydrogen layer in Jupiter's atmosphere) which easily exceeds the yield strength of both the projectile and target, causing them to deform, melt, and/or vaporize. This stage ends when the projectile is destroyed by shock waves.

The second stage is excavation wherein the transient crater cavity forms. The shock and subsequent rarefaction waves that travel through the target physically move the target material in a process that eventually opens the crater to a size many times the projectile's initial diameter (this is one of the primary differences between low-velocity and hypervelocity impacts). The target's gravity takes a more important role in the cavity's formation during this phase. The crater will initially be excavated to a depth ~3 times its final depth, which is ~30% the transient diameter regardless of final simple or complex morphology. For simple craters, the transient diameter is ~85% the final diameter, and for larger complex craters, it is ~50-65% the final diameter (these morphologies are discussed in Section 1.3); it is smaller than the final cavity due to slumping that occurs during the next stage. During this stage, most of the ejecta is deposited: Jets of still-solid, melted, and vaporized material "squirt" from the edges of the projectile's contacts which form an ejecta blanket and potentially secondary craters. The distance the ejecta (and secondary craters) travel is based primarily upon the target body's gravity and the impactor's velocity. However, recent work suggests that terrain may also play a role in this, at least in the extent and distribution of secondary craters (Robbins and Hynek, 2011d, or Section 4.2).

The third and final stage of crater formation is modification, not to be confused with the modification discussed in Section 1.4.2. Though one can argue the modification phase progresses through geologic time until the crater is destroyed, this usually refers to the main collapse phase. The main collapse is dominated by the target's gravity, but the local properties of

the crust will influence this process (*e.g.*, Pike, 1980; Boyce *et al*., 2006; Robbins and Hynek, 2011c). This phase begins after the crater is fully excavated and is still a simple bowl shape. Loose debris slide down the interior walls of smaller craters, further-widening them and causing them to grow shallower. Large craters will form complex morphology: large chunks of the wall collapse forming terraces, and a rebound effect causes central peak(s) or a ring to rise. One or more rings form if the rebound that forms the peak "overshoots" the stability of the rock, at which point it collapses back into a ring (this is the same phenomenon observed in simple milk drop experiments). Over a much greater timescale in larger craters (but still generally instantaneous in a geologic context), isostatic rebound causes the floor to rise and flatten, further departing from a bowl morphology.

The timescale for each phase is instantaneous in a geologic sense; it is this relative rapidity that allows craters to be important tools for understanding global stratigraphic relationships (see Section 1.4.1). The initial compression phase lasts $\tau_{\text{compression}} = L/v_i$, where L is the diameter of the impactor and v_i its velocity. The ~40-50-meter projectile that likely formed the ~1.2-km-diameter Meteor Crater in Arizona, USA thus spent a small fraction of a second in this stage. The excavation stage is dependent upon the diameter D of the crater and gravity g of the impacted object, $\tau_{\text{excavation}} = \sqrt{D/g}$, so Meteor Crater took ~10 seconds to excavate. The modification stage will take a few times that of the excavation, so overall, Meteor Crater, a ~1.2-km-diameter feature, took under 1 minute to form. In comparison, the large, 222-km-diameter crater Lyot on Mars took ~10-15 minutes to form, while the giant 2500-km South Pole-Aitken basin on the Moon may have taken ~2 hours.

1.3. Basic Crater Properties and Morphologies

Craters range in size from micrometer-scale zap pits or microcraters (as seen on lunar samples) to giant basins thousands of kilometers in diameter (*e.g.*, South Pole-Aiken Basin (2500 km) and Mare Imbrium (1123 km) on the Moon; Caloris Basin (1350 km) on Mercury; and Utopia (3300 km) and Hellas (2300 km) on Mars). Despite spanning over nine orders of

magnitude in size, all craters form with the same three basic characteristics: A cavity below the surrounding surface, a raised rim above the surrounding surface, and ejected material surrounding the rim. This assumed basic morphology aids in the study of craters because deviation from this basic model is indicative of subsequent modification or properties of the formation of the crater itself.

Within those three basic characteristics, crater morphology changes significantly based upon crater size. The size-morphology classification can be broken down into three main categories: simple, complex, and multi-ring basin. The transition diameter at which a crater will form as simple vs. complex is primarily proportional to g^{-1}, where g is the surface gravity of the target body (*e.g.*, Gilbert, 1893; Pike, 1988). However, the transition between these types does not occur at an exact diameter for a given planetary surface: Not all craters smaller than 6 km are simple just as not all craters larger than 6 km are complex on Mars. First, it is dependent upon the type of morphology being examined (*i.e.*, while central peaks and wall terraces are both characteristics of complex craters, central peaks on Mars are prevalent in craters with diameters $D \gtrsim 5.6$ km, but terraces at $D \gtrsim 8.3$ km (Robbins and Hynek, 2011c, see Section 3.6.2)). Second, it is dependent upon the physical properties of the crust in which it formed; the primary factor is the strength of the crust for smaller craters and strength and thickness of the underlying lithosphere for multi-ring basins (*e.g.*, McKinnon and Melosh, 1980; Pike, 1980; Melosh, 1989).

Simple craters are a bowl-shaped depression below the surface with a raised rim and surrounding ejecta blanket (until the latter two may be removed through erosion). (See Appendix C for examples of crater morphologies.) Meteor Crater in Arizona and the crater Linné on the moon are classic examples of simple craters. Simple craters' cavities are steepest at the rim and gradually shallow in slope until the center is reached. Simple craters have no lower diameter limit, but they do have an upper limit: For the Moon, simple craters are generally craters smaller than ~15 km (Pike, 1977, 1988), while on Mars, the transition between simple and complex morphologies is generally between 5 and 8 km (Pike, 1980, 1988; Boyce and Garbeil, 2007; Robbins and Hynek, 2011c), though simple craters as large as 15 km have been

observed (Robbins and Hynek, 2011c).

Complex craters display distinctly different internal morphology than simple craters. Instead of a gentle bowl-shaped cavity, complex craters have sloping walls that terminate in a mostly flat floor. Nearly all pristine, complex craters have outwardly slumping terraced walls. These terraces are observed to trap impact melt (rock that was melted due to the energy of a hypervelocity impact) which indicates they formed during the initial crater formation as opposed to subsequent mass wasting (Melosh, 1989). The smallest complex craters usually have a peak in the center that is composed of material below the floor that was uplifted through an elastic rebound effect. This is much like the rebound when a small object is dropped into a pool of water (Melosh, 1989). Central peaks have been observed to rise above the surface outside the crater (*e.g.*, crater Theophilus on the Moon, various craters on Mars (Robbins and Hynek, 2011b)), though it is rare to have them higher than the rim itself. Somewhat larger complex craters display a central ring as opposed to a peak; the transition diameter to a ring also scales as g^{-1}. A transition to this peak ring morphology on the Moon is seen in craters generally larger than ~140 km (Melosh, 1989). This transition on Mars is significantly more difficult to discern because only nine craters display this morphology (all are $D > 100$ km except one), despite over 300 craters being $D > 100$ km. Given that the majority of these larger craters formed early in Mars' history and have undergone significant modification (Robbins and Hynek, 2011b), this is likely due predominantly to erosion processes removing the peak rings.

Multi-ring basins are historically considered the largest craters and are generally more difficult to recognize due to their size and age. On the Moon, basins are the next size-based morphologic type beyond the peak-ring type of complex craters (*e.g.*, Mare Orientale on the Moon), though it is less apparent that this is the case for large basins on other bodies (*e.g.*, Caloris on Mercury, Argyre and Hellas on Mars (see Section 3.2.1), and Valhalla on Callisto). Melosh (1989) argues that these basins are dissimilar to lunar multi-ring basins and, even if some can be shown to be of the lunar type, the transition diameter to this morphology does not appear to scale inversely with gravity; this indicates their formation and collapse mechanism is different

than that of simple and complex craters. He does, however, emphasize that the basic basin morphology - a very large (hundreds to thousands of kilometers) diameter, relatively shallow depth (~few kilometers), and various ring-like collapse features - is the largest observed type of crater. Basins have an added effect: Because they are so large, the energies required to form them can also cause dramatic tectonic effects to manifest across the entire body. For example, at the antipode to Caloris Basin on Mercury, the terrain is chaotic in nature with faults and significantly modified craters, suggesting vertical jostling by several kilometers (Spudis and Guest, 1988). On Mars, the antipode to Argyre basin is the Elysium volcanic complex and the antipode to Hellas basin is the Tharsis volcanic complex, though a causal as opposed to coincidental link between these has yet to be confirmed.

Another feature of many craters is that they produce secondary craters during formation. These are formed by blocks of material thrown from the planetary surface during the excavation phase of impact. These blocks are ejected with a range of angles and velocities, impact the surface, and create their own smaller, shallower craters. Due to the ballistic nature of ejecta, they often form in chains that are oriented radially to the primary crater or have biaxially symmetric morphologies with a long axis radial to the primary (Shoemaker, 1962, 1965). The ejected material has much slower velocities than the initial impact, and so the secondary craters will usually not be the radially symmetric simple type. Due to energy conservation, secondary craters will always be smaller than primary craters, typically less than 5% the diameter of the primary and more often less than 2.5% (McEwen and Bierhaus, 2006). However, in rare cases secondary craters as large as 15% of the primary have been suggested (Robbins and Hynek, 2011d).

1.4. The Utility of Craters in Understanding Planetary Processes

Because of the universal crater properties and established impact history in the inner solar system (Fig. **1**), craters are an important tool for understanding terrestrial bodies. One can examine craters individually to discern local processes (*e.g.*, aeolian deposition, fluvial erosion, lower crust composition), or one can study a large group of craters to learn about a broad region

of a planet's surface, ages, and variations within properties of the crust. Similarly, laboratory experiments of impacts can be scaled to larger sizes only so much before they break down, so studies of large craters across the solar system allow tests of models and experiments and can lead to new avenues of research.

1.4.1. Relative Surface Ages

There are two basic premises behind using craters to age-date a surface: (1) The longer a surface is exposed, the more craters accumulate upon it, and (2) over geologic time, craters are distributed randomly on a planet. With these simple assumptions, one can count how many craters are on one surface vs. another to determine which is older: Older surfaces have more craters over a given area. Taking this a step further, one can separate the counted craters into diameter size bins to create a size-frequency distribution (SFD) crater plot (c.f., Arvidson *et al*., 1979). The histogram can be integrated from the largest diameter to the smallest, such that the smallest diameter bin will contain the sum of all the craters observed (cumulative SFD). A feature of these cumulative SFDs is that on logarithmic axes the distribution of cumulative number of craters vs. diameter sizes is approximately linear, mirroring the production function if no crater removal processes have taken place. Since a surface will collect more craters as it ages (assuming no other processes take place to remove them), isochrons can be established for reference in dating surfaces of a certain age (an isochron is an idealized, modeled curve on a SFD that represents what the crater distribution should be for a surface of a given age from that model). This is generally based significantly upon models extrapolated from the Moon (the most recent comprehensive works are: Ivanov, 2001; Neukum *et al*., 2001; Hartmann and Neukum, 2001; Hartman, 2005).

That is the first major limitation of crater-based surface ages: Crater counting itself can only yield *relative* ages. It is possible to estimate surface ages based upon present-day observed craters, and this has been attempted and refined many times for Mars throughout the last ~40 years (*e.g.*, Chapman and Jones, 1977; Ivanov, 2001; Hartmann and Neukum, 2001; Hartmann,

2005). This is less of a limitation on the Moon because the *Apollo 12* and *14-17* missions returned samples of the lunar regolith and rocks from different-aged surfaces, and these rocks were subsequently dated via radiometric methods (Rb^{87}/Sr^{87} and U^{238}/Pb^{206}) (*e.g.*, Heiken *et al*, 1991; Stöffler and Ryder, 2001). Geologic mapping of the moon via stratigraphic relationships, volcanic flows, and impact crater density permits categorization of the lunar surface into distinct groups based on similar features and ages. The major lunar epochs are based upon major impact events because impacts occur in a geologic instant and a large enough impact has effects that can be traced a large distance from the site. For example, the most recent lunar epoch is the Copernican, covering the time since Copernicus crater formed ~1 Ga ago (the others from most recent to oldest are Eratosthenian, Imbrian, Nectarian, and Pre-Nectarian) (Stöffler and Ryder, 2001). Copernicus has a large ejecta blanket and rays that extend a significant distance from the crater rim that permit stratigraphy to be established over a large portion of the lunar surface. By following these kinds of features and correlating them with crater densities, each part of the surface can be assigned a relative age date. These can then be calibrated with the *Apollo* returns and assigned absolute ("actual") ages. Efforts have since been made (*e.g.*, Hartmann and Neukum, 2001; Ivanov, 2001; Hartmann, 2005) to extrapolate the cratering rate from the Moon to Mars to better constrain Martian chronology.

A second limitation involves sheer number statistics: The smaller the number of craters counted, the larger the statistical uncertainties. Uncertainties on crater SFDs are the square-root of the number in each bin (Arvidson *et al*., 1979). This is because craters are distinct features - one crater is one crater - so they follow Poisson statistics where the standard deviation from the mean N is $\sqrt{N}$. Therefore, when attempting to date one region relative to another, it behooves the investigator to utilize as many craters as possible. Unfortunately, this is not always viable, such as when attempting to date a small region, a young region, and/or when using low-resolution data.

A third difficulty is repeatability: One researcher counting craters in a region will not necessarily count the same number for a given diameter range as another. They may not even

count the same number as they did the last time they attempted it. Hartmann *et al*. (1981) and Lissauer *et al*. (1988) estimate that uncertainties based upon this alone will generally introduce an uncertainty of a factor of $1.2-1.3\times$, while this researcher found differences of >4% (Robbins *et al*., 2011) and Kirchoff *et al*. (2011) found differences on the few-percent level. Similarly, solar illumination angle will affect crater counts: If the sun is too close to the meridian when the image was taken, crater shadows will not be long enough to make them easily identifiable. Experimental results with the same terrain imaged at different incidence angles suggest the ideal angle range is ~70-80° (*e.g.*, Wilcox *et al*., 2005; Ostrach *et al*., 2011).

The fourth main difficulty in using craters to age-date surfaces is that of saturation. While a surface ages, it will accumulate more craters: a cumulative size-frequency plot will have a slope of $b \approx -3$. However, this is only true to a point. Beyond a given crater density, no new craters will be able to form without erasing an equivalent area of existing craters. At this time, no new information can be gleaned from craters of that size since the number per bin will no longer increase. Because smaller craters accumulate more quickly than larger craters, smaller craters will become saturated first. The slope on a cumulative SFD when saturated is $b \approx -1.8$, but it is usually approximated as $b \approx -2$ (*e.g.*, Hartmann, 2005).

There are two different types of saturation - one is theoretical and the other is what happens on a real planetary body. First, geometric saturation is the theoretical saturation of a surface when craters are arranged in a honey comb-like hexagonal closest-packing, such that the maximum number possible may be emplaced without overlap. Since, in theory, an infinite number of craters could be emplaced if one continued to shrink their size, a practical limit was placed upon the derivation where two orders of magnitude would be considered part of a hexagonal pack. It was found that in this case, the number of (saturated) craters of a given diameter is $N_s = 1.54D^{-2}$ (Gault and Wedekind, 1978). The second, practical type is "equilibrium," sometimes referred to as "empirical saturation." This is the practical limit when craters are deposited randomly on a planetary body. Experiments by Gault and Wedekind (1978) showed that when randomly deposited, craters would reach equilibrium at 1-10% of geometric

saturation, with 5-7% being the mean. No planetary surface comes close to geometric saturation; the closest known is on Mimas, and it is only for craters 10-20 km in diameter that equilibrium is as large as 13% of geometric saturation (Melosh, 1989).

The fifth and final main complicating factor involves secondary craters. Secondary craters were first problematized a half century ago (Shoemaker, 1962) and, while further work was done over the years (*e.g.*, Shoemaker, 1965; Oberbeck and Morrison, 1974; Wilhelms *et al*., 1978), the issue was generally ignored by the planetary community until recent years with a pair of papers (Bierhaus *et al*., 2005; McEwen *et al*., 2005). Their work showed that secondary craters can indeed confound planetary ages and crater statistics over large portions of the surface. Despite 50 years of study, secondary craters remain a relative enigma in terms of secondary crater SFD (*e.g.*, McEwen and Bierhaus, 2006; Ong *et al*., 2011; Robbins and Hynek, 2011d), where secondary craters will be emplaced relative to the primary (*e.g.*, Lucchitta, 1977; Schultz and Singer, 1980; McEwen and Bierhaus, 2006; Preblich *et al*., 2007; Robbins and Hynek, 2011a, 2011d), or even a model that can predict if secondary craters will be produced in abundance or paucity from a primary impactor. There is no solid model for how these form nor for their properties, so they must be taken into account on an individual basis by individual researchers, some of whom doubt their existence (*e.g.*, Neukum *et al*., 2006) or influence (*e.g.*, Hartmann, 2007). Generating large global databases of craters with features complete down to small sizes is therefore an important step in understanding secondary craters: They begin to allow detailed studies of secondary craters in a uniform, global, and terrain-dependent manner (Robbins and Hynek, 2011d, or Section 4.2).

1.4.2. Modification Effects on Craters

As a surface accumulates craters, the craters themselves will be emplaced according to a production function with slopes of $b \approx -3$ on a log-log cumulative size-frequency graph during the present day (various lines of evidence suggest this has changed throughout time, *e.g.*, Strom *et al*. (2008)). It will continue to accumulate craters until it reaches an equilibrium point, at

which time no new craters can be deposited of that size range, and the slope will turn over to $b \approx -2$. However, this only occurs if there are no other processes affecting the craters. On airless bodies such as the Moon and Mercury, this is not usually a complicating factor; on Mars (and to a much greater extent, Earth), it is the *de facto* case, and craters' modification and removal yield important clues to the planet's history.

Physical weathering is an important geologic process that acts to move material from a higher elevation to a lower one or transport it in general. Impact craters themselves are the simplest weathering that occurs on all planetary surfaces. These both destroy the surface in which the crater formed and deposit a blanket of ejecta in the surrounding terrain. The gravitationally driven process of mass wasting will also affect craters on all bodies (not to be confused with the modification stage of crater formation, discussed above). The effects will be a general lowering of the crater's uplifted rim and infilling of the crater floor from rim material, outside material, and wall material that has slumped, rolled, or fallen in.

The addition of a substantive atmosphere (Venus, Earth, Mars, and Titan) will greatly speed the weathering process, not only because wind itself will transport suspended material, but also because it will drive particles along the ground (creep) and transport them via saltation. Adding a low-viscosity liquid (*e.g.*, liquid water (Earth, Mars) or ethane (Titan)) increases the weathering rate again because of the sheer increase of mass: Liquids are much denser than gases under most circumstances, and so a flowing liquid will carry much more kinetic energy, allowing it to transport or erode a proportionally larger amount of material. High-viscosity fluids (*e.g.*, lava on Venus, Earth, Moon, and Mars) will result in even higher rates of erosion due to the greater kinetic energy; in a practical sense, lava will more likely cover and bury a region as opposed to carry and deposit material from one place to another. On bodies with temperatures close to the triple point of a molecule (*e.g.*, H_2O on Earth and Mars, C_2H_6 on Titan), thermal erosion will also play a role where the melting of permafrost will dramatically weaken the rock and can lead to collapse or more rapid erosion through the processes discussed above. The general effects of endogenic weathering on the size-frequency crater population are to remove

craters, and it is more likely to remove smaller craters than larger ones because smaller craters are shallower. For this latter process, studying partially buried impact craters can show the depth of lava burial, but this is only the case if one knows *a priori* what the original crater depth should have been, requiring regional studies into crater depth-diameter relationships (see Section 3.5).

The modification processes mentioned above (impacts, mass wasting, erosional, and burial) are the main ones that will modify the existing crater population on Mars. As a crater is modified, the depth will decrease and the crater diameter will increase; estimates are that the crater diameter can grow by up to 30% (*e.g.*, Melosh, 1989; Craddock, *et al*., 1997; Craddock and Howard, 2002). Lacking a raised rim at this point, it is much easier to transport material (aeolian and fluvial deposition) into the crater cavity, and it will eventually reach the point where it is completely filled (Craddock, *et al*., 1997), although it may still be detectable via subtle albedo differences or a topographic depression (Frey, 2006, 2008; Robbins and Hynek, 2011b).

These alteration mechanisms will affect a local surface uniformly (*e.g.*, Chapman and Jones, 1977), so a smaller crater will "feel" the effects of erosion more easily than a large crater. For this reason, it is possible to estimate the erosion or deposition rates based upon the smallest crater size that differs from a production or equilibrium crater population. For example, if there is an erosion rate of 1 μm/yr and craters 1 m-deep are emplaced once every 1 Ma, then the surface will have a significant deficit of ≲1 m-deep craters because they will be eroded at the same rate they form. One km-deep craters, meanwhile, would be much less affected. For this reason, the small impactor population and frequency of impact is open to much more interpretation than the larger ones: (1) The small crater population is more easily eroded so it is more difficult to compare with an expected production function, (2) the production function is poorly defined at smaller diameters because observing small solar system objects and determining a census is limited by their visibility, and (3) compounding effects of secondary craters at these diameters confuse the crater census and add further uncertainty to comparison with observed impactor populations.

If one assumes these issues have a minimal effect or can be well modeled and accounted

for in the analysis, then the erasure effect also can be used to roughly determine major erosive events at various locations through time. For example, Mars' highlands have a significant deficit of craters $5 \lesssim D \lesssim 30$ km (*e.g.*, Chapman and Jones, 1977; Barlow, 1988; Robbins and Hynek, 2011b). Craters smaller than this are in production. This is interpreted to mean Mars suffered a substantial erosive event in its early history that resulted in the removal of many of those craters (*e.g.*, Chapman and Jones, 1977; Craddock and Maxwell, 1993) or it had a different production function at that time (*e.g.*, Barlow, 1988). By examining the morphology of the individual craters and the surfaces around them, it is thought that fluvial processes cause most of the erosion (*e.g.*, Craddock and Maxwell, 1993; Craddock and Howard, 2002). The erosion cut-off time can be estimated based upon what crater sizes are in production, since it will take longer to accumulate craters 1 km across than craters 1 m across.

1.4.3. Types of Crater Distribution Graphs

From the above discussion, the size-distribution of craters on a planetary surface can inform a researcher of numerous processes that have occurred both on the surface and to the impactor population. To analyze these, there are three different types of graphs that can be generated from crater data that only require knowing the diameters of the craters. These are crater "size-frequency distributions" (SFDs) (see Arvidson *et al*., 1979). The three types of SFDs are incremental SFDs (ISFDs), cumulative SFDs (CSFDs), and R-plots (relative plots). Except for specialized applications, such as database comparison, all SFDs should be normalized to the surface area on which the craters were identified. Crater SFDs fundamentally follow a power-law distribution, where there are many more smaller craters in a population for a given number of larger craters. For this reason, SFDs are displayed on log-log axes. Examples of these three types for the same two regions of the planet Mars are shown in Fig. **2**; the regions show a relatively young section of Mars centered around Utopia Basin (25-45°N, 110-150°E) and a comparatively old portion of the Martian southern highlands (25-45°S, 140-180°E). The areas of each are the same, 2.3×10^6 km^2.

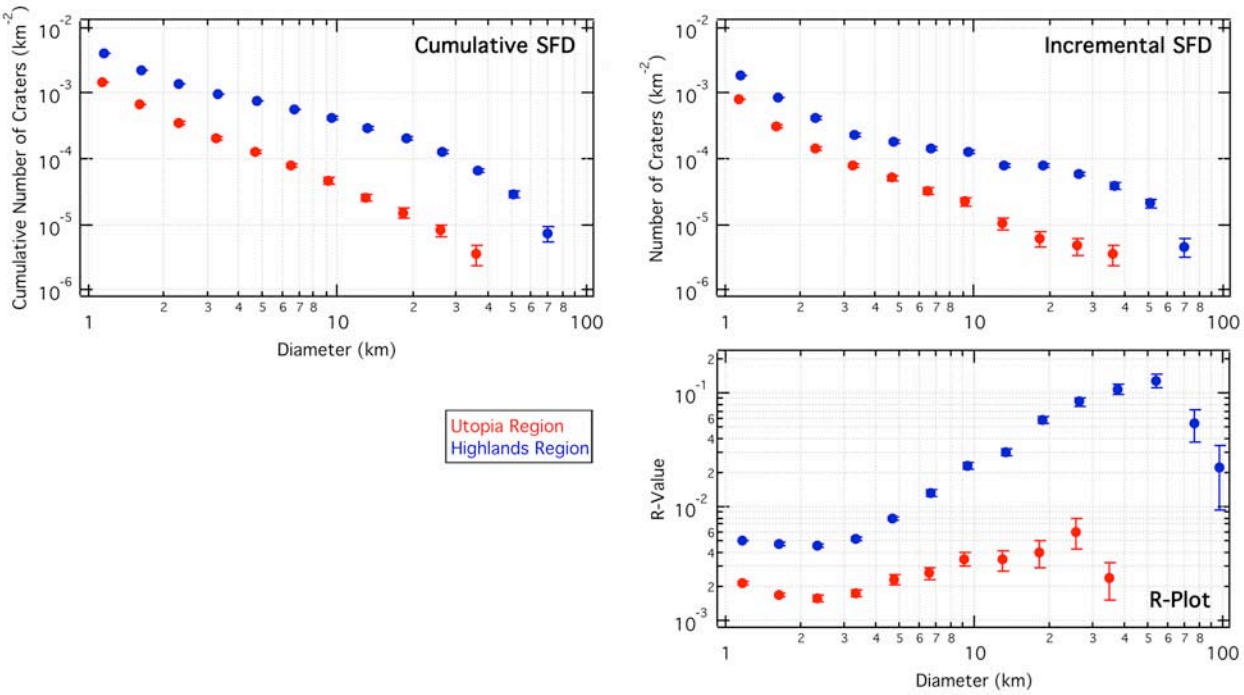

Figure 2: Examples of incremental, cumulative, and R-plots size-frequency distributions of the same two areas of Mars.

ISFDs are, at their core, a histogram of craters where the diameter is plotted on the abscissa and number of craters per diameter bin are displayed on the ordinate. The diameters are binned such that they are evenly spaced on the horizontal axis. The common diameter interval is D to $\sqrt{2}D$ (Arvidson *et al*., 1979). Individual researchers may vary this interval depending upon the range and number of craters in their data, but they will usually do so in integers N of the D to $\sqrt[N]{2}D$ range and not have coarser binning than recommended by Arvidson *et al*. (1979).

CSFDs are generated usually as a derivation from an ISFD. The data from the ISFD are integrated (discretely summed because the data are not continuous) from larger diameters through smaller diameters such that the smallest diameter bin contains all craters within the sample region. CSFDs are much more common in the literature than ISFDs and it is for these types of plots that crater isochrons are usually calculated. An alternative method of generating a CSFD is to sort the craters from largest to smallest diameter bin and then display diameters on the abscissa and row number on the ordinate since the row number will be the sum of the number of all craters larger than it. Because CSFDs are - by nature - cumulative, their values at smaller

diameters are resolution-independent.

Both ISFDs and CSFDs show that craters usually follow a simple power-law distribution. Production functions on a CSFD from present-day cratering rates typically have slopes $b \approx -3$, while cratering during the Heavy Bombardment and LHB have been shown to probably follow different slope distributions (*e.g.*, Barlow, 1988; Strom *et al*., 2008). Examining crater populations for deviations from the expected slopes are the most common use of these kinds of plots, but many researchers find them unsuitable for ready visual inspection of these differences.

Hence, the R-plot SFD type can be used. This is a type of ISFD where the data are normalized to a $b = -3$ slope such that a crater population with an ISFD $b = -3$ slope will be a horizontal line. Similar to the other types, the horizontal axis contains crater diameter and the diameter bins are again in intervals from *D* to $\sqrt{2}D$. The value *R* is calculated from Eq. 1:

$$R = \frac{\bar{D}^3 N}{A\left(D_b - D_a\right)} \tag{1}$$

where $\bar{D}$ is the geometric mean of the diameters of the craters between D_a and D_b or, if these are unavailable, then the diameter bin boundaries ($\bar{D} \approx \sqrt{D_a D_b}$); *N* is the number of craters in the diameter bin, *A* is the surface are of the region in which craters are identified, and the diameter bins are $D_a < D_b$ (Arvidson *et al*., 1979).

Different groups of researchers each prefer different SFD types. When comparing results with other groups, one must be cognizant of this. For example, W.K. Hartmann (*e.g.*, Hartmann (2005)) prefers the ISFD display. His isochron work (Hartmann, 2005) is determined for an ISFD and so when using the Hartmann isochrons, one must use the ISFD type plot. Alternatively, G. Neukum (*e.g.*, Neukum *et al*., 2001) prefers CSFD plots and so when utilizing that group's isochrons and comparing with their data (*e.g.*, Neukum *et al*., 2001), one must also use a CSFD. Meanwhile, other researchers, such as Strom (*e.g.*, Strom *et al*., 2008) and Chapman (*e.g.*, Chapman *et al*., 2002) prefer R-plots. It is generally recommended that at least an R-plot and ISFD or CSFD are displayed for the same data in publications (Arvidson *et al*., 1979), though this recommendation is rarely followed.

1.5. The Importance of Detailed Crater Catalogs

The above discussion details the formation process of impact craters, their basic properties, and uses. While this discussion is fundamental to understanding craters and their importance, its utility is severely diminished without actually having craters in a catalog or database to study (both terms – catalog and database – are used interchangeably throughout this document). Uniformly generated crater databases from a single method and a single researcher or group are fundamental to using craters for a diverse range of investigations – from better understanding the impact process to age dating to discerning the properties across the planetary surface upon which they are emplaced.

Combining different groups' catalogs can lead to biases within the metacatalog, as discussed above and estimated by Hartmann *et al*. (1981) and Lissauer *et al*. (1988) to be a factor of $\sim 1.2-1.3\times$. This basic concept formed one of the core justifications for compiling the original *Catalog of Large Martian Impact Craters* (Barlow, 1988) and its revision (Barlow, 2003), and it was a prime factor in generating global catalogs since (*e.g.*, Stepinski *et al*., 2009; Salamunićcar *et al*., 2011; Robbins and Hynek, 2011b, 2011c). Inclusion of more and smaller craters permits more detailed studies to be done, allowing detailed stratigraphy and age relationships (*e.g.*, Tanaka *et al*., 2011), as well as broad, uniform studies of secondary crater characteristics and relationships relative to their primaries (Robbins and Hynek, 2011d).

Detailed morphologic and morphometric data significantly assist in the above tasks. At a fundamental level, characterizing the interior morphology of craters results in the formulation of basic scaling laws discussed above (Section 1.3) and below (Section 3.6). Morphometric information about crater topography (depth, rim height, etc.) permits testing of fundamental scaling laws of crater depth-to-diameter ratios (Section 3.5). Once these have been established for a fresh crater population (requiring crater degradation/modification state (see Section 2.4.4)), changes among fresh crater depth-to-diameter ratios can be used to track different strengths of the planet's crust (Section 3.5.1), and different infilling/erosion rates across the surface (Section 3.2.5). Observations of ejecta blanket morphology from the first Mars flyby missions identified

cohesive, layered ejecta blankets on Mars not previously observed in the solar system and only now found on Mars, Ganymede, and Europa (see Barlow *et al*., 2000, and references therein) (Section 3.3.3.1). Careful morphologic classifications included in a global database allow for craters to be studied in a uniform, global way and, when combined with morphometric properties, permits testing of formation hypotheses.

Put concisely, the broad, fundamental importance of impact crater databases is: They allow detailed, uniform studies of planetary surfaces, applicable to a wide variety of diverse and important applications from predicting effects bombs and missiles to planning for planetary catastrophes to basic science research. To fulfill the potential of modern data for allowing this work on Mars, I have manually compiled the largest database to-date of impact craters on a single body: the planet Mars in this case. The craters number 631,333 in total and 378,540 with diameters $D \geq 1$ km. In this dissertation, I explain how I generated the database (Section 2) and a broad overview of its characteristics and a re-examination of classic scaling laws (Section 3) that will serve as a basis for future investigations. I then use the database to investigate some of the properties of secondary craters (Section 4). Finally, I delve deeper into the use of small craters, where I identified an additional ~100,000 craters within volcanic calderas and used them to partially reconstruct the history of volcanism across the planet (Section 5) in one of the most common applications of impact crater counting.

2. A New Global Database of Mars Impact Craters to 1 km: 1. Database Creation, Properties, and Parameters

Note: This paper is in preparation as: Robbins, S.J., and B.M. Hynek. "A New Global Database of Mars Impact Craters to 1 km: 1. Database Creation, Properties, and Parameters." (in prep. for Icarus). Though it has not yet been submitted, it is cited in this dissertation as "Robbins and Hynek, 2011b." Sections have been re-numbered and some reformatting has been done to fit the formatting of the rest of this dissertation. References have been combined with all others at the end of this dissertation. Acknowledgments have been combined with others at the beginning of this dissertation.

Abstract: Impact craters have been used as a standard metric for a plethora of planetary applications for many decades, including age-dating, geologic mapping and stratigraphic relationships, as tracers for surface properties, and as locations for sampling lower crust and upper mantle material. Utilizing craters for these and other applications is significantly aided by a uniform catalog of craters across the surface of interest. Consequently, catalogs of craters have been developed for decades for the moon and other planets. We present a new global catalog of Martian craters statistically complete to diameters $D \geq 1$ km. It contains 378,540 craters, and for each crater it lists detailed positional, interior morphologic, ejecta morphologic and morphometric, and modification state information. In this paper, we detail how the database was created, the different fields assigned, and statistical uncertainties and checks. In our companion paper (Robbins and Hynek, 2011c, this volume), we discuss the first broad science applications and results of this work.

2.1. Introduction

Since Galileo first turned his telescope to the moon and identified the three-dimensionality of craters (Galilei, 1610), people have been cataloging craters on the solar system's solid bodies. Some of the first modern crater catalogs were generated in preparation for the *Apollo* missions in the 1960s with other geomorphologic features (*e.g.*, Kuiper, 1960; Schimerman, 1973), followed by more methodic and global catalogs in the subsequent decades (Pike, 1977, 1988 and references therein; Wood and Andersson, 1978). When the first images of Mars were returned by *Mariner 9*, craters were cataloged there, as well. The first global crater database of Mars was created by Nadine Barlow, published two decades ago (Barlow, 1988), and it contained all 42,284 craters with diameters $D \geq 5$ km identifiable from *Viking* images. The database contains the locations and diameters of craters along with basic morphology, though it is referenced in the Mars Digital Image Model 1.0 (MDIM 1.0) and hence crater locations are no

longer accurate in the present MDIM 2.1. Nonetheless, this has stood as a reference set for the past two decades and is distributed as a standard package with other Mars datasets by the United States Geological Survey (USGS).

Since that time, higher-quality and -resolution imagery has been taken of Mars, as has topographic data, which can be used to produce a new generation of a Mars crater catalog. Barlow is in the process of updating the "Catalog of Large Martian Impact Craters" (*e.g.*, Barlow, 2003), which will update the locations and diameters, remove false positives, and include some missed craters $D \geq 5$ km from the original catalog; it will also include topography information, more morphology, and a more detailed degradation state (c.f. Barlow, 2004 for a discussion of degradation state). Besides manual identification methods, automated approaches have been made to cataloging Martian impact craters. Notably, Stepinski *et al.* (2009) published a catalog stated to be complete to roughly $D \sim 3$ km (see Section 2.7.5.2). It was created by purely automated machine-learning techniques utilizing the *Mars Global Surveyor*'s Mars Orbiter Laser Altimeter (MOLA) data (Zuber *et al.*, 1992; Smith *et al.*, 2001). It contains the locations, diameters, and depths of all identified craters, approximately 79,000. Since MOLA data were used to define MDIM 2.1, the Stepinski *et al*. (2009) catalog is in the MDIM 2.1 system. An additional meta-approach has been used to combine existing crater catalogs into a single database and location (*e.g.*, Salamunićcar *et al.*, 2011). This method relies upon a computer algorithm to match craters across input databases and return an average location and size. These are subject to manual checking. This has resulted in a database with ~129,000 craters (see Section 2.7.5.3).

While global crater catalogs are perhaps the most useful, local or type ones have been generated for Mars' craters since the first imagery was returned over four decades ago. These have been amassed with different purposes for each one. A distinct advantage of smaller catalogs is they can go into greater detail in terms of morphologic and morphometric crater properties due to the shear time involved for each crater. Examples of global type catalogs are usually limited to fresh craters (*e.g.*, Roddy *et al*., 1998; Boyce and Garbeil, 2007), though some

are incredibly specialized, such as a catalog that only includes crater-exposed bedrock (Tornabene *et al*., 2010).

We are delivering an independently created Martian crater catalog with 378,540 craters complete to diameters $D \geq 1.0$ km, though we possess and will distribute the additional ~250,000 craters used to ensure this completeness on an individual basis upon request. All craters were manually identified and measured as discussed in Section 2.2. The catalog also contains detailed topographic information (Section 2.3), interior morphology including degradation state and whether the crater is a secondary (Section 2.4), ejecta morphology (Section 2.5), and ejecta morphometry (Section 2.6). We discuss the completeness of the current release of this database in Section 2.7, and science results are laid out in our companion paper, this volume: "A New Global Database of Mars Impact Craters to 1 km: 2. Global and Regional Properties and Variations, and Their Implications to Surface Properties and Gravity Scaling." Appendix A lists all the parameters found in this database.

2.2. Crater Identification and Position, Diameter, and Ellipse Parameter Measurements

The bulk of crater identification and classification was done using THEMIS Daytime IR planet-wide mosaics (Christensen *et al.*, 2004). The THermal EMission Imaging System (THEMIS) aboard the *2001 Mars Odyssey* NASA spacecraft is a multi-spectral thermal-infrared imager, sensitive to wavelengths between 0.42-0.86 μm and 6.8-14.9 μm. The bands were chosen to be sensitive to mineralogy of interest to the Mars Exploration Program (*e.g.*, carbonates and hydrothermal silica). One of the initial goals for the instrument was to create a global mosaic of the planet at 100 m/pix in both day and night from which - among a broad array of applications - thermal inertia maps could be calculated. The average local time for daytime observations is 4:30 P.M. to yield a high phase angle with shadows and heating effects sufficient for geomorphologic feature identification.

As of this writing in early 2011, the instrument and spacecraft are still in operation, continuing to provide data nine years after orbit insertion. Mosaic revision from the stream of

returned images is still being done, though the public release cycle is much less frequent. The current public version was released on June 23, 2010, at 100 m/pix from the band centered at 12.57 μm. It has roughly ~99% global coverage of usable data with the largest gaps in the high northern latitudes. The mosaics are constructed from a semi-controlled net to the MOLA basemap (Hare, pers. comm.). This results in small offsets when compared with MOLA in some areas in the present release of a maximum of ~1 km, though there is image doubling in some areas due to the lack of a complete control net and blending.

In *ArcGIS* software, THEMIS Daytime IR mosaics were used to manually locate all visible craters with diameters $D \gtrsim 1$ km in approximate local coordinate systems. The THEMIS Daytime IR dataset initially used covered ~90% of the planet at 256 pix/deg resolution (230 m/pix at equator). In August 2010, the new THEMIS mosaics at 100 m/pix were used for the final stages of the database and all morphology; THEMIS data are publicly available through USGS's PIGWAD website. Global mosaics were searched a total of four times for craters to ensure as complete a database as possible. The final search was the only search made with the June 2010 data release.

Crater identification was accomplished using *ArcGIS*'s editing tools to draw a polyline that traced the visible rim of each crater. Partial rims were only identified for the parts that were visible. Polylines were created with vertex spacing of approximately 500 m such that each representative rim ideally consists of $\sim 2\pi D$ vertices where D is the crater diameter (see Fig. **3**). All vertices were saved as double-precision points in decimal degrees units. Analysis of all polygons was completed in *Igor Pro* software due to its advanced data visualization capabilities and familiarity with its built-in programming language.

The initial crater search used both THEMIS and Viking maps. Most latitudes were searched in the standard Mercator cylindrical projection while those poleward of ±65° were searched in a polar stereographic projection. The second search was done in the same manner except the on-screen scale was decreased to identify possible missed larger craters. The third search relied upon MOLA topographic maps at the highest resolution available (up to 1/512° per

pixel at the poles (14 m/pix at 70° latitude), 1/128° per pixel equator-ward of ~65-70° latitude (463 m/pix at 0° latitude)) to identify craters that may have a topographic signature but not an obvious visual one (similar to "quasi-circular depressions" (Frey *et al.*, 2002) though Frey *et al.* do not claim that all identified features are craters). From the first two searches, 286,623 craters had been identified, and an additional 5,651 craters were identified with the MOLA search. While this represents an increase of only 1.97%, it represents an increase of 4.06% for craters $D \geq 5$ km, indicating that inclusion of topographic data in crater identification is an important tool.

The final search was completed at significantly higher on-screen scale due to the increased fidelity of the new THEMIS Daytime IR mosaics that were used exclusively for this step. Up to this point, the goal for the database had been to be statistically complete to 1.5-km-diameter craters. However, a large portion of the planet was complete to ~1.25 km while regions near the north pole were closer to ~3.0 km; the higher resolution mosaics available allowed the final search to succeed in bringing statistical completeness across the entire planet to D~1.0 km (Fig. **4**). Statistical completeness in this work is defined numerically from an incremental size-frequency plot; the diameter bin *D* greater than the diameter bin with the largest number of craters is considered to be the statistical completeness size (see Section 2.7.1). Due to the increased THEMIS resolution as well as the smaller crater sizes examined, the resolution at which vertices were laid down was increased by a factor of 2× to 1 point every 250 meters. 25% of the planet was searched again after this pass to verify completeness of identified craters.

2.2.1. Circle Fitting

All crater polylines were read into an *Igor Pro* file and fitted with a custom-written non-linear least-squares (NLLS) circle fitting routine. The basic theory behind a NLLS algorithm is to guess the parameters that best fit the data and then successively refine them by calculating the difference between the equation being fitted with those parameters and the actual data. For a circle, with three parameters (center *x*, center *y*, and radius), the initial guesses do not have to be accurate but should be non-zero. The algorithm employed started by converting the decimal deg-

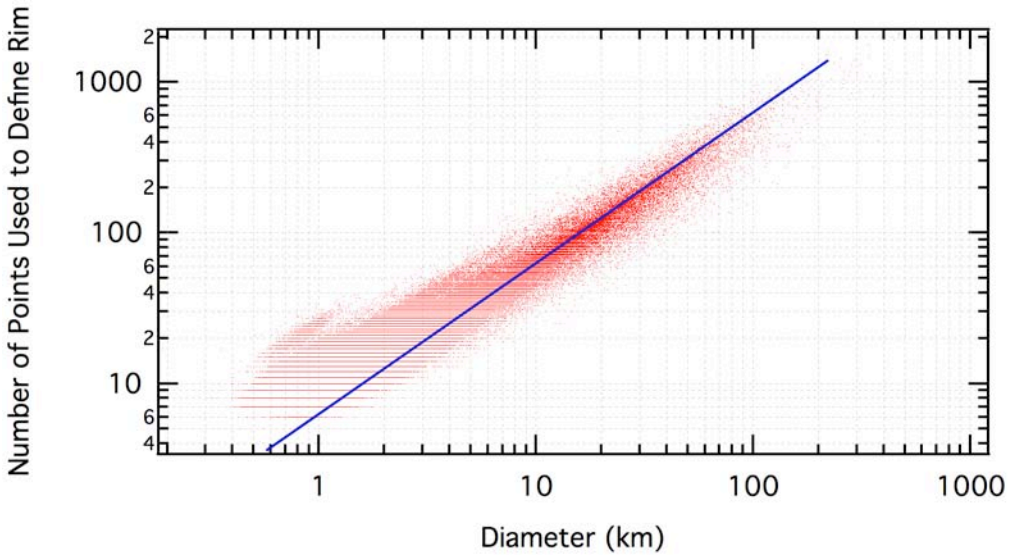

Figure 3: Number of points used to define each crater versus the crater diameter. Blue line is $2\pi D$. Points below the blue line are mostly due to only partial rims that are visible on the planet today. Points above the blue line are due to both occasional circling of craters twice to better-define the rim (especially at small diameters) and due to projection effects away from the equator. The cluster of points above the line around $D \approx 1$ km is from the final search where vertex resolution was increased to one point every 250 m. Posterization in the lower right is due to discrete points being used and the nature of logarithmic plots.

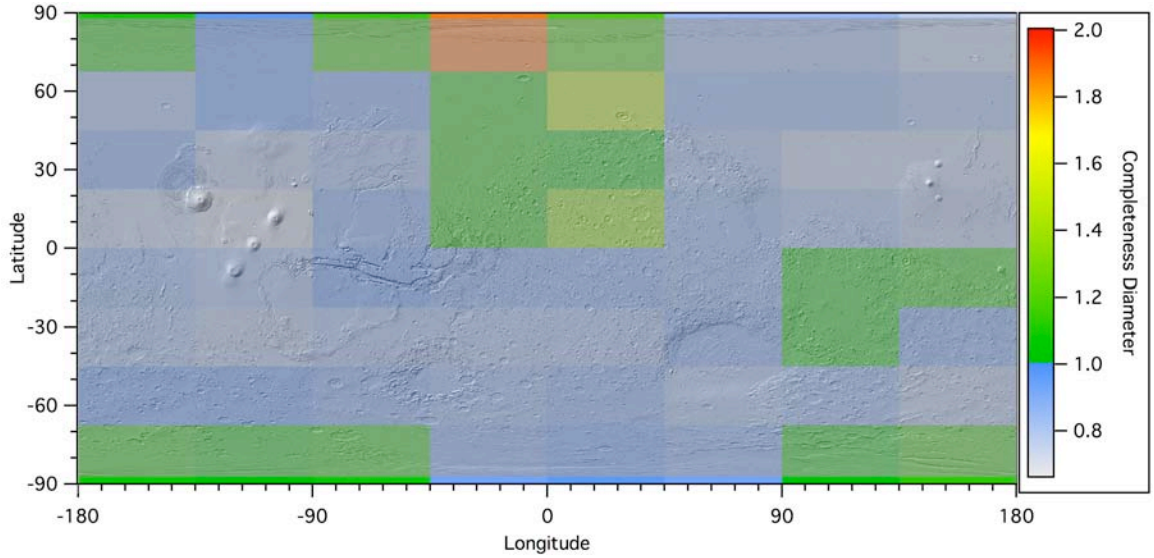

Figure 4: Color-coded area plot showing statistical completeness of crater diameters across the planet (see Section 2.7.1). Bins are 22.5° latitude by 45° longitude resolution. Finer resolution gives skewed results near the poles due to small number statistics. The low completeness in the bin centered at 78.75°N, -22.5°E is due to the young, large Lomonosov impact crater and the north polar cap, and the one centered at 56.25°N, 22.5°E is due to the similarly young, large Lyot impact crater. This is discussed further in Section 2.7.1.

rees of a crater's vertices into kilometers from the center of mass (the average of all x values and y values), eliminating all first-order projection effects. The vertices were then fit with the NLLS circle algorithm that saved the best-fit center latitude and longitude as well as the circle's radius. Latitude and longitude were converted back into decimal degrees, and the radius was multiplied by 2 and saved as the diameter. Uncertainties in the fit parameters were also saved (see Section 2.2.4).

2.2.2. Ellipse Fitting

Ellipse fitting was done by another custom-written NLLS algorithm in *Igor Pro*. There were five free parameters in this fit: a is the semi-major axis, b the semi-minor axis, x_0 the center longitude, y_0 the center latitude, and θ is the tilt of the ellipse's major axis. Ellipse fits to an arbitrary tilt in Cartesian coordinates are unstable because the partial derivatives are dependent upon either the inverse-square or -cube of the semi-major and -minor axes (see Appendix B). If a or b become small, the fit will rapidly approach infinity; if they become large, the fit will approach 0. An intelligent guessing of the major and minor axes was employed by taking the average of the maximum minus the minimum of the crater's longitudinal (x) and latitudinal (y) extents. These were multiplied by a random number drawn from a Gaussian distribution with $\mu = 1.0$ and $\sigma = 0.25$ and saved as the initial guesses for the major and minor axes. The tilt angle initial guess was drawn from a uniform distribution between $\pm\pi$ relative to a long axis oriented along a North-South line. Parameters were monitored during each fit iteration to verify they did not become too large nor small, and the fit was re-done up to five times with the requirement that it converged upon identical parameters at least three times (this is discussed in greater detail in Appendix B). If the fit converged, the crater's center latitude and longitude were recorded along with the major and minor axes, tilt angle, eccentricity e, and ellipticity ε. Eccentricity was calculated as $e = \sqrt{1 - b^2/a^2}$ and ellipticity is defined as $\varepsilon = a/b$.

2.2.3. Uncertainties in Crater Measurements

Because every crater was traced by hand and not by an unbiased (or uniformly biased) computer algorithm, there was a certain amount of random uncertainty inherent in every vertex identified. At the most basic level, an uncertainty of ±0.5 px was present based upon the limits of the data even if crater rim-tracing was perfect (~115 m at the equator for the first two searches, ~233 m at the equator for the third, and ~50 m at the equator for the final). There is also an inherent error in the digitization of an ellipse, and this is discussed in Section 2.2.4. Besides these two factors which can be estimated from theory, there was additional human error in the accuracy of each tracing.

The human error followed a Gaussian distribution about the true rim for a crater of a given size as measured by the residuals from numerous crater fits. This Gaussian was modeled from a sampling of ~40,000 craters via the following method: (1) After fitting a circle to a crater, the radial distance of each identified vertex was subtracted from the fitted circle radius. (2) The standard deviation of these residuals for each crater was calculated. (3) These standard deviations versus the crater diameter were fit to a power-law which modeled well the distribution, where the fit was of the form $\xi = y_0 + A \cdot x^p$ where ξ is the recorded value; y_0, A, and p are fit parameters; and x is the "true" location of the vertex. The fit parameters were calculated to be $y_0 = 0.015 \pm 0.001$, $A = 0.024 \pm 0.000$, and $p = 0.938 \pm 0.003$.

To understand the effects of this on the final crater database, an ideal circle of different diameters was modeled with each size having $2\pi D$ vertices. To the x and y value of each vertex, random noise drawn from a Gaussian distribution was added where the standard deviation of that Gaussian was given by the modeled power-law described above. For example, a D = 5 km crater was modeled to have a standard error in each vertex of ~±0.12 km. A Monte Carlo set of simulations both fitting a NLLS circle and ellipse to the model crater was run. The ratio of the fitted diameter versus the true diameter of the circle fit was recorded as was the ellipticity ε as a tracer of the uncertainty in the ellipse fit. This simulation was performed for 10,000 craters each at diameter between 1.0 and ~53 km in multiplicative intervals of $2^{1/4}D$.

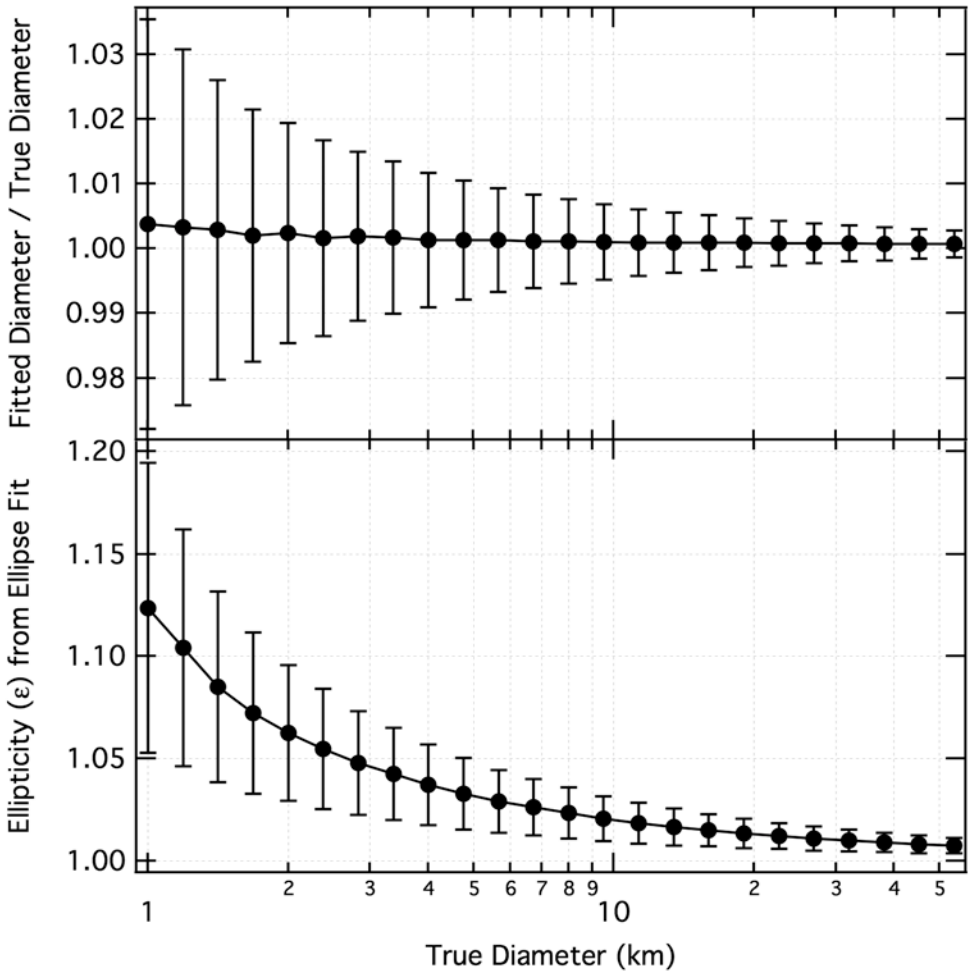

Figure 5: Both panels show the results of Monte Carlo simulations using the NLLS circle and ellipse on a "noisy" circular crater model. Ten thousand simulations for each diameter point were conducted (1.0-53 km in $2^{1/4}D$ multiplicative intervals), and the mean and standard deviation of the results are shown (at larger diameters, error bars are smaller than the symbol size). Top - Deviation of the circle-fit diameter from the true model diameter, where 1.00 would be a perfect match. Bottom - ε, which should be 1.00 for the modeled circle.

The mean and standard deviation of each simulation set of circle diameters were recorded and plotted against the true diameter (Fig. **5**, top panel). A very small aliasing of 0.4% was present at the smallest diameters. For D = 1 km, the Monte Carlo simulations show the NLSS fit is 100.4±3.2% of the true diameter with this noise model; it drops to <100.1% for $D \gtrsim 10$ km, and the $\mu \pm \sigma$ range of the fits was within the true diameter for all crater ranges examined. It should be noted that this is an over-estimate for most of the small craters since the majority of $D \sim 1$ km craters were identified in the final search at higher resolution - both imagery and on-screen

display. A comparable model is run for the increased resolution of the final crater identification (noise model: $\xi = (-0.009 \pm 0.000) + (0.041 \pm 0.000) \cdot x^{0.781 \pm 0.003}$). The $D = 1$ km value is 100.3±2.8%.

The ellipticity ε should be 1.0 for all cases (*a* and *b* should be the same) if the fit were perfect and the noise level 0%. The mean and standard deviation of $\varepsilon(D)$ are shown in Fig. **5**, bottom panel. Fits to smaller craters were significantly different from their true values as expected based on the following thought experiment: A 1.0-km-diameter crater will have approximately 6 vertices and be 5 pixels across. If one of those vertices is 1 pixel "outside" of the true circle, while another is 1 pixel "inside," a ~6 by 4-px ellipse results with $\varepsilon = 1.5$; it will be less if the offsets are not two vertices apart. Therefore, it is incredibly "easy" to get large ellipticities from such small craters simply due to very small errors in tracing. ε fell below the 1.1 level for $D \gtrsim 1.5$ km, and it fell below the 1.05 level for $D \gtrsim 2.5$ km.

An alternative way of presenting these data is how likely the ellipse fit resulting in a value ε is a true representation of that value for a stated *a priori* confidence level. This can be done by creating a histogram of the Monte Carlo results for each diameter test and calculating a

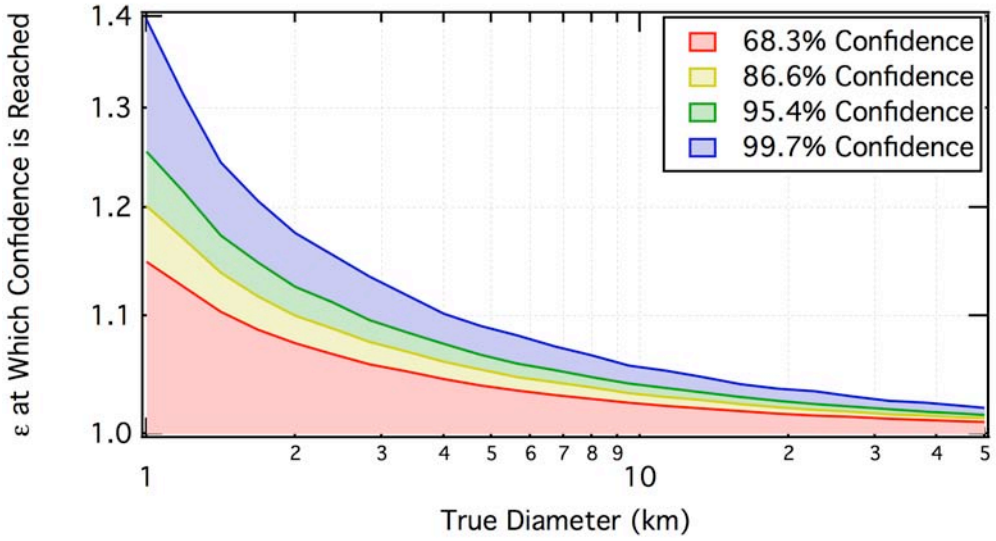

Figure 6: For the uncertainty model described in the text, the shaded regions represent all ε at which the confidence that the fitted ε is a true representation of the crater's ε for a given confidence level. For example, if one wanted to state with 95.4% confidence (2σ) that a D = 2 km crater had a certain ε value, they could only do so for $\varepsilon > 1.44$ from this database.

cumulative probability distribution from it. The ε value at which the fraction of simulations is equal to the confidence level is then determined. This was graphed for 68.3%, 86.6%, 95.4%, and 99.7% confidence levels in Fig. **6** (corresponding to 1, 1.5, 2, and 3σ in a Gaussian distribution). From this Figure, a crater diameter must be D > 2.2 km for the confidence to be 68.3% that a derived $\varepsilon < 1.1$ is a true reflection of the crater. D > 4.0 km, >5.7 km, and >8.2 km are the requisite diameters for the 86.6%, 95.4%, and 99.7% confidence levels, respectively.

2.2.4. Uncertainties in Circle-Fit Parameters

A FORTRAN95 code released as "ODRPACK95" by Zwolak *et al*. (2004) is incorporated into the *Igor Pro* software. It can analytically calculate uncertainties for implicit functions (functions that are not a simple function y of x) was used. This package was incorporated into the NLLS circle-fitting algorithm discussed above to calculate formal uncertainties in the fitted central latitude and longitude and the circle's diameter. These are found in the catalog (see Appendix A). The uncertainties relative to the crater diameter were plotted, and the results were binned in multiplicative intervals of $2^{1/16}D$. A piece-wise power-law function (Eq. 2) describes the uncertainty:

$$\delta D = A \cdot D^{p} \begin{cases} A = 0.017 \pm 0.004,\ p = 0.531 \pm 0.058 & ,\ 5.78 \le D \le 150 \text{ km} \\ A = 0.032 \pm 0.009,\ p = 0.121 \pm 0.250 & ,\ 1.50 \le D \le 5.78 \text{ km} \\ A = 0.023 \pm 0.004,\ p = 1.122 \pm 0.862 & ,\ 0.86 \le D \le 1.50 \text{ km} \end{cases} \quad (2)$$

where δD is the uncertainty in km for a given crater diameter D in km. This can be applied in the following examples: The average fit uncertainty $\delta D(D = 1 \text{ km}) = \pm 0.02$ km (2%), $\delta D(D = 5 \text{ km}) = \pm 0.04$ km (1%), $\delta D(D = 10 \text{ km}) = \pm 0.06$ km (0.6%), and $\delta D(D = 50 \text{ km}) = \pm 0.14$ km (0.3%). These formal uncertainties may appear somewhat small, but analytically they are the best estimates from the data of what the uncertainty *from the fit* to each crater. Additionally, analysis of several craters with higher-resolution imagery resulted in very similar diameters with a general deviation at the ~few-percent level. Examination of these relative to the power-law of the mean of a Gaussian uncertainty in the circle fits from Section 2.2.3 suggests similar values at small diameters, but values closer to ~1% for $D > 10$ km. These are about an

order of magnitude smaller than the quoted uncertainty in the Barlow (1988) database of ~±10%.

Finally, there is a theoretical uncertainty from simple digitization: When a continuous shape is discretely digitized, a resolution-dependent uncertainty results, similar to that discussed in Section 2.2.3. This is described by Sladoje and Žunić (1997), who found that with ellipses of approximately this size with the lower resolution at D~1 km, the absolute error is on the order of ~10%. At resolutions corresponding to craters D~10s km, the absolute error is on the order of 1% or less. Since this is generally comparable to the fitted errors overall from ODRPACK95, the numerical method from the data was used as opposed to the theoretical one from Sladoje and Žunić (1997).

2.3. Determining Crater Topographic Properties

One key difference between this extensive database and the current public Barlow catalog is the inclusion of a myriad of topographic properties. Only in the past decade has wide-spread planetary topography been available for Mars, making a uniform derivation of rim heights, surface elevation, and crater floor depth possible (Smith *et al.*, 2001). The Stepinski *et al.* (2009) catalog includes depth information from an automated method, while that information was derived manually for this catalog and is being manually derived for Barlow's revised catalog (pers. comm.).

The instrument that collected the data used for this work is the Mars Orbiter Laser Altimeter (MOLA) (Zuber *et al.*, 1992; Smith *et al.*, 2001). The instrument operated by measuring the light-time-return of a 1.064 μm laser pulse sent from *Mars Global Surveyor*, through Mars' atmosphere, reflected off the surface, and returned to the craft and collected in a 0.5-m parabolic mirror. The instrument had an emission rate of 10 Hz for each 8 ns pulse which, based on the average orbital speed, resulted in an along-track footprint spacing of ~300 m while each footprint was ~160 m in diameter due to spreading; inaccuracies in spacecraft orbit reconstruction result in uncertainties of ~100 m of where the footprint is centered. The across-track spacing varied significantly with latitude but was generally <2 km at the equator and

smaller closer to the poles. Range resolution was approximately 0.37 m though vertical accuracy is ~1 m due to spacecraft orbit uncertainties (Smith *et al*., 2001). The instrument operated for several years before it failed and was used as a passive detector after having returned approximately 595 million topographic measurements that now form its primary dataset (Neumann *et al*., 2003a, 2003b).

The reduced and calibrated MOLA data are available in two primary formats – point/shot and gridded. MOLA Precision Experiment Data Record (PEDR) is the former and is the actual latitude, longitude, and range to the surface for each 595 million points returned over the operating lifetime of the instrument. Ideally, these are the data that would be used in any analysis because they have undergone the least amount of manipulation. In contrast, the MOLA Experiment Gridded Data Record (MEGDR) is the binned and interpolated MOLA data across the planet. Due to the fidelity of the data, MEGDR is available in up to 1/128° per pixel (~463 m/pix at the equator). Due to the spacecraft orbit, higher MEGDR are available near the poles at up to 1/512°/pix. MEGDR were used in this work (as described below) because MEGDR were searched similarly to THEMIS maps and this required a uniformly gridded dataset. Using PEDR would have required a rough visual interpolation to discern craters independently of the THEMIS markings, defeating the purpose of using PEDR to begin with.

2.3.1. Manual Topographic Measurements

After crater identification and fitting, the second cataloging step was to use MOLA gridded topographic data (Smith *et al.*, 2001) at 1/128° resolution to derive relevant topographic information for each $D \geq 3$ km crater. The height of the rim, elevation of the surrounding surface, and greatest depth of the crater cavity were recorded. This was done in *Igor Pro* software using custom-built algorithms. Manually, an *N*-dimensional polyline was created that identified points along the crater rim. A second polyline was created to identify the surface outside of the crater and its ejecta to estimate the pre-impact surface elevation; this was the most prone to uncertainty. A third polyline identified the lowest points in the floor of the crater.

Because of the non-idealities of the Martian surface (*e.g.*, craters often overlap other topographic features or each other), this is a step that cannot yet be effectively performed with the same accuracy by an automated algorithm.

From these three polygons, the average rim height, average surface elevation, and average crater floor depth were calculated along with the standard deviations as an estimate of the uncertainty in these measurements. MOLA MEGDR count data were used to eliminate gridded points with 0 actual PEDR points that went into them. In addition to the topographic information, NLLS circle and ellipse fits were performed from the rim polygons to serve as a verification and validation of the THEMIS-based diameters (see Section 2.3.4 for a discussion of this comparison). The total number of points of the polygons (as well as the polygons themselves) were also saved so that: (1) A researcher may exclude from further analysis craters that had less than a certain number of points identifying, for example, the rim; (2) if different or better algorithms for determining circle or ellipse fits are created in the future, they can easily be run on the polygons without needing to recreate them; and (3) it allows for spot-checking of random and outlying craters for both self-consistency and consistency between different researchers. Keeping track of this information and the uncertainties associated with each parameter in the new database allows for a more robust statistical analysis than has previously been done. This has not been included in other crater databases and will be of benefit to the user of the final, released product.

This step could not be performed for all craters due to the coarser resolution of the MOLA gridded data compared with THEMIS. The final cut-off is that craters $D < 3$ km were not analyzed due to the inherent data limitations as discussed below and in section 2.7.2. Any craters that either (a) cannot be seen in the MOLA data, or (b) have too few non-interpolated pixels to be accurately analyzed (generally fewer than 5-10 pixels across) were also not analyzed in this step.

The approach described above is different from what some researchers have done in the past. Notably different is that topographic data were used in lieu of photoclinometric and

shadow techniques (*e.g.*, Davis and Soderblom, 1984; Pike, 1988). But even from topographic data, different researchers use a somewhat different definition of rim height and floor depth, namely using the maximum elevation along the rim and the minimum depth in the floor instead of an average (Stepinski *et al.*, 2009). However, the method used here is not without precedence, as it follows that used by the IMPACT program developed by Mouginis-Mark *et al.* (2004), or other manual methods such as those by Boyce *et al.* (2005).

2.3.2. Using Gridded Versus Spot MOLA Topography Data (MEGDR vs. PEDR)

Potential questions with regards to the original location of the MOLA data points arose when using the MEGDR data. While many unmistakable artifacts from poor coverage in areas were avoided, a separate analysis of the topographic derivation by using the original spot data in a few locations was performed: The entire PEDR data record comprises roughly 595 million points (Neumann *et al.*, 2003a), and even when culled to just latitude, longitude, and elevation, it takes over 14 GB of disk space and brings standard modern workstations to a crawl. Consequently, craters on 1/8 of the planet were compared, corresponding to two of the regions in which the 1/128° MEGDR data are available. The first is a near-equatorial region, 0°-90° E and 0°-44° N. The second is a polar region, 180°-270° E and 44°-88° S.

The saved polygons from the main MEGDR topographic analysis were used. A nearest-neighbor search was performed for the closest PEDR point that matched a polygon vertex from the ~39 million PEDR points in each region. An arbitrary threshold that the closest PEDR point must be within 2 gridded pixels in MEGDR was set (1/64°, or 926 meters at the equator). If the closest was beyond this, then the original polygon point was eliminated from this test. Any duplicates were also eliminated (since two vertices could have the same closest PEDR point). With the new topography points from PEDR for the crater rim, surrounding surface, and crater floor, the same topographic analysis was performed: Mean elevation and standard deviation each were calculated for the rim, surface, and floor points.

To estimate the robustness of using MEGDR versus PEDR, the magnitude of the

difference of the means for the two rims (MEGDR and PEDR), surfaces, and floors values was analyzed. It was compared with the $\mu \pm \sigma$ calculated from the MEGDR analysis to determine if they were within the original estimated uncertainty range. Overall, the differences were on the scale of 10s of meters with 50% of the 17,190 craters having rim elevation differences <8.0 m, surface differences <5.8 m, and floor elevation differences <3.2 m. 95% of the craters had rim elevation differences <40 m, surface differences <41 m, and floor differences <32 m. When comparing the differences with the standard deviation computed for the MEGDR means, 0.94% were larger than the standard deviation for surface elevation, 0.13% had surface elevation differences larger than the standard deviation, and 10% had floor elevation differences greater than the standard deviation. Given the meaning of a "standard deviation" being one would expect ~68.3% of the data to fit within it, results of 10% for the floor, <1% rim, and ~0.1% for the surrounding surface indicates using MEGDR as described above is reliable.

No significant trend with crater diameter was observed. The only one observed was that the largest outliers - where the differences between the MEGDR and PEDR elevation means were greatest - were for the smallest craters (as expected; see section 2.3.3 below); but, these were outliers and no statistically significant trend line could be fit through the mean difference as a function of diameter. Additionally no significant trend was observed in the offset as a function of latitude except at latitudes poleward of ~75° where the differences from the two data sources became less, likely due to the significantly higher point density.

As a test of the initial nearest-neighbor assumption, both regions were again analyzed but had the neighbor threshold changed to 1 MEGDR pixel (1/128°, or 463 m at the equator). The results were nearly the same, though differences were slightly larger (~5-10 m for 50% of the craters and 40-55 m for 95% of the data; the percentages with differences larger than the standard deviations were statistically identical).

From these analyses, it can be concluded that using the 1/128° MEGDR data sets, when avoiding clear interpolation artifacts, yields statistically identical results to using PEDR data for this kind of topographic analysis.

2.3.3. Robustness of MOLA Gridded Data Compared with Point Data

Some may argue that MOLA data are not practical for analyzing crater topography for diameters smaller than ~6-10 km (Boyce (pers. comm.) and Mouginis-Mark (pers. comm.)). In some cases, this is clearly true, especially with automated methods, due to two main reasons. First, simple gaps in the MOLA coverage result in interpolation that smooths the MEGDR and decreases topographic relief (*e.g.*, Mouginis-Mark *et al.*, 2004). However, these are usually easily avoidable because they are fairly clear when encountered. The second is more insidious: The MOLA instrument recorded data with an along-track spacing of ~300 m and had a surface spot size of ~160 m (*Smith et al.*, 2001). For smaller craters, on the order of 5 km, this could result in (a) the instrument missing the deepest portions of the crater floor, and (b) the instrument missing the crest of the crater rim. In either of these cases, a subdued crater profile would be derived and there is no obvious indication from the data that this would be in err. This is a situation where photoclinometric and shadow methods would likely obtain superior results *if* the surface has a uniform albedo.

To roughly characterize this potential offset, three pairs of craters $D \sim 5$ and ~ 20 km were selected at random from regions around 0°, -40°, and -80° North latitude and were examined with PEDR data overlaying THEMIS mosaics. An example at each diameter is shown in Fig. **7**. The MEGDR data that were used to identify the rims in roughly half the cases were found to fall within 2 pixels of the THEMIS rim crest, a distances chosen because that is comparable to the spot size of the MOLA footprint (there were significantly more at higher latitudes). When eliminating the rim points that did not have a PEDR point within that 2 THEMIS pixel tolerance, the rim heights calculated were affected by ±25 m at 0°, ±20 m at -40°, and ±10 m at -80°. These were all within the stated standard deviation recorded from the original MEGDR analysis. These indicate that rim heights in this database are reliable estimators given the MOLA data fidelity. Future work using HRSC (High-Resolution Stereo Camera aboard *Mars Express* (Neukum *et al*., 2004; Gwinner *et al*., 2010)) digital terrain models at ~100 m/pix scale may indicate the reliability of measurements on smaller craters.

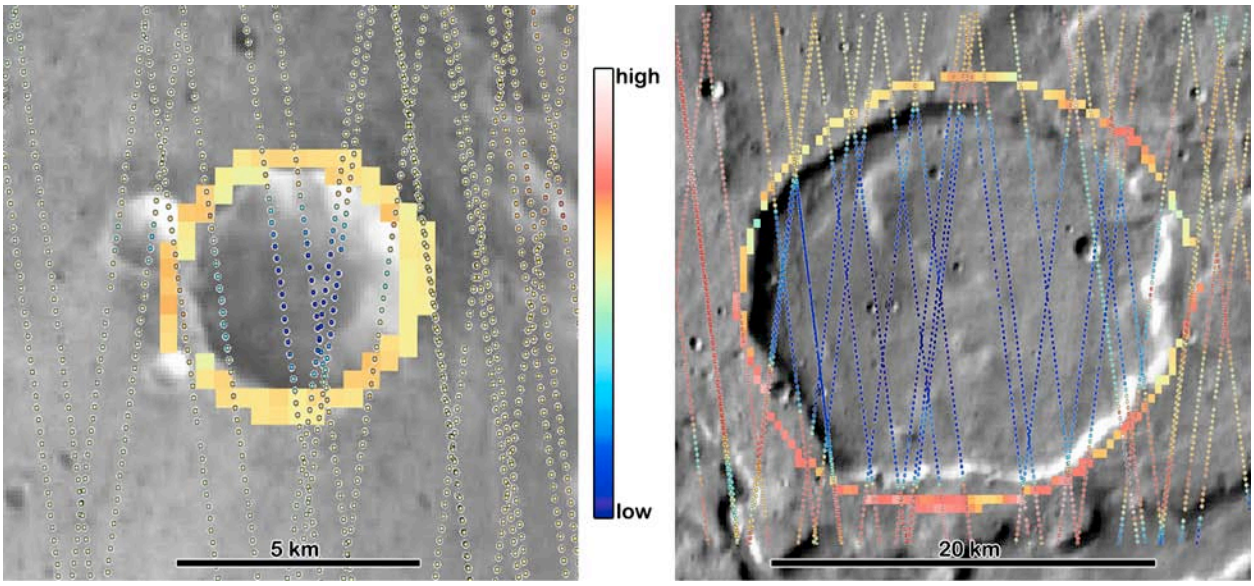

Figure 7: Images showing two craters with MOLA PEDR and MEGDR data overlaid. Left crater is D = 5.8 km (-1.5°N, 102.1°E) and right crater is D = 21.1 km (-40.1°N, 173.5°E). The background image is THEMIS Daytime IR mosaic. Colored squares around the rim are the MEGDR data that were used to define the rim height in the main topographic analysis. Smaller colored circles show the PEDR tracks. Where a circle does not overlap a square, the MEGDR data point had no actual data and was purely interpolated. All PEDR points are shown, but only those that were within two THEMIS pixels of the crater rim were used in the comparison analysis in this section.

Because of this, and since the MOLA data can resolve craters down to $D \sim 3$ km, this entire range was utilized for this catalog. Though the results may be slightly subdued, and individual persons may opt to not use them if they choose to use this catalog, they are still included and their aggregate results are used in the companion paper, this volume (Robbins and Hynek, 2011c).

2.3.4. Comparing THEMIS- and MOLA-Derived Diameters

Agreement between THEMIS- and MOLA-derived crater diameters is fairly good throughout the database. Fig. **8** top panel illustrates the absolute difference between these two values and Fig. **8** bottom panel shows the relative difference. In these, there is a slight discontinuity in the binned values at the 5-km point. This is because craters were analyzed in MOLA data first for all THEMIS diameters $D \geq 5$ km and then $3 \leq D < 5$ km. Besides this, an internal consistency was used for craters $D \geq 5$ km where a MOLA-derived diameter needed to be within ±25% of the THEMIS value to not be rejected (the assumption being that interpolation

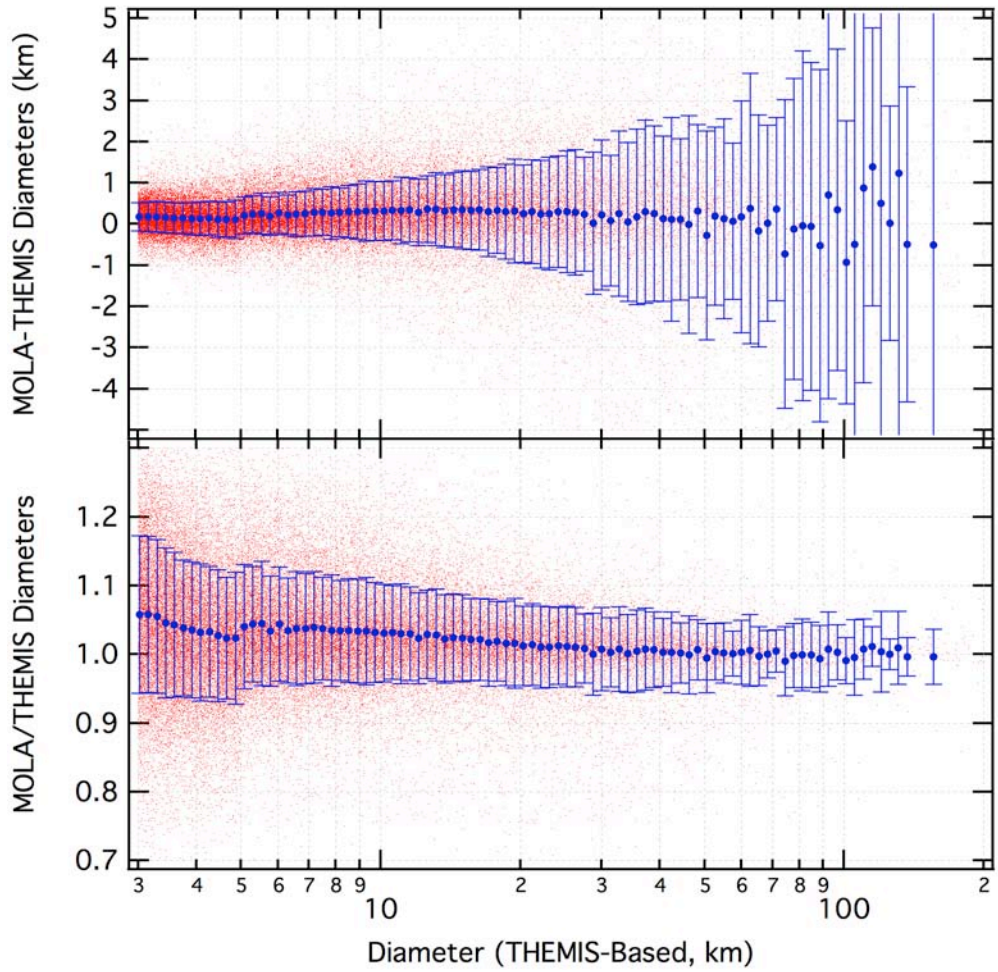

Figure 8: Each point is a single crater comparing the THEMIS- and MOLA-measured diameters. Data have been binned in multiplicative $2^{1/16}D$ intervals with means and standard deviations displayed for the craters in that bin. Graphs are cropped to show regions of interest and statistical significance. See text for explanation of discontinuity at 5 km. Top Panel - Absolute difference between THEMIS- and MOLA-derived crater diameters. The values are slightly above but still very close to 0, indicating that MOLA generally resulted in slightly larger crater diameters by an average of ~0.25 km over most diameter ranges. Bottom Panel - Relative difference between THEMIS- and MOLA-derived crater diameters. Over all diameters, the 100% parity is maintained within the standard deviation, though there is a distinct trend towards larger MOLA results at smaller diameters.

artifacts and/or little to no topographic relief masked the crater in MOLA data). For the $3 \leq D < 5$ km range, this was modified to be ±50% because it corresponded to a less significant absolute difference.

Despite this change at the 5-km point, the data clearly show reasonable agreement between the two methods. In absolute terms, ≥68% of the craters are within 1 km agreement in the two measurements at all crater sizes. Considering the level the uncertainty from the NLLS

circle fit to the THEMIS rims from Section 2.2.4, this a more than acceptable spread. While the offset is reasonably constant without a statistically significant trend away from ±0 (although the means are consistently >0 for $D \lesssim 30$ km), this means that the relative difference shows a distinct trend towards >100% (parity) as diameters get larger (Fig. **8** bottom panel). In fact, it is well represented by the power law $D_{\mathrm{MOLA/THEMIS}} = 1.00 + 0.41 D_{\mathrm{THEMIS}}^{-1.52}$. While this is fairly minor even for D = 3 km craters (aliased to larger diameters by 5%), it is statistically an important effect to keep in mind, not just when using these for analysis but also when exploring the effects of resolution limits on relatively small features. For example, the Stepinski *et al*. (2009) MOLA-based crater catalog shows a statistically significant increase in number of craters for ~3.5 < D < 7 km over both this database and the Barlow database (Barlow, 1988). This comparison issue is explored in greater detail in section 2.7.5.

2.4. Crater Interior Morphology and Degradation State Classification

Basic size-dependent crater morphology was recognized as early as 1893, by the head of the United States Geologic Survey, G.K. Gilbert (Gilbert, 1893), and was in use by the community within a century (*e.g.*, Dence, 1968; Cintala, 1977; Wood, 1978; Melosh, 1989). This crater database follows that basic schema and adds to it. The database contains three columns of interior crater morphology: The first column is the basic crater type, the second notes any features of interest in the crater walls, and the third column notes features upon the crater floor. Appendix C provides archetypal examples of morphology types used. Additionally, there are three more columns of information for each crater that can be loosely classified as "morphology." The first is the degradation state (sometimes referred to as preservation(al) state or modification state) which is how fresh or eroded the crater appears. Second is a subjective confidence measurement of how certain the authors are that the feature identified is actually an impact crater. Third is another subjective measurement of how likely the identified crater is a secondary crater. If it is identified as a probable secondary, the catalog ID of the primary is included if it can be determined. These are explained in detail in the following subsections.

2.4.1. Basic Crater Types

All craters were visually inspected to determine morphology in 100 m/pix THEMIS mosaics with rare assistance from ~5-7 m/pix CTX images (ConTeXt Camera from Mars Reconnaissance Orbiter (Malin *et al.*, 2007)). Craters were first categorized based on simple gravity-controlled shape and abbreviated with three letters: Simple (Smp), complex (Cpx), and basin (Bsn). Simple craters are bowl-shaped. Complex craters are characterized by the presence of central peaks/rings, wall terraces, and/or a flat floor (Melosh, 1989). The basin classification was used for any crater larger than ~500 km in diameter; there is no agreed-upon transition diameter for where a large crater becomes a basin except in the case of multi-ring basins, such as Orientale on the Moon (Mars does not have any obvious present-day examples of these). Differentiating between a simple and complex crater was not attempted in all cases. For example, a partially filled simple crater will have a flat floor and become fairly identical morphologically to a small pristine complex crater that originally had a flat floor. For such cases, this column was left empty under the philosophy that it is better to omit than to provide wrong information.

Additional letters were sometimes appended; in the simple-complex transition range ($5 \lesssim D \lesssim 8$ km), the additional letters may be present *without* Smp or Cpx preceding them. These are based on the morphologic types identified in Barlow and Bradley (1990) and are used to indicate: Flat Floors (FF), Central Peaks (CPk), Central Pits (CPt), Summit Pits (SuPt), Peak-Ring (PkRg) (observed nine times), Unclassifiable/Chaotic (Unc), and "Central Mesa" (CMa) (observed nine times). In this manner, a complex crater with a summit pit will be listed as "CpxSuPt." The Unc type was used when it was not possible to identify characteristics of the original floor of the crater due to subsequent infilling or fracturing. FF craters were only indicated for the complex type, as simple morphology always forms as a bowl but later modification may give it a flat floor. Not infrequent were transitional-sized craters that appeared to be simple due to their bowl shape but had central peaks. In these cases, simply a "CPk" was indicated. Finally, the "CpxCMa" designation, indicating a "central mesa," applied to large

craters in the complex size regime that have a mesa-like central region that spans ~50% of the crater's diameter.

2.4.2. Crater Walls

The second interior morphology column notes any features of interest in the crater walls. In the case of multiple features, a backslash ("/") separates multiple items. Possible features identified in the database are: Terraced, Bench (sometimes called "concentric" in the literature), Gullies (at THEMIS resolution), and/or a channel breaching the wall along with the compass direction (*e.g.*, "Channel SE" indicates a channel breaches the southeast wall). If tectonic features such as graben run through the crater and its walls, this is indicated in the floor morphology section, described in Section 2.4.3.

The former two are formational features. Terraces occur in complex craters due to weakness in the target material that leads to fracturing circumferential to the crater rim (Melosh, 1989). Bench/concentric craters are generally small craters that have a rim, a drop to a mid-level "bench" that is fairly flat and extends over a sizeable part of the crater's radius, and then drops to a more typical crater depth for that diameter; this bench extends over the boundary in a layered target of weak (top) and strong (bottom) material before breaching the stronger material towards the center (Melosh, 1989). The latter two are modification features that can occur at any time after the crater has formed. The "gullies" refers to any thin, channel-like pattern that runs down the crater wall at the resolution of the THEMIS maps. This can be simple mass wasting, or it may be due to aquifers bursting (*e.g.*, Malin and Edgett, 2000) or melting from snow deposits (Christensen, 2003). The "Channel" term is *only* used when the channel breaches the crater wall and the channels must be many km long. They may or may not show obvious flow-like features and/or deposits into the crater.

2.4.3. Crater Floors

Additional features of interest on the crater floor were noted in a third interior morphology column (see Appendix C for examples). This includes a generic "Floor Deposits"

that does not presume an origin. Floor Deposits were indicated in any complex crater that did not have a uniform floor texture, was not of the other types, or clearly had a large amount of burial (this would also be reflected in the degradation/modification state). It was indicated in simple craters if the crater rim opened to the surrounding surface and was at the same elevation, or if it was not bowl-shaped.

Other possible values in this column are: Fractured, Channel, Dunes, Valley Deposits, Slump Deposits, Landslide Deposits, Ejecta Deposits (from an external crater), Tectonics, Alluvial Fan (from Moore and Howard, 2005), and Delta (from Di Achille and Hynek, 2010). Fractured indicates a highly fractured crater floor (sometimes referred to in other databases as "chaotic"), and this is separate from Channel that designates a crater that has one or more channels running through it (there must be a visible channel through the crater, not just breaching the wall). Dunes indicates if sand dunes are present. Valley Deposits are where a channel opens into a crater and material appears to have gathered at its mouth. "Slump Deposits" are floor deposits that appear to be the result of mass wasting from the crater rim and/or walls, while "Landslide Deposits" are a sub-class that have a specific fan-like morphology that may be fluvial in nature or triggered by another impact event near the crater rim. "Ejecta Deposits" are cases where another, external crater's ejecta is within the crater of interest; if there is ejecta on the crater floor due to a crater that formed completely inside the crater in question, this was not indicated. "Tectonics" are cases where extensional or compressional features are present in the crater floor, such as graben or wrinkle ridges.

2.4.4. Determination of Crater Degradation States

There is a lengthy history of studying the degradation(al)/modification/preservation(al) states of craters by processes of gravitational mass wasting such as landslides, aeolian deposition and erosion, and fluvial erosion. Selected examples include the use of crater degradation to study gradational epochs (Grant and Schultz, 1990), a broad overview by Grant and Schultz (1993), more detailed studies of crater morphology including topographic dependence by

Craddock *et al.* (1997), and studies of specific regional degradation such as by Barlow (1995).

Classifying the degradation state of craters is where, unfortunately, every researcher has his or her own system. Historically, crater degradation states have been reduced to three or four different classes that range from ghost (craters that are almost completely buried or eroded so they are barely visible) to pristine craters (such as by Craddock and colleagues, *e.g.*, Craddock *et al.*, 1993, 1997). A distinct benefit of this system is that with fewer classes, there is a larger step between each class and consistency is more likely to be maintained. With high-resolution data and data types other than imagery (such as topography and thermal inertia), Barlow (2004) recently advocated for a more detailed eight-class system based on 0-18 possible points a crater can be assigned. These points are based on the crater depth (0-5), rim preservation (0-4), ejecta preservation (0-4), state of the interior (0-5), and relative thermal inertia of the crater's immediate surroundings versus those farther away (0-2). Points are combined and then scaled to give a 0-7 preservation class. This has the benefit of both utilizing disparate data to derive a preservation class and having a system closer to a continuum of degradation states.

Table 1: Schema used to define degradation states ("class") for craters. Craters are classified with three morphologic characteristics and the relative depth from topography (if available). The corresponding rank is converted to a degradation class. The majority of craters in a given class will have characteristics from that row, but that is not always the case. It is possible - if highly unlikely - for a crater to ha, for example, a "Sharp" rim while having no ejecta and being mostly infilled.

Relative Depth	Rim	Ejecta	Interior	Rank[3]	Class
<1/4 (1)	Rimless (1)	None (1)	Mostly Infilled / Highly Modified[1] (1)	4-6 (3-4)	1
¼-1/2 (2)	Slightly Elevated (2)	None (1)	Significant Deposits / Modification[1] (2)	7-9 (5-6)	2
½-3/4 (3)	Some Degradation / Modification[1] (3)	Some Erosion / Modification (2)	Some Infilling / Modification[1] (3)	10-13 (7-9)	3
>3/4 (4)	Sharp[2] (4)	Pristine (3)	Pristine (4)	14-16 (10-11)	4

[1]Modification includes: Gullying/dissection, fracturing, lava flows, ice flows, mass wasting (*e.g.*, from the rim), superimposed cratering, etc.

[2]Does not necessarily mean "pristine" (*i.e.*, can have a small crater superimposed or a very small bit of modification).

[3]Parenthetical values are if depth information is not present.

While the Barlow (2004) system may be more ideal, it is not feasible for the much larger number of craters in this database. Instead, this work uses some of the objectiveness that system suggests, but it has been shrunk in scope to the more traditional four-class system as listed in Table **1**. In using this, some of the simplicity of four-class systems is preserved while also preserving more of the objectiveness with distinct criteria of the Barlow (2004) system.

In this analysis, crater "Relative Depth" was based on the local depth/Diameter ratio rather than a global average. As discussed in the companion paper (Section 3.5) and elsewhere (*e.g.*, Stewart and Valiant (2006)), this is important to take into account because even pristine craters near the Martian poles (poleward of ~±40° latitude) are, overall, significantly shallower than craters closer to the equator. If this were not taken into account, then craters near the poles would consistently be 1 or 2 classes less preserved than their equatorial counterparts which would introduce a significant systematic error.

All intermediate classifications in the rank and class are preserved in-house, but only the final class is included as the `DEGRADATION_STATE` column in the released crater database.

2.4.5. Is This Crater a Secondary?

Secondary craters are a long-standing problem and debate that has no definite solution nor unified model for its importance. The first step in understanding them is to differentiate between a primary and a secondary crater. In this database, this discrimination is based on classic morphologic characteristics of secondary craters (Shoemaker, 1962; Shoemaker, 1965; Oberbeck and Morrison, 1974; and McEwen and Bierhaus, 2006):

- Is the crater highly elliptical with the long axis oriented towards a much larger crater?
- Is the crater entrained within a chain of craters radial to a much larger crater?
- Is the crater a member of a large group of craters, the overall group shape having a major axis radial to a much larger crater?
- Is the crater surrounded by chevron ejecta that points to a much larger crater?

If a crater in the database fit some of these characteristics, an indication as a possible or

probable secondary crater in the column SECONDARY was made. Values were a trinary N, M, or Y, indicating "No," "Maybe," and "Yes." "Maybe" indicates the crater displays some secondary morphologic characteristics, but it cannot be determined with certainty if it is actually a secondary crater. "Yes" indicates that the crater is a secondary beyond reasonable doubt. Where possible, the CRATER_ID was given following a ";" if the primary for M or Y secondary craters could be identified. For example, if a crater was identified as a secondary and the primary identified as 01-2-34567, then the field SECONDARY would read "Y; 01-2-34567".

2.4.6. Is This a Crater?

In several cases (~1% of the total analyzed), features included in the database are somewhat ambiguous as to whether it is a crater, or if a crater, an exogenic crater (as opposed to, *e.g.*, an endogenic collapse pit crater). The database field CONFIDENCE_IMPACT_CRATER contains, on a scale of 1-4, the subjective probability that the feature identified is a crater. Out of the 78,895 craters $D \geq 3$ km that were morphologically classified in this release, 183 (0.23%) were listed as 1, 378 (0.48%) as 2, 683 (0.87%) as 3, and the remaining 98.42% as 4. This amount of uncertainty is well within the variance between researchers (Lissauer *et al*., 1988).

2.5. Crater Ejecta Morphology Classification

Fresh craters and those with light to moderate degradation/modification will display ejecta surrounding the crater rim. Typically, continuous ejecta blankets will extend to ~1 crater radius from the crater rim while additional rays of ejecta can travel much farther (*e.g.*, Tycho Crater's ejecta on the Moon has been mapped half-way across the body (Wilhelms and El-Baz, 1977)). On the Moon and Mercury, simple radial ejecta where the material was ballistically emplaced from the excavation of the crater cavity is the only type observed. Throughout the literature, this has been referred to simply as "radial," and this database follows the recommendations of Barlow *et al.* (2000), abbreviating it as "SLERd" (single-layer ejecta, radial). Examples of ejecta types discussed here are found in Appendix D, and a preliminary discussion of these ejecta types is addressed in the companion paper (Robbins and Hynek, 2011c,

this volume (Section 3.3.3)).

From the first spacecraft images returned of Mars, a new ejecta type was observed that was comprised of one or more cohesive layers of material. Throughout the literature, these have been referred to under a diverse range of names, including flower (Costard, 1989), composite (Johansen, 1979), and various Types and Classes (*e.g.*, Mouginis-Mark, 1979; Blasius and Cutts, 1980; Horner and Greeley, 1987; Costard, 1989). The Mars Crater Morphology Consortium convened in the late 1990s to codify a set of recommendations for a standardized nomenclature for these features (Barlow *et al.*, 2000), and with only very slight modifications, that is used in this database.

This database contains five fields for every crater that describe ejecta if it is present for the crater and if that column relevant. The first is `NUMBER_LAYERS` and if present has a value ≥1 describing the number of layers of *cohesive* ejecta (simple radial ejecta is not included in this count). The second is `MORPHOLOGY_EJECTA_1`. For radial ejecta, "SLERd" is in this column. For the cohesive layered ejecta, the Barlow *et al.* (2000) nomenclature is followed: Layered ejecta (LE) displays several morphologic sub-types that are used in its five-letter classification. The first is how many layers of ejecta are present – a single layer (SLE), two (double) layers (DLE), or three or more layers (MLE). The second main type discriminator is if the ejecta terminates in a rampart it has an R as the fourth letter; if not, it is termed "pancake" and the P is the fourth letter. If *any* part of the ejecta edge displays a rampart morphology, even if the rest does not, the R designation is given in lieu of P in this catalog. Third is how the edge of the ejecta terminates, whether it is sinuous or fairly circular. The lobateness factor Γ defines this as:

$$\Gamma = \frac{\text{area of ejecta}}{\pi\left(\text{radius of circle with equivalent area}\right)^2} \tag{3}$$

If $\Gamma \leq 1.5$, the ejecta is circular (*e.g.*, SLEPC). If $\Gamma > 1.5$, the ejecta is sinuous (*e.g.*, SLERS).

Barlow *et al.* (2000) also recommended that when multiple types of ejecta are present around a single crater, the terms be combined. For example, a crater that displays one continuous layer of ejecta in addition to radial ejecta would be designated "SLERSRd." It is on

this point that this database deviates from those recommendations. Instead, a backslash ("/") is used to indicate multiple classifications for multiple layers. This is done for expandability and to provide better information. For example, a class of craters found in the mid-northern latitudes is DLE, but the inner layer is PC while the outer is RS. Hence, this is designated as "DLEPC/DLERS" in this database. In another example, sometimes there will be a radial ejecta component between two cohesive ejecta layers. Pure radial non-cohesive ejecta is *not* considered a layer in the S/D/M classification, so in this case the designation would be "DLEPC/DLERd/DLERS."

The third ejecta morphology field describes the overall texture of the LE blanket and it provides additional information about its edge; this is found in `MORPHOLOGY_EJECTA_2` as a two- or four-letter code. The first two letters are either "Hu" or "Sm" which stand for "hummocky" and "smooth" to describe how the ejecta blanket appears in THEMIS Daytime IR data. These two are always present in this column if there is a layer of ejecta present while there may or may not be an additional two letters used. If present, they are "BL," "SL," "Am," or "Sp." These stand for "broad lobes," "small lobes," "amorphous," and "splash." "Broad lobe" is used when the separation between different lobes of a layer is more than 50% of the extent of the layer; this is measured by eye and is not an exact delineation. "Small lobe" is where the terminus of the ejecta is more of a serrated "crinkle scissor" type, though it is more precisely defined as when the separation between these serrations does not extend more than 50% of the extent of the ejecta (this is also not exact). The "amorphous" type is for an overall ejecta shape that is generally asymmetric, blobby, "amoeboid"-like. "Splash" is when the ejecta appears as a splash onto the surface with the ejecta generally extending far from the crater rim but separated into many different strands.

A final, optional, fourth column `MORPHOLOGY_EJECTA_3` was occasionally used to describe unique shapes of ejecta blankets. These types are: Butterfly, Rectangular, Splash, Bumblebee, and Pin-Cushion. In addition to these, "Pseudo-Butterfly" and "Pseudo-Rectangular" are occasionally used to describe the ejecta around a single crater. Occasionally, a

binary impact will occur and the two craters overlap, their touching rims being straight between the two. In this case, there may be cohesive ejecta that appears to be squeezed between the two in which case "bumblebee" is used for both craters. Finally, even if there is no ejecta but the crater is at the head of what on Earth would be considered a sandbar, the term "Sandbar" is placed in this column of morphology. Examples of these are all found in Appendix D.

Butterfly ejecta occurs around a fairly elliptical crater. This ejecta will have a zone of avoidance at the edge of the crater at one end of the major axis; this avoidance zone typically covers ~120-130° (Robbins and Hynek, 2011c). The ejecta has the farthest extent from the crater almost immediately past this zone, and it stays relatively far from the rim throughout most of the length of the crater. It will narrow as it approaches the other end of the major axis and have nearly a similar zone of avoidance, though it will still be present in a substantially reduced extent. It will typically have one or two "tendrils" extending beyond this. If the ejecta is similar but does not, for example, have a total zone of avoidance, does not nearly disappear at the other end of the major axis, or if the ejecta does not have an obvious farthest extent immediately past the zone of avoidance, the ejecta is considered "Pseudo-Butterfly." Seventy-one craters were classified as having butterfly ejecta, while 98 were classified as pseudo-butterfly.

Rectangular ejecta may have a similar genesis to the Butterfly type, but it has a nearly 180° zone of avoidance at both ends of the major axis, and it will extend a nearly constant distance from the crater's edge along the rest of the crater. The Splash type is the same as the "Sp" suffix in the second morphology classification. Pin-Cushion ejecta is exclusive to the –-PC (first morphology column) and Hu (second morphology column) type. In the THEMIS Daytime IR mosaics, this crater appears to be bulbous with a pitted texture, appearing at the THEMIS 100 m/pix data to resemble a pin cushion. This may be due to overlying radial ejecta as this often had a `MORPHOLOGY_EJECTA_1` classification of "SLERd/SLEPC," although this only became apparent at the higher 100 m/pix data and was not clear in the 230 m/pix mosaics.

In all of these morphology information columns, a single value applies to all layers of ejecta for that crater. If there are multiple layers that have a distinct morphology, then

backslashes ("/") are used to separate them with the innermost layer first, second listed second, and so on for the first two morphology columns; it is specified in the third morphology column to which layer the designation applies. If there are, for example, three layers of ejecta where the inner and middle are sinuous rampart, the outer is circular pancake, all are hummocky, the inner has "short lobes" while the middle and outer has broad lobes, and the inner is of the butterfly type, the columns would have the following information:

1. MLERS/MLERS/MLEPC
2. HuSL/HuBL/HuBL
3. Inner is Butterfly

Finally, there is a comments column `MORPHOLOGY_EJECTA_COMMENTS` that may contain additional information about the ejecta. An example that was frequently used is, "There may be a cohesive layer within the Rd ejecta."

2.6. Crater Ejecta Morphometry Measurement

While the morphologic crater ejecta classification is somewhat subjective, this database also contains an objective measurement of ejecta blankets of the cohesive layered ejecta type in all cases where this could be measured. Due to some image clarity, completeness, and indistinct contacts, it was not possible to measure all ejecta.

2.6.1. Outlining Ejecta and Calculating Their Properties

Ejecta were identified in THEMIS Daytime IR global mosaics and outlined with 1 vertex every 500 m, identically to how crater rims were traced as described above. A note was made in the *ArcGIS* shapefile designating the ID of the crater that the ejecta shape belonged to. These were then imported into *Igor Pro* software along with the already processed crater rim data. Using the same algorithms as with the crater rims, the ejecta outlines were projected from decimal degrees to kilometers from the centroid after factoring in the spherical surface of Mars. After this, for every outline, the following data were calculated and stored to the designated database columns (where # refers to a number between 1 and 5, inclusive):

- `LAYER_#_PERIMETER`: Perimeter of each outline (units are km).
- `LAYER_#_AREA`: Area of each outline using a standard geometric method for the area of an irregular polygon:

$$A = \frac{1}{2}\sum_{i=0}^{n-1}\left(x_i y_{i+1} - x_{i+1} y_i\right) \quad (4)$$

where n is number of vertices, x is longitude, and y is latitude. The ideal area of the crater (πr^2) is subtracted, and the final area of the ejecta is recorded (units are km^2).

- `LAYER_#_LOBATNESS`: The lobateness, Γ, is calculated (Eq. 3) (unitless) using the ejecta area before the crater's area is subtracted.
- `LAYER_#_EJECTARAD_EQUIV`: The equivalent ejecta radius (units are km) - also known as "runout distance" - is calculated as:

$$\text{runout distance} = \sqrt{A_{\text{ejecta+crater}}/\pi} - r_{\text{crater}} \quad (5)$$

- `LAYER_#_EJECTARAD_REL`: Relative equivalent ejecta radius is the runout distance divided by the crater's radius and is also known as "ejecta mobility" (unitless).

Ejecta perimeter and area are self-explanatory and are standard definitions. Ejecta lobateness in this sense is similarly a standard definition and has been used for several decades with no modification (*e.g.*, Kargel, 1986). However, it should not be confused with the *number* of flow lobes that are observed, which confusingly is also termed "lobateness" by a few researchers (*e.g.*, Barnouin-Jha and Schultz, 1998). Runout distance and its derived ejecta mobility, however, have had two different definitions. The first is the one used here that uses an average ejecta extent because it offers a characterization of the overall energy and viscosities involved (*e.g.*, Barlow, 2005, 2006). The second is the maximum extent of the ejecta to determine the absolute farthest the cohesive ejecta could flow given the impact energy available (*e.g.*, Mouginis-Mark, 1979; Costard, 1989). Unfortunately, the two are not easily relatable, and the data would need to be re-processed using the other definition for a meaningful comparison.

2.6.2. The "Infinite Coastline of Britain" Problem: Fractal Nature and Differing Resolutions

A limitation of the utility of ejecta perimeters, areas, and lobateness is the inherent fractal nature of the shape studied and limits of resolution - both the imagery used and the frequency of vertices in the polygons created to represent them. This was first formalized in 1967 by fractal pioneer Benoît Mandelbrot who described it in terms of measuring the coastline of Britain (Mandelbrot, 1967). He found a power law relationship between the length of coastline and the length of the side of a polygon to represent the coastline, but the power law exponent varied for different coasts. Similarly, the non-linear problem of perimeter will vary with the complexity of the ejecta, and while a SLEPC ejecta may be well-represented by a single vertex every kilometer, a complex SLERS may require 10 vertices in the same space to properly represent the perimeter at THEMIS resolution. Similarly, 1 vertex every kilometer may work well for a SLEPC blanket surrounding a 20-km-wide crater, but significant resolution artifacts would arise for a similar blanket surrounding a 1-km-wide crater.

Several case studies were performed to illustrate this dependence and its significance. Different SLE ejecta were chosen to represent different sizes and different types. For smaller craters ($D \lesssim 10$ km), CTX data were used to afford higher resolution in this analysis. For these craters, the ejecta was defined by a polygon with vertices spaced every 50 meters (5 and 10 times higher resolution than used for the catalog). In processing, this resolution was reduced in 50-m intervals down to a resolution of one vertex every 5 km. For larger craters, THEMIS Daytime IR images were used. Ejecta was outlined with a vertex every 100 meters and this resolution was reduced in 100-m intervals in the analysis. Table **2** lists the craters used in this study and their properties. Fig. **9** illustrates the lobateness resulting from the different resolutions. Lobateness is graphed because it roughly normalizes the different crater diameters and ejecta types and it is linearly related to the ejecta perimeter.

As is apparent, there is not a predictable power law that can describe the change in lobateness with differing resolution, crater size, ejecta type, etc. The only two conclusions that can be made were apparent *a priori*, namely that craters with larger lobateness continue to have a

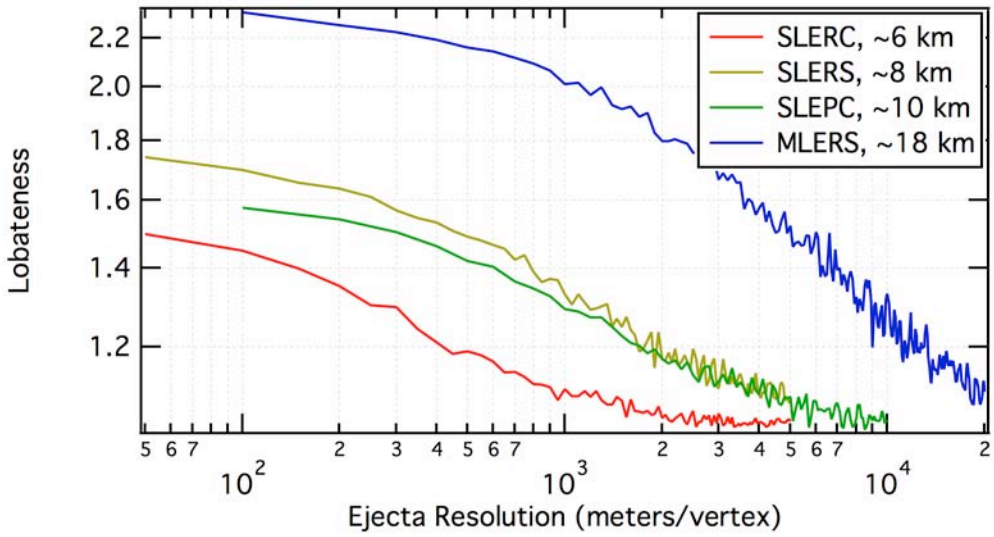

Figure 9: Effect of different resolutions for different crater ejecta morphologies on the derived lobateness. Each type behaves differently as measured by the slope and shape of the curve. Resolution was reduced until there were 10-20 vertices that defined the ejecta perimeter.

Table 2: Craters and properties of the craters used in studying the fractal nature of ejecta.

Crater ID	Diameter	Latitude	Longitude	Ejecta Type 1	Ejecta Type 2
14-1-12282	5.7 km	4.3°	138.2°	SLEPC	HuSL
02-1-06899	8.2 km	5.0°	-152.7°	SLERS	HuBL
14-1-02638	10.3 km	30.3°	108.0°	SLEPC	Hu
14-1-11724	18.0 km	5.4°	102.4°	MLERS[1]	HuBL

[1]Outer ejecta layer was analyzed.

larger lobateness at changing resolutions, and that lobateness decreases with decreasing resolution. Any direct comparison between different databases that have the ejecta outlined in different ways at different resolutions would be arbitrary and inconclusive. The only meaningful comparison is relative (*i.e.*, if the ejecta of crater 1 is larger than that of crater 2 in both databases A and B). Otherwise, the only comparisons that should be made are internal to the database, and even then the ejecta morphometry should only be compared to similarly sized craters (*e.g.*, the values for a 3-km crater will not be reflective of actual morphometry differences relative to a 100-km crater).

2.7. Database Completeness

Completeness of this database is at several different diameters depending upon what information is being queried:

2.7.1. Identified Craters - Statistical Diameter Completeness

The statistical completeness of the database is based upon crater size-frequency distributions: The global database was divided into regions based upon 22.5°x45° latitude/ longitude intervals and an incremental size-frequency distribution was generated from the craters within each bin (based on Arvidson *et al.* (1979), except with multiplicative $2^{1/16}D$ intervals instead of $2^{1/2}D$ intervals; the finer resolution was a reflection of the large number of craters in the database). Completeness was defined to be the next-larger diameter bin after the diameter bin with the most craters within each latitude/longitude region (Fig. **4**). A key assumption of this is that the crater population is well behaved and will continue to increase in number as sizes decrease, at least to diameters significantly smaller than those measured here. Therefore, any decrease observed is due to missing craters in the database rather than a property of the surface.

As a whole, this is a reasonable assumption as previous work has extensively shown that the crater production function increases at least to decameter scales on Mars (*e.g.*, Hartmann, 2005). Locally, this does not always hold. There are a few regions in Fig. **4** that show completeness to diameters >1.0 km. Several of these regions (25% of the planet) were searched again for missed craters, and though craters on the order of ~1% were identified that had not been previously, this could not account for the lower completeness level. It is therefore likely that a geophysical process has acted to remove the ~1-km crater population in these regions at times recent enough such that they have not had time to re-accumulate. In many cases, this was the formation of another large crater and emplacement of its ejecta blanket; in others, aeolian or burial processes likely played a dominant role.

This was especially the case observed around 0°N, 0°E, where several large crater rims were seen with almost no small craters at THEMIS resolution. In the high northern latitudes where Lomonosov and Lyot craters are (65°N, -9°E and 51°N, 29°E, respectively), these craters

and their associated ejecta dominate the region and likely explain the relative paucity of ~1 km craters. The reason these large craters can affect such a broad latitude/longitude bin is (a) they are close to the poles so the bins cover less spatial area, and (b) the crater and its associated ejecta will reset a large area except for craters large enough to remain visible. While craters will have formed since the impact, there may not have been enough time to accumulate enough $D \sim 1$ km craters to affect the size-frequency distribution based on this completeness criterion.

The end result of this analysis is a global mean completeness level of $D = 0.96$ km, with a range $0.76 < D < 1.87$ km when binned at 22.5° latitude by 45° longitude. With the two outlier regions containing Lyot and Lomonosov craters removed, the mean is $D = 0.94$ km and maximum $D = 1.32$ km around the Arabia Terra region. The database as released contains 378,540 craters $D \geq 1.0$ km. The entire database has an additional 252,793 craters $D < 1.0$ km that were removed from this release but may be obtained by contacting the corresponding author.

2.7.2. Topographic Data Completeness

MOLA data resolution is significantly coarser than THEMIS Daytime IR (except near the poles), the limitations of which were addressed earlier in this paper. Because of occasional gaps that were much more deleterious to smaller craters, 100% coverage was not possible. Fig. **10** shows the fraction of craters that could be analyzed with MOLA data as a function of diameter, and this drops precipitously for $D \lesssim 4$ km. (The discontinuity at 5 km is due to different criteria for rejecting MOLA-based measurements for $D \geq 5$ km craters and $3 \leq D < 5$ km craters.)

2.7.3. Ejecta Morphology and Morphometry Completeness

In the current release of this database, ejecta morphology and morphometry are complete to 5.0-km-diameter craters ($N = 47{,}345$). The additional 331,195 craters that are $1 \leq D < 5$ km will be classified and analyzed in a future release.

2.7.4. Crater Morphology Completeness

In the current release of this database, interior morphologies are complete to $D \geq 3.0$ km craters ($N = 78{,}895$). The additional 299,645 craters $1.0 \leq D < 3.0$ km will be classified and ana-

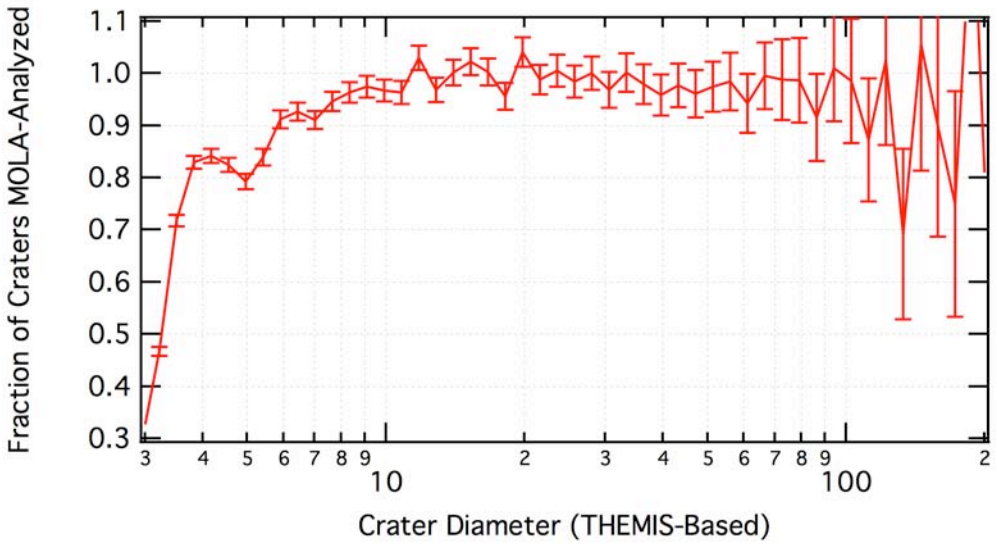

Figure 10: Ratio of a size-frequency diagram of THEMIS-based crater identifications to MOLA-based in multiplicative $2^{1/8}D$ bins. Values above 1.0 indicate more craters were identified in topography than in images; this is solely an artifact of slightly different diameters arising from the two different analyses. Values can get much higher at larger diameters because there are fewer craters per bin, which is why this graph is truncated at 200 km. The fall-off to <50% identification validates the cut-off at 3 km.

lyzed in a future release. However, there are some cases where the morphology is ambiguous, especially in determining the difference between a complex, flat-floored crater or a simple, slightly in-filled or relaxed crater in the ~5-8 km-diameter range. In these cases, the first morphology column was left blank rather than give potentially erroneous information.

Degradation state is similar to ejecta morphology/morphometry and is only complete for $D \geq 5$ km in this release. Secondary crater classification in the current release is only complete for a select grouping of craters analyzed in Robbins and Hynek (2011a, 2011d).

2.7.5. Comparison with Barlow (1989, 2003), Stepinski et al. (2009), and Salamunićcar et al. (2011) Databases

At present, there are three other completed indiscriminant global catalogs of Martian impact craters: The original from Barlow (1988) and her in-progress revision (Barlow, 2003), the automated MOLA-derived Stepinski *et al.* (2009) catalog, and a composite catalog created by correlating several other crater catalogs (Salamunićcar *et al.*, 2011) that undergoes periodic revisions and is currently in version MA130301GT. Barlow's is complete to $D = 5$ km, the Stepinski *et al.*'s claims completeness to $D \approx 3$ km, while Salamunićcar *et al.*'s is $D \approx 2$ km.

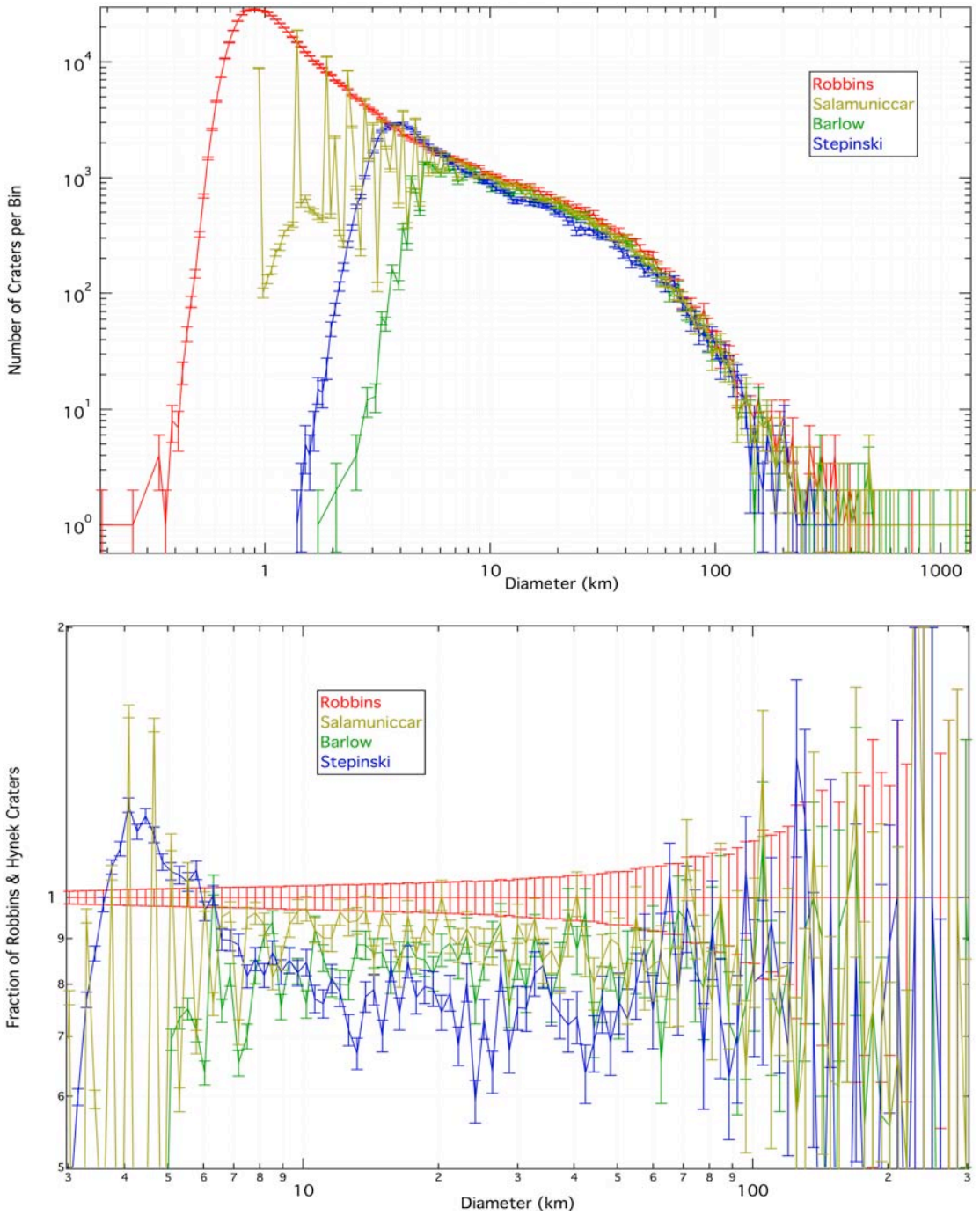

Figure 11: Comparison between four global Martian crater databases with craters binned in $2^{1/16}D$ intervals. The original Barlow database is not complete to D = 5 km, though the current in progress version (Fig. **12**) is closer to this work. The Stepinski database displays a marked increase in craters $3 < D < 7$ km, the likely reason discussed in the text. Salamuniccar database relative to this shows good agreement until diameters $D < \sim 6$ are reached, at which point their diameters are posterized as discussed in the text. Top - Incremental size-frequency distributions over all ranges included in each database. Note the released database will only contain $D \geq 1$ km craters. Bottom - Ratio of incremental size-frequency distributions relative to the database in this paper. Error bars were calculated by the square-root of the counts in the incremental size-frequency bin divided by the counts in the bin for this database. Note the diameter range is a sub-set of the top panel.

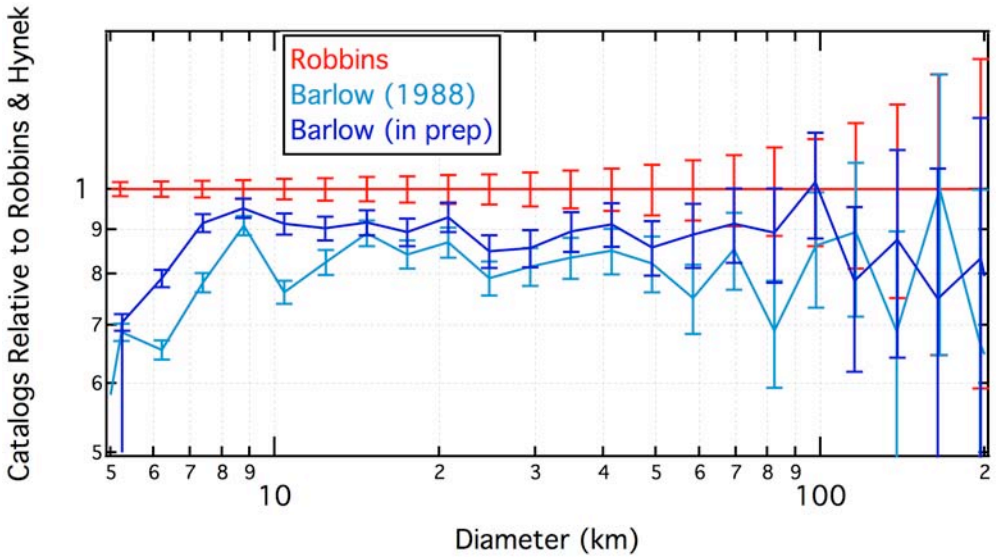

Figure 12: Similar comparison to Fig. **11**, bottom panel, but binned in $2^{1/4}D$ intervals to better show where differences exist and increase number statistics. Horizontal error bars indicate bin width. The "Barlow (in prep)" is a pre-release northern hemisphere catalog supplied by Barlow (pers. comm.) and is unpublished and subject to change.

A detailed comparison of all craters between these three and this catalog is beyond the scope of this paper, but a first-order comparison via an overall crater size-frequency distribution from the four can be done. As shown in Fig. **11**, there is generally good agreement, though over a broad range of diameters ($5 \lesssim D \lesssim 200$ km) this database has slightly more craters. This is likely due to four total searches for craters utilizing multiple datasets as well as the use of the very latest high-resolution THEMIS mosaics. When looking at each catalog, there are marked differences at small diameters.

2.7.5.1. Barlow (1988)

The original Barlow database was created before modern computers and displays allowed for image use and manipulation generally taken for granted today. *Viking* 1:2M photomosaic hardcopy maps examined and craters were measured by hand and recorded to create the catalog. *Viking* images on average had the same nominal resolution as THEMIS, but significant spatial variance resulted in a non-uniform image set. Nevertheless, as the first of its kind, the database that has formed the foundation of significant work since its publication contained 42,284 craters including some $D < 5$ km, though it was not claimed to be complete to those sizes. In light of

recent data, a revised version is underway (*e.g.*, Barlow, 2003). When looking at the original catalog, Fig. **11** shows that the original was also not complete to D = 5 km. A pre-release of the northern hemisphere was supplied by Barlow and compared in Figure **12** with this database and the original Barlow (1988) catalog. It is more complete than the original, but differences remain where, in general, this catalog has more craters than Barlow's. However, this difference is well within the $1.2-1.3\times$ difference between researchers identified by Hartmann *et al*. (1981) and Lissauer *et al*. (1988). Overall, there are 15,812 northern hemisphere craters $D \geq 5$ km in this catalog, 12,920 in Barlow (1988), and 14,200 in the new in prep. edition.

2.7.5.2. Stepinski et al. (2009)

The total number of craters in this catalog is 75,919. It was created through an automated computer algorithm that first identifies round, symmetric topographic depressions in the MOLA MEGDR 1/128° product. The next step is to select these depressions and determine whether they are craters through a trained machine-learning technique. There are significantly fewer $D > 100$ basins identified by Stepinski *et al*. (2009) than in the catalog presented here, likely due to significant erosion and superposed features muting the topographic signal of the original crater. However, this cannot explain the discrepancy around $3 < D < 7$ km where the Stepinski catalog makes a sharp increase in crater size-frequency, surpassing even this one at ~6 km, before cresting at ~4 km and decreasing below the number identified here at ~3.5 km. This phenomenon is likely due to the aliasing and nature of the MOLA instrument and data, as described in Section 2.3. For this reason, it is recommended that although the catalog from Stepinski *et al.* (2009) is "statistically complete" to ~3 km diameters, researchers exercise caution at $D \lesssim 7$ km.

2.7.5.3. Salamunićcar et al. (2011)

The Salamunićcar *et al*. (2011) catalog and previous iterations were constructed via a semi-automated technique. Previously compiled crater catalogs (such as those in the previous two sub-sections) were used as input. From these, the craters are correlated to determine duplicates, and duplicates are averaged. All output crater candidates are manually verified and

re-measured if deemed incorrect. The final catalog contains all morphometric measurements from the original input catalogs and so this is a true meta-catalog of impact craters. The authors state that global completeness is "up to ~$D \geq 2$ km," containing 85,783 craters $D \geq 2$ km (130,301 craters in total when including smaller diameters). However, the catalog in this paper contains 128,907 craters $D \geq 2$ km alone, 50% more. Thus, while their regional completeness may be to that level, it is far from globally complete to 2 km. In addition, it is difficult to perform a direct comparison between their catalog and this one at smaller diameters because their crater diameters are frequently rounded to odd values: For example, there are 2331 craters listed with diameters 4.16 km, 1300 as 2.924 km, and 10,489 with diameters 1.849 km. This results in posterization on the incremental size-frequency diagram displayed as Fig. **11**; a cumulative diagram retains this effect and so is also inadequate for a comparison.

2.8. Conclusions and Database Availability

We have completed the first global Mars crater database that is statistically complete to 1-km-diameter craters, numbering 378,540 entries, and it will be available for public release shortly. The database was manually generated by detailed examination of THEMIS Daytime IR mosaics at 232 m/pix and 100 m/pix scales as well as from MOLA gridded data at 1/128° per pixel (463 m/pix). It is the first to make use of global 100 m/pix THEMIS mosaics that allowed us to provide unprecedented coverage. The MOLA data used for topographic analysis is the *de facto* standard (*e.g.*, Mouginis-Mark *et al.*, 2004; Stepinski *et al.*, 2009) and we include several topographic measurements along with derived products in the catalog (*e.g.*, the rim height above the surface).

The database contains a robust set of statistical uncertainties in basic crater properties, and overall statistics and confidence intervals are described in this paper. Besides basic positional, size, and topographic depth information, this database contains detailed morphologic and morphometric ejecta properties, interior morphologic indicators, and modification state information for each crater (to a certain diameter limit in this release, as discussed in the text)

(see Appendix A for all data columns included).

The catalog compares well over a large range of crater diameters with other published catalogs. Analysis of this vast catalog is underway, as illustrated in our companion paper (Robbins and Hynek, 2011c, this volume) where we illustrate global crater distributions as a baseline before examining morphologic distributions and then re-analyze the simple-to-complex transition and depth-to-diameter scaling laws. Pending review, we will be making this database freely available for download via the Mars Crater Consortium section of USGS's PIGWAD server (http://webgis.wr.usgs.gov/pigwad/down/mars_crater_consortium.htm). We are also making a web-query site that allows users to download craters and features based on user-selectable fields and options that will be available at http://mars.sjrdesign.net.

3. A New Global Database of Mars Impact Craters to 1 km: 2. Global and Regional Properties and Their Implications to Gravity Scaling

Note: This paper is in preparation as: Robbins, S.J., and B.M. Hynek. "A New Global Database of Mars Impact Craters to 1 km: 2. Global and Regional Properties and Variations, and Their Implications to Surface Properties and Gravity Scaling." (in prep. for Icarus). Though it has not yet been submitted, it is cited in this thesis as "Robbins and Hynek, 2011c." Sections have been re-numbered and some reformatting has been done to fit the formatting of the rest of this dissertation. References have been combined with all others at the end of this dissertation. Acknowledgments have been combined with others at the beginning of this dissertation.

Abstract: We have generated a new, 378,540-entry, global crater database of Mars, statistically complete for craters with diameters $D \geq 1$ km. In its current release, this database contains detailed morphologic and morphometric data for craters $D \geq 5$ km and interior morphologies for craters $D \geq 3$ km (future releases will extend these to smaller diameters). We use this database first to reexamine previously observed distributions and patterns to show its fidelity and then to further explore global relationships. Distributions of central pit and summit pit craters are studied and we find the geographic distribution supports a volatile-dependent formation model. With detailed topographic data for the largest crater database to-date, we have analyzed crater depth-to-diameter ratios for simple and complex morphologies across various terrains and for the planet as a whole, and we investigated the simple-to-complex morphology transition. We find results similar to those in the published literature, but we find a substantial terrain dependence on the simple-to-complex transition which occurs at ~11-km-diameter craters at high latitudes. This suggests a model that requires melting of volatiles during high-latitude crater formation that fill the crater during the modification phase but will still support the simple morphology to larger diameters. Overall, this database is shown to be comparable to previous databases where there is overlap and to be useful in extending prior work into new regimes.

3.1. Introduction

Having a uniform database of objects and features from which to refer, draw on, and analyze forms the backbone of much research in most fields of science today. Astronomy is no exception with catalogs predating recorded history and the first relatively large one compiled by the Greek astronomer Hipparchus over 2100 years ago. The advent of the telescope and better views of the heavens accelerated this tradition all the way to the present day where many terabytes are relegated to storing these data. The planetary science community has its own niche, and a subsection within that is held by crater catalogs.

Crater catalogs or databases (the term is used interchangeably in this work) can inform a

variety of investigations of planetary processes, surface properties, physics, and geology. The utility and application of a crater catalog almost always goes beyond the original scope and applications of the person or group who generated it. Large, generalized databases are thus the most useful because they can be applied to diverse questions.

To this end, we have compiled the largest planetary crater database that exists today. This Martian crater catalog contains 378,540 craters with diameters $D \geq 1$ km. In a process thoroughly described in our companion paper (Robbins and Hynek, 2011b, this volume), we include many dozen morphologic and morphometric descriptors for each crater; in the current release, interior morphology are included for craters $D \geq 3$ km, and ejecta morphology and morphometry and crater degradation states are included for craters $D \geq 5$ km.

To both illustrate the fidelity and utility of this work, we have reexamined many previous general trends and properties of Martian impact craters from throughout the literature. On a basic level, we illustrate the global distribution of giant basins, hundred-kilometer-sized craters, intermediately sized craters, and few-kilometer craters and show they agree well with previous work (Section 3.2). We also examine the fresh crater population in the context of global circulation models in that section. We continue to crater and ejecta morphology in Section 3.3, exploring the distribution of crater central peaks, central pits, summit pits, intracrater dune fields, and both radial and cohesive layered ejecta. Section 3.4 addresses revision of Martian crater topographic properties with the new data; it shows that rim heights are $\sim 2\times$ smaller than are found on the Moon. Sections 3.5 and 3.6 present detailed recalculations of the depth-to-diameter function for simple and complex craters and the simple-to-complex morphology transition. This is done globally and by terrain that yielded disparate results discussed in Section 3.7.

3.2. Global Crater Distributions

The global crater distribution of Mars is generally well characterized in the literature, especially for larger (multi-kilometer) sized craters. Besides existing generalized crater databases (*e.g.*, Barlow, 1988; Stepinski *et al.*, 2009; Salamunićcar *et al.*, 2011), global mapping

efforts have identified large craters and used smaller craters to deduce stratigraphic relationships and ages (*e.g.*, Scott and Tanaka, 1986; Tanaka, 1986; Greeley and Guest, 1987; Tanaka *et al.*, 2011). In addition to global studies, regional or type studies have been completed, such as mapping craters on the poles (*e.g.*, Banks *et al.*, 2010), mapping fresh craters (*e.g.*, Boyce and Garbeil, 2007), identifying craters formed in the last few years (*e.g.*, Byrne *et al.*, 2009; Daubar, 2011) determining ages of major impact basins (Nimmo and Tanaka, 2005), and age-dating larger craters themselves (Werner, 2008). What has not been previously shown is the global distribution of small, kilometer-scale impact craters, and this work is the first such study because it is the first time such a catalog exists. This section begins with basin and large crater distributions to provide context while the remainder examines small and fresh crater locations.

3.2.1. Basins ($D \gtrsim 1000$ km)

There are seven broadly recognized basins on Mars with $D \gtrsim 1000$ km, and these are listed in Table **3** (Scott and Tanaka, 1986; Greeley and Guest, 1987; Nimmo and Tanaka, 2005). They are included in this discussion for completeness' sake and values should be treated as approximate. The basins Acidalia, Chryse, and Prometheii have less than 50% of their rim identifiable today. In cases of Acidalia, Chryse, Utopia, and Hellas, the rim that is visible is mostly vague with the rims of Acidalia and Hellas by far the least distinct. All of these basins are ancient, dating to the Noachian epoch of Mars' geologic history (Nimmo and Tanaka, 2005). Isidis, the best preserved, is the youngest with an estimated age ~3.9 Ga, while Argyre is also well preserved and has an estimated age ~4.0 Ga (Nimmo and Tanaka, 2005). Prometheii's northern rim is reasonably clean and preserved, but the bulk of the basin lies beneath Mars' south polar cap, limiting any study. The remaining four are estimated as $\gtrsim$4.1 Ga (Nimmo and Tanaka, 2005).

The explicit qualifier of "broadly recognized" in the proceeding paragraph is because many different researchers and groups have suggested other impact basins on the planet. One of the more recent and contentious is the proposition that the entire northern lowlands (the Borealis

Table 3: Large accepted basins on Mars with approximate latitude, longitude, and diameters. In this table, location has been rounded to the nearest degree and diameter to the nearest 100 km.

Name	Latitude	Longitude	Approx. Diameter
Acidalia	47° N	338° E	2300 km
Argyre	-48° N	316° E	800 km
Chryse	25° N	328° E	1700 km
Hellas	-38° N	075° E	2200 km
Isidis	13° N	088° E	1200 km
Prometheii	-85° N	091° E	1200 km
Utopia	40° N	080° E	3200 km

basin) is the result of a now-identified potential impact event (Andrews-Hanna *et al.*, 2008). This is disputed because others model that such a planet-altering impact would nearly destroy the planet (*e.g.*, McGill and Squyres, 1991), and endogenic processes may adequately explain the dichotomy (*e.g.*, Šrámek and Zhong, 2010 and references therein). Similarly, many other basins and large craters have been suggested on the planet in work done mainly by Frey (*e.g.*, Frey, 2006, 2008). For example, Frey (2008) suggests fully 20 basins on Mars with diameters $D >$ 1000 km. However, while these are perhaps more accurately referred to (as the author does) as "quasi-circular depressions," these features and similar smaller ones are not broadly recognized by the community as definitively of impact origin.

3.2.2. Large Craters (100 - ~500 km)

Three hundred one craters $100 \leq D \lesssim 500$ km are identified in this catalog and shown in Fig. **13**. Of the seven craters $D > 400$ km in this group, three are unnamed. The largest in this range is an unnamed crater southeast of and partially buried by Schiaparelli (-6° N, 13° E, $D \approx 510$ km). The remaining two unnamed craters are located at -18° N, 331° E (~470 km) and -37°N, 3° E (~430 km). The four named craters are Schiaparelli, Huygens, Cassini, and Antoniadi. The 301 craters in this group are not uniformly distributed across the planet, as is clear in Fig. **13**. The craters in this range reflect both the Martian crustal dichotomy and the major volcanic provinces in that there are fewer craters at higher northern latitudes and the Tharsis and Elysium regions are devoid of large craters.

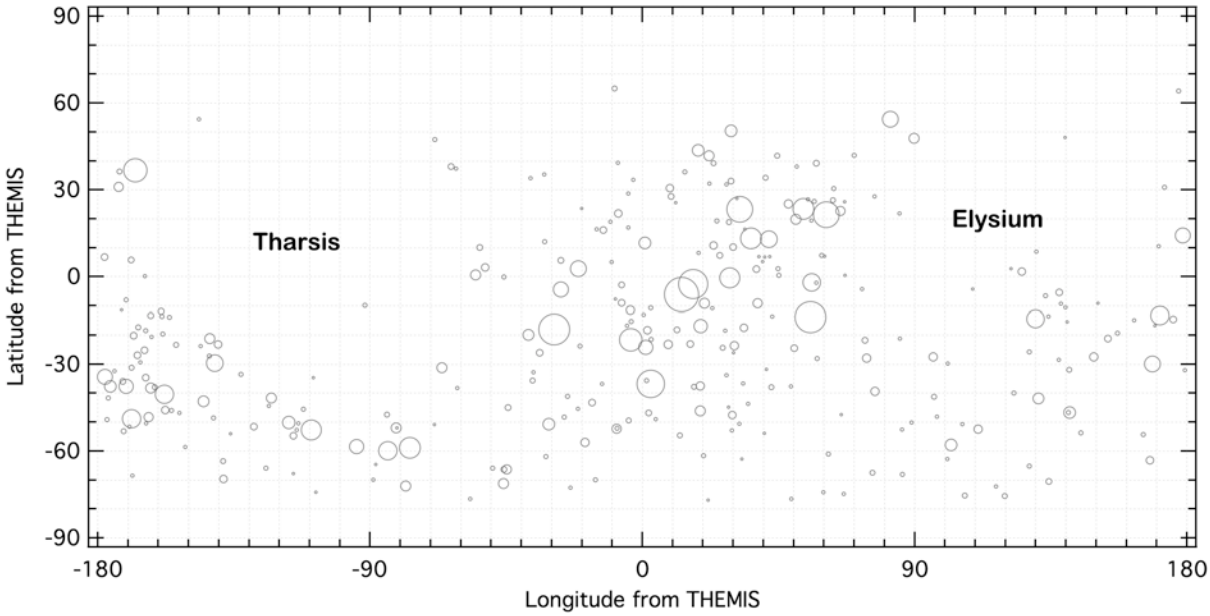

Figure 13: Locations and relative sizes of craters $100 \leq D \lesssim 500$ km on Mars. The large void around 20° N, -110° E is due to the Tharsis volcanic province, and the corresponding one ~100° E is due to the Elysium province.

3.2.3. Intermediate-Sized Craters (5-50 km)

This size range of craters has been well studied in the literature since imagery was first returned from spacecraft (*e.g.*, Chapman and Jones, 1977 and references therein; Tanaka, 1986 and references therein; Barlow 1988 and references therein). This range of craters, the locations of which are shown in Figure **14**, is mostly complex in morphology (save a very few simple craters up to ~15 km in diameter). Much of the early and current age-dating and stratigraphy work is done with this range of craters (see above references), and they inform studies of erosion rates, crustal strength, and scaling laws as will be discussed in subsequent sections. In a reflection of relative ages represented by crater densities in this size range, there are 560 craters per 10^6 km^2 on the averaged Noachian terrain, 207 on Hesperian, and only 98.4 on Amazonian. As a more detailed example, Chapman and Jones (1997) proposed there had been a large obliteration event early in Mars' history that buried craters $D \lesssim$ 20-30 km based on a relative lack of them. The same kind of deficit at this diameter range is observed in this database over much of the planet.

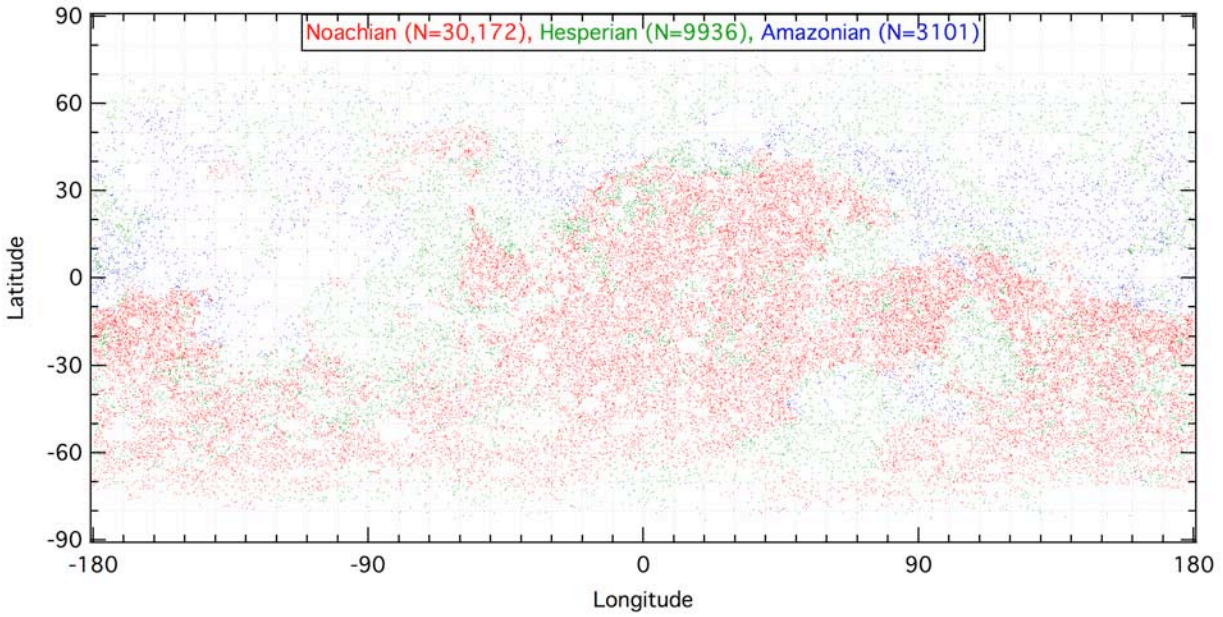

Figure 14: Map showing the distribution of all $5 < D \leq 50$ km Martian craters as a function of terrain age. Red dots represent craters on Noachian terrain, green are Hesperian, and blue are Amazonian. Terrain ages are from the Mars geologic maps (Scott and Tanaka, 1986; Greeley and Guest, 1987).

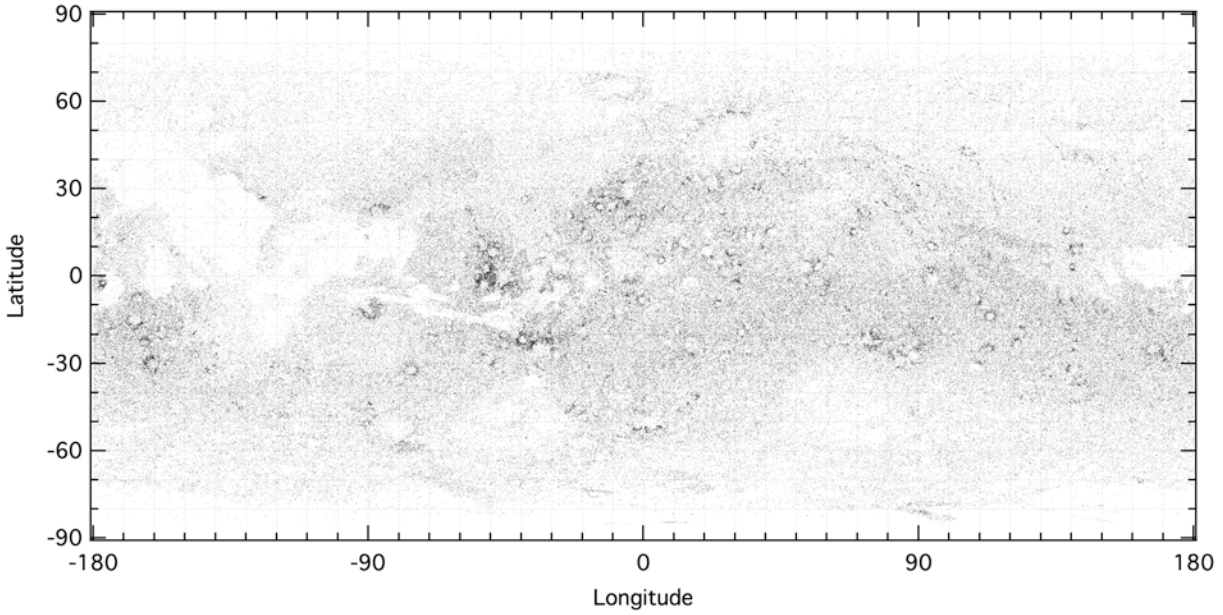

Figure 15: Locations of all $1 \leq D < 3$ km craters on Mars included in this database. This includes secondary craters; future releases of the database will have these separately marked.

3.2.4. Small Craters (1-3 km)

The small, $1 \leq D < 3$ km crater distribution on Mars is illustrated in Fig. **15**. The distribution of small craters can be used as a proxy for estimating relative regional ages - similar

to the larger size range discussed above - where more craters indicate an older surface and fewer craters indicate a younger surface. Readily visible as young surfaces due to their relative paucity of craters are the major basis Argyre and Hellas, the Olympus Mons volcano and three Tharsis Montes, Cerberus Planitia, Valles Marineris, and both polar caps. More locally, there is clear contamination from secondary crater fields closely surrounding individual large primary craters such as Lomonosov (65.3°N, -9.3°E) and Oudemans (-9.8°N, -91.8°E) (see Robbins and Hynek, 2011d (Section 4.2) for discussion of these fields). In addition, arcs of craters through Isidis are visible, emanating from Lyot crater (50.8°N, 29.3°E), and these are interpreted as secondary crater clusters from that large impact (Robbins and Hynek, 2011a (Section 4.1)).

3.2.5. Fresh Craters

Crater degradation/modification states were classified on a four-point scale. This was determined from analyzing each crater rim for sharpness and relief (1-4 pts), ejecta preservation (1-3 pts), floor infilling (1-4 pts), and relative depth/Diameter ratio (1-4 pts, determined based on latitude region; see Section 3.5). Points were added and then scaled to a final 1-4 class where 1 was the most modified and 4 was a pristine or nearly pristine crater. See the companion paper, Robbins and Hynek (2011b) for more detailed discussion of this classification (Section 2.4.4). These data are included in this release for all craters $D \geq 5$ km.

On an airless and geologically dead body, the distribution of fresh craters is nominally uniform over the surface since it should be of a uniform older age. On a body with an atmosphere and more recent geologic activity, such as Mars, the fresh crater distribution is instead a likely indicator of volcanic and aeolian erosion/modification efficiency across the planet (*e.g.*, Greeley *et al.*, 1992; Grant and Schultz, 1993) and periglacial processes on small craters near the poles. Fig. **16** shows the global distribution of $D \geq 5$ km fresh craters, and Fig. **17** shows the percentage of fresh $5 \leq D \leq 50$ km craters relative to all craters in that range. At a basic level, these show that weathering across the planet is far from uniform. Fresh craters are concentrated towards the equatorial regions and mid- to high-northern latitudes (between ~100-

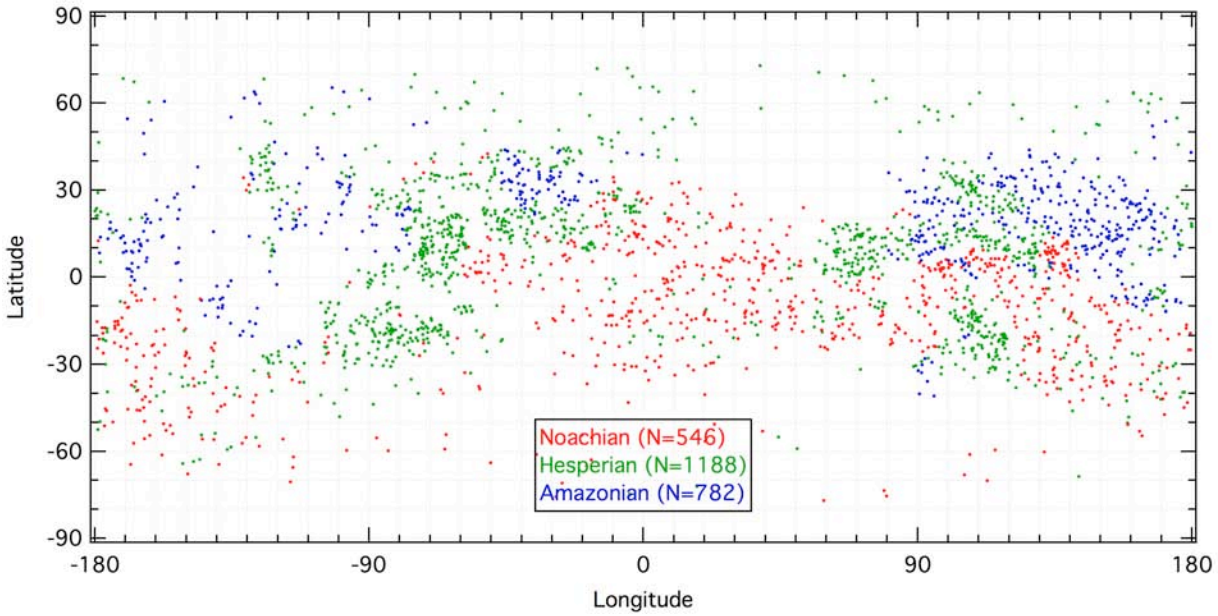

Figure 16: Scatter plot showing the distribution of all fresh $D \geq 5$ km fresh craters. Fresh craters are generally concentrated close to the equator but show a larger latitude range centered at ~200°E. Red dots represent craters on Noachian terrain, green are Hesperian, and blue are Amazonian. Terrain ages are from the Mars geologic maps (Scott and Tanaka, 1986; Greeley and Guest, 1987).

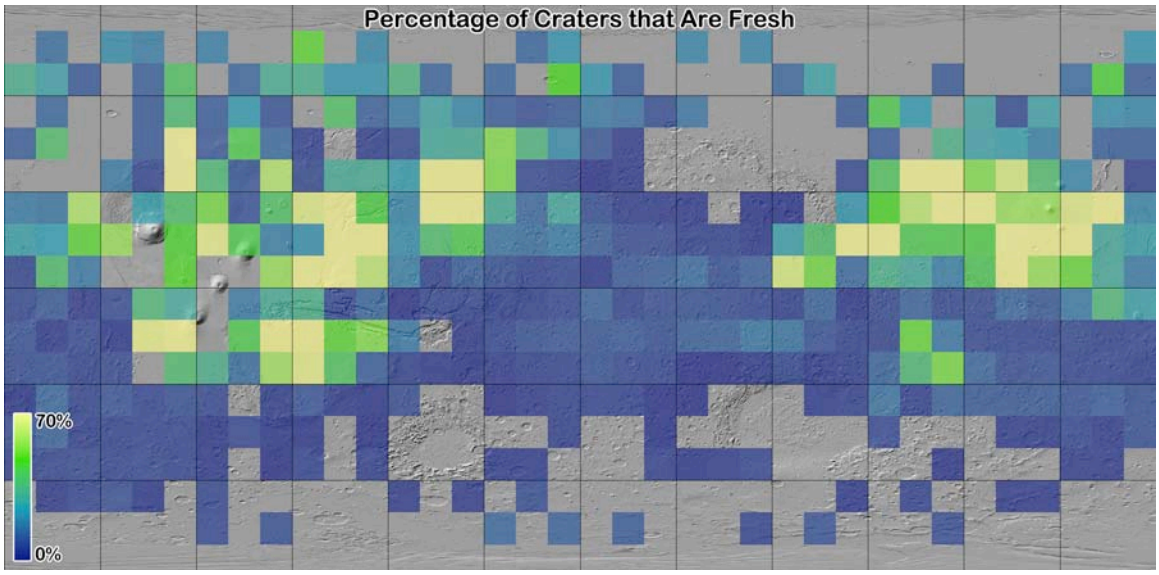

Figure 17: Area density plot showing the relative fraction of craters in 10°x10° bins that are fresh versus the population of all 5-50-km-diameter craters. Gaps are where there were not enough craters for an analysis or there were 0% fresh craters. Graticules are 30°.

300°E). They are also more frequently found on younger terrain, as expected: Spatially, there are 14.5 craters per 10^6 km^2 of Noachian terrain, 24.8 for Hesperian, and 17.3 for Amazonian.

The greatest fractional concentrations of fresh craters (Fig. **17**) are centered around the major volcanic provinces Tharsis, Elysium, and Syrtis Major, and the three basins Chryse, Isidis, and Utopia. A smaller concentration is also located between the two volcanoes Tyrrhena and Hadriaca Paterae. One can conclude from this that fresh craters are at least $2\times$ more populous on volcanic terrain than other surfaces. There is a general abundance above the average in the mid- to high-northern latitudes, as well, that likely reflects their relative youth.

In looking at atmospheric effects, Greeley *et al*. (1993) ran Mars global circulation models (GCMs) of Mars' atmosphere to examine predicted versus identified dust deposition. They found aeolian activity is high in the southern subtropics (~15-30°S), northern plains, fretted terrain, and surrounding the Tharsis and Arabia Terra regions. They expected low aeolian activity in Tharsis, Arabia Terra, and Elysium. Overall, the fresh crater distribution found in this database does not match that predicted by Greeley *et al*. (1993).

Better computers, topography models, and numerical techniques have advanced GCMs over the past few several years. The recent work by Haberle *et al*. (2003) compares more favorably with the crater results. They predict higher winds around Elysium, Tharsis, north and west of Tharsis, and south of Elysium around ~30-60°S. Except the last region, this is in general agreement with the fresh crater distribution from Fig. **17**.

Positive correlation with recent GCMs supports the hypothesis that fresh craters track well with atmospheric circulation. They also indicate that older models such as by Greeley *et al*. (1993) are inaccurate. As newer models are developed, further correlation experiments should be done. This does not mean that terrain type may not play a role. As indicated above, fresh craters favor Hesperian-aged terrain by number density and volcanic and basin terrain by type. However, these are likely well correlated themselves with the GCMs which must take into account topography, so decoupling these effects may not be practical nor possible.

3.3. Crater Morphologies Across Mars

Crater interior morphologies are included in this release for craters $D \geq 3$ km and ejecta morphologies are included for $D \geq 5$ km. The interior morphologic indicators include basic morphologic type (simple or complex) if it could be determined and indicators for central peaks, central pits, and summit pits. Morphology descriptors of wall features such as terraces and floor features such as tectonics, channels, dunes, and other floor deposits are also noted. Ejecta morphologies and morphometries are detailed for Martian cohesive layered ejecta blankets. The general distributions and properties of crater morphologies are described in this section and compared with previous works.

3.3.1. Distribution of Central Peaks, Pits, and Summit Pits

A classic feature of a fresh complex crater is a central peak, produced by rebound during the crater formation process. Central peak craters number 3049 in this database. They represent a steady global average of ~6.3% of all craters $D \geq 15$ km, yet they comprise a disproportionate number of fresh craters (>90% of fresh craters $D \geq 15$ km contain central peaks). This likely indicates that many craters classified as "CpxFF" (complex, flat-floored) or "CpxUnc" (complex, unclassifiable) were originally central-peak craters but the peak has since been buried or eroded. This interpretation is buoyed by Fig. **18** (the fraction of craters $5 \leq D \leq 50$ km with central peaks) which clearly shows that central peak craters are generally present in a relatively even fraction throughout most of the planet. There is a noticeable deficit in a band of the southern highlands arcing from Argyre basin up to the equator at the meridian and back down through Hellas. Interestingly, this does not correlate well with Fig. **17**, the fraction of fresh craters by area. The fraction of central peaks is mildly enhanced in Arabia Terra and in the southern highlands south of ~60°S and between East longitudes ~-90° to ~+90°. These imply the prevalence of central peaks is not completely a function of basic crater scaling laws and aeolian erosional processes.

A feature of some central peak craters on Mars is a pit in the middle of the peak, a classification of "summit pit." Martian craters as well as those on Jupiter's moons Ganymede and Europa will also sometimes display central pits; these pits are also occasionally observed in

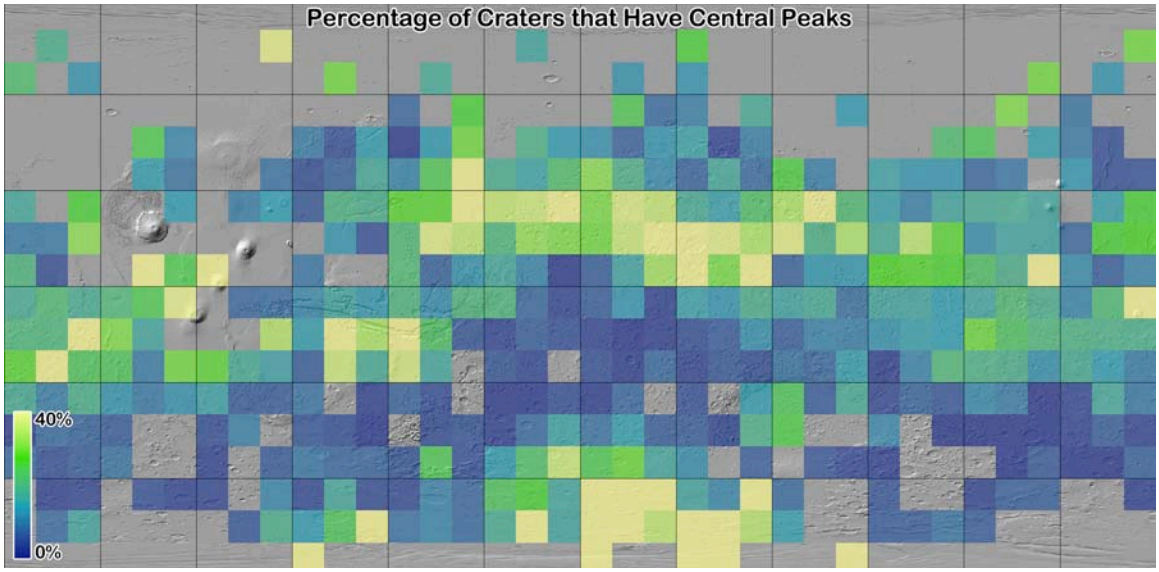

Figure 18: The fraction of craters $5 \leq D \leq 50$ km in 10°x10° bins that have central peaks. Underlying image is MOLA shaded relief. Gaps are where there were no craters, graticules are 30°x30°.

simple craters – unlike central peaks and, by extension, summit pits. Explanations for the genesis of these pits on crater floors or peaks are varied and include (1) vaporization of volatiles within the target during crater formation which releases gas near the center of the forming cavity (Wood *et al*., 1978; Senft and Stewart, 2008), (2) collapse of a central peak (Passey and Shoemaker, 1982), (3) excavation into layered target materials (Greeley *et al*., 1982), and/or (4) a melt-drainage model whereby liquid produced near to and during the impact forms a transient lake in the crater center that subsequently drains into the subsurface, leaving behind a central pit (Croft, 1981; Bray *et al*., 2006; Alzate and Barlow, 2011). The fraction of craters with summit pits (672 craters in all) are shown in Fig. **19**, and the fraction with central pits (1811 total) are shown in Fig. **20**.

It is difficult to draw many conclusions from the distribution of summit pit craters because of the small numbers involved, though they do generally agree with findings by Barlow (2011): They are prevalent in Arabia Terra, southwest of Tharsis, and southwest of Elysium. They appear to correlate well with the distribution of central peaks. This would not be surprising if their genesis is of the collapse mechanism suggested by Passey and Shoemaker (1982). However, there is a noticeable enhancement in the distribution north of Tharsis, and this is not observed in the

central peak distribution. There is likely a cryosphere near the surface at higher northern latitudes (Boynton *et al*., 2006) that would indicate a volatile-dependent origin. How ever, the significance of this is questionable: In each bin at that latitude (60-70°N), the number of craters with summit pits is 1. This lacks any statistical significance and so should not factor into any attempt to explain its formation other than as a footnote.

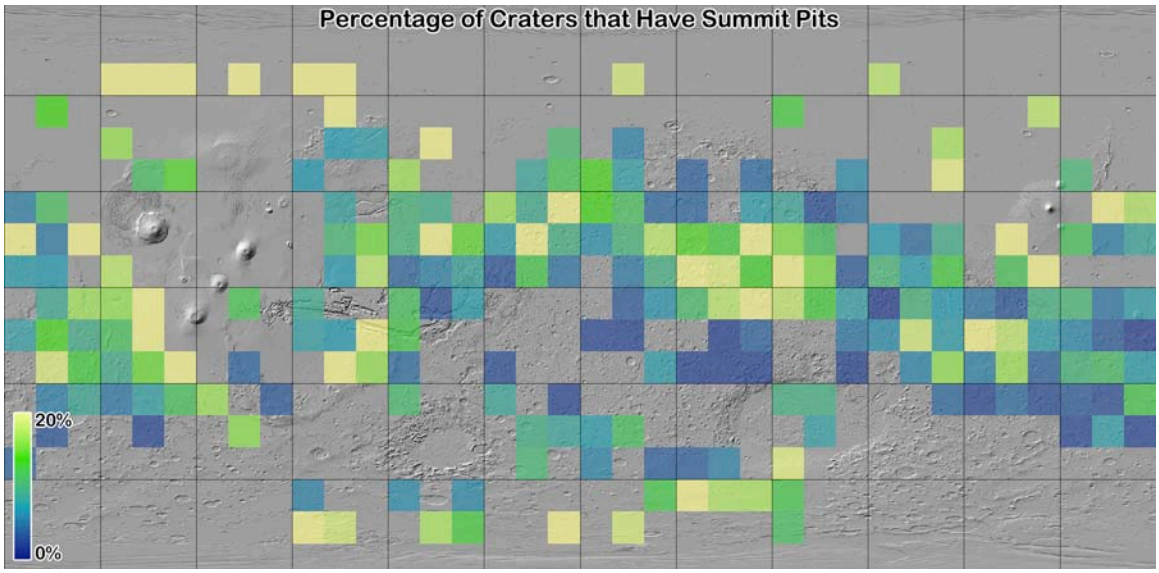

Figure 19: The fraction of craters $5 \leq D \leq 50$ km in 10°x10° bins that have summit pits. Underlying image is MOLA shaded relief. Gaps are where there were no craters, graticules are 30°x30°.

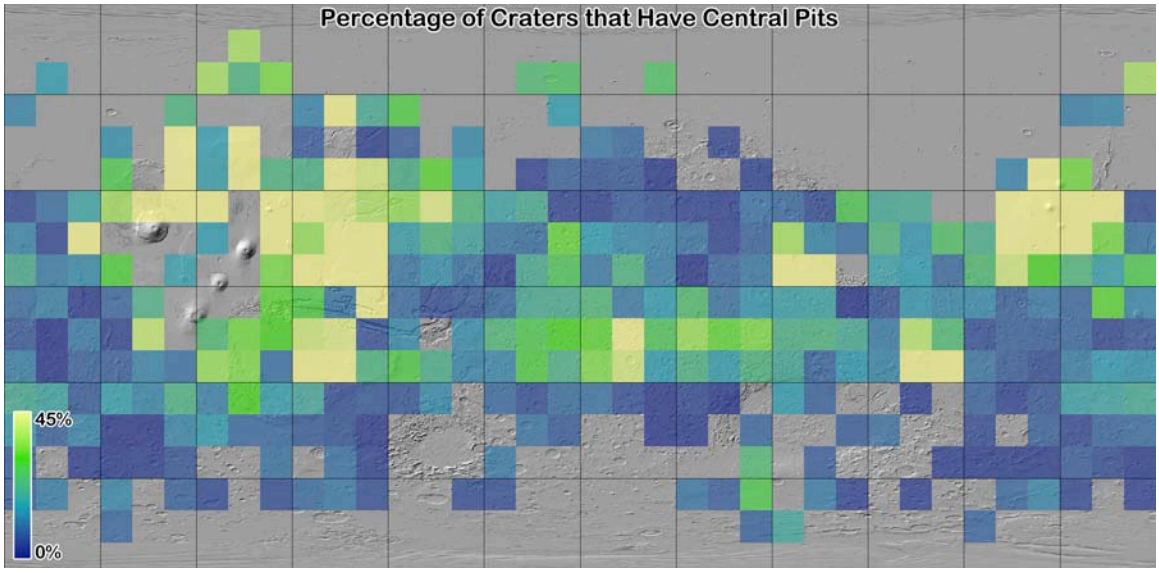

Figure 20: The fraction of craters $5 \leq D \leq 50$ km in 10°x10° bins that have central pits. Underlying image is MOLA shaded relief. Gaps are where there were no craters, graticules are 30°x30°.

Central pit craters are found to be enhanced relative to the global average around all volcanic centers, in general agreement with the findings by Barlow (2011): Tharsis, Elysium Syrtis Major, the Tyrrhena-Hadriaca corridor, and even southwest of Hells around Pitysua, Amphitrites, Peneus, and Malea Paterae. There is also an enhancement near the meridian and from about 0-30°S latitude. While these correlate with the fresh crater population, this is likely because the fresh craters correlate well with the volcanic terrain.

Subsurface ice near the equatorial Martian latitudes is not stable unless obliquities are >27°, and it is not stable in the Elysium region until obliquities are >30° (Mellon and Jakosky, 1995); if ice is present today near the equator, it is likely buried far below the surface (Clifford, 1993; Boynton *et al*., 2002). If the evacuation into subsurface liquid water reservoirs were the formation mechanism of central pits on Mars, though, one would expect significant concentration of central pit craters near the poles; this is not observed. Similarly, the central pit craters are generally among the fresh crater population (92% were a degradation state of 3 or 4), and they are missing in the high southern latitudes where central peaks were prevalent. Thus, they are likely not a collapse from a central peak. Of the four proposed mechanisms, the volatile vaporization and subsequent collapse and/or impact into layered material both fit the distribution observed, for volcanic terrain is generally enriched in volatiles, and it is often layered. The now-favored melt-drainage model in the literature (*e.g.*, Alzate and Barlow, 2011) appears to be less likely given the distribution, though it cannot be ruled out on this alone given the modeling that supports it (see Alzate and Barlow, 2011, and references therein). Further morphometric and mineralogy work may help constrain this, distinguish between the two, or show that one of the other mechanisms is more plausible.

3.3.2. In-Crater Dune Fields

Sand dunes on Mars are found both inside and outside of craters, and a comprehensive analysis culminated with the release of the Mars Global Digital Dune Database (MGD^3) by Hayward *et al.* (2007); this was supplemented by Hayward *et al*. (2008) and Fenton and

Hayward (2010). The original database was bound by ±65° latitude, omitting the poles, and it was constrained by the imagery at the time. Approximately 550 dune fields across the planet were included. The recent supplements expanded this coverage and identified a total of 1190 dune fields globally, both in and out of impact craters. In compiling this crater database, 777 craters $D \geq 3$ km were identified as containing dunes, and their locations are shown in Fig. **21**.

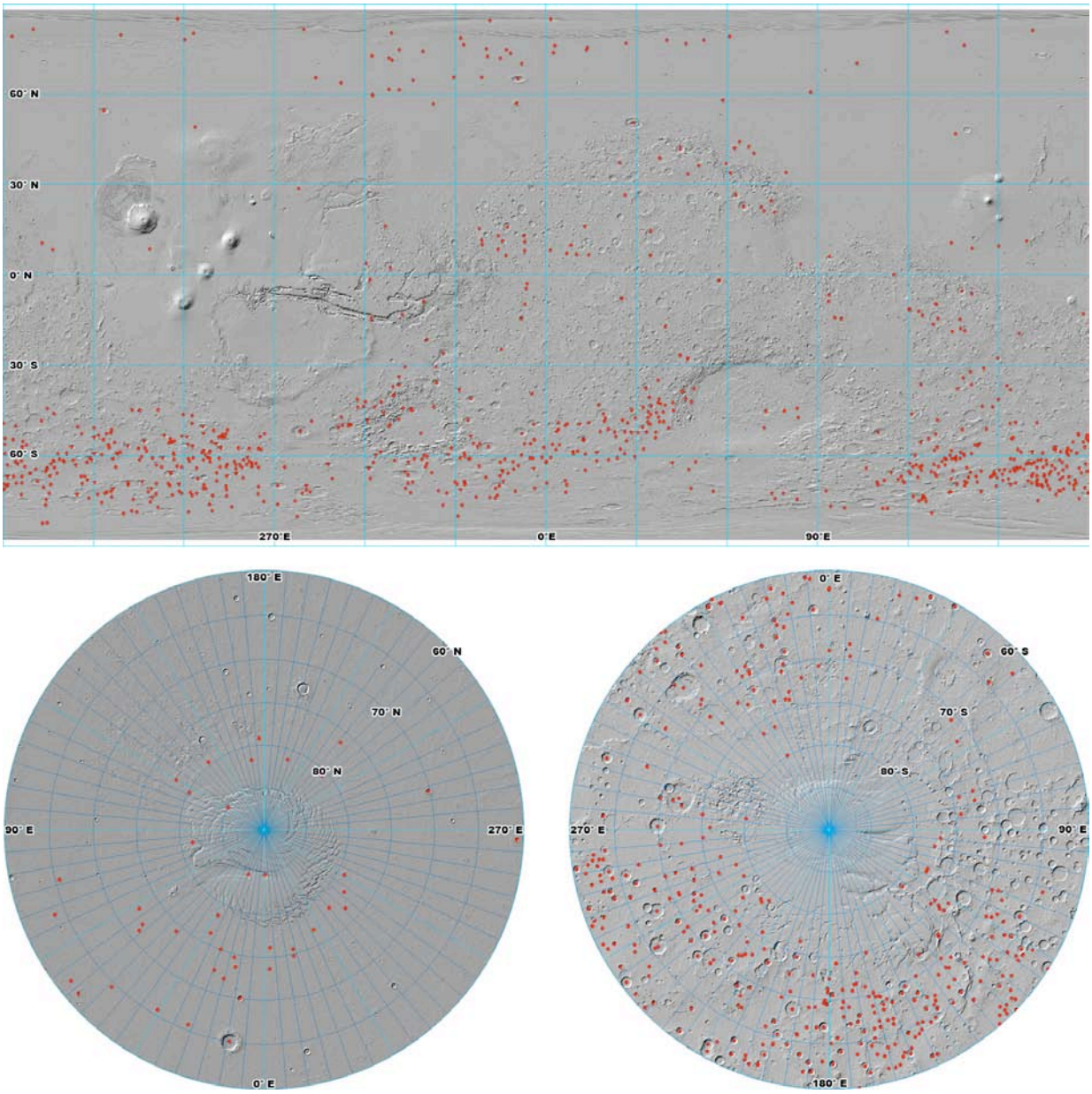

Figure 21: Locations of Martian dune fields in craters $D \geq 3$ km for Mercator (top) and north (bottom left) and south (bottom right) polar projections with MOLA-shaded and -colored relief underneath (Smith *et al.*, 2001).

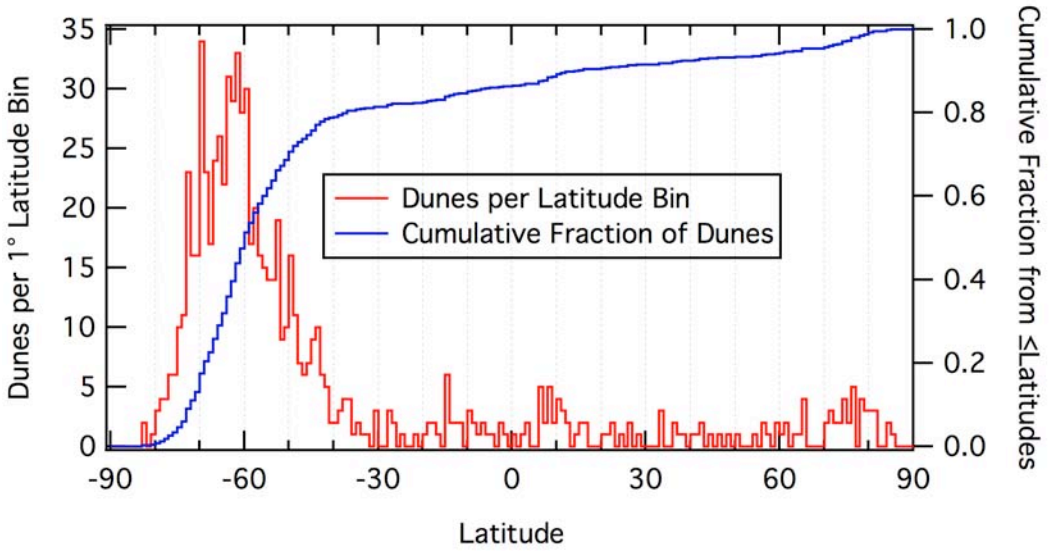

Figure 22: Latitudinal distribution of dunes within impact craters on Mars in 1°-wide bins. Red curve shows a basic histogram while blue is cumulative from the south to north pole and normalized to the total.

From Fig. **21**, a similar distribution as Hayward *et al.* (2007) is found with a large concentration west of Hellas, west of Argyre, and a large number between ~100° and 270°E longitude, south of ~50°S latitude. Numerous fields in the high southern latitudes between ~100° and 270°E agree well with Fenton and Hayward (2010). From Fig. **22**, the vast majority of these dunes (76%) are located south of -45°N, while 37% are located poleward of ±65°, indicating the original release of MGD^3 was missing at least 1/3 of in-crater fields. Northern dune fields are now present in MGD^3, but the relative abundance north of Acidalia were not observed, and there are some disparate results. For example, Hayward *et al*. (2008) identified 41 intracrater dune fields 65-90°N, while this database contains 36 (though this is within Poisson counting errors). Conversely, this database contains 30 craters 30-65°N latitude, while the MGD^3 contains eight. Future collaborations should better inform both datasets.

Preservationally, craters that contain dunes are generally more modified than average, as might be expected. 67% of them were marked with a "1" or "2" degradation state on the four-point scale, while 1% were a "4." This could be expected from comparison of the distribution with the overall fresh crater distribution in Section 3.2.5, as they are anticorrelated: Dunes are prevalent at southern latitudes where fresh craters are not, and the closest overlap in relative

densities is at roughly 60°S, 180°E. Following Section 3.2.5, this also correlates well with modern GCMs. However, there *are* otherwise fresh craters that do contain dunes - including several that are counted as "deep" among the deep crater population (see Section 3.5.2.3). This indicates that some large dune building on Mars likely took place in the recent past and may still be occurring today, in agreement with Fenton and Hayward (2010), who estimate that dune fields visible today formed an average of <1 Ma ago.

3.3.3. Ejecta Morphologies

Crater ejecta usually indicates crater youth, and on the Moon it is useful for geologic mapping and age relationships. On the Moon, craters display pure radial ejecta where the material has been ballistically emplaced during the excavation phase of crater formation as individual particles ejected during impacts. When probes returned the first images of Mars, however, a wholly new class of ejecta was observed. The terminology has varied significantly over the years (see companion paper, this volume (Section 2.4)), but the term "layered ejecta" is now part of the standardized nomenclature (Barlow *et al*., 2000). This database contains morphologic indications for ejecta and morphometric data for the layered type that will be explored in brief in this section for craters $D \geq 5$ km.

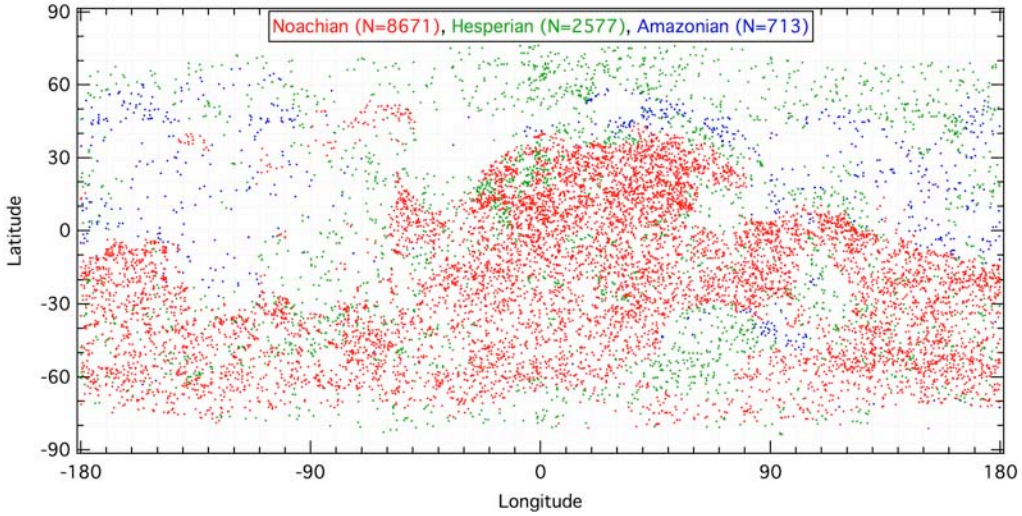

Figure 23: Scatter plot showing the distribution of all radial ejecta craters $D \geq 5$ km. Red dots represent craters on Noachian terrain, green are Hesperian, and blue are Amazonian. Terrain ages are from the Mars geologic maps (Scott and Tanaka, 1986; Greeley and Guest, 1987).

3.3.3.1. Radial Ejecta

Of the 46,482 craters $D \geq 5$ km in this database, radial ejecta is the sole ejecta type in 13,025 craters. They are shown as a function of terrain age in Fig. **23**. The spatial density on each terrain type is per 10^6 km^2: 161 Noachian, 54 Hesperian, and 23 Amazonian. It is clear from this that radial ejecta on Mars can still be visible around ancient craters, otherwise the distribution should be even. In fact, the relative densities are more disparate than those from the fresh crater population, as one would expect if this were the case.

3.3.3.2. Layered Ejecta

When Martian layered ejecta craters were first examined, it was thought they were part of a type evolution that started with multi-layered craters that erode to single-layer ejecta craters that finally erode to pedestal craters (McCauley, 1973; Arvidson *et al*., 1976). Woronow and Mutch (1980) and Mutch and Woronow (1980) were among the first to quantitatively examine the geometric properties of the ejecta of each and determine they are not evolutionarily related. Since then, two hypotheses emerged for a formation process of the layered ejecta. One holds that they are formed when an impactor hits a volatile-rich sub-surface, the impact energy melts or vaporizes the volatiles, and the ejecta acts like a fluid as a result (*e.g.*, Carr *et al.*, 1977). The other states that they form when the severity of the impact causes atmospheric vortexes and winds, but this generally requires a thicker Martian atmosphere to account for the extent of ejecta (*e.g.*, Schultz and Gault, 1979; Schultz, 1992). It is possible a combination of both models is at work on Mars (*e.g.*, Barlow, 2005; Komatsu *et al*., 2007).

Over the years, these forms of ejecta have only been observed on Venus, Mars, Ganymede, and Europa (*e.g.*, Barlow *et al*., 2000; Boyce *et al.*, 2010). The lack of atmosphere on Ganymede and Europa indicates that an atmosphere and hence the atmospheric vortex model is not required for the formation of these kinds of ejecta, but the intense surface heat on Venus would suggest that volatiles within the impact medium may also not be necessary in some formation situations. Determining the morphometric characteristics of each should help constrain these and discriminate between the two in different cases. Motivationally, if it can be

shown that morphometric analysis required volatiles for the ejecta to form, then high concentrations of these crater types could indicate where subsurface water may be for future human exploration. To this end, an introduction to the distributions and characteristics is presented here, and future work will focus on combining these with mineralogic, thermal inertia, and crater age dating of the ejecta blankets themselves to distinguish between the models.

Of the 46,482 craters $D \geq 5$ km in this database, a total of 12,621 craters are surrounded by layered ejecta blankets: 9265 are single-layered (SLE), 2571 are double (DLE), and 785 are multiple (three or more) (MLE). (See Robbins and Hynek (2011b) for a detailed description of all ejecta morphologic and morphometric properties in the database.) The Barlow Database (Barlow, 1988) over these diameters contains 3221, a factor of $\sim 4\times$ fewer. There is a size dependence observed on the number of layers. The largest SLE crater is a 111-km-diameter crater, the largest DLE is 78 km, and largest MLE is 83 km. These could be considered outliers, though, and insignificant in determining the onset of these features because all types start to increase dramatically on a size-frequency diagram at $D \sim 30-40$ km; they are statistically identical in frequency for $D \gtrsim 20$ km. For MLE, the peak in frequency is sharp and for craters

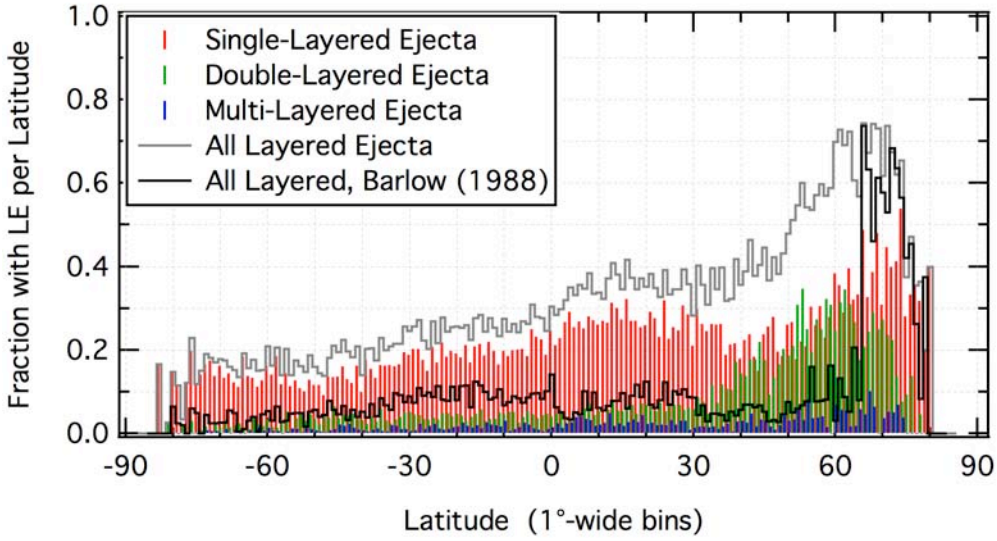

Figure 24: Distribution of layered ejecta craters, by type, per latitude bin. Red, green, and blue indicate SLE, DLE, and MLE distribution, respectively, while the grey line shows the sum of all three. For reference, the sum of all LE types from Barlow (1988) is shown as a black line.

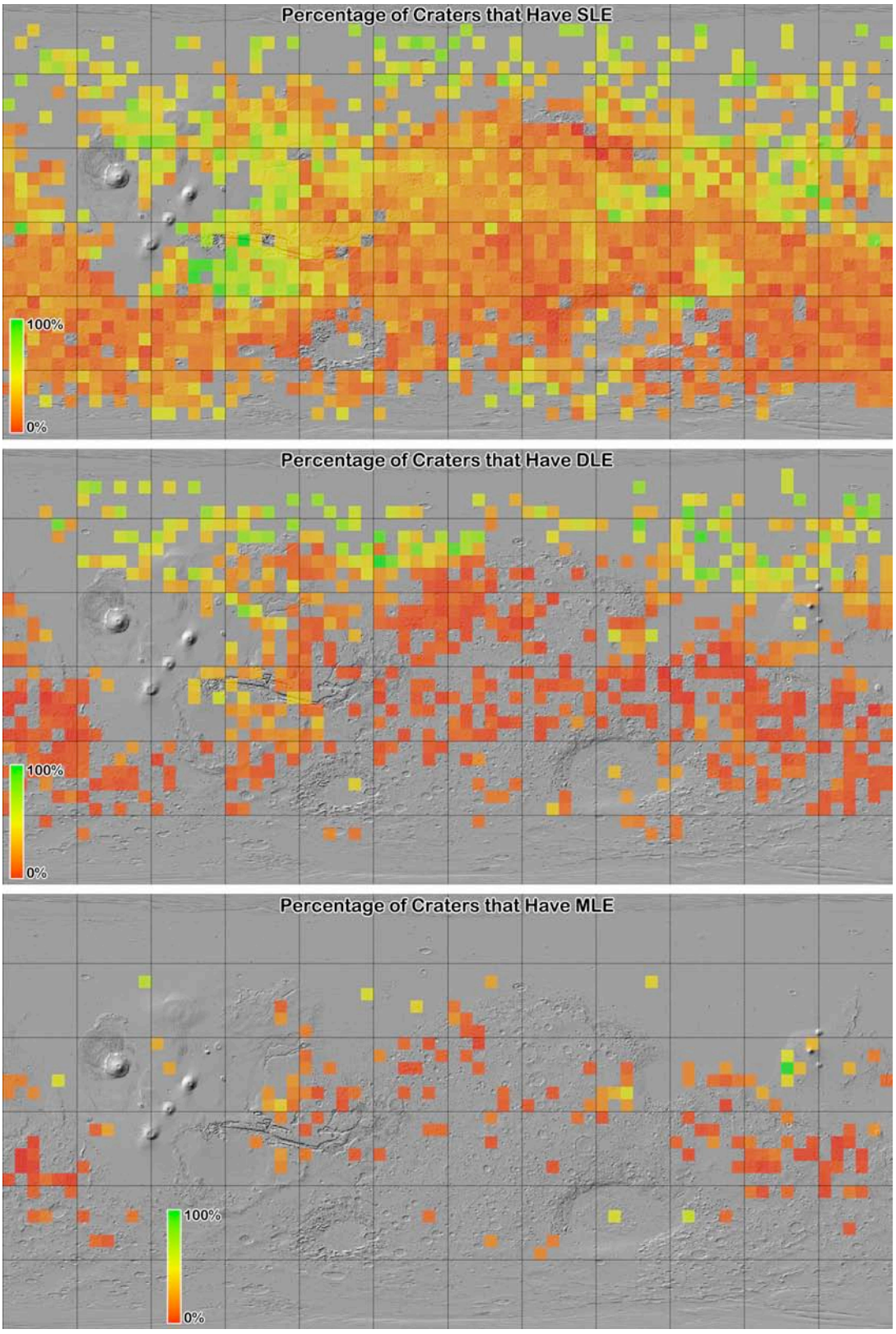

Figure 25: The fraction of craters $5 \leq D \leq 50$ km in 5°x5° bins that have layered ejecta blankets. Underlying image is MOLA shaded relief. Gaps are where there were ≤1 craters per bin, graticules are 30°x30°.

D = 17 km; it is rarer for a crater to display MLE blankets at smaller diameters. The peak for DLE is broader with a maximum at 12 km. No peak has been found for SLE craters, likely due to the size cut-off at 5 km for crater ejecta in this release of the catalog.

These craters are not distributed uniformly across the planet, a feature that has been known for many years (and characterized, for example, in Barlow, 1988). When examining the latitude-dependence, Fig. **24** clearly shows these craters are more numerous in the northern hemisphere and especially at high northern latitudes 50°-80° N. The enhancement around 10°N is likely due to volcanic terrain abundance at this latitude, discussed below. Barlow and Perez (2003) and Barlow (2005) found a relatively even distribution across the planet with a marked spike ~65-80° N. Another feature of the Barlow Database that this catalog reproduces well is the significant increase of DLE craters ~40-75°N (though Barlow and Perez (2003) found a tighter latitude range). Any mechanism to explain these features must include this as a hard constraint.

Expanding this distribution in longitude is shown in the three-panel Fig. **25** shows all SLE, DLE, and MLE craters as a fraction of all craters within a $5° \times 5°$ bin, similar to analyses in Barlow and Perez (2003) from Viking data. Clearly visible are several trends. First, SLE craters dominate all volcanic terrains (that have a significant number of craters on them). They also dominate in the high northern latitudes. DLE craters are similar though they clearly dominate at higher northern latitudes as indicated in Fig. **24**. In general, there was no longitude dependence upon the distribution of DLE craters, though there was a slight increase in the eastern Tharsis and lower Valles Marineris region. It is difficult to draw conclusions from the MLE distribution due to small numbers (even at coarser binning, global trends do not show). The most that can be confidently stated is that the MLE distribution does not disagree with the SLE distribution, and there is a significant enhancement around Elysium. These all agree with the general conclusions from Barlow and Perez (2003) with the main anomaly being the concentration of SLE craters to the southwest of Valles Marineris. This could be an artifact of the way the data are presented: In Fig. **24**, LE types are shown as a fraction of all craters, but in Barlow and Perez (2003), the data are discussed and displayed as a fraction of craters with ejecta.

Table 4: Average ejecta mobility values for select layered ejecta types.

	SLE	DLE Inner	DLE Outer
Global	1.4	1.4	2.5
<-40°N Latitude	1.6	1.5	2.5
±30° Latitude	1.2	1.2	1.8
>+40°N Latitude	2.0	1.5	3.2

A morphometric characteristic examined is ejecta mobility, the extent to which the ejecta travels relative to the crater radius. This database uses the average extent, following Barlow (2005). It reproduces her findings well, though the ejecta mobility is a little less in this work (see Table **4**). As a global average, ejecta mobility of SLE craters averages 1.4 versus 1.5 found by Barlow (2005). DLE inner layers are 1.4 (versus 1.5) and the outer is 2.5 (versus 3.2). The ejecta mobility maximums were found to be 8.8, 4.9, and 11.7, comparable if slightly larger than Barlow (2005). An additional feature identified in early work (Mouginis-Mark, 1979) is a latitude dependence with ejecta mobility where, near the poles, the average is up to 2.0 versus the equatorial average of 1.4. This catalog's data show a similar trend, while the change happens at ~±30-40°. Ranges poleward of ±40° were examined separately from an equatorial region ±30°, and values are reported in Table **4**. Polar crater layered ejecta is found to travel farther than equatorial, while that in the northern hemisphere travels farther than in the south. This is placed in context with other morphometric data from this catalog in the Discussion (Section 3.7).

3.4. Crater Shapes

Basic crater shapes have been measured for decades (*e.g.*, Pike, 1976), and this database provides the ability to verify and update these morphometric values on Mars. For this analysis, only fresh craters of degradation class 4 were used (1964 simple and 1413 complex). This section addresses crater rims and surface-to-floor scaling. Scaling of crater depth (rim-floor) as a function of diameter is described in Section 3.5. Both of these rely upon accurate rim height measurements, a value that is in question given the relatively coarse nature of MOLA gridded

data. The fidelity of measurements in this database was addressed in detail in Robbins and Hynek (2011b) (Section 2.3). To within the uncertainty quoted in the database in rim heights, it was found that the measurements from gridded data were accurate when compared with the MOLA point data.

The first feature often addressed is rim height above the surrounding surface. At a basic level, this scales with crater diameter, and Melosh (1989) reports generalized results based on lunar data that rim height is ~4% of the crater diameter. However, examination of the Martian craters in this database shows a well-defined Gaussian distribution of this relationship for simple craters 1.9±0.7% and 1.4±0.6% for complex craters. This rim height is $>2\times$ smaller than what is typically reported. A possible explanation is that this database uses the average elevation around the crater rim instead of the highest point, but that is unlikely to be able to account for this large of a difference. Similarly, Melosh (1989) quotes the surface-to-floor depth of simple craters to be ~20% the crater diameter, but the simple craters in this database have a relationship of 8.9±1.9%. This is again $>2\times$ smaller than what is typically reported. Complex craters are shallower with a surface-to-floor depth 6.2±1.9% the crater diameter.

When looking at a diameter-dependence for rim height, fresh craters were examined in the method detailed below for depth/Diameter relationships. For fresh simple craters, a power law $h = 0.011D^{1.300}$ was fit, and a relationship of $h = 0.025D^{0.820}$ was found for complex craters (where h is rim height and D is crater diameter). In contrast, Garvin *et al*. (2003) found $h = 0.04D^{0.31}$ for simple craters (significantly different) but $h = 0.02D^{0.84}$ for complex (statistically identical). Better topographic data for smaller-diameter craters should help determine which - if either - is accurate.

Another way to examine scaling is to measure rim height relative to the overall rim-to-floor crater depth. This is found to follow a Gaussian with a mean 16±6% for simple craters and 18±6% for complex craters. The similar if slight offset indicates that the uplift and overturn that results in rim formation scales well through these two crater morphologies.

3.5. Global depth/Diameter Relationships

The ratio of a crater's depth to its diameter is one of its most fundamental properties, but it is one that was not directly measurable for extraterrestrial craters until the last decade. Prior, crater depths were estimated through photoclinometry and shadow lengths, processes that rely on knowing sun angles and assuming a uniform surface albedo (*e.g.*, Chapman and Jones, 1977; Pike, 1976, 1977, 1980, 1988; Davis and Soderblom, 1984). With the inclusion of the MOLA instrument on *Mars Orbiter*, global laser altimetry data has allowed for the uniform measure of crater topographic properties provided in this database. These were measured from the MOLA gridded data (MEGDR) as described in Robbins and Hynek (2011b). Briefly, crater rims and floors were identified in MEGDR data and the average elevation of points along the rim and deepest sections of the floor were used to compute the rim-to-floor depth (used in this analysis). This was found to be accurate when compared with the MOLA point data (PEDR), though debate remains as to whether the MOLA data accurately reflect the true rim crest and true lowest points on crater floors for smaller craters (D < 7 km). Limited random sampling performed in Robbins and Hynek (2011b) suggests that the recorded values are accurate to within the uncertainties that were also recorded. Future work comparing these data with the *Mars Express*'s High-Resolution Stereo Camera (HRSC, Neukum and Jaumann (2004)) should clarify this, but at present the MOLA data are still used.

Previous work by Garvin *et al.* (2003) estimated a $d = 0.21D^{0.81}$ relationship for simple craters $D \leq 6$ km, and $d = 0.36D^{0.49}$ for complex craters $D > 6$ km. Boyce and Garbeil (2007) find a similar curve of $d = 0.315D^{0.52}$ for complex craters $D \geq 7$ km. While hesitant to quote a global average for reasons discussed below, this database yields a simple crater relationship of $d = 0.179D^{1.012}$ and a complex one of $d = 0.286D^{0.582}$; these are comparable to previous works, though there is some variation as one may anticipate. This section discusses the depth-to-diameter relationship for Martian craters from this crater database and goes into significant detail on regional variations in this function.

3.5.1. Regional depth/Diameter Relationships

Across the surface of a planetary body, one might expect the ratio of a crater's depth to diameter to be constant since it is a gravity-dominated feature (Melosh, 1989). But, while gravity dominates, terrain properties control this final ratio, as illustrated in this section. This affects any "global" depth/Diameter ratio (*d*/*D*) one may quote, as has been done throughout the literature for decades (*e.g.*, Pike, 1980; Garvin *et al*., 2000, 2003; Boyce and Garbeil, 2007; Stepinski *et al*., 2009). To illustrate this, craters were separated by simple and complex morphologies and then into different diameter ranges. Diameter ranges within each morphology were done because there is no set, quotable ratio for the *d*/*D* value for fresh simple or complex craters – even though it is quoted as 1:5 and 1:10-100, respectively (Pike, 1977; Melosh, 1989).

All craters were divided into six diameter ranges that each encompassed roughly a factor of 2× in size. Smaller ranges had small-number problems that limited the overall utility, while

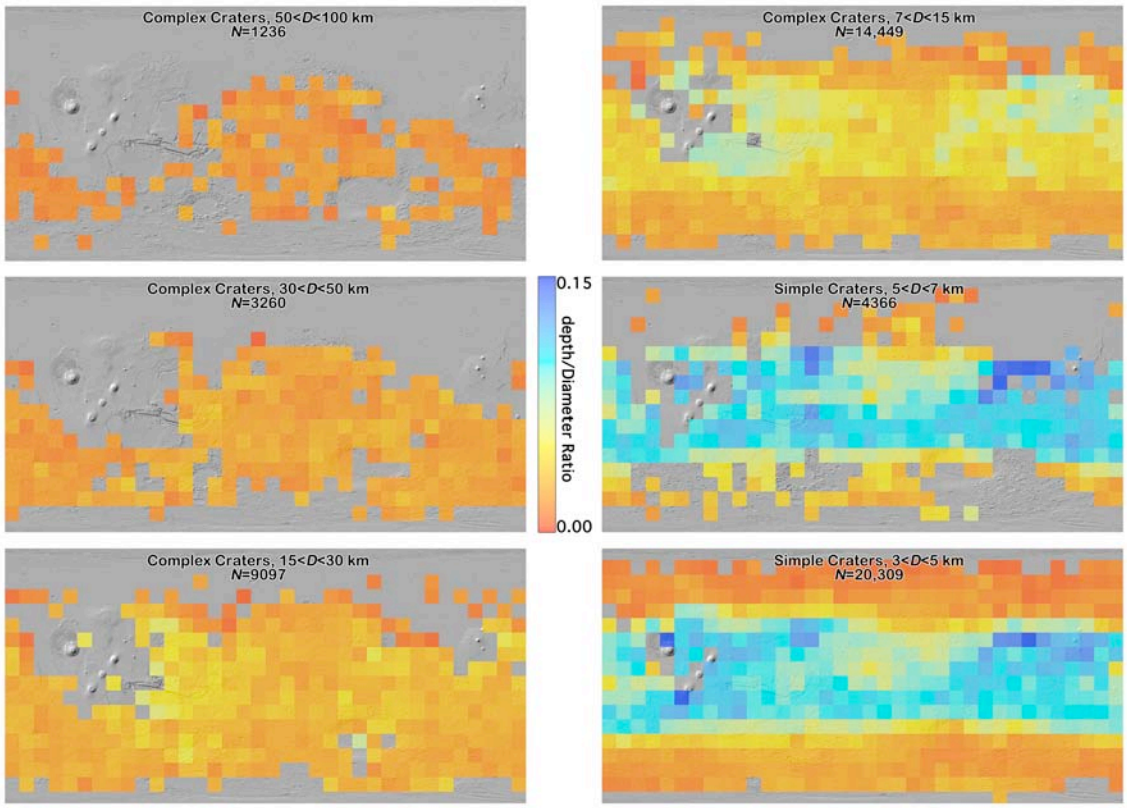

Figure 26: Six panels showing binned crater depth/Diameter ratios across Mars in 10°x10° bins; bins with $N < 5$ craters were removed. Four panels show complex craters and two are simple. All utilize the same color scale range of a depth/Diameter ratio of 0.00-0.15.

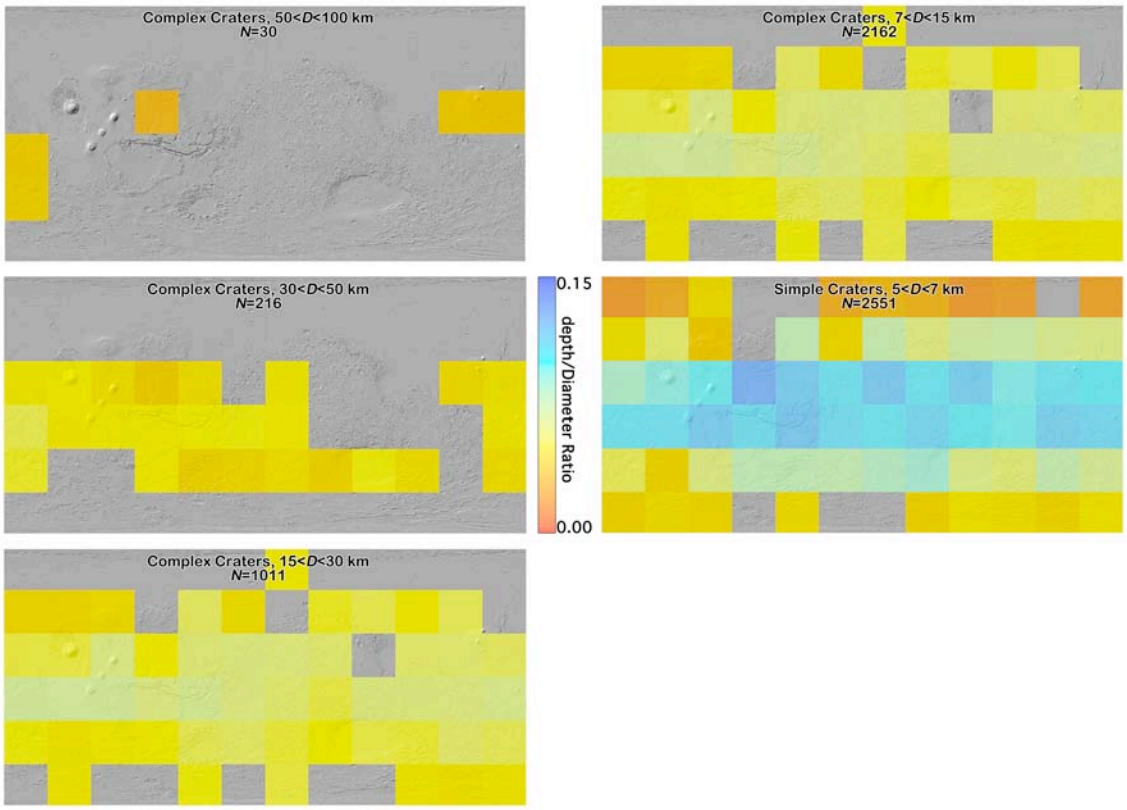

Figure 27: Five panels showing binned fresh (degradation states 3 and 4) crater depth/Diameter ratios across Mars in 30°x30° bins; bins with $N < 5$ craters were removed. Four panels show complex craters and one is simple (3-5 km-diameter crater degradation states were not calculated for this release of the crater database). All utilize the same color scale range of a depth/Diameter ratio of 0.00-0.15.

larger ranges muted the differences and hence analysis that could be done. Simple craters were separated into two ranges – 3-5 km (N=20,309) and 5-7 km (N=4366). Complex craters were separated into four: 7-15 km (N=14,449), 15-30 km (N=9097), 30-50 km (N=3260), and 50-100 km (N=1236). Craters were then binned into $10° \times 10°$ latitude/longitude bins and the mean d/D value was calculated; bins with <5 craters were removed. These are shown in Fig. **26**. A similar analysis was done for fresh craters only, illustrated in Fig. **27**, in $30° \times 30°$ bins and omitting the smallest diameter range. The results were comparable given the limitations, as discussed below.

Readily apparent from Fig. **26** is significant global variation. To first-order, craters $D \lesssim 20$ km poleward of ~±40° latitude are significantly shallower than their counterparts closer to the equator by as much as a factor of $2-3\times$. Second-order effects are that craters near the major volcanic complexes - Tharsis and Elysium - are deeper than the general average, and craters

within the Isidis, Utopia, and northern Chryse / southern Acidalia impact basins are the deepest on the planet, on average. Similar results were observed by Boyce *et al*. (2006), except they did not identify this effect in northern Chryse (this was not in their study area). In the equatorial range, the shallowest craters are within Arabia Terra, unique from the southern highlands. The patterns noted here disappear at larger crater diameters, or at least as far as can be determined based upon the smaller numbers. The last remnants of the pattern are in the 15-30 km range, showing the deeper craters around Tharsis and Elysium and shallower craters towards the north pole, but not the south. $D > 30$ km craters do not show this.

Analysis of the fresh crater population (degradation states 3 and 4) shown in Fig. **27** support the majority of these observations: Craters are shallower near the equator and deeper near the poles, and this effect persists up to the $D \leq 30$ km range. The more localized findings of deeper craters in the northern hemisphere basins is not found, though this is likely because of small number statistics; finer binning in the $5 \leq D \leq 7$ km simple crater range removes bins over those regions due to small numbers, so the effects are averaged out at the coarser binning shown. Deeper craters at small diameters are observed over the Tharsis region, though. The shallower craters observed in Arabia Terra are not observed at smaller diameters but are somewhat visible between 7 and 30 km, though the difference is slight. This overall agreement between Figs. **26** and **27** support the interpretation that Fig. **26** is generally indicative of the fresh crater population and the interpretations that follow.

The equatorial/polar dichotomy disappearing for $D > 30$ km craters is likely because larger craters formed with enough impact energy to be deep enough and no longer feel the effects of the local crust. Thus, their final shapes are nearly completely dictated by gravity scaling instead of being terrain-controlled. The pattern at smaller diameters of shallower craters towards the poles is likely explained by a near-surface cryosphere (Boynton *et al.*, 2002) that is weaker and cannot support a deep crater, relaxing to a shallower depth. This implies that the crust overlying the major impact basins Chryse, Isidis, and Utopia, is stronger than the average Martian surface today, supporting the deeper crater cavities. Expanding upon the argument from

Boyce *et al*. (2006), this shows that the local crust is stronger by at least a factor of 2× than most other surfaces on Mars. Mineralogical mapping in future work may help characterize the rock, as there are suggestions of regional olivine-rich units in southern Isidis that may play a role in this (Hamilton *et al*., 2003; Hoefen *et al*., 2003). Alternatively, the similarity with deeper craters on volcanic terrain and the gravitational load in the regions suggest these basins may be buried by volcanic material, and that could be stronger than the average Martian crust to ~1 km depths (*e.g.*, Searls and Phillips, 2007). A separate hypothesis - and it is possible that all three may be in play to various degrees - is that the terrain may be particularly fine-grained in some areas of these basins. Work suggests (*e.g.*, Soderblom *et al*., 1973, 1974; Schultz and Lutz, 1988) that fine-grained fill materials can produce anomalously deeper craters and that this material is found in at least some of these regions.

3.5.2. The d/D Relationship for Mars

3.5.2.1. Variation with Latitude and Terrain Type

As is readily apparent from Fig. **26**, except for craters $D \gtrsim 30$ km there is no uniform, global depth/Diameter ratio even for a small diameter range that can be quoted for the planet because of a significant shallowing near the poles. This must be taken into account when considering a relationship "for Mars" and when using it to determine different things at an automated level, such as its role in crater degradation state classification. Besides being important from a physical standpoint and understanding the near-surface crust, it is necessary to have an *a priori* estimate for how deep a crater likely was when it formed for purposes of estimating erosion and infilling. For example, if one were to use a global estimate for a $D = 5$ km simple crater ($d = 0.8$ km) and found it to be filled with lava with 0.2 km deep cavity remaining, then one would assume 0.6 km of burial. But, if this crater was poleward of ~40°, the actual d/D relationship yields a fresh crater depth of $d \approx 0.3$ km, so there is only 0.1 km of infill.

In the following sub-sections, craters were separated into seven different regions: First, a global average was done as has been worked on for several decades for comparison purposes.

Next, two latitude ranges were analyzed based upon Fig. **26** and Section 3.5.2.2 – poleward of ±40° and equatorward of ±40°. Finally, four terrain types were analyzed based on geologic maps by Scott and Tanaka (1986) and Greeley and Guest (1987).

3.5.2.2. Bimodal Nature

Stepinski *et al.* (2009) clearly showed *d*/*D* are bimodal for craters equatorward of ~±40°, the deep craters being "severely depleted southward of ~38°S." Their work was among the first to study this in a broad, systematic way, though they used a sub-set of 2444 craters to do so. Previous research dating to 1993 (Mouginis-Mark and Hayashi, 1993) used 109 fresh craters 20-40°S and found a general shallowing trend farther south, but their lack of large numbers of craters limited the spatial analysis and robustness of their work. Similarly, Boyce and Garbeil (2007) identified this feature by using a test population of 6047 craters throughout the planet. Mouginis-Mark and Hayashi (1993) attributed this to a cryosphere, and Stepinski *et al*. (2009) identified this as a possible contributor, as well. Stepinski *et al*. (2009) also raise the possibility of surficial mantling deposits as suggested by Soderblom *et al.* (1973, 1974). Boyce and Garbeil (2007) have a different interpretation. They suggest there is a gap in crater ages separated by the Late Noachian / Early Hesperian boundary that was the result of "abrupt onset and cessation of an episode of terrain degradation" as suggested by Craddock and Maxwell (1993). This would reflect a very rapid 10 μm/yr erosion/infill rate (current estimates are ~1-10 nm/yr (Golombeck *et al.*, 2006)). They suggest the contrast with higher latitudes indicate these erosion processes were not active there or other processes erased their effects.

Similar results are found in this database, as illustrated in Fig. **28**. Simple craters tended to have slightly deeper *d*/*D*, as would be expected from Section 3.5.1, so they are not plotted separately. In Fig. **28**, two different datasets are shown – the overall results for all craters as small red dots and craters with a degradation state of 4 as larger blue dots. An alternate definition of degradation state, only used in this analysis, removes the discriminator of depth/Diameter ratio (green dots). This work finds similar results as Boyce and Garbeil (2007) and Stepinski *et al.* (2009), but from a broader examination, more detail can be gleaned.

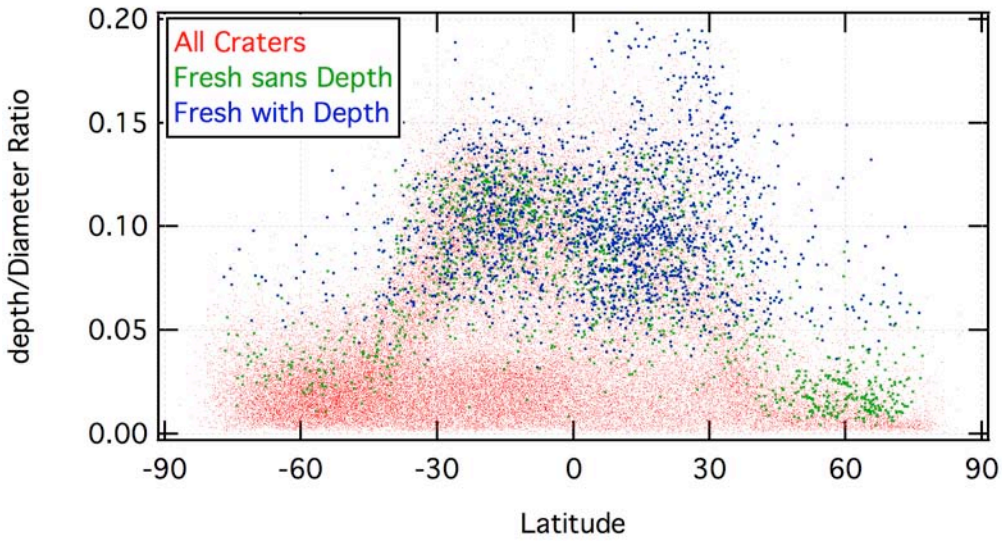

Figure 28: Scatter plot showing all craters with only fresh craters over-plotted. Red dots represent all craters, green symbols are fresh craters based only on morphology, and blue symbols are fresh craters that include depth/Diameter ratio as a parameter (craters in both sets will be blue).

First, the same pattern of a gradual *d*/*D* decrease in the deepest craters occurs over the ~10° range of ±30-40° latitude. However, the north and south hemispheres vary significantly in the magnitude of the difference. In the south, which is what previous works looked at (likely due to the larger crater population in that hemisphere), the *d*/*D* changes from a relatively tight distribution of ~0.0.8-0.14 and decreases to ~0.04 with outliers that go up to ~0.10. In the northern hemisphere, there is significantly more spread with *d*/*D* ranging from ~0.08 up to ~0.20. In the higher northern latitudes, there is a shift where a large number of craters are concentrated at shallow ~0.02 ratios but with a nontrivial number of craters as deep as ~0.05-0.10 at high northern latitudes.

Most of this is reflected well in the "all craters" population in Fig. **28**. The pattern is mirrored in the "Fresh sans Depth" population of craters; this is shown because, despite analysis in the next section, there may still be more significant terrain dependence than the deepest craters *d*/*D* relationship shows (there are 50% more fresh craters with this definition than with the full definition). The craters using the full definition of "Fresh" show similar patterns for equatorial craters but very few are present at higher latitudes.

There are several pieces of data that can inform the interpretation of these observed trends. This discrepancy between the northern and southern hemispheres can be partially explained by the presence of large impact basins and volcanic complexes in the northern hemisphere that contain the deepest craters on the planet (see Section 3.5.1). Though this can explain the differences up to ~30-40°, it is not adequate for the higher northern latitude discrepancy. A possible explanation is that the crustal thickness in the southern hemisphere may add strength to the rock, allowing it to support deeper crater cavities. In the north, the ice table may be both thicker and closer to the surface - indeed, *Phoenix* at 68.22°N found ice just a few centimeters from the surface (Smith *et al*., 2009). The enhanced relaxation cannot support deep craters, so even otherwise morphologically fresh craters are still comparatively very shallow. Another possible contributing factor could be that there is a more diverse terrain in the higher southern latitudes than in the north. In the north, the northern part of Tharsis and Utopia are present, but otherwise the terrain is predominantly the low northern plains and polar cap. The high southern latitudes contain major volcanoes, the southern half of the comparatively fresh Hellas and Argyre basins, southern highland terrain, and the residual polar cap. While these are offered as likely contributing factors, this should be an area of future investigation.

3.5.2.3. Deepest Craters Method

Arguably, measuring the deepest, freshest craters is likely to produce the best estimate of the original, pristine, just-after-formation crater depth-to-diameter ratio. This method has been utilized in the past several times, notably by Garvin *et al.* (2003) and Boyce and Garbeil (2007). The former used the deepest 25% of their simple craters from which they estimated a $d = 0.21D^{0.81}$ relationship from 469 craters for $D \leq 6$ km, and $d = 0.36D^{0.49}$ for complex craters $D > 6$ km. The latter examined craters $12 \leq D \leq 49$ km and found a relationship of $d = 0.315D^{0.52}$, in reasonable agreement with Garvin *et al*. (2003).

The methodology of Boyce and Garbeil (2007) is what was used here: They separated craters into diameter size bins and then iteratively used the single deepest, average of the two deepest, average of the three deepest, etc. craters in each bin through which to fit a power law.

They found the slope of the power law was a constant 0.52±0.004 despite increasing the number of craters, while the amplitude of the power law fit changed from 0.363 to 0.356 to 0.333, decreasing with increasing numbers of craters. This was expected and helped to confirm they were sampling the results of the underlying physical process rather than secondary effects, and it produced a more robust result. The value quoted above is for the five deepest craters.

Repeating their example, craters from this database were binned in multiplicative $2^{1/8}D$ bins. Larger intervals were used, where the deepest two craters were averaged together and a power law fit, then the deepest 3, 4, 5, 10, 15, 20, and 25 per bin. For complex craters $6 < D < 90$ km, the exponent reached a constant level for 3 or more craters with a range of $0.572 - 0.593$ and mean 0.582±0.008. While this is slightly greater than their value, it is still fairly close and can be explained because of the use of a larger dataset and diameter range. Also similar to their results, the amplitude started large at 0.360 and proceeded to decrease linearly when including 4 or more craters ($A = -0.0025N + 0.2938$ where A is the amplitude and N is the number of craters). While a smaller amplitude is reported here than in Boyce and Garbeil (2007), this can be explained in that their definition of crater depth was average rim height to the deepest pixel on the floor; the definition used in this database was average rim height and the average of many floor pixels (at least $N = 3$).

The analysis for simple craters was not as straight-forward. The exponent on the fit varied significantly until at least four craters were included, at which point the range was $0.985 - 1.038$ with a mean 1.012 ± 0.020. This is steeper than Garvin *et al.* (2003) and likely represents a larger dataset over a broader region of the planet (global) from their work. The robustness of this exponent in other analyses in this work indicates it is likely not anomalous. The amplitude of the fit decreased dramatically from a maximum of 0.271 to an average of 0.179 ± 0.001 for the 10-25 deepest crater fits.

Based on this work, the averages are what will be quoted as the "final" values for the global depth/Diameter relationship on Mars for these craters and they are reported in Table **5**. The amplitude from the 4 deepest craters fit for complex craters is used because that was the

onset of an observed linear decline. When exploring this further, the craters were separated into regions – northern plains, southern highlands, polar, and volcanic – and separated by latitude – equatorward of ±40°, and poleward of ±40°. The regressions were again run, and the results are found in Table **5**.

When examining the craters poleward of ±40° latitude, in both simple and complex crater cases there was no convergence upon a single value for either the exponent or amplitude of the fit for simple and for complex craters. This may be due to relatively small number statistics, but there were still several thousand craters being analyzed and this is an unsatisfying and unlikely

Table 5: Crater depth/Diameter ratios on Mars have been quoted as overall global averages for decades, but examination of the global distribution shows there are variations based on terrain. This table shows the simple (top line) and complex (bottom line) depth/Diameter relationship when are divided into a variety of terrain types. The number *N* of craters in this table is the number used in the "All Craters" analysis.

		Deepest Craters	Fresh Craters	All Craters
Global	Smp (N = 37,091):	$d = 0.179D^{1.012}$	$d = 0.097D^{1.061}$	$d = 0.047D^{1.284}$
	Cpx (N = 32,021):	$d = 0.286D^{0.582}$	$d = 0.250D^{0.527}$	$d = 0.107D^{0.559}$
-40° to +40°	Smp (N = 24,875):	$d = 0.175D^{1.022}$	$d = 0.084D^{1.245}$	$d = 0.078D^{1.106}$
	Cpx (N = 22,290):	$d = 0.280D^{0.570}$	$d = 0.229D^{0.567}$	$d = 0.155D^{0.464}$
≤-40°, ≥+40°	Smp (N = 12,210):	$d = 0.177D^{0.724}$	$d = 0.083D^{1.073}$	$d = 0.014D^{1.465}$
	Cpx (N = 9742):	$d = 0.244D^{0.579}$	$d = 0.174D^{0.629}$	$d = 0.032D^{0.881}$
Northern Plains	Smp (N = 3693):	$d = 0.165D^{1.094}$	$d = 0.073D^{1.311}$	$d = 0.011D^{1.992}$
	Cpx (N = 1308):	$d = 0.479D^{0.359}$	$d = 0.274D^{0.502}$	$d = 0.227D^{0.158}$
Volcanic Terrain	Smp (N = 2471):	$d = 0.212D^{0.886}$	$d = 0.182D^{0.718}$	$d = 0.091D^{1.010}$
	Cpx (N = 1008):	$d = 0.291D^{0.526}$	$d = 0.240D^{0.539}$	$d = 0.209D^{0.451}$
Southern Highlands	Smp (N = 23,087):	$d = 0.235D^{0.777}$	$d = 0.154D^{0.821}$	$d = 0.051D^{1.261}$
	Cpx (N = 23,850):	$d = 0.303D^{0.571}$	$d = 0.231D^{0.556}$	$d = 0.112D^{0.541}$
Polar Terrain	Smp (N = 727):	–	–	$d = 0.0028D^{1.843}$
	Cpx (N = 202):	–	–	$d = 0.014D^{1.161}$

reason. To extend the trend, additional regressions with 30 and 50 deepest craters were calculated. For simple craters, a trend emerged with $N \geq 10$ craters for the exponent to be $p = 0.014N + 0.667$. Similarly, a line could be fit for the amplitude $A = -0.013N + 0.237$. Since it is for $N = 10$ craters that a predictable pattern emerged, it is those values quoted in Table **5** and used in determining crater degradation state for this latitude range (see companion paper, this volume). A similar pattern was present for $N \geq 5$ craters for the complex regression, $p = 0.038N + 0.448$ and $A = -0.023N + 0.313$. Thus, it is the $N = 5$ regressions quoted in Table **5** and used to determine crater degradation state.

This indicates that, as expected from Section 3.5.2.1, craters are shallower overall at higher latitudes. This must be taken into account when utilizing *d*/*D* as a proxy for crater degradation state, for it will result in anomalously degraded craters at these latitudes. Of interest, the complex slope is very similar to that for the globe, but the slope for simple craters is significantly shallower. This is likely due to two main reasons. First, as identified in Boyce *et al*. (2006) and discussed in Section 3.5.1, the very deepest and largest simple craters are in Chryse, Utopia, and Isidis, generally south of 40°N latitude; while these will be included in the global analysis, their absence here will decrease the amplitude of the largest few diameter bins and hence decrease the exponent. Related, the second likely contributing factor is that the crustal strength is significantly less, and the inability to support deeper cavities will likely scale with crater diameter, also decreasing this exponent. It should be noted, however, that the slope calculated here is very similar to the simple crater relationship calculated by Garvin *et al*. (2003).

While the relationship poleward of ±40° was subject to significant differences, perhaps unsurprisingly the relationship equatorward of ±40° was very similar. This is easily explained by the deepest craters being in this region of the planet and so an algorithm designed to capture the deepest ones would pick up on these in a global distribution. Regressions over the same *N* range as for >±40° were run with the simple craters converging for $4 \leq N \leq 30$ craters per bin, with the exponent 1.022±0.021 and amplitude 0.175±0.002. Complex craters did show a slight decrease in slope as *N* increased beyond 5, but the magnitude of this decrease was <8%. The

average over $10 \le N \le 30$ was 0.570±0.010 and the amplitude 0.280±0.001. Overall, these results are in good agreement with the global average and are within the quoted ranges.

Analysis by terrain type for the deepest craters method yielded higher amplitudes for the complex crater *d*/*D* relationship for all three analyzable terrains - northern plains, volcanic terrain, and the southern highlands. (Polar craters numbered too few to be analyzed with this method.) The difference was greatest in the northern plains where the amplitude was fully 67% greater than the global function. However, the exponent was significantly shallower, only 62% of that for the global relationship. This would indicate that smaller craters start out deeper in the northern plains but then do not increase in depth as rapidly. Similarly, the exponent on the simple crater function for the volcanic terrain and southern highlands was shallower while the amplitude was just slightly higher, indicating a similar trend as with complex craters in the northern plains.

3.5.2.4. Fresh Craters Method

Recent work to define the *d*/*D* relationship for Mars (*e.g.*, Garvin *et al.*, 2003; Stewart and Valiant, 2006) has generally relied upon identifying and measuring the depth and diameter values of morphologically fresh/pristine craters. The Garvin *et al*. (2003) results are described above and agree generally well with the deepest crater method. Stewart and Valiant (2006) limited their analysis to five regions on Mars and examined relatively few craters in each: Acidalia Planitia ($N = 29$), Utopia Planitia ($N = 53$), Isidis Planitia ($N = 24$), Lunae Planum ($N = 48$), and Solis Planum ($N = 33$). Utopia and Isidis were identified previously in this work, Boyce *et al*. (2006), and Stepinski *et al*. (2009) as having deeper craters than the average terrain, and they found deeper *d*/*D* when just looking in those regions ($d = 0.404D^{0.41}$ for Utopia and $d = 0.351D^{0.41}$ in Isidis). Acidalia is north of the Chryse impact basin and is around the region identified above as also having deeper than average craters, and they identified a relatively deep crater relationship there, as well, of $d = 0.384D^{0.38}$. Interestingly, the slopes in all of these relationships are shallower than identified by the work from this crater database, indicating that they found, by comparison, either smaller craters to be deeper or larger craters to be shallower.

Another possible explanation is that there may be relatively large uncertainties due to the comparatively small number of craters in their study.

The analysis in this section mimics this approach and only uses craters that are classified with a degradation state of "4" (fresh). This process is slightly incestuous because one of the four parameters in crater degradation state is the crater depth relative to the established d/D relationship. To minimize how recursive this process is, the deepest crater d/D was used to define that part of crater degradation state such that this fresh crater method could be relatively independent. Overall, 2704 craters $D \geq 5$ km were identified as "fresh" in this database. Of those, 934 were classified as simple (831 were equatorial of ±40° and 103 poleward), and 1060 were complex (976 were equatorial of ±40° and 84 were poleward).

As an overall global average, the slope of the fresh simple and complex craters was similar to the deepest crater method, varying at the few-percent level and likely within the noise. The amplitude of the fit is expectedly smaller than the deepest crater method, though the difference is roughly a factor of $2\times$ for simple craters but only ~15% for the complex craters. This is easily explained in that the fresh craters method is sampling an ensemble of terrains (the whole planet) and that the deepest crater method is simply picking the deepest ones which have been shown to be terrain-dependent. The relative lack of a difference at the larger, complex crater diameters can be interpreted as these craters are less dependent upon terrain type than smaller craters and therefore there are fewer deepest craters that then get averaged out.

Regressions were again run for the sub-regions, and the results are shown in Table **5**. Overall, the separation by latitude range is similar to the trend found for the deepest craters, though it should be emphasized that small numbers towards the poles ($N = 103$ for simple and $N = 84$ for complex) may limit the robustness of the fits. Analysis by terrain type could not be done for the polar terrain craters because the numbers were too small. Overall, the terrain separation did not yield significantly different results than the global analysis except in three values. First, the exponent in the simple crater fit for the northern plains was substantially steeper than both the global average and equatorial range. Second, the amplitude for the simple

craters in volcanic terrain was twice that of the global average and the latitude separations, indicating that simple craters start substantially steeper in volcanic terrain, but the exponent was smaller, indicating that as they increase in diameter, the depth does not grow correspondingly as large as for the global average.

3.5.2.5. Average Across Crater Depths and Degradation States

An additional method that may have dubious intrinsic physical meaning is that of taking an overall average of depths of craters for a given diameter. This was done in Stepinski *et al.* (2009) to define $d = 0.025D^{1.6}$ for simple craters D < 7 km, and $d = 0.22D^{0.47}$ for complex craters $D \geq 7$ km based on a combined total of 3666 craters. Earlier, Garvin *et al.* (2003) produced overall average results for simple craters $D \leq 6$ km of $d = 0.21D^{0.80}$ from 2263 craters. This is only slightly different from their results for the deepest craters, and it is significantly different from the Stepinski *et al*. (2009) function.

Fitting was done in the same manner as the previous sections, and results are reported in Table **5**. In this case, *all* craters were included in these numbers rather than the deepest or freshest. Globally, the complex crater function was similar in slope to the overall average, though it was slightly shallower, and the amplitude was 37%. This indicates that as a whole, Mars' crater population has been infilled/modified relatively evenly across diameter ranges, though there may be slightly more infilling at larger sizes. This is interpreted as larger craters are generally older and so would be more infilled on average than a broader age range at smaller diameters. The simple crater population is significantly different, for it has an amplitude of 26% the deepest craters but an exponent 27% greater. Borrowing from the above interpretation of exponent differences in complex craters, this indicates that more small simple craters are significantly infilled than larger ones. While this may be the case, it could also be an artifact of the MOLA data used in this analysis as discussed in the companion paper (Robbins and Hynek, 2011b) and the beginning of this section. Further work examining each crater with MOLA shot data and/or comparison with higher resolution DTMs are necessary to resolve whether the latter issue is a significant factor. Both of these are significantly different from Stepinski *et al*.'s

(2009) results.

Division of the craters along the ±40° latitude lines resulted in somewhat different results to those found in Section 3.5.2.3 with the deepest craters. In regions poleward of ±40°, the amplitude of the fits decreased by a factor of $\sim 3\times$, while the amplitude of the fits for craters equatorward of ±40° increased by a factor of $\sim 1.5\times$. Interestingly, the exponents underwent the opposite, where the equatorial craters' exponents dropped by ~20% while the polar simple craters rose by 14% and complex by 58%. This was the steepest complex crater relationship found in this work except for the polar terrain separation. Interpretation of these results for amplitude is straight-forward and discussed above, for polar craters are shallower because of a weaker crust likely due to a cryosphere. The exponents are a different matter, and most significant are the poleward results. The hypothesis discussed above that the anomalously large exponent for simple craters may be due to MOLA artifacts should be less significant near the poles because of higher point density due to the *Mars Global Surveyor* orbit; thus, these results should be *more* robust than their equatorial counterparts, but the slope is greater. If this is a real phenomenon, this would indicate the former interpretation for the global results is more likely, that smaller craters are more infilled than larger ones, which would seem to belie a normal sequence of events: larger craters preferentially form earlier on a surface while more smaller craters form later, and assuming an even rate of infilling/erosion, the d/D slope should remain fairly steady while the amplitude decreases. More work on this issue should be done to unravel this result.

The all-crater average when craters were separated by terrain yielded a few interesting results. First, the polar terrain craters could be analyzed with this method, and as expected they were significantly shallower than the global average. The simple craters' fit function had an amplitude of 6% the global and the complex was 13%. However, the power law exponents were significantly steeper by 43% and 107%, respectively. This can be explained by the proposal in Section 3.5.1: Smaller craters will feel the effects of the terrain much more than larger craters. Thus, the polar terrain will cause a significantly shallower crater, but as craters get larger the terrain dominance lessens and normal gravity scaling dominates more. Otherwise anomalous

were the craters on volcanic terrain with amplitudes a factor of 2× greater than the global average. However, this can be fairly easily explained by fresh craters dominating Martian volcanic terrain (64% are degradation states 3 or 4) and so more modified, shallow craters do not lower the average.

3.5.3. Synthesis of the depth/Diameter Relationship

Crater depth/Diameter relationships are an important tool to understanding how craters form and then how craters differ from what is expected. Investigation into this relationship was done in three main ways – deepest craters, fresh craters, and all craters – and investigated for the entire globe, different latitude bands, and specific terrain types. Overall, the results are reasonably consistent with most previous work in this area (*e.g.*, Garvin *et al.*, 2000, 2003; Stewart and Valiant, 2006; Boyce and Garbeil, 2007) though it varied from the automated analysis of Stepinski *et al*. (2009).

The work presented here was incremental in revising these relationships: Within the nineteen different method-region combinations for both simple and complex craters, the results were generally self-consistent. Significant variations were generally expected due to the particular analysis conducted. For example, the deepest craters method consistently yielded the deepest d/D relationship while the all-crater averages were always the shallowest. The exponent slopes were also generally consistent among each other, though a few outliers did exist as explored in the previous subsections. Overall, though, it is reassuring that the different methods yielded similar results with most differences easily explained. This is the first work to examine these relationships through multiple methods and compare them.

The application of this analysis to future research should probably be limited to using the deepest craters method results when separated by terrain type. If a crater is emplaced in a terrain that was not covered by the four major ones analyzed here, then researchers should use the latitude bands. Using the global average will result in underestimating original crater depth in some cases such as on volcanic terrain, or overestimating original depth in locations such as near

the poles.

3.6. The Simple/Complex Morphology Transition and Gravity Scaling

Simple craters are small and bowl-shaped while complex craters are large and have a variety of interior morphologies such as wall terraces, central peaks, and flat floors. Fundamentally, the transition diameter between simple and complex craters has been observed to be a function of the surface gravity of the target object (*e.g.*, Baldwin, 1949; Quaide *et al*., 1965; Malin and Dzurisin, 1977; Pike, 1977). However, it is also at least in part controlled by target material strength (*e.g.*, Pike, 1980; Pike, 1988). Determining the diameter at which an impact crater will transition from simple to complex morphology can inform studies of the target, its properties, and the role of gravitational collapse and elastic rebound. These are the main mechanisms during crater formation's modification phase that produce complex morphologies. While the diameter of this transition is necessarily a range because different morphologies will be begin to form at different diameters, the diameter of this transition was found to be roughly 6 km for Mars with no significant terrain dependence (Pike, 1988). This value has been argued about over the years with each new dataset of craters, and in that tradition this database was mined to determine if Pike's 1988 conclusion should be revised.

3.6.1. Based on Floor Shape

A crater is considered to be within the basic complex type when it displays a flat floor morphology that is not due to post-formation infilling. Additional features are often characteristic of complex craters, but these are addressed in subsequent sections. To the goal of discerning the average diameter transition from simple to basic complex morphology, all craters in the database (Robbins and Hynek, 2011b) were classified - if possible - into these basic types. Craters in the ~5-8 km-diameter range were not classified if it was not clear if they were either pristine complex flat-floored craters or infilled (modified) simple craters.

Three histograms were created to quantify this: all craters, all simple craters, and all complex craters. The simple and complex crater histograms were then divided by the overall database

histogram, and these are displayed in Fig. **29**; the sum of the two is also shown. The simple-complex transition diameter is where the fraction of complex craters is greater than simple craters, and it is 6.9 km (Fig. **29**). This diameter proved to be robust when separated into two latitude ranges – ±40°, and poleward of ±40° – the equatorial band having a transition location of 7.0 km and 6.9 km for the polar (well within any reasonable uncertainties). Examining craters at higher latitudes, however, yields interesting results: Poleward of ±60°, the transition occurs at 7.7 km, and at >±70°, it rises to 8.0 km (this is fairly robust as there are still >1000 craters in the database around the diameters of interest). Separating these by northern and southern hemispheres yields a transition at 8.1 km for <-70°N, and those >+70°N have a transition ~8.4 km. A similar effect was found when separating by terrain type as in Section 3.5.2: Polar terrain craters had a transition of ~7.9 km while the other three (northern plains, southern highlands, and volcanic) were ~7.0 km. This is similar to findings by Garvin *et al*. (2000).

The dependence upon latitude and terrain has not been quantified before. As discussed, the transition is a consequence of collapse under gravity due to surpassing the strength of the tar-

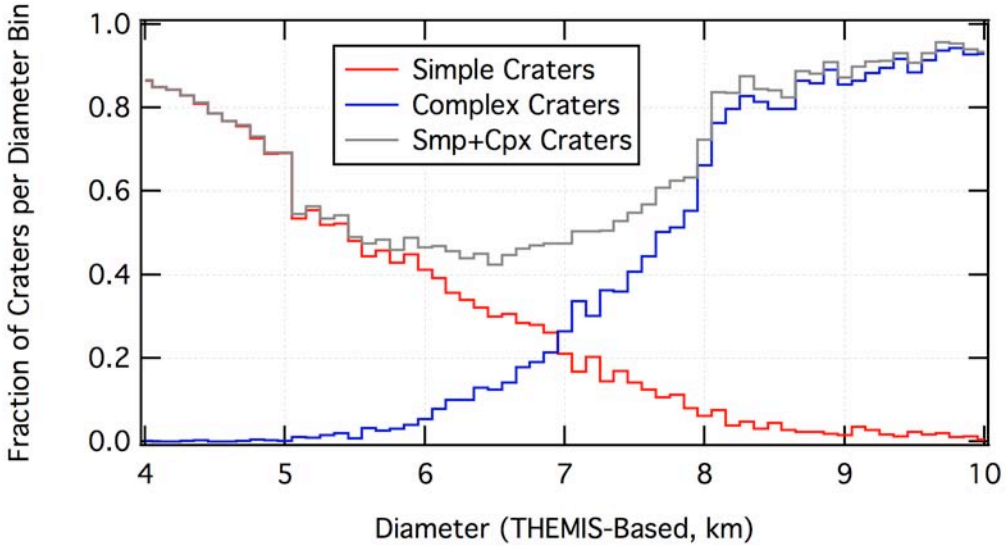

Figure 29: Three histograms were created as a function of diameter: All craters, simple craters, and complex craters. The simple and complex crater histograms were divided by the histogram for all craters and are plotted here, their sum shown in grey. The deficit relative to 100% of all craters being classified between ~5-8 km is due to the conservative classification to avoid classifying infilled simple craters as flat-floored pristine complex craters and vice-versa.

get. This runs contrary to what one would expect for the Martian crust for, as graphically illustrated in Section 3.5, the higher latitudes of the planet are likely dominated by a near-surface cryosphere (Boynton *et al*., 2002) and the cryosphere at northern latitudes is probably closer to the surface (Section 3.5.2.2). From this, one would expect an impact into an ice-solidified crust would vaporize volatiles and weaken the crust, permitting gravitational collapse to a complex crater at smaller diameters rather than strengthening it for transitions at larger diameters. A possible explanation is that water in the surface causes it to act more fluid during the modification phase of crater formation. The result will be material gently sloping down the crater walls, shallowing the bowl, but maintaining the bowl shape and thus resulting in a simple crater classification.

3.6.2. Based on Other Complex Crater Morphologies

Expanding on the morphologic method to examine transition diameter is by looking at what diameter range other complex crater morphologies begin to form. Although Pike (1980, 1988) examined several morphologies (flat floor (addressed above), central peak, scalloped rim, terraced wall, ballistic ejecta, flow ejecta), in this analysis the morphologies are limited two to additional ones – central peaks and terraced walls. Central peaks form by rebound of the crust during crater formation. Terraces are a collapse feature from the walls during crater formation. While these are fundamentally different processes, and they will manifest at different crater sizes, they are each a good morphologic indicator of failure of the crust to support a simple bowl and hence display a complex crater. Craters were binned similarly as in the basic morphology, discussed above. An average was taken at the diameter where the fraction of the craters that contained the feature was stable. Then, the diameter at which 50% of the average was reached was considered the transition diameter.

Central peaks were present in an average of 6.3% for crater diameters $D \geq 15$ km. 50% of this - where 3.2% of the craters had central peaks - was reached at $D = 5.6$ km. The smallest crater with a central peak was ~2 km, but it did not reach the 5% steady-state level until $D \geq 3.3$

km. Performing the same analysis on equatorial craters shows a smaller diameter transition D = 4.8 km, while the >±40° latitude range yielded a larger diameter of 11.3 km. Similar results were found on volcanic and southern highlands terrain while there were not enough craters for an analysis on polar. The northern plains, however, were significantly different with a transition to central peaks at D = 8.4 km.

Terrace morphology did not reach a steady state until $D \approx 15$ km, and this was at a level of 21%. 50% of this was reached at D = 8.3 km. The smallest crater with wall terraces was ~3 km, but it did not reach 5% of steady-state until $D \geq 4.5$ km. Performing the same analysis on equatorial craters shows a slightly smaller diameter transition of D = 7.5 km, while the >±40° latitude range yielded a significantly larger transition diameter of 16.9 km. Terrain-dependent results were similar to the global average except for polar where again small numbers made this analysis difficult; the smallest diameter crater with visible terraces on polar terrain was 10 km.

These values are in rough agreement with Pike (1980) who found transition diameter from central peaks and terraces to be in the 6-8 km-diameter range with the prevalence of wall terraces at larger diameters than central peaks (he found a difference of a factor of $2\times$, though this work and methodology shows it to be $1.5\times$). The latitude range-dependent trend observed here supports the idea from flat floor morphology that it is more likely this is a real feature of the craters rather than an error in classification.

Issues with erosion of these more complex features are likely significant, for one would expect the vast majority of larger complex craters form with terraced walls and likely central peak features from basic cratering physics (Melosh, 1989). For example, when only examining fresh craters, terraces were identified in >90% of craters $D \geq 20$ km, and central peaks were present in 55% of $8 < D < 13$ km craters and >90% of $D > 14$ km craters. However, erosion should affect these features relatively evenly across the crater diameters, so this should not significantly affect results (Craddock *et al*., 1997).

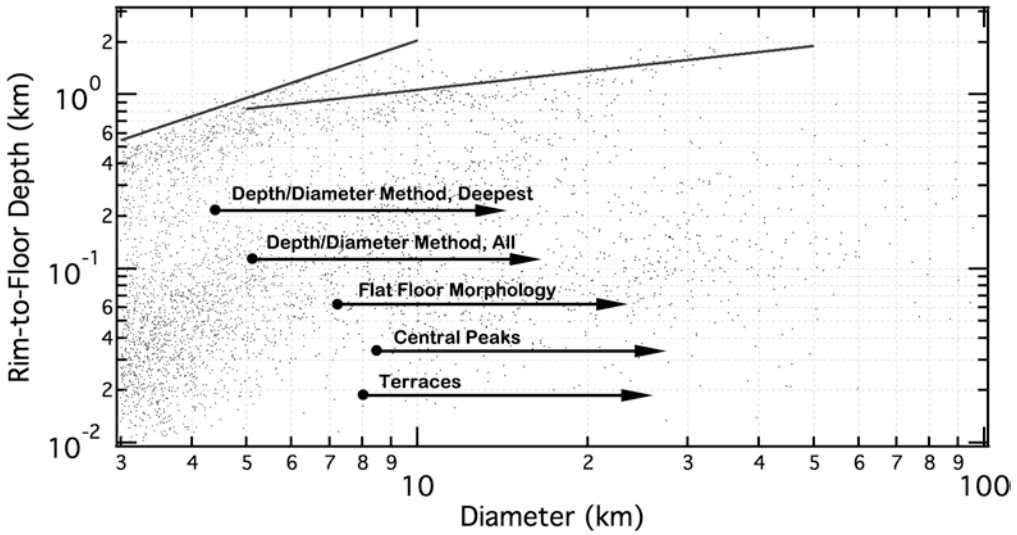

Figure 30: Simplified diagram illustrating the diameter at which the simple-complex transitions are observed for the northern plains. Dots are craters, and the two crossing lines are the best-fits for simple and complex deep craters. Arrows indicate the transition diameter from simple to complex for each of the labeled characteristics examined. Vertical offset is arbitrary.

3.6.3. Based on depth/Diameter

A more common method of determining transition diameter is on a crater depth versus diameter plot (*e.g.*, Fig. **30**). On these, simple craters will have a relatively steep slope compared with complex craters, and there will be a "knee" where they intersect. Some overlap is present due to target, impactor, and other variances, but in general this occurs over a narrow diameter range. Indeed, when fitting the slopes to a power law function (Section 3.5.2), there is an exact diameter at which the slopes intersect. This diameter is what is used and reported in this section.

Globally, for the deepest craters method, the transition diameter is 3.0 km. The fresh crater method puts the transition at 5.9 km, while the all-crater average is 3.1 km. Transitioning to the equatorial latitude band, the diameter goes down slightly for all cases - following the pattern in the previous two sections - to 2.8 km, 4.4 km, and 2.9 km. The higher latitudes saw mixed results with a spurious 9.2 km result for the deepest craters method due likely to small numbers, 5.3 km for the fresh method, and 4.2 km for the global average. Overall, these are nearly all smaller than the simple-to-complex transition diameter than when based upon morphology alone. This phenomenon was observed in previous work by Pike (1988) not only on

Mars, but also on Earth, Mercury, and the Moon. A figure similar to his Fig. 11 is shown as Fig. **30**, illustrating this point as well as showing the general diversity of the onset of these morphologic and morphometric characteristics.

3.6.4. Synthesis of the Simple/Complex Morphology Transition

Overall, this is the first work to utilize a modern global crater database to re-examine the simple-complex morphology transition on Mars. It does so with respect to multiple morphologic and morphometric indicators and a latitude and terrain dependence. The results of this analysis of independent morphologic and morphometric transitions are summarized in Fig. **31** and Table **6**. Only the transition diameters for the deepest craters *d*/*D* relationship are used to calculate the arithmetic and geometric means (except for polar terrain). These means are very close to each other, and the standard arithmetic would normally be used but Pike (1988) used geometric so that is included as a comparison. The means for the global distribution are 6.0 km average and 5.6 km geometric; the standard deviation is ±2.3 km. Pike (1988) calculated ~6 km for the transition. The other results are in Table **6**.

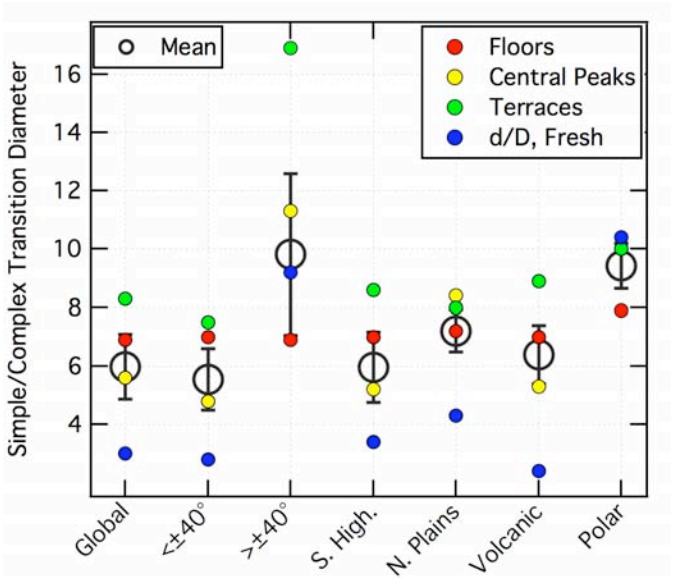

Figure 31: Combined results from using different morphologic and morphometric indicators to determine the transition between simple and complex crater morphology on Mars. Solid circles are points showing each result discussed in the text, the key to which shown by the legend to the upper right. Black open circles are the arithmetic means for all morphologic data and results from the deep crater *d*/*D* method (since that is considered the most robust technique (see Sections 3.5.2 and 3.5.3)). Error bars are the standard deviation from the means of the three or four values divided by $\sqrt{N}$.

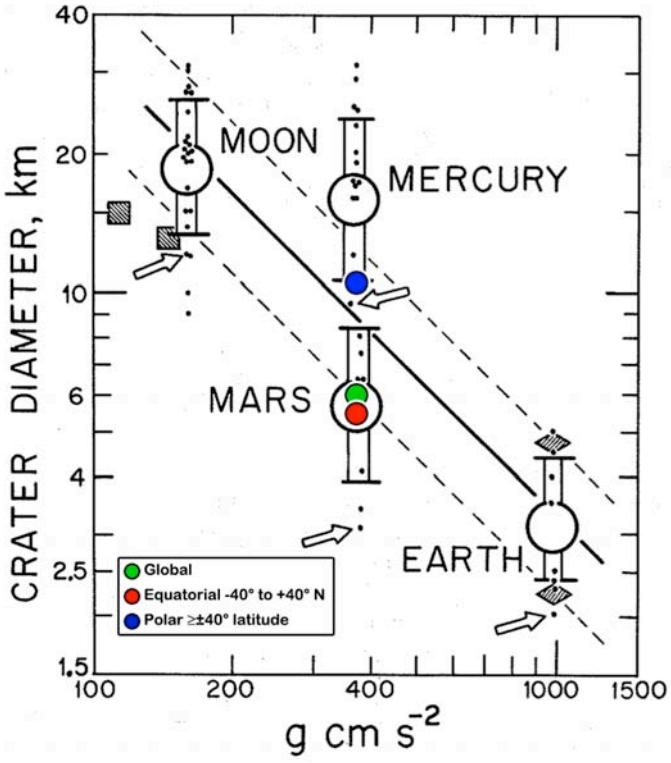

Figure 32: Background Figure is from Pike (1988, reproduced without permission), illustrating surface gravity versus onset of complex crater morphology for the large inner solar system bodies (except Venus) and Ganymede and Callisto (squares). Each small black dot is from Pike (1988) and represents a different morphologic indicator (*e.g.*, the previous subsections); he analyzed 230 Martian craters. Arrows point to *d*/*D* results. Large circles are geometric means and bars are standard deviations. The solid black line is a best-fit, while the diamonds are for different targets on Earth and the dashed lines extrapolations of the fit for those targets (lower is for sedimentary rock, upper is crystalline). Overplotted in color are the results from this work (arithmetic means).

Table 6: Summary of transitional diameters for different Martian terrains and derived through various means discussed in the text (all units are km).

	Global	<±40°	>±40°	S. High	N. Plains	Volcanic	Polar
Floors	6.9	7.0	6.9	7.0	7.2	7.0	7.9
C. Peak	5.6	4.8	11.3	5.2	8.4	5.3	–
Terr.	8.3	7.5	16.9	8.6	8.0	8.9	10.0
d/*D*, Deep	3.0	2.8	9.2	3.4	4.3	2.4	10.4[1]
A. Mean	6.0	5.5	11.1	6.1	7.0	5.9	9.4
G. Mean	5.6	5.2	10.5	5.7	6.8	5.3	9.4
Std. Dev.	2.3	2.2	4.3	2.2	1.9	2.8	1.3

[1]There were not enough craters to derive a reliable function for the "deepest" crater method for polar terrain craters. The "all-craters" method value is quoted in its stead, and it was used to compute the averages and standard deviation.

This work supports Pike's 1988 analysis from *Viking* imagery that indicated different transition diameters for different simple/complex morphologies, as is indicated by the overlap shown in Fig. **32**. It is, however, significantly more robust, utilizing thousands of craters across the globe instead of 230 craters. It used a variety of modification states as well as and only fresh craters as a check. The global results fit very well within Pike's synthesis and lie directly upon the lower dashed line of Fig. **32** that indicates similarity with sedimentary rock on Earth.

Of particular interest, though, is the latitude and terrain dependence shown. This result was robust in the previous sections: The equatorial range of <±40° latitude showed slightly smaller transitions while the polar range was significantly larger for nearly all morphologic and morphometric indicators (though the ranges do slightly overlap, as shown in Fig. **31**). The observational implication is that crust in the equatorial band of Mars is less competent and craters will undergo gravitational collapse during the modification phase of formation more readily. By the same token, the northern plains consistently had significantly larger transition diameters and the means are correspondingly greater. Meanwhile, the crust closer to the poles is more competent and less prone to this form of collapse. Interestingly, this runs contrary to the basic interpretation of crater depth/Diameter data discussed in Section 3.5. That indicated the crust was weaker near the poles because even morphologically fresh craters were a factor of $\sim 2-3\times$ shallower than their equatorial counterparts. These disparate relationships are addressed in Section 3.7.

3.7. Discussion and Conclusions

We have explored the basic crater distributions, morphologic distributions, morphologic relationships, and morphometric relationships from a new global crater database of Mars. This database was shown to be statistically robust (companion paper, this volume), and we examined many previously known trends to illustrate its agreement with previous work. We also expanded the analysis to illustrate the utility in discerning new trends and relationships as well as to refine some that have been studied for decades.

In basic crater distribution across the planet, we illustrated this database is coincident with previous research in global distributions and age-related trends. Expanding this to smaller diameters illustrates significant new work and forms the bulk of the number of craters in this database. The small crater population shows finer age variations across the surface in contrast with the 5-50-km-diameter population, and it also starts to inform studies of secondary crater populations (Robbins and Hynek, 2011a; Robbins and Hynek, 2011d). A new analysis comparing the fresh crater population with global circulation models of the planet agree well, and future work may yield tighter constraints or inform other processes that may protect craters from aeolian erosion.

Our work examining crater interior morphologies (central peaks, summit pits, and central pits) provides validation of our database, updates older results (*e.g.*, Barlow and Bradley, 1990), and extends other modern ongoing work to the southern hemisphere (Barlow, 2010, 2011). Central peak distribution generally correlates with fresh craters, but there is disagreement at central longitudes in the southern hemisphere. Further efforts in understanding this should be fruitful, as will further exploration into the distribution of Martian central pits and summit pits. The terrain in which these latter features are found supports a model that incorporates volatiles in their formation, though the specific model is open to interpretation from our cursory analysis (*e.g.*, Wood *et al*., 1978; Croft, 1981; Senft and Stewart, 2008; Alzate and Barlow, 2011). Morphometric analysis may support this and is underway by other researchers (Barlow, 2010, 2011; Alzate and Barlow, 2011). We examined the intracrater dune distribution, comparing it to the Mars Global Digital Dust Database (MGD^3) (Hayward *et al*., 2007; Hayward *et al*., 2008; Fenton and Hayward, 2010). In general, good agreement was found between our catalog and theirs, with small differences the subject of future collaboration. The largest difference was the inclusion of $\sim 4\times$ more dunes at latitudes 30-65°N in this catalog.

The distribution of radial ejecta was found to reproduce terrain ages reasonably well despite the craters forming after the terrain, illustrating that radial ejecta can be preserved over long periods of geologic time on Mars. Layered ejecta blanket data is abundant within the

database, comprising nearly 50% of the data columns with ejecta morphology and detailed morphometry. Extensive mining of this data for purposes of better explaining these features and their formation is the subject of future work in prep., but in this paper we showed its general agreement with previous work in the area (*e.g.*, Mouginis-Mark, 1979; Schultz and Gault, 1979; Barlow and Bradley, 1990; Barlow and Perez, 2003; Barlow, 2005) and demonstrated its utility in refining previous distributions and trends.

Our database provides detailed topographic information about craters, and this has resulted in updating some of the basic scaling laws as applied to Mars. Overall, we found that Martian craters display rim morphometries that are $\sim 2\times$ smaller than their lunar counterparts reported in Melosh (1989). This is the case for rim height and surface-to-floor depth each relative to crater diameter, and these hold for both simple and complex crater morphologies.

In further application to fundamental scaling, we examined crater depth-to-diameter ratios (d/D) as an incremental update to previously identified trends and values, though this was the first analysis to compare three different methods from the same dataset for deriving the d/D relationships on Mars. We illustrated the known global dichotomy of deeper craters in equatorial regions and shallower craters towards the poles, and we expanded upon this to show a previously unobserved secondary effect of a North/South dichotomy. This shows a wider variation of crater depths towards the equator in the north compared with the south, but the opposite was the case at polar latitudes. The high northern latitude craters showed a very tight and shallow distribution of depths compared with the south, likely indicating a nearer surface cryosphere and more uniform terrain. We reexamined the basic crater d/D relationship, as well, for both the global average and subregions. Within each, we characterized d/D for simple and complex craters in terms of the deepest craters, fresh craters, and all craters. Our results for the global average compare well with previous work, and our results within the terrain dependence reflect the dichotomy observed before. These differences are important, and they must be taken into account when using crater depth to estimate erosion, infilling, and other modification processes. Otherwise, one will interpret all high-latitude craters as degraded relative to equatorial ones.

These *d*/*D* results were then placed into the context of one of the other basic crater scaling laws of at what diameter does a crater transition from simple to complex morphology in a method similar to what has been done in the past (*e.g.*, Pike, 1977, 1980, 1988). Three morphologic indicators were examined - basic morphology (bowl vs. flat floor), central peaks, and wall terraces - and the intersection of the *d*/*D* fits were our morphometric criterion. We again segregated by terrain as well as examined the global relationship. Our results agree very well with Pike (1988) for the global population, and this lends credibility to the incredible difference observed between latitude bands: We found the simple-complex transition occurs at ~11 km at high polar latitudes rather than the ~6 km global average (Fig. **31**).

Taken with the *d*/*D* information, we propose a model where the higher latitude craters will begin to form as they do elsewhere through the contact and excavation stage. During excavation, the impact energies will melt and vaporize ices in the surrounding crust. This will weaken the crust where vaporized, and intense ground movements cause the wet crust to flow like mud. During the modification phase, the crust is not strong enough to support the deep cavity characteristic of equatorial simple craters, but the viscous fluid-rich material will relax, decreasing the crater depth but maintaining a bowl shape. A central peak, generally the first complex morphologic indicator, does not form until $D \sim 11$ km in the poleward of ±40° subset and there were only two found in the polar terrain subset. So either the central peak does not form in this suggested "mud crust" until significantly larger diameters are reached, or it does form but quickly collapses and does not leave behind an indicator it existed.

The effect is simple craters are maintained at larger diameters, but they are shallower than equatorial ones. This is more significant in high northern latitudes where there is likely a nearer surface and/or thicker cryosphere to better facilitate this. This is supported by the cohesive layered ejecta morphology distribution found in the northern hemisphere where their presence is also more prevalent than in the southern. The concentration of DLE craters in high northern latitudes supports this, for it is likely that at least this type requires a volatile in the subsurface to form based on the type's abundance over SLE on Ganymede (Boyce *et al*., 2010).

Overall, this new crater catalog with 378,540 craters $D \geq 1$ km is comparable to previous ones where they overlap, and the additional morphologies and morphometries have proven to be an unparalleled asset in studying the surface of Mars. Through this work, we have proven its utility and hope others can make use of it. Pending review, we will be making this database freely available for download via the Mars Crater Consortium section of USGS's PIGWAD server (http://webgis.wr.usgs.gov/pigwad/down/mars_crater_consortium.htm). We are also making a web-query site that allows users to download craters and features based on user-selectable fields and options that will be available at http://mars.sjrdesign.net.

4. Secondary Craters from Near and Far

The issue of secondary craters on planetary bodies has been fraught with disagreement, conflicting studies, and general confusion in the planetary community for the past 50 years. Many researchers have studied secondary craters, some statistically, some through modeling, and others through case studies. I have begun to use this Mars crater database to help answer some of the questions about the relative importance of secondary craters, their distribution locally in terms of location and size-frequency, and to make the new discovery of very distant secondary clusters from a single large impact. This adds to the growing body of recent work on secondary craters, illustrating that secondary craters are indeed an important contribution to crater populations and must be appropriately accounted for in deriving planetary surface ages and relative stratigraphy.

This section is divided into two main parts, and both are derived from the global crater database. The first addresses the discovery of distant secondary craters found up to 25% of the way across the planet from their primary crater, Lyot. Next is a detailed exploration and quantification of the nearby secondary fields surrounding 24 relatively large primary craters in the first-of-its-kind study.

4.1. Distant Secondary Craters from Lyot Crater, Mars, and Implications for Ages of Planetary Bodies

Note: This paper is in print as: Robbins, S.J.; and B.M. Hynek. (2011) "Distant Secondary Craters from Lyot Crater, Mars, and Implications for Ages of Planetary Bodies." Geophysical Research Letters, 38, L05201. doi: 10.1029/2010GL046450. It is cited in this dissertation as "Robbins and Hynek, 2011a." Sections have been re-numbered and some reformatting has been done to fit the formatting of the rest of this dissertation. References have been combined with all others at the end of this dissertation; in-line references have retained their GRL-style formatting. Acknowledgments have been combined with others at the beginning of this dissertation. Color versions of the figures are used instead of the black-and-white versions in the published journal article. Minor changes to the journal text have been made.

Abstract: The population of secondary craters - craters formed by the ejecta from an initial impact event - is important to understand when deriving the age of a solid body's surface. Only one crater on Mars, Zunil, has been studied in-depth to examine the distribution, sizes, and number of these features. Here, we present results from a much larger and older Martian crater, Lyot, and we find secondary crater clusters at least 5200 km from the primary impact. Individual craters with diameters >800 m number on the order of 10^4. Unlike the previous results from Zunil, these craters are not contained in obvious rays, but they are linked back to Lyot due to the clusters' alignment along great circles that converge to a common origin. These widespread and abundant craters from a single impact limit the accuracy of crater age-dating on the Martian surface and beyond.

4.1.1. Introduction

Crater counting is the only way to estimate absolute ages on solid surfaces without returned samples, akin to the Apollo missions. This practice has been refined and utilized for decades (*e.g.*, *Arvidson et al.* [1979]; *Hartmann* [2005]). A fundamental assumption of crater age-dating is that crater formation is a stochastic process. Nearly half a century ago, *Shoemaker* [1965] identified the issue of secondary craters (craters that form from the ejecta of a larger primary impact event and are necessarily smaller). The subject of secondary craters was controversial but generally ignored in the literature until *Bierhaus et al.* [2005] identified $>10^4$ secondary craters that contaminate crater statistics on Jupiter's moon Europa, and *McEwen et al.* [2005] identified $>10^6$ around the fresh crater Zunil on Mars.

Understanding the role secondary craters have on local and global crater statistics is important, especially because the crater population with diameters $D < 1$ km on Mars may be significantly contaminated by secondary craters [*McEwen and Bierhaus*, 2006]. Secondary

fields are typically manifest as a visible and tight annulus around the primary, though recent work has shown that secondary fields can be several thousand kilometers from the primary [*Preblich et al.*, 2007]. With current and forthcoming high-resolution imagery of Mars, the Moon, and Mercury, case studies of fields of secondaries from large primary craters are necessary to assess their effects on the overall crater population.

Here, we discuss the identification of thousands of secondary craters originating from one of the largest fresh craters on Mars: Lyot crater is a 222-km-diameter peak-ring crater centered at 50.5°N, 29.3°E (Fig. **33**), with a Middle Amazonian age of ~1.6-3.3 Ga [*Tanaka et al.*, 2005; *Dickson et al.*, 2009]. The secondaries are up to 25% of the way across the planet, and there could be countless more not clearly linked to Lyot due to degradation, resurfacing, resolution limitations, or lack of easily identifiable tight clusters. Besides the basic identification of Lyot secondaries in the near- and far-field (Section 4.1.2), we detail their size-frequency distribution relative to primary craters (Section 4.1.3), and discuss implications (Section 4.1.4).

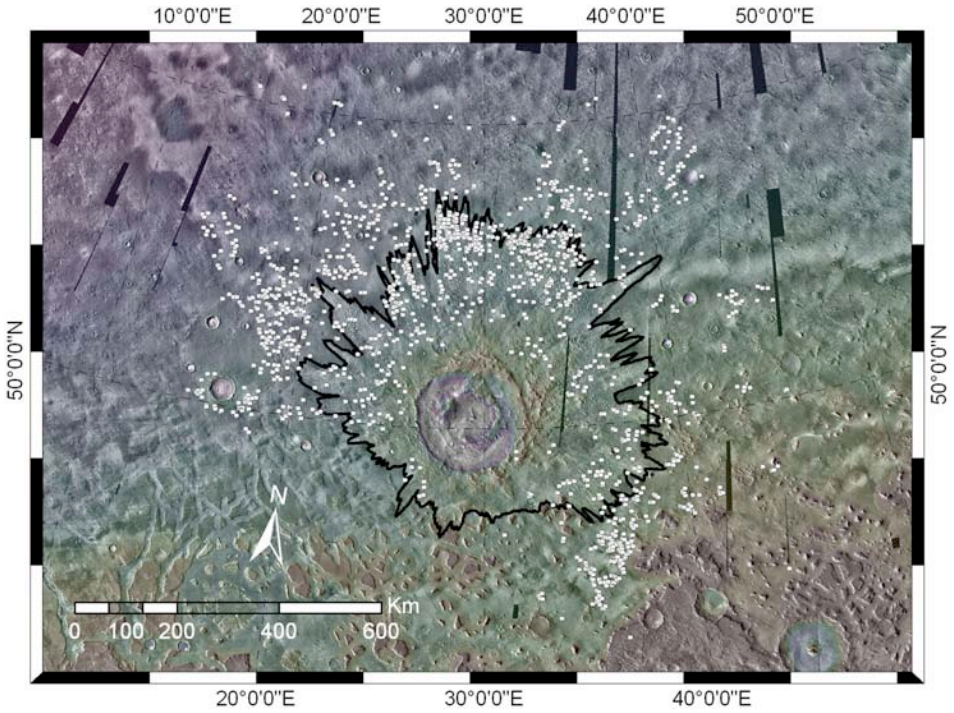

Figure 33: THEMIS Daytime IR mosaic [*Christensen et al.*, 2004] showing the region around Lyot crater in a local sinusoidal projection. The continuous ejecta blanket of Lyot is outlined in black and the identified near-field secondaries are shown as white circles. Black regions correspond to gaps in the THEMIS data.

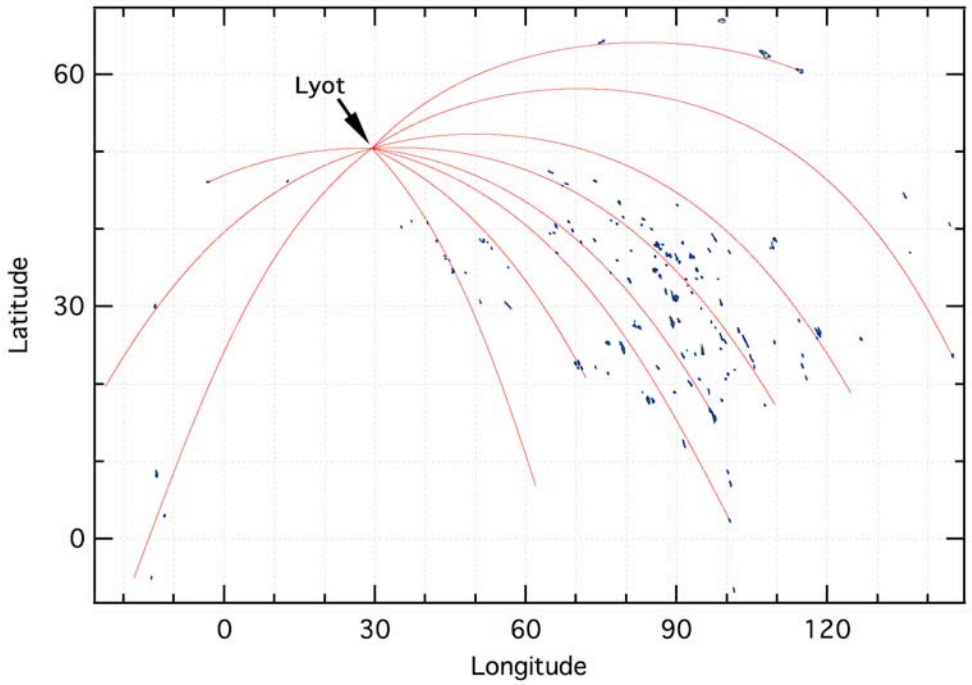

Figure 34: Distribution of identified secondary crater clusters from Lyot. Arcs are representative examples of great circles between Lyot and distal secondary craters. Dark outlines show each cluster.

4.1.2. Identification of Craters and Secondary Clusters

Over 450,000 craters ≳1-km-diameter have been identified on Mars in a nearly completed global Mars crater database [*Robbins and Hynek*, 2010]. Craters were visually identified in ArcGIS software using 100 m/pix global THEMIS Daytime IR mosaics [*Christensen et al.*, 2004], and rims were mapped using ArcGIS's edit tools. Polygons representing crater rims were imported into Igor Pro where a non-linear least-squares (NLLS) circle-fit algorithm was used to calculate each crater's diameter and center latitude and longitude. The NLLS algorithm corrects for map projection by converting the polygon's geographic coordinates into meters from the polygon's centroid, accounting for the first-order spherical surface of Mars.

The global database's small crater distribution contains numerous clusters that appear to trend radially from Lyot crater at distances up to ~5200 km. Over 90% are in the quadrant southeast of Lyot (Fig. **34**). Determining if these clusters likely originated from Lyot was not aided by observable rays nor a nearly crater-free landscape as is the case with Zunil [*McEwen et*

al., 2005]. Great circles were traced between the potential clusters and Lyot to determine if the cluster was aligned with it (*i.e.*, a circle described by the intersection of the surface of a sphere with a plane passing through the center). Coriolis effects were ignored because they were of order ~few degrees in this work (Skinner and Nava, 2011).

The formula prescribed by *Vincenty* [1975] was used to construct great circle arcs via an iterative approach: An initial bearing along the great circle connecting the starting position (the cluster) and ending position (Lyot) was calculated. Then, the point 1 km from the starting point along the bearing was calculated (~1/60° at the equator; resolution tests at 10 km and 100 m showed differences <0.0005°, or <30 m). At this point, a new bearing was calculated and the process was repeated until Lyot was reached.

Potential Lyot secondary clusters were initially identified by visual inspection from the database, but a more robust clustering algorithm was run to isolate potential groups: Every crater $D \leq 5$ km was analyzed for its distance to all other craters within 2°. If the fifth-nearest crater was within 10 crater diameters, it was considered to be in a potential cluster; otherwise it was removed. The fifth-nearest was chosen to eliminate random over-densities; in the clusters observed initially, several dozen craters are often closely packed with rims touching. Candidate clusters were visually inspected in THEMIS mosaics to validate the cluster and determine, based upon morphology, if the cluster was composed of secondaries. Great circle arcs were drawn between the secondary clusters and Lyot to test orientation (*e.g.*, Fig. **34**). This only identifies *clusters* of craters and frequently fields of smaller craters were observed that were also likely from Lyot but not included in this study. In this case, "fields" define regions of craters that show an over-density from the background that are probably secondaries, and "clusters" are craters that are packed closely with rims often touching.

The search identified 143 distinct clusters of 10-300 craters each, where craters have diameters $D >$ ~800 m. A total of 5341 craters from the global database were extracted as members of these distant secondaries, similar in magnitude to the number identified on Europa [*Bierhaus et al.*, 2005]. The closest cluster is ~700 km away (~6 crater radii) and the farthest is

~5200 km (~46 crater radii). Close secondaries occur in an annulus around Lyot with generally distinct morphologies [*Shoemaker*, 1962, 1965; *Oberbeck and Morrison*, 1974] (Fig. **33**), while "distant" or "far" clusters are not as clearly linked to Lyot. These two populations are examined separately in Section 3.

4.1.3. Size-Frequency Distribution of Secondary Clusters

Crater size-frequency distributions (SFDs) were calculated following *Arvidson et al.* [1979] with some modifications: Craters were binned in multiplicative $2^{1/8}D$ intervals for purposes of slope-fitting. Finer binning than the more standard $2^{1/2}D$ was used to bring out detail in the SFDs that would otherwise be obscured. Craters were binned such that $D_{\text{bin}-1} < D_{\text{crater}} \leq D_{\text{bin}}$, putting all craters in a diameter bin that is the largest crater size in that bin. Since the distribution of craters is not even across all diameter bins, nor does it have a single typical power-law distribution with a slope of -2, the local slope between each bin and the next-smallest was used in order to shift the diameter to a more robust weighted mean:

$$D_a = \frac{D_a - D_{a-1}}{1 + N(D_{a-1})/N(D_a)} + D_{a-1}$$

where $N(D_a)$ is the number of craters at diameter bin D_a. This has a side-effect of having bins that are unevenly spaced in log(*D*)

Three additional features in our SFD algorithm were run on the incremental SFDs. The first removes the largest bins with too few craters – this cut-off was set at <3 craters in a cumulative bin to eliminate some issues with small-number statistics. The second removes incremental bins (and hence cumulative bins) that had no craters within them. The final feature removes bins below the estimated statistical completeness; we defined this as the incremental bin with the greatest number of craters. Error bars were calculated by $\pm\sqrt{N}$ Poisson statistics [*Arvidson et al.*, 1979]. Once these operations were performed, the incremental SFDs were integrated (discretely summed) to yield a cumulative SFD (Figs. **35** and **36**). Comparative R-plots (Figs. **35** and **36**) were calculated with similar adjustments. All slopes quoted in this paper are fits to the incremental SFDs with -1 added to yield a statistically accurate slope on a

cumulative SFD [*Chapman and Haefner*, 1967].

4.1.3.1. Close Secondary Craters

Secondary craters are easier to identify close to their primary crater because they are usually entrained in its ejecta and show an over-density as an annulus around the primary. Lyot

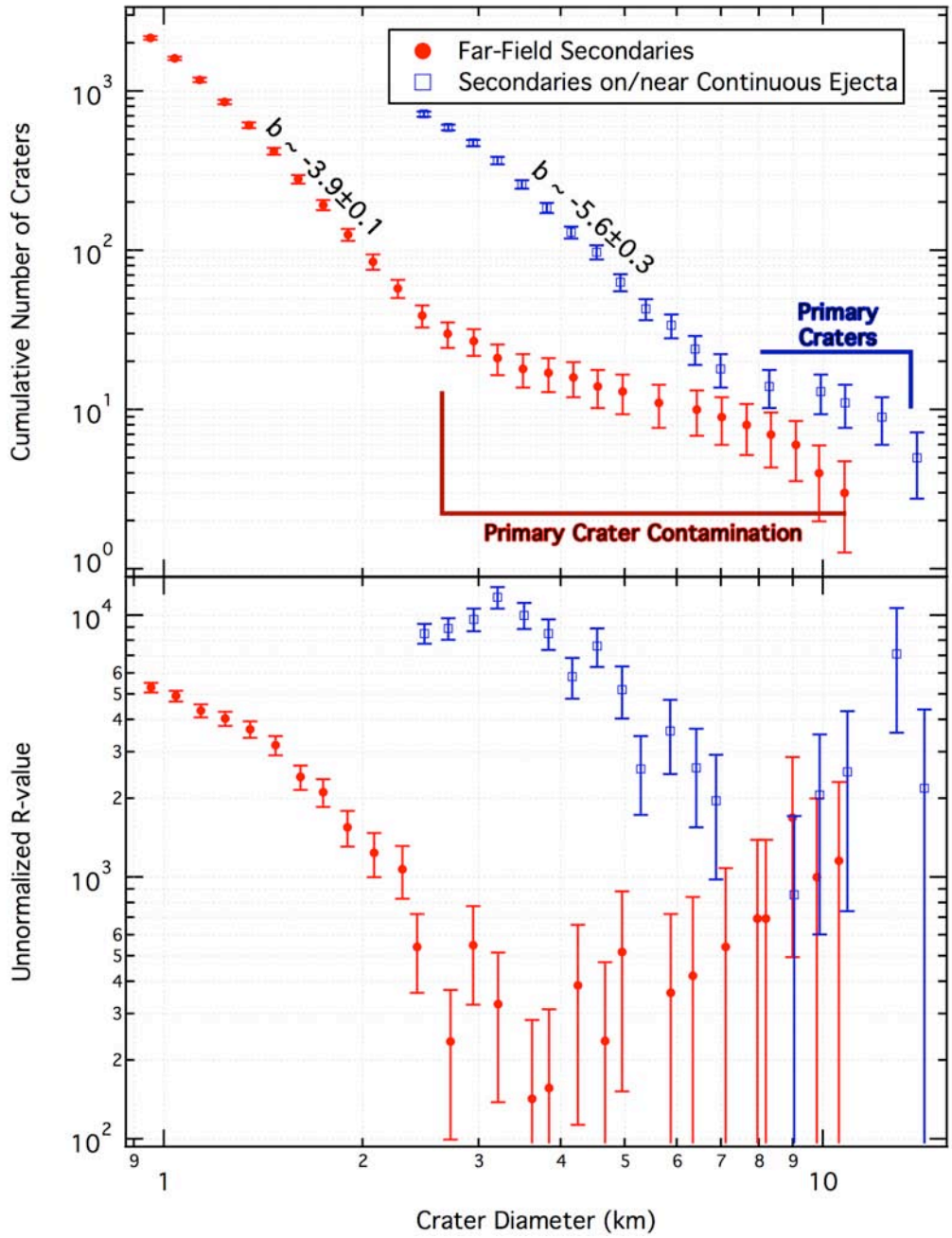

Figure 35: Lyot's nearby secondary crater size-frequency distribution (SFD) and the overall SFD of far-field secondaries. The slope for the nearby secondaries is significantly different from the typical SFD slope of -2 [*McEwen and Bierhaus*, 2006].

is a good example and has a large secondary field nearby (Fig. **33**). Most secondary craters identified are found in long troughs emanating radially from Lyot in its continuous ejecta (Fig. **33**). The largest crater with secondary-type morphology is a D = 28 km crater just outside the northwest rim, though this is abnormally large at 13% the primary's diameter. The largest alternative is an 11-km crater to the northwest which fits the canonical 5% of primary size relation [*Melosh*, 1989]. 1719 of these nearby secondary craters were extracted and their SFD is displayed in Fig. **35**. The diameter range $3.2 < D < 7.0$ km has a power-law slope of -5.6±0.3. This is significantly steeper than a normal crater population with slopes between -2 and -3, but it is typical for secondary crater populations [*McEwen and Bierhaus*, 2006].

4.1.3.2. Distant Secondary Clusters

All 5341 craters in Lyot's far-field clusters were combined into one SFD (Fig. **35**); based on SFD slopes, $D > 2.5$ km craters are likely mostly primaries, but the overall contamination by primaries is minimal since $D > 2.5$ km craters comprise 0.3% of the total. The power-law slope is -3.9±0.1 for $1.0 < D < 2.5$ km. To determine if this was representative, SFDs of all 26 individual clusters with $N \geq 50$ craters were created and slopes were fit over approximately the same diameter range; the power-law exponent ranged between -3.4 and -11 with μ=-5.2 (σ=1.6) and median -4.7. The five largest clusters ($N > 120$) averaged -5.1 with a range of -3.9 to -6.9. Given the somewhat small numbers involved, we consider these to be consistent with secondary populations but emphasize there is a spread in slope.

4.1.3.3. CTX-Based Case Studies of Distant Secondary Crater Clusters

Complementary to the THEMIS-based identification, six clusters were re-analyzed with CTX imagery (ConTeXt Camera from Mars Reconnaissance Orbiter [*Malin et al.*, 2007]). The clusters were selected at random from those with complete CTX coverage. Ranging 5.5-7.5 m/pix scale, crater cluster members down to $D \approx 25$ m were identified. The extended SFDs for two clusters are shown in Fig. **36**, illustrating that higher resolution data yields the same quantitative results as THEMIS for the larger $D >$ ~800 m. However, the SFD slope abruptly changes at $D \approx 500$ m, and the power-law slope ranges between -1.4 and -2.0. This

pattern was noted in all test cases and likely extends to the other clusters, the significance of which is discussed below.

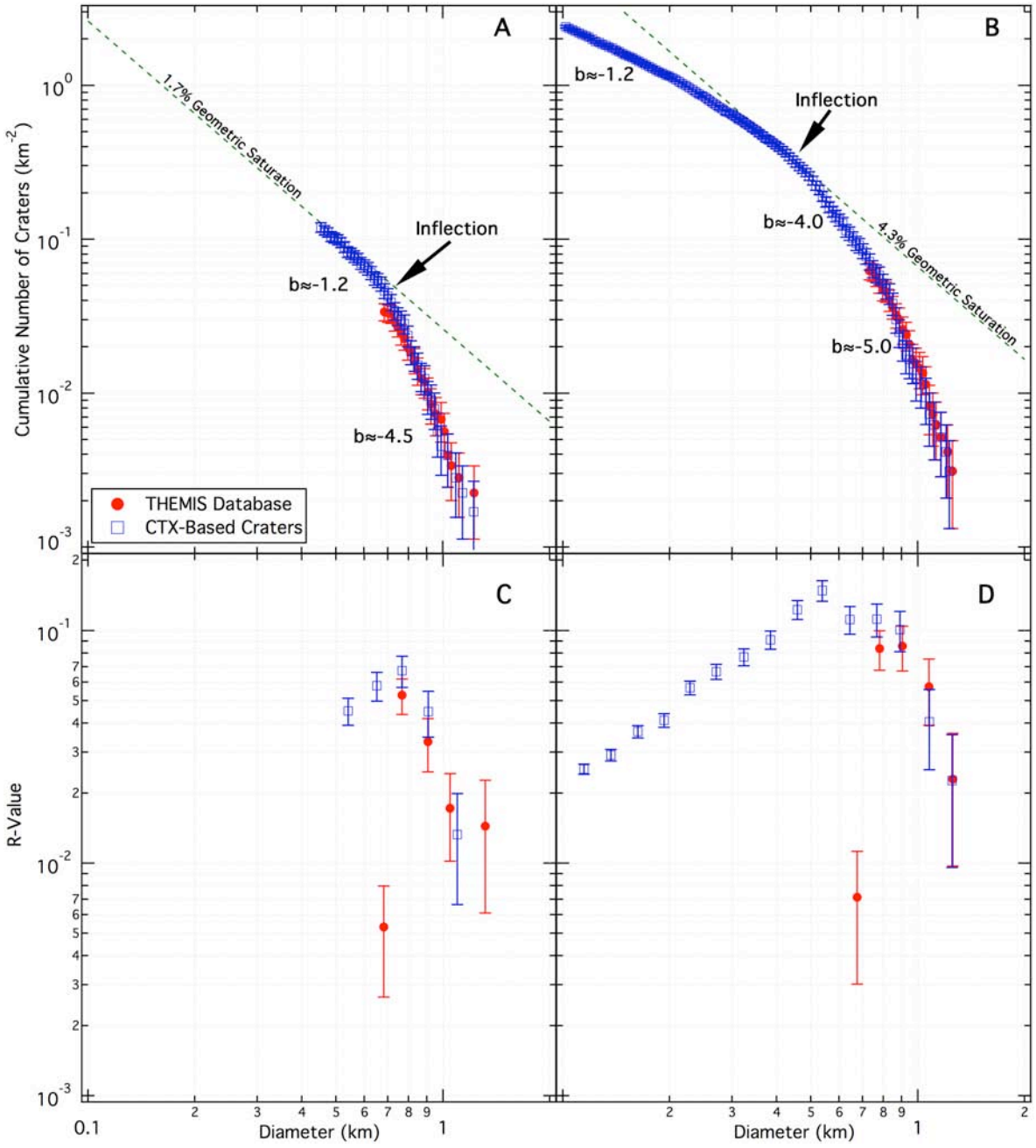

Figure 36: Two case-study SFDs of distant secondary crater clusters analyzed both from the THEMIS-based crater database [*Robbins and Hynek*, 2010] and re-analyzed in CTX imagery (top row is cumulative SFD, bottom row is same data in an R-plot). The two clusters analyzed are located at 31.5°N, 89.2°E (A, C), and -8.3°N, -13.4°E (B, D). Cluster A/C's decameter inflection can be explained by crater saturation [*Melosh*, 1989], but B/D's cannot because for D < 300 m the slope is constant and below empirical saturation. For illustration purposes, the cumulative SFDs are binned in $2^{1/32}D$ intervals and the R-plots in $2^{1/4}D$ intervals.

4.1.4. Discussion and Conclusions

Previous identification of Zunil crater secondaries found on the order of 10^8 craters with $D \geq 15$ m up to 3600 km from the primary [*Preblich et al.*, 2007]. Lyot crater is significantly larger (D = 222 km vs. 10.1 km) and significantly older (~1.6-3.3 Ga vs. ~200-550 ka [*Kreslavsky*, 2008]). Identification and analysis of Lyot secondaries provides another important constraint for the overall study of secondary craters' effects on crater statistics and, by extension, their use in dating planetary surfaces.

We have identified ~150 secondary crater clusters up to 1500 km farther from their primary than Zunil, or nearly 50 crater radii. They are mainly located southeast of Lyot; six clusters were found southwest and four east and northeast. The continuous ejecta blanket has a preferential east-northeast direction (Fig. **33**). The ejecta distribution would seem to conflict with the secondary clusters, but it can be explained by modification and burial towards the south, an interpretation supported by Mars geologic mapping [*Tanaka et al.*, 2005]. Due to the ambiguity, we infer the impactor hit Mars obliquely from the west, but determining compass quadrant is more open to interpretation. The impact produced deep radial troughs filled with secondary craters within ~1-2 crater radii from the rim - different from Zunil which produced very few secondaries within 16 crater radii [*Preblich et al.*, 2007].

Lyot also produced on the order of 10^4 identifiable far-field secondary craters $D \gtrsim 800$ m in clusters, although there are likely many more. The overall SFD matches previous work on Martian secondaries [*McEwen and Bierhaus*, 2006], but we found a different pattern at $D \lesssim 500$ m from our CTX-based studies. Since CTX resolution is more than sufficient to identify all decameter-size craters, we interpret this to be a real feature in these secondary crater clusters. In two of the six cases, this can be attributed to crater saturation [*Melosh*, 1989] (see Fig. **36**). Three additional non-mutually exclusive hypotheses may explain this feature: First, steep SFD slopes cannot continue to indefinitely small sizes due to a cut-off in the production function; with large craters, this is thought to be ~2 orders of magnitude before the volume of material needed would exceed the volume of material excavated [*McEwen et al.*, 2005].

Although volume estimates suggest these secondaries are insufficient in number to reach this limit, it remains a likely contributor. A second explanation could be infilling: over 3.3 Ga, to fill a D = 500 m secondary crater (~50-m deep) would require a rate of 15 nm/yr, but this is at least 10× faster than observed (*e.g.*, *Golombek et al.*, [2006]). A third hypothesis is that only blocks of a sufficient size can be coherently launched from a large primary, travel several thousand kilometers, and form a secondary cluster; the requisite cut-off would be ~10-20 m in this case [*Melosh*, 1989]. Calculations [*Melosh*, 1989] show that stony projectiles $D \lesssim 1$ m would be filtered traveling through Mars' present-day atmosphere. However, the clusters traveled 700-5000 km, $\gg 10\times$ the current scale height of Mars' atmosphere, which could plausibly filter blocks of the requisite size. If the CTX SFDs are treated as a model for all identified clusters, Lyot may have produced a minimum of 10^6 craters $D > 50$ m and 10^7 craters $D > 15$ m, similar to Zunil. This is very likely a lower limit due to erasure processes, inability to locate all clusters, and exclusion of possible crater fields from Lyot.

The implications for using craters to age-date surfaces are significant: First, in agreement with previous work, secondary crater contamination needs to be considered and can significantly affect crater size-frequency distributions (Figs. **35-36**). Near large craters, it is an important factor at multi-kilometer scales (Fig. **33**, **35**). Isolated secondary clusters have steep SFDs and if one were to include these craters when age-dating a sizeable surface, it will result in an erroneously older surface age. While the issue of a large number of secondary craters contaminating kilometer-sized crater statistics has been known for years [*e.g.*, *Wilhelms et al.*, 1978], it has been generally ignored. Second, this study shows that one cannot rely upon a nearby primary crater to use as a criterion for determining if a cluster is secondary in nature - something that is still a point of contention in the community. Third, the inflection to shallower slopes at D < ~500 m (Fig. **36**) illustrates a phenomenon that should be studied further: Forthcoming studies from lunar and mercurian high-resolution imagery may elucidate this anomaly, providing discriminating tests of the proposed hypotheses. Further case studies of secondary craters on Mars and other bodies are needed since Lyot and Zunil show significant

differences. A more robust model and understanding of secondary cratering is needed to better constrain planetary surface ages and their implications for the history of the solar system.

4.2. Close Secondary Crater Fields from 24 Primary Craters, Mars, and Prospects for Understanding Nearby Secondary Crater Production

Note: This paper is in review with JGR: Robbins, S.J.; and B.M. Hynek. "Close Secondary Crater Fields from 24 Primary Craters, Mars, and Prospects for Understanding Nearby Secondary Crater Production." Journal of Geophysical Research. doi: 10.1029/2011JE003820. It is cited in this dissertation as "Robbins and Hynek, 2011d." Sections have been re-numbered and some reformatting has been done to fit the formatting of the rest of this dissertation. References have been combined with all others at the end of this dissertation; in-line references have retained their JGR-style formatting. Acknowledgments have been combined with others at the beginning of this dissertation.

Abstract: Crater statistics are used across a wide variety of applications on planetary surfaces, one of the most notable being estimating relative and absolute ages of surfaces. This requires an assumed cratering rate over time and that craters be randomly distributed. Secondary craters - craters that form from the ejecta of an impact event - belie this assumption by creating higher crater density in a local area at a single time, significantly affecting crater statistics. There has been substantial debate over the relative importance of secondary craters, and our findings in this Mars study indicates that these events can be very significant and cannot be ignored when age-dating surfaces. We have analyzed secondary crater fields found close to 24 primary craters on Mars. Among other findings such as terrain control over secondary crater field characteristics, we conclude that a single large impact event can significantly affect crater statistics at the ~1-5-km-diameter level over a significant fraction of a planetary surface. We also suggest a potential way to avoid significant contamination by the majority of secondary craters that occur close to the primary impact event without the need to manually classify every crater as primary or secondary. Our findings are specific to Mars, but further work will likely show the patterns are applicable to other solid bodies.

4.2.1. Introduction

Crater counting on solid surfaces is the only way to estimate absolute ages on objects and regions without returned samples, akin to the Apollo missions. This common practice has been refined and utilized for decades (*e.g.*, *Arvidson et al.*, 1979; *Hartmann*, 2005). A fundamental assumption of crater age-dating is that crater formation is a stochastic process. However, half a century ago, *Shoemaker* [1962] identified the issue of secondary craters - craters that form from the ejecta of a larger primary impact event and are necessarily smaller than the primary. The subject of secondary craters was generally ignored in the literature until *Bierhaus et al.* [2005] identified $>10^5$ secondary craters that contaminate crater statistics on Jupiter's moon Europa, and *McEwen et al.* [2005] identified $>10^6$ secondaries around the fresh crater Zunil on Mars.

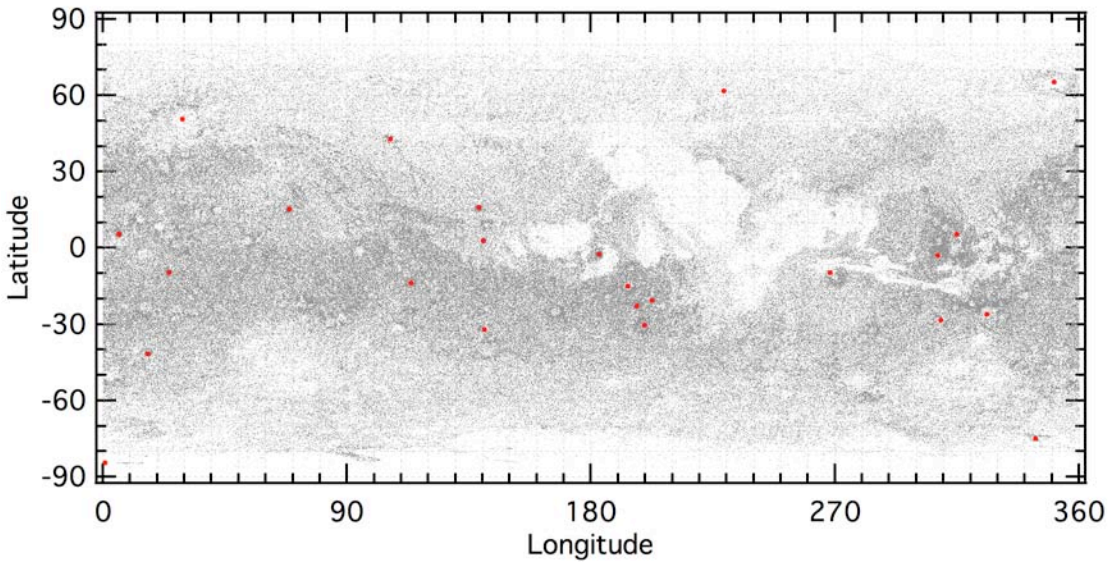

Figure 37: Distribution of all ($D \geq 0.9$ km) craters on Mars from the global Mars crater database [*Robbins and Hynek*, 2010]. Each grey dot is a single crater. Red circles are the locations of all primary craters in this study.

Understanding the role secondary craters have on local and global crater statistics is important, especially because previous research suggests that the crater population with diameters $D < 1$ km on Mars may be significantly contaminated by secondary craters [*McEwen and Bierhaus*, 2006], though in this work we show the number may be significantly larger over broad regions of the planet. Classically, fields are usually a relatively visible and tight annulus around the primary, though recent work has shown that secondary fields can be several thousands of kilometers from the primary [*Preblich et al.*, 2007; *Robbins and Hynek*, 2011a]. With the present and upcoming availability of high-resolution imagery of Mars, the Moon, and Mercury, detailed studies of fields of secondaries near to and far from large primary craters are becoming more important to better understand their effects on the overall crater population and hence their use and utility in discerning stratigraphy and absolute ages (*e.g.*, *Hartmann*, 2005; *Tanaka et al.*, 2011).

Using a new global Mars crater database statistically complete to diameters $D = 1$ km [*Robbins and Hynek*, 2010], we have identified 24 primary craters with prominent and large fields of secondary craters surrounding them (Fig. **37**). While this kind of study has been

discussed briefly and theoretically in the literature (*e.g.*, *Schultz and Singer*, 1980; *McEwen and Bierhaus*, 2006), and more have been conducted on very distant secondaries (*e.g.*, *Lucchitta*, 1977; *Bierhaus et al.*, 2005; *McEwen et al.*, 2005; *Preblich et al.*, 2007; *Robbins and Hynek*, 2011a), there has not been a detailed investigation of several of these nearby fields. We analyze these fields in terms of number and fraction of the primary's diameter, distribution around the primary, and provide a way to account for these fields via automated methods. We discuss our methodology in identifying these craters in Section 4.2.2, explore the secondary field surrounding several primary craters in order of largest to smallest primary diameter in Section 4.2.3, summarize results and discuss implications in Section 4.2.4, and provide conclusions and potential future investigations in Section 4.2.5.

4.2.2. Identification of Primary Craters and Their Close Secondary Clusters

Over 450,000 craters ≳1-km-diameter have been identified on Mars in a global Mars crater database [*Robbins and Hynek*, 2010]. Craters were visually identified in ArcGIS software using 100 m/pix global THEMIS Daytime IR mosaics [*Christensen et al.*, 2004], and rims were mapped using ArcGIS's edit tools. Polygons representing crater rims were imported into Igor Pro where a non-linear least-squares (NLLS) circle-fit algorithm was used to calculate each crater's diameter and center latitude and longitude. The NLLS algorithm corrects for map projection by converting the polygon's geographic coordinates into meters from the polygon's centroid, accounting for the first-order spherical surface of Mars. It is important to note that craters are identified regardless of morphology in this database, hence it is representative of all craters $D > 1$ km, both primary and secondary, on Mars.

When identifying craters and looking at the small crater distribution, numerous examples of torus-shaped distributions of craters throughout the planet were observed (*e.g.*, Fig. **37**). Further examination showed that these always surrounded a relatively large crater and, in general, most of these smaller craters had at least one morphologic characteristic that identified it as a secondary crater such as subdued topography, elongation, tightly-packed clustering, or

herring bone ejecta patterns [*Shoemaker*, 1962, 1965; *Oberbeck and Morrison*, 1974] (see Figs. **38**, **40-42**). Twenty-two such fields were selected that were from mainly pristine primary craters, clearly linked to the larger primary through trough or ejecta entrainment or axially symmetric morphologies that traced a path back to the primary (*e.g.*, Figs. **38**, **40**, **41**, **42**), and studied in greater detail (Section 4.2.3 and Table **7**); a 23rd large crater was studied additionally with CTX imagery (Section 4.2.3.8) while a 24th was studied exclusively with CTX and is discussed in Section 4.2.3.9 (CTX is ConTeXt Camera from Mars Reconnaissance Orbiter [*Malin et al.*, 2007]). Care was taken to minimize contamination of these secondary crater fields with small primary craters, but there is likely inclusion at the ≲1% level.

4.2.3. Size-Frequency Distribution of Secondary Clusters

Crater size-frequency distributions (SFDs) were calculated following *Arvidson et al.* [1979] with some modifications: Craters were binned in multiplicative $2^{1/8}D$ intervals for purposes of slope-fitting. Finer binning than the more standard $2^{1/2}D$ was used to bring out detail in the SFDs that would otherwise be obscured. Craters were binned such that $D_{\text{bin}-1} < D_{\text{crater}} \leq D_{\text{bin}}$, putting all craters in a diameter bin that is the largest crater size in that bin. Since the distribution of craters is not even across all diameter bins, nor does it have a single typical power-law distribution with a slope of -2, the local slope between each bin and the next-smallest was used in order to shift the diameter to a more robust weighted mean:

$$D_a = \frac{D_a - D_{a-1}}{1 + N(D_{a-1})/N(D_a)} + D_{a-1}$$

where $N(D_a)$ is the number of craters at diameter bin D_a. This has a side-effect of having bins that are unevenly spaced in log(*D*).

Three additional features in the SFD algorithm were run on the incremental SFDs. The first removes the largest bins with too few craters – this cut-off was set at <3 craters in a cumulative bin to eliminate some issues with small-number statistics. The second removes incremental bins that had no craters within them. The final feature removes bins below the estimated statistical completeness; this was defined as the incremental bin with the greatest num-

Table 7: All primary craters studied in this work with relevant data for each. Craters are listed in the order of decreasing primary diameter. "Section" is the section of the text, if present, that discusses the primary crater and its associated secondary field in more detail. "SFD Slope" ± values are statistical uncertainties in the fitted slopes. "Annulus Parameters" are $\mu \pm \sigma$ of fitted Gaussian from binning in units of 10% the primary crater radius. "Terrain" is a broad terrain classification into one of six categories: Volcanic, S. High. (Southern Highlands), Trans. (transitional between volcanic and southern highlands), N. Plain (Northern Plains), M.F.F. (Medusae Fossae Formation), and Pole/Polar (very near or embedded in a polar cap).

Crater Data	Section	$N_{secondaries}$	SFD Slope	Range Fitted (km)	Annulus Parameter ($r_{primary}$)	Terrain
50.8°N, 29.3°E, 222 km (Lyot)	3.1	2001	-5.2±0.7	3.2-7.0	2.4±0.9	N. Plains
-26.0°N, 326.0°E, 153 km (Holden)	3.2	1541	-5.5±0.7	2.7-5.9	2.3±0.8	S. High.
65.3°N, 350.7°E, 131 km (Lomonosov)	3.3	940	-8.0±1.2	3.2-5.8	2.6±1.1	N. Plains
-9.8°N, 268.2°E, 124 km (Oudemans)	3.4	385	-6.0±1.0	1.7-3.2	2.1±1.3	Volcanic
-14.9°N, 193.6°E, 88.6 km		563	-4.0±1.5	2.7-4.9	2.3±0.9	S. High.
-2.9°N, 307.8°E, 78.8 km		508	-4.7±1.0	2.1-4.5	2.0±0.6	Trans.
-30.3°N, 199.8°E, 77.6 km		987	-4.8±0.4	1.5-4.5	2.8±0.9	S. High.
-28.4°N, 309.0°E, 77.2 km (Ritchy)		350	-4.1±1.5	1.7-2.9	2.2±0.6	S. High.
-32.1°N, 140.8°E, 63.1 km (Horowitz)		281	-3.7±0.7	1.2-3.2	2.9±0.8	S. High.
-13.8°N, 113.5°E, 58.5 km		123	-4.2±0.7	1.2-3.2	2.3±0.7	S. High.
-22.7°N, 196.8°E, 55.5 km		435	-4.7±1.5	1.7-2.9	2.1±0.7	S. High.
-9.7°N, 24.4°E, 51.4 km		213	-3.3±0.7	1.3-3.5	1.9±0.6	S. High.
15.2°N, 68.8°E, 47.1 km		259	-4.2±0.7	1.1-3.0	1.9±0.8	S. High.
42.8°N, 106.1°E, 46.3 km (Nier)		187	-6.9±1.7	1.3-2.1	3.1±1.3	Volcanic[2]

5.3°N, 5.8°E, 45.0 km	3.5	174	-4.3±1.3	2.3-4.7	2.2±0.6	S. High.
-41.7°N, 16.5°E, 41.9 km		280	-5.5±1.1	1.2-2.2	1.7±0.6	S. High.
15.9°N, 138.6°E, 37.1 km		256	-5.0±1.9	1.3-2.1	3.0±1.0	Volcanic
-20.6°N, 202.5°E, 34.4 km		153	-4.5±1.4	1.3-2.5	2.1±1.5	S. High.
-2.4°N, 183.0°E, 36.3 km	3.6	596	-7.9±2.3	1.5-2.3	1.8±0.7	M.F.F.
-74.8°N, 343.9°E, 30.4 km		250	-3.8±0.4	1.1-2.4	3.3±1.0	Polar
3.0°N, 140.3°E, 29.4 km	3.7	239	-4.0±0.5	1.5-3.2	2.9±0.8	M.F.F.
5.4°N, 314.9°E, 25.3 km		122	-4.7±0.9	1.0-1.7	2.5±0.5	Trans.
-84.4°N, 0.5°E, 24.2 km (McMurdo)	3.8	217[1]	-5.2±1.4	1.1-2.1	3.4±1.0	Pole
61.7°N, 229.0°E, 19.3 km	3.9	1915[1]	-6.6±1.0	0.4-0.8	5.5±1.6	Volcanic

[1]This crater's secondary field was exclusively analyzed with CTX data.

[2]The Utopia basin is assumed to be volcanic for this purpose [*e.g.*, *Thomson and Head*, 2001].

ber of craters. Error bars were calculated by $\pm\sqrt{N}$ Poisson statistics [*Arvidson et al.*, 1979]. Once these operations were performed, the incremental SFDs were integrated (discretely summed) to yield a cumulative SFD. Comparative R-plots (Figs. **39**, **43**) were calculated [*Arvidson et al*., 1979] with similar adjustments. All slopes quoted in this paper are the slopes to linear NLLS fits of the $\log_{10}$ of incremental SFDs with -1 added to yield a statistically accurate slope on a cumulative SFD [*Chapman and Haefner*, 1967]. All uncertainties in the slopes include the statistical uncertainties discussed above; without them, the uncertainties on the slopes are significantly smaller.

Fifteen of the primary craters analyzed were generally similar to each other and non-unique in regards to this study, and these results are reported in Table **7**. The remainder have unique context and/or properties that bear further discussion, and these are addressed in the following sub-sections.

4.2.3.1. Lyot Crater

Lyot crater is a 222-km-diameter fresh peak-ring crater located at 50.8°N, 29.3°E. It is one of the largest relatively young craters on the planet, having been dated to a Middle Amazonian age of ~1.6-3.3 Ga [*Tanaka et al*., 2005; *Dickson et al.*, 2009]. This crater and its distant secondary crater population are discussed in-depth in *Robbins and Hynek* [2011a], and this work looks more closely at the "nearby" secondary field, so-called in that work to differentiate it from secondary craters found up to 5200 km from Lyot. Lyot's secondary craters are found as close as on Lyot's rim, and the near craters that still display clear secondary morphologies (Fig. **38**) extend up to ~7 crater radii from the rim (750 km). The largest crater with secondary-type morphology is a D = 28 km crater located just outside the northwest rim, though this would be abnormally large at 13% the primary's diameter. The largest alternative is an 11-km crater to the northwest which fits the canonical 5% of primary size relation [*Melosh*, 1989].

Morphologically, Lyot's secondary craters are clear to identify: Long, deep, radial troughs extend from Lyot up to ~300 km from the crater rim, and within them are numerous

craters. These craters are generally not circular but are either amorphous in shape or biaxially symmetric with the axis of symmetry tracing back to Lyot; in many cases, they look heart-shaped (Fig. **38**A). The non-circular shape is generally attributed to the crater being formed under a lower impact energy [*Melosh*, 1989], and the preferential direction is due to the clear directional component of the secondary impactor's velocity. Farther from Lyot, the secondary craters are no longer entrained within troughs nor emplaced on Lyot's continuous ejecta blanket. Instead, the

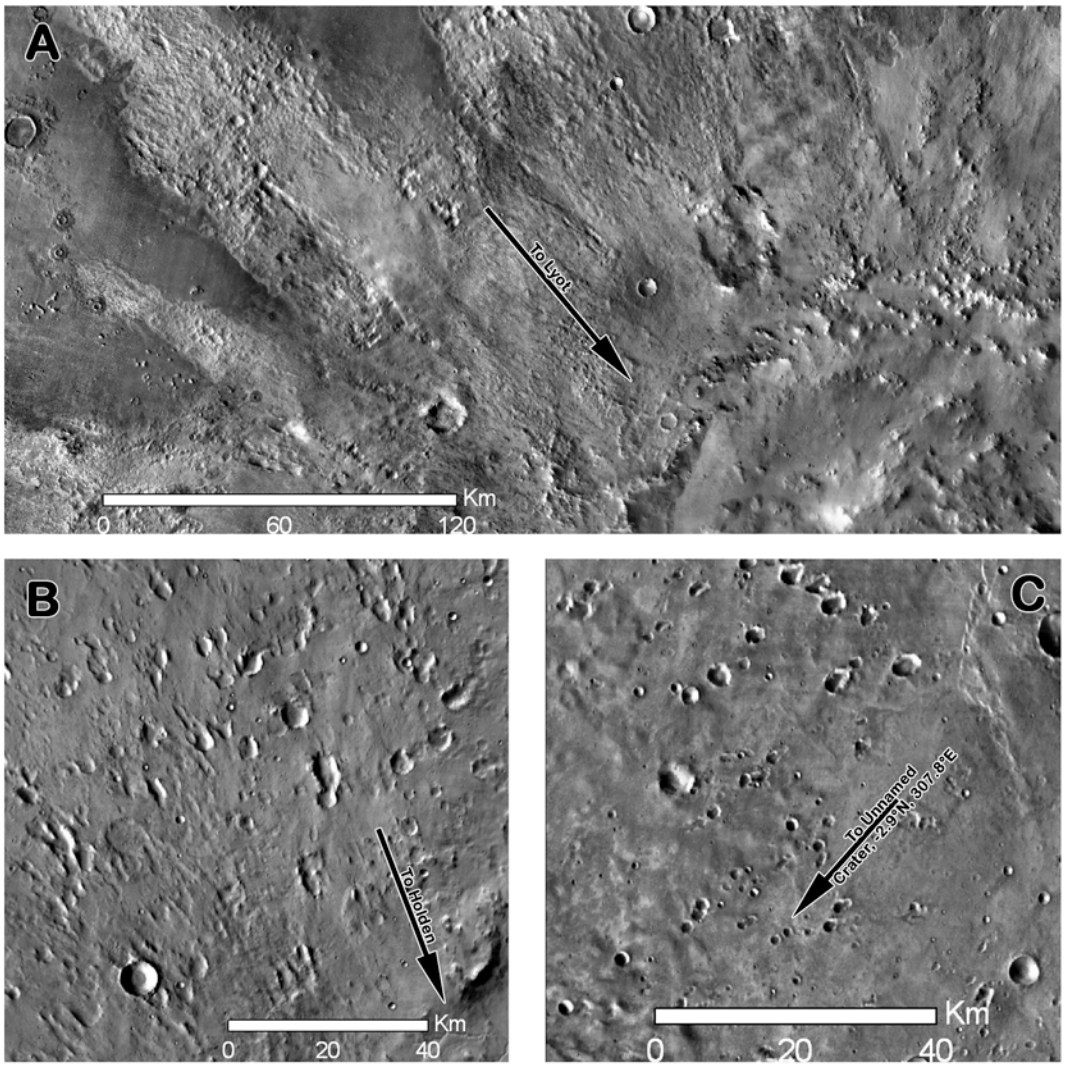

Figure 38: Examples of morphologies seen in secondary crater fields that were studied in this work. Panel A shows craters embedded within Lyot's ejecta. Panel B shows classic asymmetry, herring-bone patterns, and the crater is narrower and deeper on the side facing the primary. Panel C illustrates that some secondary craters display morphologies similar to primary craters with only a small amount of elongation or over-density indicating they are secondaries instead.

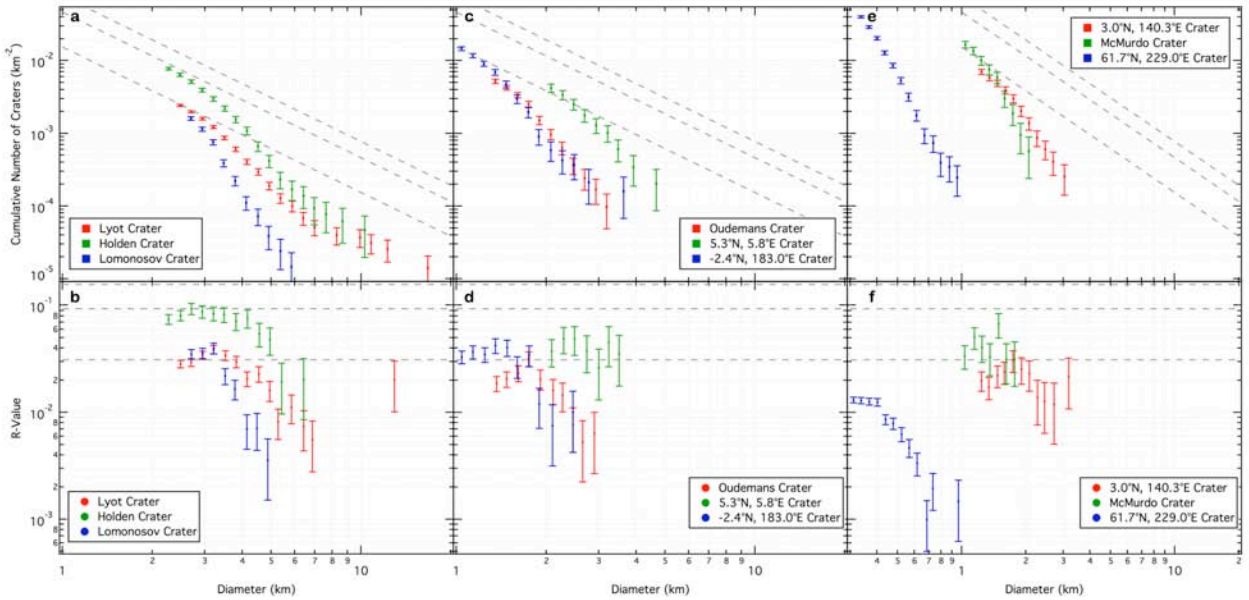

Figure 39: Cumulative size-frequency distributions (top row) and R-plots (bottom row) of all secondary crater fields discussed in Section 4.2.3. Panels a and b show the craters in the first three subsections, panels c and d are the next three, and e and f illustrate the final three. All vertical axes are the same in the top row and they are the same in the bottom row. The horizontal axes are the same for panels a-d but differ for e and f. Dashed lines show 1%, 3%, and 5% of geometric saturation (geometric saturation is defined as $1.54D^{-2}$ [*Melosh*, 1989].

crater shapes point back towards Lyot and still occur in clusters, but these morphologic clues are less clear the farther from Lyot. Even farther, as discussed in *Robbins and Hynek* [2011a], the secondary craters display a general lack of classic secondary characteristics and are instead identified from clustering properties.

2001 nearby secondary craters from the database were extracted for Lyot, a 15% increase from *Robbins and Hynek* [2011a] due to further searching (Table **7**). They are generally found in an annulus around Lyot though this is not obvious until a histogram of distances from the crater center is created; the mean distance is 2.4 crater radii from Lyot's rim (270 km). When plotted in a size-frequency diagram (Fig. **39**a,b), the diameter range $3.2 \leq D \leq 7.0$ km has a slope of -5.4±0.7. This is significantly steeper than a typical crater population with a slope between -2 and -3, but it is typical for secondary crater populations [*McEwen and Bierhaus*, 2006]; it was also generally typical for the other fields studied in this work, though a range of slopes were observed (see Table **7** and Section 4.2.4 for implications).

4.2.3.2. Holden Crater

Holden Crater is a large, 153-km-diameter flat-floored crater located at -26.0°N, 307.8°E. It is one of the most morphologically degraded craters in this study, and it has been dated to the Noachian epoch (≥3.7 Ga) [*Scott and Tanaka*, 1986]. This crater is of special interest due to the Uzboi Vallis channel that flows into its southwest side, the presence of lake deposits and other aqueous features [*Grant et al.*, 2008], and it is a finalist landing site candidate for the *Curiosity* lander [*Golombek et al.*, 2010]. Given its ancient age and presence in the heavily cratered southern highlands of the planet, the presence of a vast secondary field that still exists today is somewhat surprising.

Holden's secondary craters are morphologically distinct from primary craters, as they almost exclusively fall into the class of highly elliptical craters with the major axis pointed radially from Holden and the distant end having little to no rim (Fig. **38**B). The vast majority of the secondaries identified are $D > 1$ km, dominating the cratering statistics over a large area, at least to the north. The secondary crater distribution around Holden is almost completely to the north of the crater; this is likely due to significant resurfacing on the southern half [*Scott and Tanaka*, 1986].

1541 craters that are probable secondaries from Holden up to ~6.5 crater radii were identified from the database (Table **7**). The annulus of secondaries is extensive and, when binned, the greatest density is 2.3 crater radii from the rim (172 km). The size-frequency distribution of the secondaries (Fig. **39**a,b) has a -5.5±0.7 slope when fitted at diameters $2.7 < D < 5.9$ km.

4.2.3.3. Lomonosov Crater

Lomonosov Crater is a fairly fresh 131-km-diameter central peak crater located at 65.3°N, 350.7°E. 940 craters that are probable secondaries were extracted from up to ~6 crater radii from the rim (Table **7**). They are all found in a tight annulus of ejecta with the greatest density 2.6 crater radii from the rim (170 km). The size-frequency distribution of Lomonosov's secondaries (Fig. **39**a,b) has a well-defined slope along $3.2 < D < 5.8$ km of -8.0±1.2. This is the

steepest slope found of the craters in this work, although the reason is not clear. One hypothesis is that it could - at least in part - be due to observational biases since large craters were preferentially not selected as potential secondaries. The problem with this hypothesis is two-fold, however. First, this should affect larger diameters more than smaller, but a uniform slope over the range fit belies that. Second, Lyot crater is nearly twice as large so this effect should be compounded, but a very stable -5.4 slope for Lyot was calculated, and a similar -5.5 for Holden's secondaries was also determined. An alternative hypothesis stems from the fact Lomonosov is the northern-most crater studied and it is well within the region of the Martian cryosphere [*Boynton et al.*, 2002]. If this crater formed when the cryosphere at that latitude was in place, one may expect fewer large craters to be produced from a likely weaker near-surface crust - a crust that may more easily fragment once the released impact energy vaporizes any solid volatiles holding fragments together. A relatively steep slope for the other high-northern crater studied (61.7°N; see Section 4.2.3.9) supports this interpretation.

4.2.3.4. Oudemans Crater

The eroded 124-km-diameter central peak Oudemans Crater is located at -9.8°N, 268.2°E. The secondary craters from Oudemans Crater are difficult to measure. The crater itself is cross-cut to the north by the western parts of the vast Valles Marineris canyon system, specifically Noctis Labyrinthus and Ius Chasma. This indicates that the crater pre-dates this section of Valles Marineris, which has been estimated to be Early Hesperian, ~3.5 Ga [*Tanaka*, 1986]. Valles Marineris also obscures the northern third of the secondaries from Oudemans, and the remaining secondaries have a highly modified morphology and are difficult to identify. Nonetheless, identification of secondary craters from Oudemans was possible due to their non-circular nature and tendency to reside in lines radial to the primary.

385 craters from the database are probable secondaries from Oudemans and extend up to ~4 crater radii from the rim (Table **7**); this is the smallest field in extent in this study and it is likely the field was once larger but it is now obscured by Valles Marineris and volcanic burial. They are all found in a relatively tight annulus of ejecta with the greatest density 2.1 crater radii

from the rim (130 km). The size-frequency distribution of the secondaries (Fig. **39**c,d) has a -6.0±1.0 slope when fitted at $1.7 < D < 3.2$ km.

4.2.3.5. Unnamed Crater at 5.3°N, 5.8°E

The 45.0-km-diameter crater located at 5.3°N, 5.8°E is shown in Fig. **40**A. 174 craters from the database are probable secondaries from this crater that extend up to ~4 crater radii from the rim (Table **7**). The greatest density is 2.2 crater radii from the rim (48 km). The size-frequency distribution of the secondaries (Fig. **39**c,d) has a -4.3±1.3 slope when fitted at $2.3 < D < 4.7$ km (5.1-10.4% the primary crater diameter). This represents one of only two cases where all secondary craters from a primary in this work are larger than 5% of the primary size. However, as shown in Fig. **40**B and C, these are morphologically secondary craters, and their relationship with the primary (Fig. **40**A and D) is in concordance with the distribution expected of secondary craters.

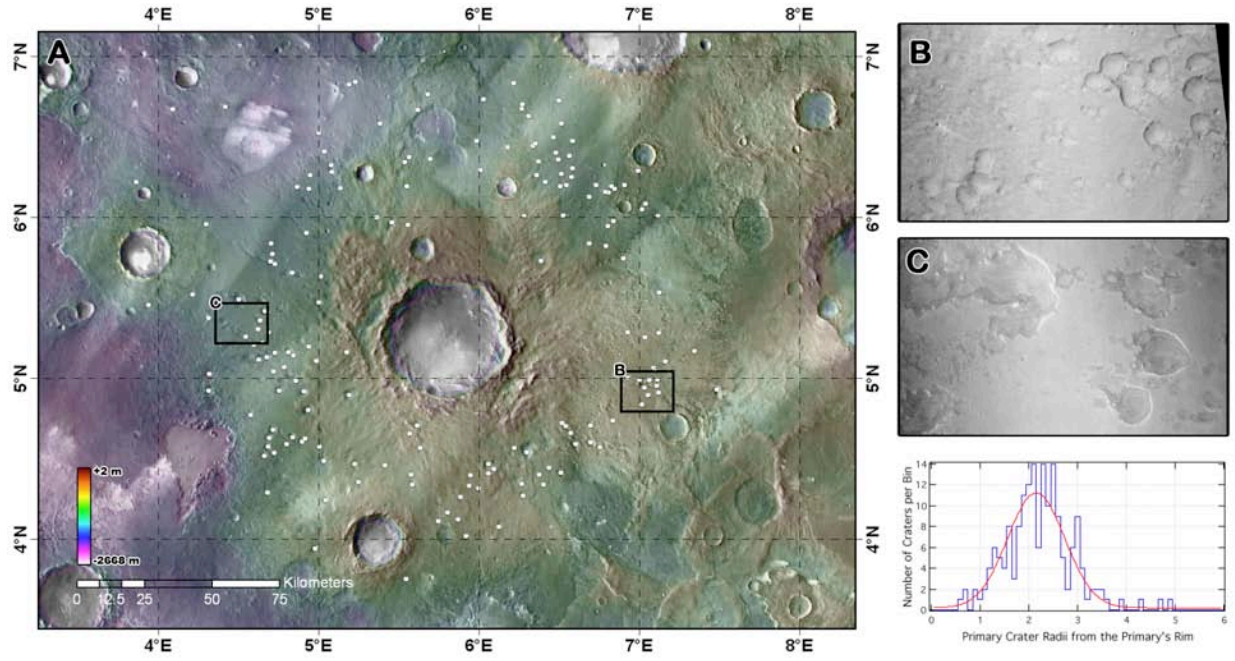

Figure 40: THEMIS mosaic of the unnamed crater located at 5.3°N, 5.8°E (main panel, A) showing the crater and its field of nearby secondary craters. MOLA topography data [*Smith et al.*, 2001] underlies the THEMIS data in (A). Close-up panels (B and C) are CTX data and show representative examples of the rather large secondary craters for this primary. All secondaries identified show a Gaussian distribution from the crater (D) and though they display fewer of the morphological characteristics typical of secondary craters, their relationship to the primary indicates they are indeed secondaries, despite being up to 10% the diameter of the primary.

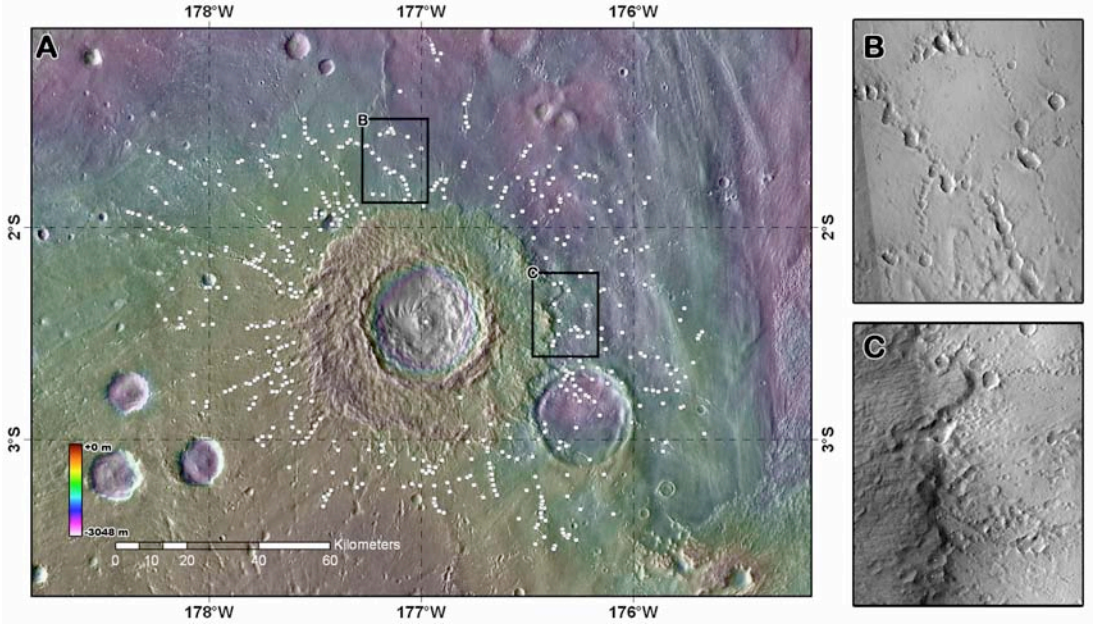

Figure 41: THEMIS mosaic of the unnamed crater located at -2.4°N, 183.0°E (main panel, A) showing the crater, its layered ejecta blanket, and a few of the "tendrils" of secondary craters observed (secondary craters identified are white circles). MOLA topography data [*Smith et al*., 2001] underlies the THEMIS data in (A). Close-up panels (B and C) are CTX data and show representative examples of these tendrils (B) and an example of some of the few secondary craters not found within them that generally abut the ejecta (C).

4.2.3.6. Unnamed Crater at -2.4°N, 183.0°E

A broad context view of the unnamed 36.3-km-diameter fresh central peak crater located at -2.4°N, 183.0°E is shown in Fig. **41**A. There is a potentially large secondary crater located 38 km from the crater's center, though it is abnormally large at D = 5.2 km, 14% the diameter of the primary (similar to the larger candidate for Lyot, Section 4.2.3.1). One may expect the largest secondary to be ~1.8 km in diameter [*Melosh*, 1989], but since there are over a dozen craters approximately this size that are included in the secondary field, an alternative "largest secondary" is difficult to discern from the others.

This crater and its associated secondary field presented an interesting and unique morphology among the ones studied in this work, only matched in part by the one in Section 4.2.3.9. It is one of the "layered ejecta" craters [*Barlow et al*., 2000] characterized by a highly cohesive ejecta blanket, though this blanket also appears to have classic radial ejecta overlaying it. There are very few secondary craters upon the cohesive ejecta, which extends an average of

0.95 crater radii from the rim. Beyond it, however, are numerous tendril-like features that are chains of secondary craters (Fig. **41**B). Very few secondary craters were identified that were not in these thin, non-linear chains; ones that were not in these were generally just outside the terminus of the layered ejecta blanket (Fig. **41**C) or they were very small and only visible in higher-resolution data. Overall, the secondary craters from this primary were also among the most deformed, being far from circular, though still morphologically fresh.

596 craters were extracted as probable secondaries from this crater at distances up to ~6 crater radii from the rim (Table **7**). Though residing in the chains and tendrils, when binned they have a peak mean distance of 1.8 crater radii from the crater's rim (33 km). This was a unique case among the crater fields studied where a log-normal distribution better-represented the radial distribution of secondary craters from the primary, which had a mean of 1.6 crater radii. The size-frequency distribution of the secondaries (Fig. **39**c,d) has a steep -7.8±2.3 slope when fitted $1.5 < D < 2.3$ km, the second-steepest in this study (Lomonosov was steepest, see Section 4.2.3.3).

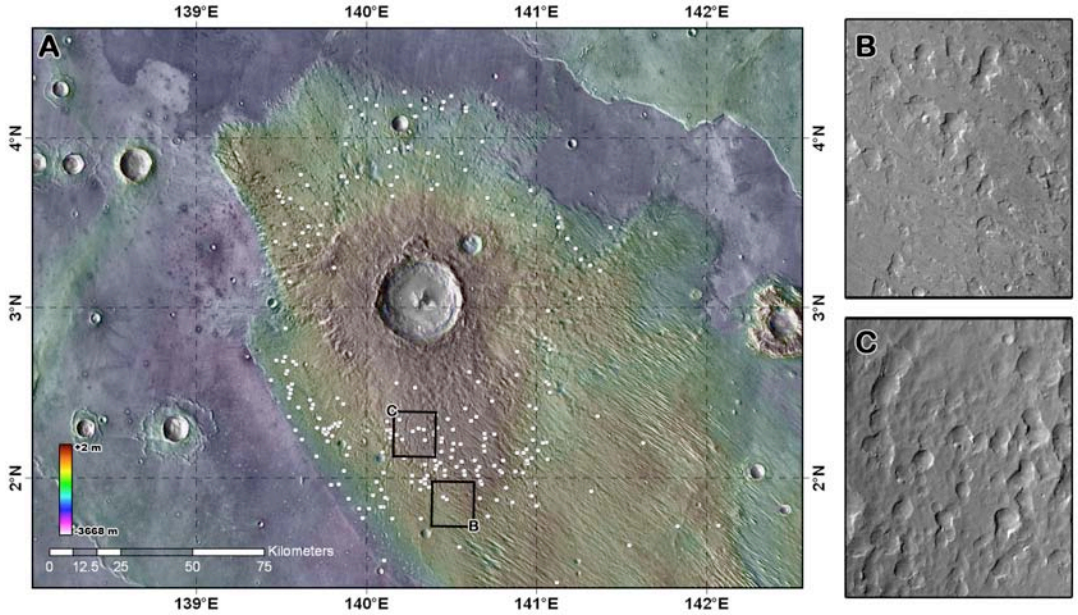

Figure 42: THEMIS mosaic of the unnamed crater in the Medusae Fossae Formation located at 3.0°N, 140.3°E (main panel, A) showing the crater and the surrounding geology for context and secondary craters as white circles. MOLA topography data [*Smith et al*., 2001] underlies the THEMIS data in (A). Close-up panels (B, C) are CTX data and show some of the secondary crater morphologies observed around this large primary.

4.2.3.7. Unnamed Crater at 3.0°N, 140.3°E

Another crater analyzed (Fig. **42**) is the unnamed 29.4-km-diameter fresh central peak crater located at 3.0°N, 140.3°E. This crater is in northwest Aeolis Planum on one of the western-most parts of the Medusae Fossae Formation (the crater in Section 4.2.3.6 is just beyond the eastern part of the Medusae Fossae Formation). This makes it an interesting and unique (in this paper) candidate for study since Medusae Fossae is some of the least dense and friable material on Mars [*Muhleman et al*., 1991; *Hynek et al.*, 2003]. The crater's continuous ejecta is clear today though it overlies subparallel yardangs of aeolian origin (Fig. **42**A). The field of secondaries abuts smooth material that has embayed the Medusae Fossae Formation, so these results likely are under-representative of the entire field for this crater. This is preferential towards the north, which may be why fully 70% of the secondary craters identified from this primary are located south of its center. The morphology of these secondary craters is among the more circular type, the secondaries generally being scattered randomly over the continuous ejecta (~1% are beyond the ejecta) and being fairly isolated from each other (Fig. **42**B). Only a few are in chains (Fig. **42**C).

239 craters from the database are probable secondaries from this crater and extend roughly 5.5 crater radii (Table **7**). They are all found in a tight annulus of ejecta with the greatest density 2.9 crater radii from the crater's rim (42 km). The size-frequency distribution of the secondaries (Fig. **39**e,f) has a -5.4±1.9 slope when fitted at $1.7 < D < 2.7$ km (5.8-9.2% the primary crater diameter). While these values are typical (see Table **7**) despite it being emplaced on Medusae Fossae, this is the second of two cases where the secondaries are all >5% the primary crater diameter (the unnamed crater at 5.3°N, 5.8°E in Section 4.2.3.5 is the other).

4.2.3.8. McMurdo Crater

The 24.2-km-diameter central peak McMurdo Crater is the most poleward crater analyzed in this study, located at -84.4°N, 0.5°E. The crater is mostly embedded within the south polar cap, indicating it is fairly young since the south polar cap is estimated to be ~10 Ma [*Herkenhoff and Plaut*, 2000]. Statistically, a ~25-km-diameter crater should form on Mars once

every ~4 Ma [*Ivanov*, 2001; *Neukum et al.*, 2001], and taken with the polar cap age constraint means McMurdo may be the youngest ~25-km-diameter crater on Mars. It has a fairly extensive secondary crater field that remains on the cap, though none are visible in the non-ice-covered terrain toward the north.

Identifying these secondary craters was initially accomplished in THEMIS Daytime IR mosaics to establish the phenomenon, but the THEMIS data are inadequate for a study similar to those presented in previous subsections. It is covered fully by CTX imagery; a mosaic was created with fourteen CTX images that cover the field, and it was rendered at 10 m/pix scale. Even with CTX data, identifying the craters was made difficult by both long-term and seasonal erosion processes that dominate the ice cap itself. Nonetheless, the data gathered is in general agreement with the secondary crater fields described for the other primary craters in this study:

217 craters were identified that are probable secondaries from McMurdo that extend up to ~6 crater radii from the rim (Table **7**). They are found scattered in the vicinity of the crater on the remnant ice cap with the greatest density 3.4 crater radii from the rim (82 km). Fitting the size-frequency distribution (Fig. **39**e,f) between 1.1-2.1 km (up to 8.6% the primary crater diameter) yields a -5.2±1.4 slope.

4.2.3.9. Unnamed Crater at 61.7°N, 229.0°E

While the crater discussed in Section 4.2.3.6 is fairly unique both in this study and on Mars, the unnamed fresh 19.3-km-diameter crater at 61.7°N, 229.0°E displays a similar morphology with long, isolated chains of secondary craters from the primary. However, in this case they are highly linear. It is also surrounded by a double-layer ejecta blanket – the only one in this study, but potentially similar in origin to the single-layer ejecta surrounding the unnamed crater at -2.4°N, 183.0°E. This crater's nearby secondary field exclusively contains craters that are below the THEMIS resolution for identification. The field is ~75% covered as of January 2011 by CTX imagery, and eleven CTX images that cover the field were mosaicked at 7.5 m/pix scale.

1915 craters were identified based on morphology from the CTX imagery that are

probable secondaries and extend up to ~10 crater radii from the rim (the most distant of any in this study) (Table **7**). They are all found predominantly in long chains, but there is a background scattering between the chains - similar to the field from the unnamed crater at -2.4°N, 183.0°E. The craters were found mainly to the northwest of the primary, possibly indicating an impact direction coming from the southeast. When binned based upon distance from the primary, the greatest density is found 5.5 crater radii from the rim (106 km), the most distant in this study. The size-frequency distribution of the secondaries (Fig. **39**e,f) has a -6.6±1.0 slope when fitted at $0.4 < D < 0.8$ km.

4.2.4. Implications

Detailed studies of known, clear secondary crater fields are important so that their properties can be extrapolated to the broader study of the possible background contamination by secondary craters of planetary surfaces [*McEwen and Bierhaus*, 2006]. From the study of 24 of these fields surrounding Mars primary craters, we find three primary implications:

First, the size-frequency distributions of the secondary craters varied with no noticeable size-dependent pattern. A weighted mean of the slopes is -4.99, which is in general agreement with previous modeling and results (*Bierhaus et al*., 2005; *McEwen et al.*, 2005; *McEwen and Bierhaus*, 2006), though slightly steeper on average. As with those previous studies, we found a distinct spread in values, being as shallow as -3.3 but as steep as -8.0. All of these are steeper than -3, the asteroidal production function [*Ivanov*, 2001; *Neukum et al.*, 2001], and -2, the saturation limit [*Melosh*, 1989]. CTX comparisons show that THEMIS results are reliable for complete identification of secondary fields at these diameters [*i.e.*, *Robbins and Hynek*, 2011a]. Thus, the secondary crater production function follows a steep slope overall, but individual craters should be treated as unique events with their own population distribution of secondaries. We posit the two dominant variables in determining the size-frequency distribution are likely to be the initial impactor's velocity and the target material's strength. The impactor velocity is directly proportional to the energy imparted and subsequent shock effects, while the target's

strength will determine how it fractures and hence the size-distribution of material for secondary impacts. If this is the case, as future modeling or experimentation may demonstrate, then nearby secondary crater populations could be used as a proxy for target strength and/or impactor velocity.

To this end, we separated the primary craters by terrain type (Table **7**). Although we are dealing with small numbers – *N*=2 for each the northern plains, pole/polar, and Medusae Fossae Formation, *N*=4 on volcanic terrain, and *N*=12 in the southern highlands – there are some suggestions of trends. The first is that the shallowest SFD slope was for the pole/polar craters with a weighted mean of -4.1. The steepest slopes were found in the northern plains and volcanic terrain with a weighted mean of -6.2. While these are suggestive and support our hypothesis, more examples are needed to determine if these are real characteristics. For example, these are also consistent with a potential preservational bias where the slopes decrease over time due to erosion and modification making it more difficult to identify smaller craters.

A second main implication of this work is that we found the secondary craters generally followed a Gaussian distribution in number density radial to the primary crater. Though we studied only 24 primary craters, they ranged in diameter from 19 to 222 km and the relative mean distance from the primary was not found to be dependent upon primary diameter (in units of primary crater diameter). This distribution had $\mu = 2.44$ crater radii, or 2.37 with the outlier from section 4.2.3.9 excluded; the median is 2.32 crater radii from the primary's rim. The mean standard deviation is ±0.87 crater radii, and while it ranged between 0.54 and 1.36 (Table **7**), this was also independent of primary crater diameter and independent of the mean of the distribution (except the maximum value outlier from section 4.2.3.9). When examining terrain type dependence, we found that craters were closest to their primary (smallest Gaussian mean) in the southern highlands, where the weighted $\mu = 2.2$; pole/polar and volcanic terrain was the most extensive at a weighted $\mu = 3.3$.

To further explore this Gaussian distribution, we re-examined a field of secondary craters initially identified in *Robbins and Hynek* [2011b]. This field surrounds the *D* = 5.2 km crater at

5.2°N, 174.6°E, and it is located within the primary caldera of Apollinaris Mons. Even with CTX imagery, it was difficult to morphologically distinguish the small secondary craters around this primary, but we identified a field based upon the over-density of craters around the main one. We have taken the 10,746 small craters identified throughout the Apollinaris Mons caldera and analyzed them for distance from the primary. Even though this includes all craters, there is a noticeable spike well above the background at a mean of 2.4 crater radii from the primary's rim. This suggests that this pattern holds over a large range of primary crater sizes, at least $5 < D < 222$ km.

Hence, the third main result is that, to avoid nearby secondary crater contamination from automated crater extraction methods from a database, one could reliably exclude 95% of all secondary craters by not using any craters with $D < 0.05D_{primary}$ within 4.2 primary crater radii of the rim (or, more easily for automated methods, within 2.6 crater diameters of the primary crater's center). Any craters actually within the primary crater cannot be simple secondaries from it, so those could be included in statistics counts.

With this in mind, we can take a broader overview of the influence that secondary craters have on local crater statistics and what this means if researchers are not careful in separating secondary craters from primary impact events when deriving stratigraphy and crater-based ages. *McEwen and Bierhaus* [2006] suggest that the majority of craters $D < 1$ km on Mars may be secondaries. While this work cannot address this issue globally, we can address the question of local crater population contamination. For example, one can look at the large Holden Crater out to 4 crater diameters from its center (Fig. **43**, left column). As expected based upon the above analysis, the incremental SFD shows a steeper than expected slope of -3.5 for craters around the ~2-5 km diameter range (~1-3% the primary's diameter, from which the slope was fit in Section 4.2.3.2 and Table **7**). If we expand this area to 8 crater diameters, which covers 4.7×10^6 km^3 (3.3% the surface area of Mars), there is less of an effect to the point one may think it is a normal production slope of -3.1. However, if the craters within 2.6 diameters of the center are removed, as suggested above, then the slope is -2.8. Finally, the ideal solution is to remove secondary cra-

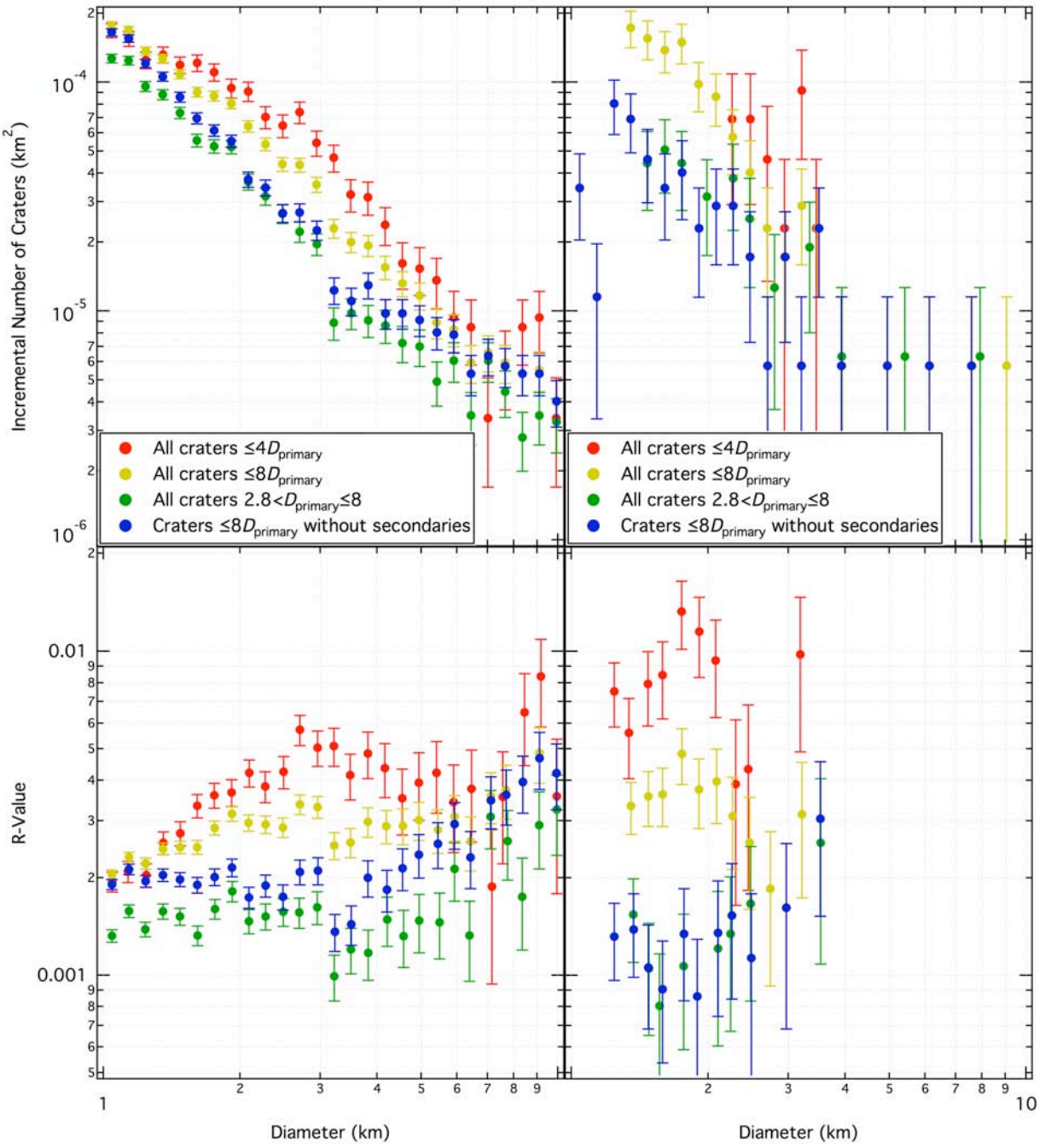

Figure 43: Examples of secondary crater contamination of primary impact craters for two examples, Holden Crater (left panels) and an unnamed 29.4-km crater (3.0°N, 140.3°E) (right panels), shown in both incremental SFDs (top panels) and R-plots (bottom panels). Overplotted in color, coded the same in all four panels, are all craters out to 4 crater diameters from the primary in red, 8 diameters in yellow, 8 diameters minus craters to 2.6 diameters in green, and 8 diameters with the selected secondary craters removed in blue.

ters by identifying them individually. The SFD looks similar, but there are some minor

differences (and the slope over that range is -2.4); regardless of these differences, the removal within 2.6 diameters is a better match to the customized secondary crater removal than the other two examples. On the R-plot, these are the only two that show the relatively flat expected slope between ~1-5 km. This also alters the fitted age on the order of 10^8 years, or ~10%, when using the Neukum production function [*Neukum et al*., 2001].

This analysis was repeated for a smaller, 29.4-km-diameter crater (see Section 4.2.3.7), in the right column of Fig. **43** with similar conclusions though somewhat different results. The slopes were -6.4±0.7, -5.1±0.3, -1.7±1.4, and -4.5±1.2, respectively. This was a primary crater emplaced on relatively young terrain, Amazonian-aged, as opposed to Holden which is itself significantly older and emplaced on more heavily cratered terrain. Hence, in this crater's case, the population of secondaries from this single event will dominate the statistics to a larger radius. Statistically, the first three population tests shown for this crater are unique, while the detailed removal of secondary craters test yields a more ambiguous result; this is due to there simply being fewer craters: With Holden in this fourth test, there were 8974 craters, whereas this one has 126. While the fits are not as conclusive, examining the data (Fig. **43**, right panels) shows the same pattern as with Holden. In fitted ages over a ~1-4 km range, the difference is 800 Ma, or ~25%.

This test was repeated for three more craters from this study (Ritchy, Nier, and the unnamed 30.4-km-diameter crater (-74.8°N, 343.9°E) near the south pole), all with similar results where the slope was over-estimated until craters were removed with the closest match to the manual identification being the $2.6D_{\text{primary}}$ radius removed, though results were mixed at how well it mimicked the behavior of manual secondary crater identification. This strongly supports the idea that secondary craters can easily dominate local crater statistics even above the D = 1 km proposed transitional diameter, though one can generally eliminate the bulk of contamination by following the steps outlined above, especially for larger primary craters.

A caveat with this is when examining more localized crater statistics, especially in young terrain. For example, the largest secondary crater identified around the 19.3-km-diameter

primary discussed in Section 4.2.3.9 was 1.0 km, 5.2% the primary. But there are numerous ~1-km-diameter primary craters within the 200-km radius field of secondary craters, and within the 50-km-radius field of suggested avoidance from the technique above. However, this surface area is ~9,000 km^2, a relatively small region to use $D \sim 1$ km craters for impact statistics - especially on such young terrain - and one that is quite clearly dominated by a relatively large primary. In an alternate case, *Preblich et al*. [2007] showed that Zunil crater's secondary field did not begin until ~16 crater radii from the rim, which is completely outside our suggested region. Hence, while we argue this method can be used in general as a way to eliminate the majority of secondary craters found close to their parent, it is still prudent to take the local features into account and to not blindly apply it to every scenario.

4.2.5. Conclusions

As we have shown in this study, the secondary craters surrounding larger primary craters generally possess at least one characteristic of classic secondary crater morphology, be it entrainment in troughs or tendrils radial to the primary, highly asymmetric, biaxially symmetric with the symmetry axis radial to the primary, or immediately surrounded by herring-bone ejecta that points back to the primary (Fig. **38**); we were unable to explore depth versus diameter relationships due to insufficient topographic resolution (secondaries should be shallower than primaries of the same size due to lower impact velocity [*e.g.*, *Melosh*, 1989; *McEwen and Bierhaus*, 2006]). While these features have all been known of for decades, the shear range of different morphologies expressed deserves more discussion. In this work and our related work towards a large, global crater database [*Robbins and Hynek*, 2010], the single-crater-thick chains and tendrils of secondaries isolated from little to no background field were only observed around craters with LE-type ejecta (*e.g.*, Fig. **41**). Where lunar-type radial ejecta was present, secondary craters were observed embedded in troughs within it (*e.g.*, Figs. **38**A, **42**). Meanwhile, even around older craters (such as Holden or the unnamed crater at 5.3°N, 5.9°E), where secondary craters were degraded, they were still generally distinguishable by non-circular shapes with a

long axis oriented radial to the primary (*e.g.*, Figs. **38**C, **40**).

From the analyses presented here, we can conclude: (1) Each primary impact event can produce a distinct size-frequency distribution of secondary craters that, when taken as a whole, have a canonical slope between -4.0 and -6.0, but individually can be significantly different, and (2) our results suggest there is a terrain dependence on the size-frequency distribution of secondary crater populations, similar to work by *Hartmann and Barlow* [2006]. (3) Secondary crater fields close to their primary tend to follow a Gaussian distribution in number versus distance from the primary, and the mean of that distribution is 2.6 crater diameters from the primary's center. This is a pattern that holds over at least 1.6 orders of magnitude of crater diameters (~5 < D < ~220 km). This can be used in automated crater counting to eliminate these craters to avoid the majority of secondary crater contamination. (4) Local and regional crater populations can be significantly contaminated by secondary craters over a large surface area; Holden Crater secondary craters will still affect size-frequency distributions over a surface area >3% of Mars' surface. (5) The local onset of this contamination can be several times the D = 1 km suggested by *McEwen and Bierhaus* [2006] for a global Martian crater population, and so even at multi-kilometer sizes, researchers must take care to avoid secondary crater contamination when using craters for age-dating purposes. For example, the secondary craters produced from just 30 Holden-sized and -type events evenly distributed around the globe would contaminate the crater population D < 5 km across the entire planet; the global crater database used in this study shows there are 95 such impacts (although they are not evenly distributed in time nor space). This is in stark contrast with recent work that suggests the contrary (*e.g.*, *Neukum et al.*, 2001; *Neukum et al.*, 2006; *Hartmann*, 2007).

Additional implications of this work not discussed in-depth in Section 4.2.4 include: (6) In a few cases, the field of secondary craters can be larger than the hypothesized maximum 5% of the primary crater's diameter (see Sections 4.2.3.5 and 4.2.3.7, Fig. **40**). (7) Nearby secondary crater fields appearing in thin tendrils or chains were only found around craters with cohesive layered ejecta (LE) -type morphology, implying a possible formation-dependent link. (8) The

LE-type ejecta morphology craters also had SFD slopes significantly steeper than the collective mean from all craters studied here. Though this may be attributed to the terrain- or preservation-dependent nature in slope addressed above, work suggests the LE ejecta formation is also terrain dependent (*e.g.*, *Barlow*, 2006; *Robbins and Hynek*, 2010). Hence, separating these two possible effects may be secondary and difficult to accomplish in future endeavors. Similarly, (9) Lomonosov's SFD slope presents an outlier that may be explained by a near-surface cryosphere, but we were unable to test this hypothesis because the only other high-northern latitude crater examined was a layered ejecta crater.

Further research into these issues and separating each potential dependent variable's effect from the others is important to understand how to account for secondary craters when primary craters are the feature of importance. Our global crater database [*Robbins and Hynek*, 2010] will contain a classification of whether a crater is a probable secondary and from which primary it originated if this can be determined, but this is only for morphologically clear secondary impacts. Degraded primary craters five primary crater radii away may look identical to a secondary at that location, especially at the kilometer scale when using 100 m/pix mosaics. This problem must be better understood as a function of terrain as well, since this study and others (*e.g.*, *Hartmann and Barlow*, 2006; *McEwen and Bierhaus*, 2006) show there may be terrain dependence upon secondary field characteristics. Examination of secondary crater fields and production on other surfaces (*e.g.* with Lunar Reconnaissance Orbiter imagery of the Moon and MESSENGER imagery on Mercury) may help further constrain this issue to better model their production so they can be taken into account in a statistical and automated manner without needing to examine the morphology of every crater. However, such a model also will be incomplete without a better understanding of secondary craters produced very far from their primary (*e.g.*, *Bierhaus et al*., 2005; *McEwen et al*., 2005; *Robbins and Hynek*, 2011a), which this study did not investigate. Overall, a more robust framework and understanding of secondary cratering is needed to better constrain planetary surface ages and their implications for the overall history of the solar system.

5. The Volcanic History of Mars: High-Resolution Crater-Based Study of the Calderas of Twenty Volcanoes

Note: This paper is published as: Robbins, S.J.; Di Achille, G., and B.M. Hynek. (2011) "The Volcanic History of Mars: High-Resolution Crater-Based Study of the Calderas of Twenty Volcanoes." Icarus. 211, pp. 1179-1203. doi: 10.1016/j.icarus.2010.11.012. It is cited in this thesis as "Robbins et al., 2011." Sections have been re-numbered and some reformatting has been done to fit the formatting of the rest of this dissertation. References have been combined with all others at the end of this dissertation. Acknowledgments have been combined with others at the beginning of this dissertation. Minor changes to the journal text have been made.

Abstract: Determining absolute surface ages for bodies in the solar system is, at present, only possible for Earth and Moon with radiometric dating for both bodies and biologic proxies such as fossils for Earth. Relative ages through cratering statistics are recognized as one of the most reliable proxies for relative ages, calibrated by lunar geologic mapping and Apollo program sample returns. In this work, we have utilized the Mars Reconnaissance Orbiter's ConTeXt Camera's images which provide the highest resolution wide-scale coverage of Mars to systematically crater-age date the calderas of 20 of Mars' largest volcanoes in order to constrain the length of time over which these volcanoes - and major volcanic activity on the planet, by extension - were active. This constitutes the largest uniform and comprehensive research on these features to date, eliminating unknown uncertainties by multiple researchers analyzing different volcanoes with varied data and methods. We confirm previous results that Mars has had active volcanism throughout most of its history although it varied spatially and temporally, with the latest large-scale caldera activity ending approximately 150 Ma ago in the Tharsis region. We find a transition from explosive to effusive eruption style occurring in the Hesperian, at approximately 3.5 Ga ago, though different regions of the planet transitioned at different times. Since we were statistically complete in our crater counts to sizes as small as ~60 meters in most cases, we also used our results to study the importance of secondary cratering and its effects on crater size-frequency distributions within the small regions of volcanic calderas. We found that there is no "golden rule" for the diameter secondaries become important in crater counts of Martian surfaces, with one volcano showing a classic field of secondaries ~2 crater diameters from the center of its primary but not affecting the size-frequency distribution, and another clearly showing an influence but from no obvious primary.

5.1. Introduction

The planet Mars has had an active geologic past with a varied surface showing evidence of past fluvial, aeolian, and volcanic activity. This is in stark contrast with the current lack of geologic activity on Mars, though recent data have illustrated a few lingering aeolian and cryogenic processes that continue to significantly shape its surface (*e.g.*, Hartmann, 2005). Noticeably missing from the list of current activity is volcanism, and an ongoing question has

been when the last volcanic episodes occurred on Mars.

Many researchers in the past have tried to answer when volcanism ended through two methods. The method that we will not be addressing in this paper involves radiometric dating of the known martian meteorites, which generally date from a few hundred Ma to about 1.5 Ga, the noticeable exception being ALH84001 which dates to ~4.5 Ga (Nyquist *et al.*, 2001) though recent estimates place it at ~4.1 Ga (Lapen *et al.*, 2010). The basaltic meteorites (ALH84001 is an orthopyroxenite) require volcanism at the time of formation, constraining the most recent episode on Mars to a maximum of 180 million years ago (the basaltic shorgottite meteorites Shergotty, Zagami, and Los Angeles) (Bouvier *et al.* 2005).

The second method of age-dating the martian volcanoes is crater-based, an established technique that assumes an older surface will have a higher crater density because it has had more time to accumulate craters (Arvidson *et al.*, 1979). Since the original images from the Mariner 9 and Viking orbiters were returned in the late 1960s and throughout the 1970s, different researchers have tried to use crater densities to successively refine the ages of the major volcanoes on the planet (*e.g.*, Blasius, 1976; Plescia and Saunders, 1979; Neukum *et al.*, 1979; Neukum and Hiller, 1981; Greeley and Spudis, 1981; Plescia, 1994; and Hodges and Moore, 1994 and references therein). In general, the utility of crater counting is greatly increased when (a) larger areas are used, and (b) smaller craters are included for the joint effect of better number statistics and a larger range of diameters for age determinations. The latter is limited usually by the data resolution for airless or nearly-airless bodies, such as Mars or the Moon.

The last 15 years has brought more orbiters to Mars with ever-higher-resolution cameras, allowing crater-based age dating of the volcanoes to be refined by dating individual features such as flows, collapses, and calderas (*e.g.*, Hartmann, 2005). It has only been in the last ~6 years that the planetary community has had sufficient imagery to derive statistically meaningful ages from areas that are as small as volcanic calderas on the planet, mainly through the use of Mars Express' High Resolution Stereo Camera (HRSC, roughly 10-30 m/pix resolution) and Mars Reconnaissance Orbiter's (MRO's) ConTeXt Camera (CTX, 5.5-7.5 m/pix resolution), resulting

in works such as Neukum *et al.* (2004), Werner (2009), and this work. Previous work with Mars Global Surveyor's Mars Orbiter Camera (MOC) by different researchers in localized parts of the planet that illustrates some lava flows are as young as a few 10s of millions of years (*e.g.*, Berman and Hartmann, 2002; Hartmann, 2005; and Roberts *et al.*, 2007).

Neukum *et al.* (2004) used HRSC images to age-date five volcanic summits - Hecates and Albor Tholi located in Elysium, and Arsia, Ascraeus, and Olympus Montes located in the vast Tharsis region (Fig. **44**). Their work is comparable to ours except in number of volcanoes dated and our completeness to decameter-scale craters. Since then, the only researcher to attempt to systematically crater-age-date the volcanic calderas was Werner (2009) who dated all 24 major volcanic constructs using HRSC data, but often all calderas were combined into one, or the calderas were not dated in favor of analyzing the flanks or other flows from the volcanoes.

Our aim was to use the CTX dataset, which offers up to 6× higher resolution than HRSC, to systematically crater-age-date recognizable calderas in the 24 major volcanoes on Mars (Fig. **44**). The previous work to systematically date the volcanoes (Werner, 2009) used HRSC, while all previous research was done by different people using various datasets, lacking

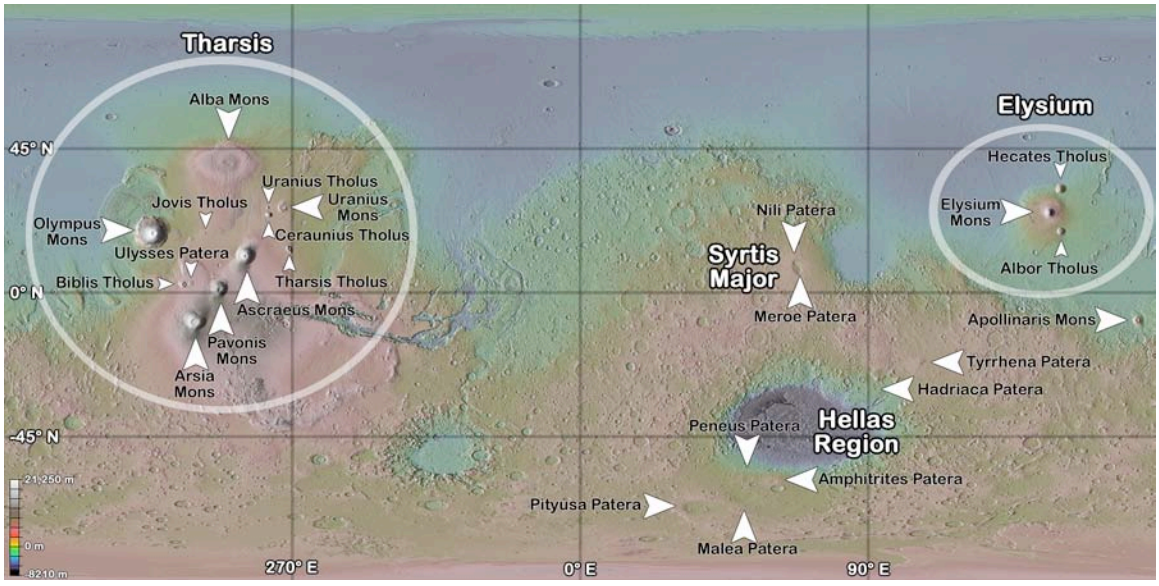

Figure 44: Underlying map is MOLA (Mars Orbiter Laser Altimeter) shaded relief (Smith *et al.*, 2001), with the arrows and labels showing the locations of the two dozen major identified volcanoes on the planet. Arrow orientation and size is not coded to anything. All volcanoes except those southeast of Hellas Basin were analyzed.

much consistency when looking at absolute ages at the 10-100 Myr precision level. This limits their utility in providing a timeline for volcanism on the planet. In this work, we were able to date 93 calderas within 20 volcanoes using a uniform, high-resolution dataset, and all the crater counting was done by a single person; the four volcanoes southeast of the Hellas impact basin (Amphitrites, Malea, Peneus, and Pityusa Paterae) have inadequate CTX coverage for this approach as of May 2010 and were not analyzed. We use these data to (a) confirm previous results of continuous volcanism throughout Mars' history until the recent past, (b) argue for dwindling and increasingly localized volcanism through time, (c) discuss the implications of the ages for the eruptive history of the Tharsis region, (d) provide a transition time from explosive to effusive volcanism, and (e) explore ancillary issues of secondary cratering and resurfacing rates.

We discuss our methods of mapping the main volcanic calderas on Mars and crater-age dating in Section 5.2. Sections 5.3-5.7 are devoted to our analysis and results for each volcano with each section describing a different province: Tharsis (Section 5.3), Syrtis Major (Section 5.4) and Elysium (Section 5.5) regions, Apollinaris Mons (Section 5.6), and the volcanoes surrounding Hellas Basin (Section 5.7). We then use these results to discuss implications for secondary cratering and resurfacing in Section 5.8, and finally the implications for the most recent volcanism in various regions of the planet in Section 5.9. We list the areas of calderas and number of craters identified in Table **8**, and we summarize our age results in Table **9**.

5.2. Method

5.2.1. Image Processing

We obtained the highest resolution visible images available with the widest coverage from a single source, the CTX dataset (Malin *et al.*, 2007) from the MRO spacecraft. This instrument records grayscale images of the Martian surface at resolutions in the range ~5.5-7.5 meters per pixel (m/pix) that are publicly available through NASA's online Planetary Data Systems (PDS) website (http://pds-imaging.jpl.nasa.gov/). We obtained the best images in terms of data quality and with the most complete coverage available for our study areas as of May

2010.

The images were processed using the United States Geological Survey's (USGS's) Integrated Software for Imagers and Spectrometers (ISIS) v 3.1 software. They were mosaicked together, projected to a standard equicylindrical spheroid, and output at a final, uniform resolution that was slightly down-sampled from the original to 10 m/pix. This was done to limit the final file sizes to a few hundred MB to make it easier to work with on modern workstations while still having enough resolution to accurately identify $D \geq 50$ m craters. The mosaics for each volcano were then imported to ESRI's ArcGIS software and the projection was confirmed by using the THEMIS Daytime IR global mosaics (Christensen *et al.*, 2004) as a base map.

5.2.2. Geomorphologic Mapping

Geomorphologic mapping was performed for all the studied volcanic summits. Map units were digitally drafted in a GIS environment using standard photogeologic techniques (*i.e.*, Tanaka *et al.*, 2005; Hare *et al.*, 2009). The geomorphologic-based interpretation of the volcanic features mainly relied on the CTX image mosaic base map and MOLA gridded topography (463 m/pix at equator). High resolution images (*e.g.* MOC, HiRISE, etc.) and topography (*e.g.* HRSC DEMs) were consulted in the cases of ambiguous contacts at CTX and MOLA scales, respectively. A combination of different criteria, including textural, morphological, topographic, and thermophysical properties (Putzig and Mellon, 2007), were used to differentiate the map units. Particularly, (a) textural/albedo pattern changes (*e.g.* smooth vs. rugged, or dark vs. bright surfaces), (b) morphologies such as scarps, terraces, and wrinkle ridges, and (c) topographic structures like circular collapsed areas and/or raised blocks throughout the main calderas of the volcanic complexes were used to distinguish several possible nested calderas.

We used a liberal approach discriminating as many subunits as possible. On one hand, this is against the general indications regarding mapping volcanic units on Mars. In fact, Tanaka *et al.* (2009) suggested that division of volcanic units on Mars is justified only for the clearest cases of distinctive primary characteristics. On the other hand, our speculative approach is

aimed at providing a detailed reconstruction of the sequence of volcanic events within each of the studied volcanic complexes. Nevertheless, although some of the several possible subcalderas were identified and discriminated based on subtle criteria, the majority of them were mapped based on conservative and characteristic temporal evidence such as stratigraphic superposition relationships, and tectonic, topographic structures, and/or erosional features suggesting modification of one specific unit but not the adjacent terrain. We show our caldera delineation in Figs. **45** and **46**.

Moreover, while we performed separate crater counts for each caldera mapped, we considered these speculative and a few were later combined for the final analysis discussed in Sections 5.3-5.7. There were occasional issues with mapping and our original goal of mapping each individual caldera event was offset by a more pragmatic approach of mapping each possible eruption event; the most obvious cases were Alba Mons (Section 5.3.1, Fig. **45**a) and Uranius Mons (Section 5.3.11, Fig. **45**k). Finally, all the surficial materials clearly superposed on the studied calderas as a result of relatively young resurfacing events were excluded from the final mapped units and thus not considered during the crater counting. These include any inferred glacial deposits and rock glaciers, alluvial materials, aeolian features, landslides, and significant crater ejecta blankets superimposed on the caldera units.

The schema in caldera numbering within each volcanic summit was based primarily on the caldera with the lowest elevation being numbered "1," second-lowest "2," etc. If it was not obvious at a glance as to what caldera was lower than another, then calderas were numbered subsequently from the closest to caldera 1 and outwards (*e.g.*, the closest would be caldera 2, next caldera 3, etc.). This is apparent in the mapping of Albor Tholus. Otherwise, in cases where elevation was not readily apparent, calderas were numbered in a counter-clockwise direction; this was used for example in the numbering of Ascraeus Mons.

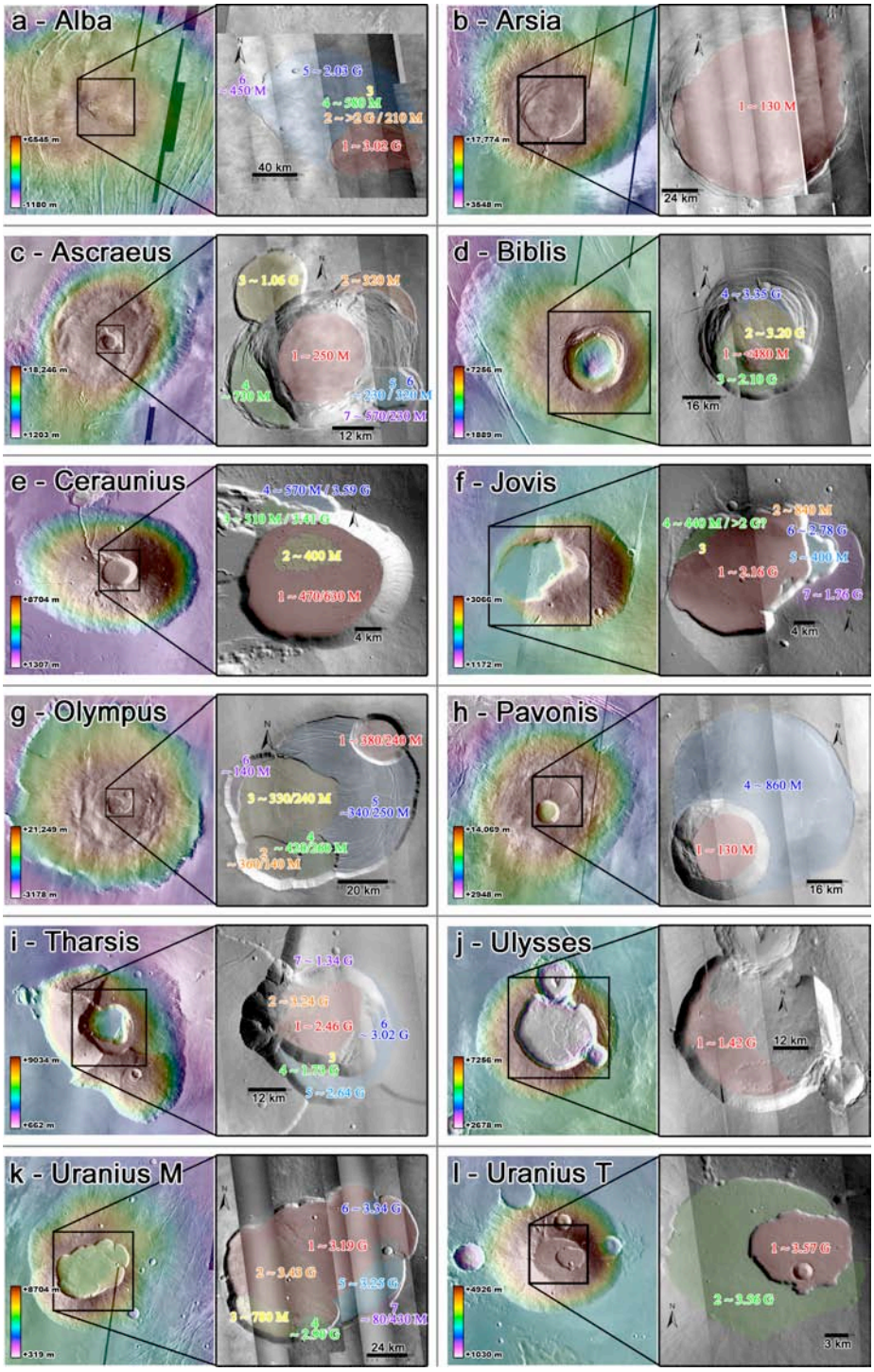

Figure 45: Left panels from each pair shows MOLA altimetry color-coded map with THEMIS (THermal EMission Imaging Spectrometer) Daytime IR underlaid for context, showing the entire volcano that we studied. Colored and labeled regions correspond to the different calderas that we identified on each summit. Call-out boxes indicate ages that we calculated, but due to readability, uncertainties are only included in the text. Volcanoes in this figure are Alba Mons (a), Arsia Mons (b), Ascraeus Mons (c), Biblis Tholus (d), Ceraunius Tholus (e), Jovis Tholus (f), Olympus Mons (g), Pavonis Mons (h), Tharsis Tholus (i), Ulysses Patera (j), Uranius Mons (k), and Uranius Tholus (l). These are the twelve Tharsis province volcanoes that we studied in Section 5.3.

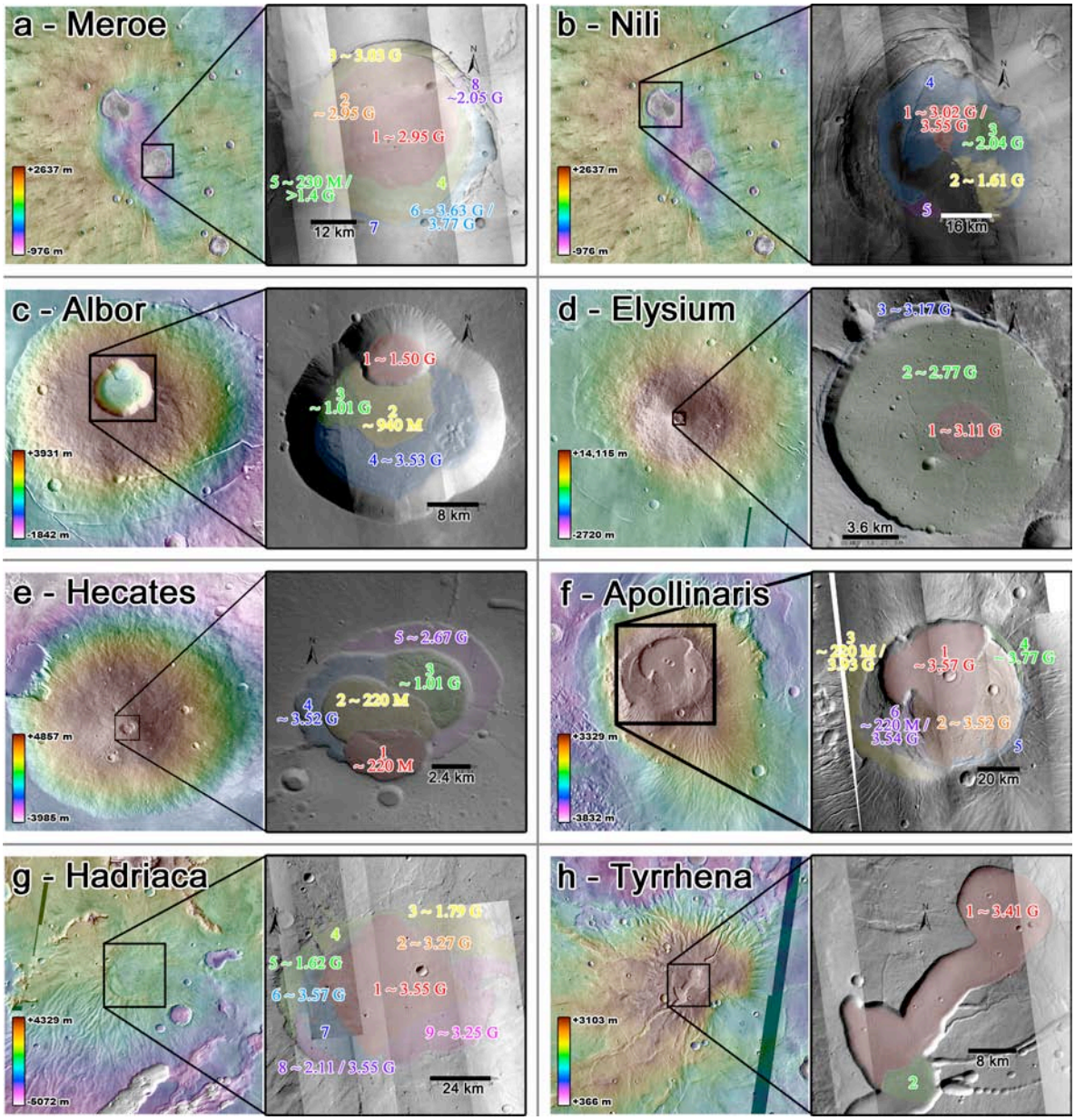

Figure 46: Left panels from each pair shows MOLA altimetry-color-coded map with THEMIS Daytime IR underlaid for context, showing the entire volcano that we studied. Colored and labeled regions correspond to the different calderas that we identified on each summit. Call-out boxes indicate ages that we calculated, but due to readability, uncertainties are only included in the text. Volcanoes in this figure are Meroe Patera (a), Nili Patera (b), Albor Tholus (c), Elysium Mons (d), Hecates Tholus (e), Apollinaris Mons (f), Hadriaca Mons (g), and Tyrrhena Mons (h). These are the two Syrtis Major calderas (a-b) discussed in Section 5.4, the three Elysium province volcanoes (c-e) discussed in Section 5.5, the lone Apollinaris discussed in Section 5.6, and the two northwest Hellas Basin volcanoes (g-h) discussed in Section 5.7.

5.2.3. Crater Counting

In ArcGIS, craters were visually identified within each caldera with the base CTX map over-sampled to a scale of 1:10,000 on-screen. Exogenic craters (from extra-planetary impactors) were differentiated from endogenic craters (such as collapse pits) by general standard morphologic characteristics, such as a raised rim and the steepness of the crater walls, while special care was given to craters lying within, on, or near any extensional features or potential collapsed lava tube features. Very tight clusters of craters that displayed near-vertical walls and flat floors were also treated as endogenic due to their probable sublimation-collapse origin and lack of exogenic impact crater characteristics (see Fig. **47**). Crater rims were outlined using ArcGIS's Editing Tools by laying down one vertex every 25 m. The combination of oversampling visually (viewing one pixel on the map as more than one pixel on the screen) and undersampling in outlining (creating one vertex for every ~2.5 pixels as opposed to every pixel) helped to reduce errors in outlining rims and reduce the time necessary for this task due to a decreased need for higher precision manual dexterity. Vertices were recorded in decimal degrees. The polygons representing each crater rim were then imported into Igor Pro software where we used an in-house non-linear least-squares (NLLS) fitting algorithm to a circle to determine the center latitude and longitude of each crater as well as its diameter.

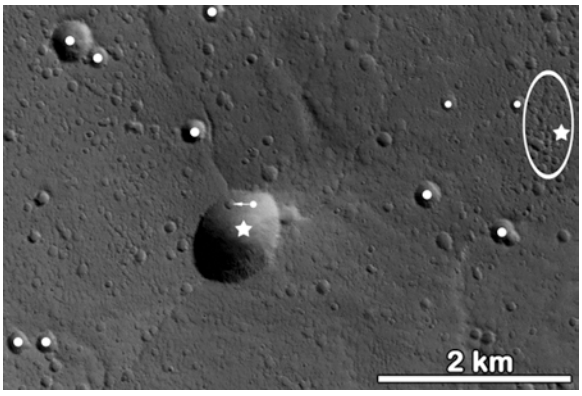

Figure 47: This is a small region within the Elysium Mons caldera (caldera 2) that illustrates two different types of endogenic craters as well as several exogenic craters. Probable endogenic craters are indicated with a star (the largest crater visible, and the region of craters within the open ellipse). These illustrate the kinds of morphologies more common to endogenic craters discussed in the text. Filled circles indicate some of the larger exogenic craters we identified due to their standard morphologic properties (see text for discussion, Section 5.2.4).

The NLLS algorithm corrects for map projection by converting the decimal degrees into meters from the polygon's centroid, accounting for the first-order spherical surface of Mars. Although this is a minor correction for craters on the hectometer scale, nonetheless it would noticeably affect fitted diameters of craters at latitudes larger than ~±30° (*e.g.*, Alba Mons). Similarly, the polygons representing volcanic calderas were imported into Igor Pro and the area was calculated using a standard geometric method after applying the afore-mentioned map projection correction. The areas for each volcanic caldera and the number of craters identified within it are shown in Table **8**.

5.2.4. Size-Frequency Diagrams and Isochron-Fitting

After crater rims were analyzed and diameters calculated, standard crater size-frequency diagrams (SFDs) were created (Arvidson *et al.*, 1979) with slight modifications, as detailed in this sub-section. These were done by binning data in multiplicative $2^{1/32}D$ intervals. Finer binning than the more standard $2^{1/2}D$ was used to bring out detail in the SFDs that would otherwise be obscured as well as to give the appearance of more continuous data given the number of craters in this study (Table **8**). Craters were placed into bins such that $D_{\text{bin}-1} < D_{\text{crater}} \leq D_{\text{bin}}$. This is effectively a ceiling function (rounds up) that places all craters in a diameter bin that is the largest crater size in that bin. If the distribution of craters were even across all diameters, then a simple average $\bar{D}_{\text{bin}_a} = \left(D_{\text{bin}_a} + D_{\text{bin}_{a-1}}\right)/2$ would suffice to place the bin diameters where they should be once binning is completed.

However, crater SFDs generally follow a $b = -2$ power law. This can be accounted for following Tanaka (1982):

$$\bar{D} = \frac{\int_{D_a}^{D_{a-1}} D \; dN_c}{\int_{D_a}^{D_{a-1}} dN_c} = \frac{3}{2}\frac{D_a^{-2} - D_{a-1}^{-2}}{D_a^{-3} - D_{a-1}^{-3}} \tag{6}$$

Unfortunately, this correction is still inaccurate because it assumes a fixed slope, and rarely did our SFDs follow that power law (*e.g.*, Figs. **48** and **49**). Rather, we factored in the local slope between the bin in question and the next-smallest in order to shift the diameter to a

Table 8: Area of calderas and number of identified craters of all volcanoes (first line km^2, second line number of craters counted) - Total area: 51,545 km^2

Volcano	1	2	3	4	5	6	7	8	9	Total
Alba	2,210^p	354^e	10.8^e	51.4^e	7,010^e	325^e				9,966
	3,140	170	29	79	3534	438				7,390
Albor	35.5^e	104^e	237^e	55.3^e						432
	221	154	100	505						980
Apollinaris	1,530^e	1,420^e	583^p	93.2^p	164^p	109^p				3,898
	6,293	4,455	755	388	582	370				12,843
Arsia	9,840^e									9,837
	39,674									39,674
Ascraeus	508^e	107^e	274^e	196^e	74.2^e	8.02^e	35.7^e			1,203
	1,683	706	3,177	1,526	203	25	307			7,627
Biblis	65.9^e	528^e	449^e	58.2^e						1,101
	13	232	242	22						509
Ceraunius	237^e	39.6^e	13.9^p	18.8^p						310
	1,279	217	118	181						1,795
Elysium	10.4^p	144^p	12.0^p							167
	301	2,985	212							3,498
Hadriaca	1,600^p	88.1^p	433^p	195^p	224^p	80.5^p	360^p	154^p	738^p	3,874
	4,721	388	1,424	659	451	160	1,576	391	2,009	11,779
Hecates	10.9^e	14.8^e	12.1^e	10.3^e	18.3^e					66.4
	6	24	23	34	58					145
Jovis	423^e	6.34^e	1.12^e	27.7^e	28.8^e	11.6^p	123^p			621
	791	17	6	41	54	23	234			1,166
Meroe	539^e	443^e	361^e	275^e	27.7^e	165^e	14.4^e	10.9^e		1,836
	756	634	472	547	17	214	27	23		2,690
Nili	121^e	204^e	138^e	939^e	47.7^e					1,452
	202	303	374	1,889	61					2,829
Olympus	218^e	238^e	945^e	240^e	1,590^e	77.3^e				3,308
	1,307	920	3,963	1,240	8,115	246				15,791
Pavonis	678^e	0.612^e	10.3^e	4,200^e						4,335
	951			7,314						8,265
Tharsis	312^e	148^e	9.29^e	14.8^e	101^e	224^p	14.4^e			884
	463	331	13	35	117	161	23			1,143
Tyrrhena	389^p	44.6^p								434
	2,028	177								2,205
Ulysses	701^e									701
	737									737
Uranius M.*	1,680^e	857^e	130^e	136^e	339^e	24.9^e	16.1^e			3,183*
	7,058	2,740	323	329	519	155	24			11,148
Uranius T.	88.4^e	261^p								349
	204	706								910

* Due to poor CTX data, only ~50% of Uranius Mons was analyzable. Actual areas for the calderas are: 3410, 1340, 486, 136, 755, 88.4, and 52.4 km^2, for a total area of 6,259 km^2.

^{p} Denotes a caldera with volcanism that was primarily explosive/pyroclastic.

^{e} Denotes a caldera with volcanism that was primarily effusive.

more robust weighted mean; this has a side-effect of having bins that are not evenly spaced in log(*D*):

$$D_a = \frac{D_a - D_{a-1}}{1 + N(D_{a-1})/N(D_a)} + D_{a-1} \quad (7)$$

where $N(D_a)$ is the number of craters at diameter bin D_a. While this is a better approximation than Tanaka (1982), it is not a substitute for ever-finer binning resolution.

With the incremental SFD created, we coded an additional three options into our SFD algorithm. The first removes the largest bins with too few craters – we set this cut-off at less than three craters in a cumulative bin to eliminate some issues with small-number statistics. The second option removes incremental bins that had no craters within them, effectively no new information. That is why there is a lack of data at some diameter locations in many of our SFDs (Figs. **48** and **49**). The final option removes diameter bins smaller than our statistical completeness. For this purpose, we defined statistical completeness as the incremental bin with the greatest number of craters. Error bars were calculated by standard $\sqrt{N}$ Poisson statistics (Arvidson *et al.*, 1979).

Once these operations were performed, the incremental SFDs were integrated to yield a cumulative SFD. All SFDs in this paper are cumulative. SFDs were then scaled by the caldera area, and we show them for the volcanoes we studied in Figs. **48** and **49** (higher resolution versions of each panel in Figs. **48** and **49** are available in online supplemental material).

Isochrons are based on the method of Ivanov (2001) and Neukum *et al.* (2001) that used pristine surfaces based on imagery at the time to derive the isochrons (see also Neukum and Hiller, 1981). This system was used instead of the Hartmann (2005) method because all comparison results in this work made use of the Neukum technique, and we wanted to provide the most direct comparison. A 1 Ga isochron is created from an 11^{th}-order polynomial production function for Mars, based on lunar crater counts and absolute ages. Another function calculates how the 1-km point should be scaled based upon the impact flux through time based on scaling from Apollo sample return calibration of the lunar isochrons. Isochron shape does not

change based on age, only the crater density (vertical offset in our plots).

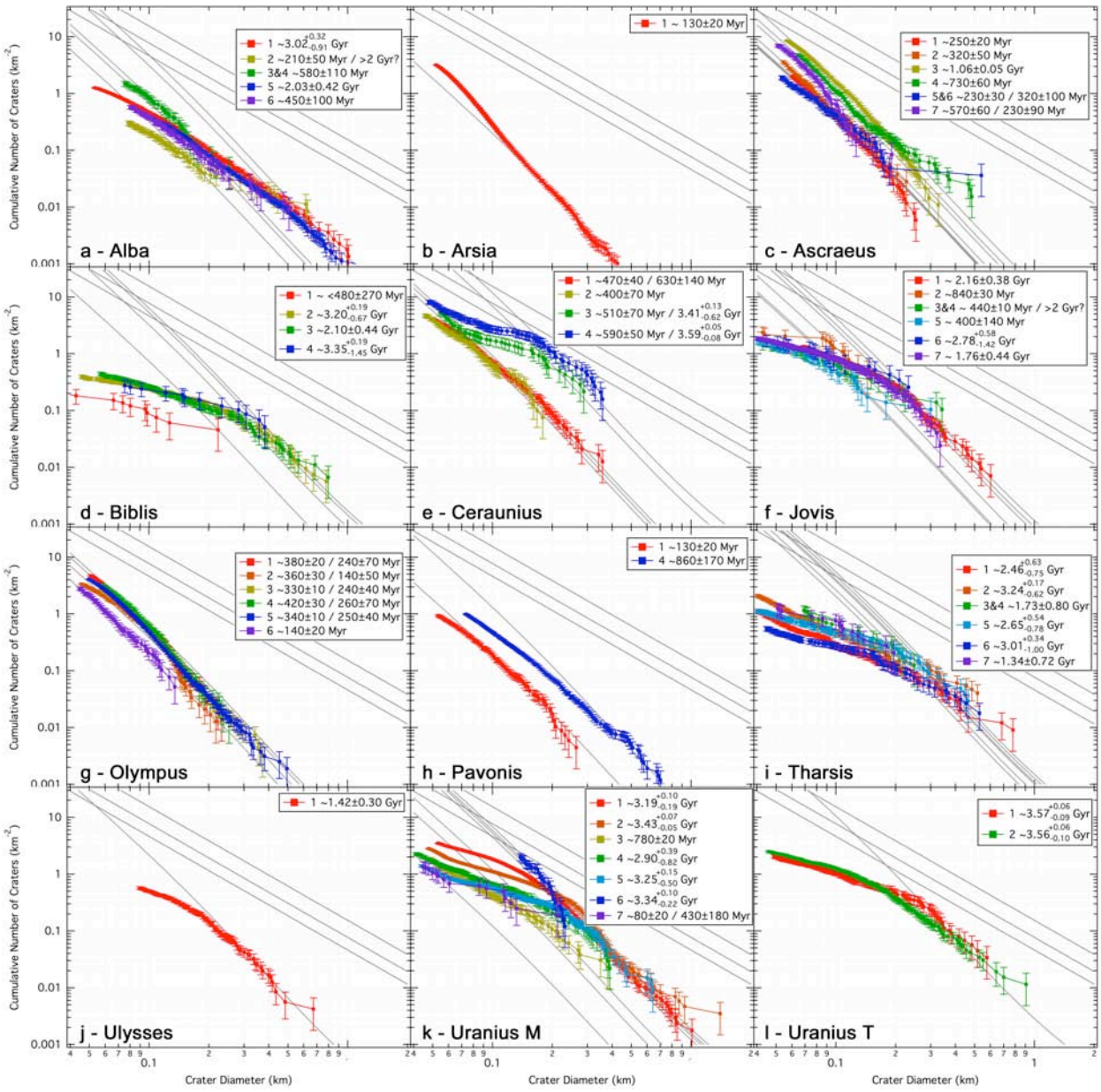

Figure 48: Size-frequency distributions for the Tharsis volcanoes in the same order as Fig. **45**: Alba Mons (a), Arsia Mons (b), Ascraeus Mons (c), Biblis Tholus (d), Ceraunius Tholus (e), Jovis Tholus (f), Olympus Mons (g), Pavonis Mons (h), Tharsis Tholus (i), Ulysses Patera (j), Uranius Mons (k), and Uranius Tholus (l). Colors on SFDs correspond to the colors used in the Fig. **45** for each volcano such that, for example, the red curve corresponds to caldera 1 in all cases. Steep diagonal grey lines are the isochrons for ages found in the legends of each panel. Shallow diagonal grey lines represent 10%, 5%, and 3% of geometric saturation based on the standard $1.54D^{-2}$ value for geometric saturation (Melosh, 1989). Larger versions of each volcano's caldera SFD are available in supplementary material online.

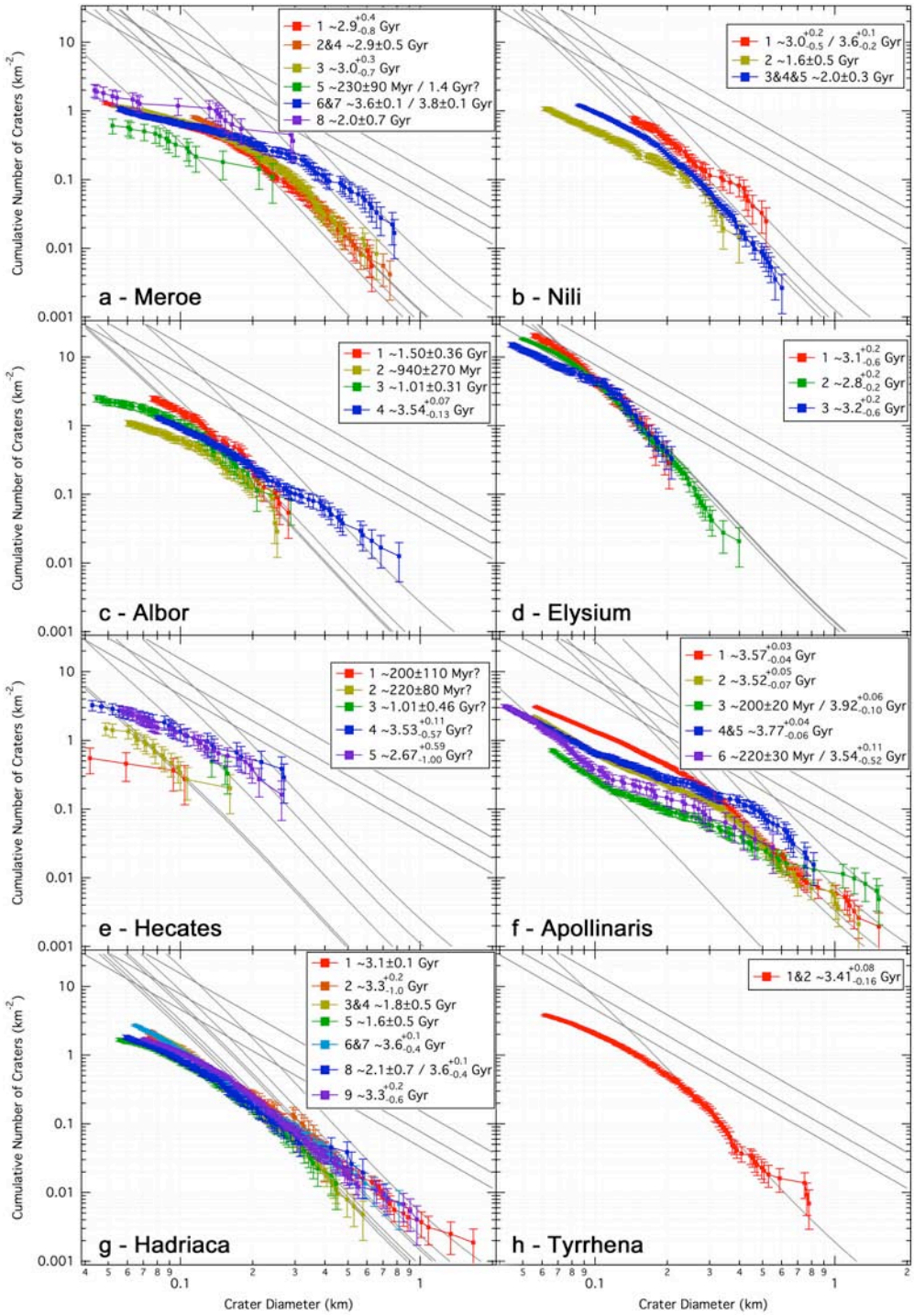

Figure 49: Size-frequency distributions for the non-Tharsis volcanoes in the same order as Fig. **46**: Meroe Patera (a), Nili Patera (b), Albor Tholus (c), Elysium Mons (d), Hecates Tholus (e), Apollinaris Mons (f), Hadriaca Mons (g), and Tyrrhena Mons (h). Colors on SFDs correspond to the colors used in Fig. **46** for each volcano such that, for example, the red curve corresponds to caldera 1 in all cases. Steep diagonal grey lines are the isochrons for ages found in the legends of each panel. Shallow diagonal grey lines represent 10%, 5%, and 3% of geometric saturation based on the standard $1.54D^{-2}$ value for geometric saturation (Melosh, 1989). Larger versions of each volcano's caldera SFD are available in supplementary material online.

To fit our data to an isochron, we used a range of diameters rather than relying upon a perhaps more standard $N(1)$ age. $N(1)$ ages proved insufficient for our study due to (a) the calderas rarely having craters as large as 1 km, and (b) the SFDs rarely falling on the same isochron at 1 km as at 100 m. We selected diameter ranges that paralleled the isochron function; other diameter ranges that did not were assumed to be affected by weathering (erosion, infilling, etc.), incomplete counts (for D<50-70 m), contamination by secondaries, or other non-age-related issues. Since our objective was to determine ages, we simply needed to find a range of diameters that fit the established isochrons. We created an algorithm to calculate the average difference between the SFD points and the model 1 Ga isochron, weighting each point the same. Using the time scaling function discussed above, we then determined the age that best fit our selected diameter range.

We determined uncertainties in our ages by taking our formal $\sqrt{N}$ error bars at each diameter bin used in the fitting and first adding them to the SFD data point. We then calculated the best-fit isochron for the new SFD. Third, we subtracted the error from the original SFD points and calculated the best-fit isochron. The original model isochron age was then subtracted from these new fitted ages to estimate the plus/minus uncertainties in each determined age. Due to the nature of the time scaling function, ages younger than ~2.5 Gyr have symmetric uncertainties. Older ones generally have larger negative uncertainties than positive.

In addition to isochrons on our SFD plots, we show 10%, 5%, and 3% lines of geometric saturation, where geometric saturation is defined by a surface having enough craters such that the creation of a new one will eliminate an equivalent existing one (Melosh, 1989). The equation for geometric saturation, $1.54D^{-2}$, has a shallower slope than isochrons and hence saturation occurs for younger ages at smaller crater sizes. One hundred percent geometric saturation does not exist on real planetary surfaces, and they generally saturate at only a few percent of geometric values. Consequently, we show various fractions since a surface may be empirically saturated at some smaller fraction of geometric saturation; in our work, we found some cases of saturation in the range 1-4% of geometric.

We note that the martian isochrons are constrained by correlating lunar crater ages with Apollo sample return absolute ages and then extrapolating to Mars based on its surface gravity, proximity to the asteroid belt, impactor velocities at ~1.4 A.U., and other scaling differences (Ivanov, 2001), but there is no absolute age dating that can yet be done for Martian samples from a known location and geologic unit. Consequently, estimates of crater model ages for Mars are estimated at present to be within a factor of ~2 (Neukum *et al.*, 2004; Hartmann, 2005). While we quote ages in this paper to the 10 Myr and our main literature comparison (Werner, 2009) quotes ages to the 1 Myr level, we realize that the inherent uncertainties in the isochrons are larger than this in every case. However, assuming similar geologic and environmental environments, the relative chronologies from the crater densities are still accurate, and we would fully expect that when absolute measurements can be done, a surface that we date to 150 Ma will be older than one dated to 100 Ma by approximately a factor of 50%. Hence, rounding to the 100 Myr decimal would be counter-productive given the number of craters studied for this work (Table **8**) and for the sake of comparison with other published literature.

5.3. Tharsis Region

The Tharsis region of Mars is the largest topographic feature on the planet. It is a vast volcanic province that covers roughly 25% of the planet's surface. Its margin is roughly circular, with an approximate diameter of 3500 km. The origin of the uplift is considered to be volcanic (*e.g.*, Solomon *et al.*, 2005), though the magmatic source and Tharsis' original location has been debated (Zhong, 2009). Twelve large volcanic constructs cover Tharsis, with five major volcanoes (Alba Mons, Olympus Mons, Ascraeus Mons, Pavonis Mons, and Arsia Mons), and seven smaller ones (Ceraunius Tholus, Uranius Mons, Uranius Tholus, Tharsis Tholus, Jovis Tholus, Biblis Tholus, and Ulysses Tholus). Most of these show an effusive type of volcanism, though notably Alba Mons and Uranius Tholus show evidence of explosive styles; we discuss this further in Section 5.9. We have analyzed all of these volcanoes through the method described in Section 5.2. Our modeled crater-count ages are presented below, alphabetically, for

these twelve volcanoes. The volcanoes are shown in Fig. **45** and their isochrons in Fig. **48** (higher resolution individual panels of Fig. **48** are available in online supplemental material).

5.3.1. Alba Mons

Alba Mons is a giant shield volcano that covers the largest area by a single volcano on the planet, its footprint approximated as an ellipse roughly 1500 by 1000 km. The center is located at 40°N, 250°E, and it is the northernmost large volcano on the planet. Its volume is difficult to measure due to its large area and estimates in subtracting out a basal layer, but previous researchers have estimated it at $\sim 2.5 \cdot 10^6$ km^3 (Ivanov and Head, 2006), making it the largest volcano on Mars by volume (Olympus Mons is roughly $\sim 1.7 \cdot 10^6$ km^3 in contrast). Alba's summit has one of the most complicated caldera complexes on the planet. After Cattermole and Reid (1984), we identified well over a dozen potential calderas, but we only mapped six separate ones on the summit (Fig. **45**a) that represent uniformly-aged surfaces, illustrating our more pragmatic approach. In our final analysis, we combined calderas 3 and 4 due to their small sizes, similar crater ages, and because they are topographically similar. The omission of parts of caldera 5 due to the presence of a probable rock glacier along its southwest walls further illustrates the special considerations we took in our mapping.

Our modeled crater ages of the final calderas are open to some interpretation due to the SFDs failing to parallel isochrons over a large diameter range (Fig. **48**a). For example, caldera 1 parallels the 3.0 Ga isochron between 0.6 and 1.0 km, and it trails to lower ages at smaller diameters; this is assumed to be evidence of resurfacing here and in many of the calderas that we studied. Caldera 5 has a few large craters emplaced within it, and fitting between 500 and 930 m yields a modeled crater age of 2.0 Ga. Caldera 6 has a SFD starting at 2.0 Ga but quickly crossing 1.5 billion years of isochrons to lie on the 450 Ma isochron between 250 and 160 m before it trails off at smaller diameters. For more detailed information, refer to Table **9**. With the inherent uncertainties in the crater statistics, calderas 3/4 and 6 have statistically identical ages, and calderas 1 and 5 are statistically identical. Caldera 2's modeled crater age is

statistically unique among Alba's calderas, at least for the main isochron fit, and we conclude that it is the youngest surface on the summit.

5.3.2. Arsia Mons

Arsia Mons is centered at -8.5°N 239°E and is the southernmost of the three Tharsis Montes which also include Pavonis and Ascraeus Mons. Arsia rises ~12 km above the surrounding surface and 17.5 km above the martian datum. It has an average diameter of 300-400 km and possesses the largest single caldera of any volcano on Mars with a diameter ~90-110 km and an area just under 10,000 km^2 (Table **8**). Geomorphologic mapping of the Arsia caldera was straightforward. The only region of uncertainty was toward the northeast where the youngest lava overflowed and continued beyond the crater rim. The extent of this northeastern buried margin was defined by extrapolation of the caldera's circular planform, as shown in Fig. **45**b. Only regions within this inferred margin were included in the subsequent counts.

Arsia is not only the largest but also one of the youngest calderas that we were able to age-date. Using a crater diameter range of 144-615 m, we date the caldera to 130±20 Ma (Fig. **48**b). This is statistically consistent with previous works by Neukum *et al.* (2004) and Werner (2009) who calculate 130 and 128 Ma, respectively, with approximately ±20% (~±26 Myr) uncertainty.

An additional feature within the large Arsia caldera is the presence of secondary crater fields. While most secondaries with classic morphology are within a few crater diameters of a large primary, no primary large enough exists in the vicinity of Arsia's caldera. These fields of secondaries (an example is shown in Fig. **50**) are plentiful and act to increase the slope on our SFD for craters smaller than ~130 m. The SFD does parallel the 280 Ma isochron between ~55-70 m, but we interpret this decreased density as the result of incompleteness in our counts rather than a second age for the surface. In this case, Arsia appears to be a case study for large and numerous fields of secondary craters without an obvious nearby primary to form them, as found previously on Europa by Bierhaus *et al.* (2005) and Mars by McEwen *et al.* (2005), and

Table 9: Modeled crater ages for each caldera with diameter range (first line, meters) and derived age (second line)

Volcano	1	2	3	4	5	6	7	8	9
Alba	600-1000	~800 / 147-180	–	110-150	500-930	160-250			
	$3.02^{+0.32}_{-0.91}$ G	>2.0 G / 210±50 M		580±110 M	2.03±0.42 G	450±100 M			
Albor	113-282	175-247	126-408	382-474					
	1.50±0.36 G	940±270 M	1.01±0.31 G	$3.53^{+0.07}_{-0.13}$ G					
Apollinaris	342-641	373-699	95-118 / 1079-1525		390-814	66-97 / 416-551			
	$3.57^{+0.03}_{-0.04}$ G	$3.52^{+0.05}_{-0.07}$ G	200±20 M / $3.93^{+0.06}_{-0.10}$ G		$3.77^{+0.04}_{-0.06}$ G	220±30 M / $3.54^{+0.11}_{-0.52}$ G			
Arsia	144-615 130±20 M								
Ascraeus	60-167 250±20 M	58-157 320±50 M	67-129 1.06±0.05 G	66-167 730±60 M	80-93 / 124-187 230±30 / 320±100 M		53-86 / 116-126 570±60 / 230±90 M		
Biblis	222	350-539	288-357	357-381					
	<480±270 M	$3.20^{+0.19}_{-0.67}$ G	2.10±0.44 G	$3.35^{+0.19}_{-1.45}$ G					
Ceraunius	89-121 / 160-247	74-109	55-69 / 157-288	50-58 / 179-227					
	470±40 / 630±140 M	400±70 M	510±70 M / $3.41^{+0.13}_{-0.62}$ G	590±50 M / $3.59^{+0.05}_{-0.08}$ G					
Elysium	102-171	87-237	106-208						
	$3.11^{+0.21}_{-0.57}$ G	$2.77^{+0.20}_{-0.23}$ G	$3.17^{+0.19}_{-0.58}$ G						
Hadriaca	551-888	253-398	258-576	–	227-373	641-814	–	288-314 / 425-576	407-551
	$3.55^{+0.06}_{-0.11}$ G	$3.27^{+0.19}_{-0.98}$ G	1.79±0.45 G	–	1.62±0.46 G	$3.57^{+0.10}_{-0.37}$ G	–	$2.11^{+0.66}_{-0.67}$ / $3.55^{+0.10}_{-0.33}$ G	$3.25^{+0.16}_{-0.57}$ G
Hecates	93-104	70-106	135-157	217-270	187-212				
	200±110 M?	220±80 M?	1.01±0.46 G?	$3.52^{+0.11}_{-0.57}$ G?	$2.67^{+0.59}_{-1.00}$ G?				
Jovis	232-357	89-116	102-113 / 321-342	–	104-144	187-232	183-321		
	2.16±0.38 G	840±300 M	440±110 M / >2 G?	–	400±140 M	$2.78^{+0.58}_{-1.42}$ G	1.76±0.44 G		
Meroe	373-528	270-563	276-474	–	106-116 / 213-242	328-416 / 463-684		141-154	
	$2.95^{+0.35}_{-0.80}$ G	$2.95^{+0.29}_{-0.55}$ G	$3.03^{+0.27}_{-0.66}$ G	–	230±90 M / >1.4 G	$3.63^{+0.04}_{-0.06}$ / $3.77^{+0.05}_{-0.08}$ G		$2.05^{+0.66}_{-0.67}$ G	
Nili	212-264 / 365-516	247-335	237-381	–	–				
	$3.02^{+0.24}_{-0.51}$ / $3.55^{+0.09}_{-0.22}$ G	1.61±0.50 G	2.04±0.25 G	–	–				
Olympus	57-113 / 141-217 380±20 / 240±70 M	97-113 / 144-217 360±30 / 140±50 M	62-104 / 164-253 330±10 / 240±40 M	67-116 / 150-227 420±30 / 260±70 M	57-91 / 154-321 340±10 / 250±40 M	45-111 140±20 M			
Pavonis	83-119	–	–	300-601					

	130±20 M	–	–	860±170 M			
Tharsis	321-463	288-350	191-247	–	258-294	357-425	179-195
	$2.46^{+0.63}_{-0.75}$ G	$3.24^{+0.17}_{-0.62}$ G	1.73±0.80 G	–	$2.64^{+0.54}_{-0.78}$ G	$3.02^{+0.34}_{-1.00}$ G	1.34±0.72 G
Tyrrhena	282-528	–					
	$3.41^{+0.08}_{-0.16}$ G	–					
Ulysses	264-407						
	1.42±0.30 G						
Uranius M.	227-551	237-516	191-217	258-365	300-474	141-195	46-60 / 116-132
	$3.19^{+0.10}_{-0.19}$ G	$3.43^{+0.05}_{-0.07}$ G	780±20 M	$2.90^{+0.39}_{-0.82}$ G	$3.25^{+0.15}_{-0.50}$ G	$3.34^{+0.10}_{-0.22}$ G	80±20 / 430±180 M
Uranius T.	264-381	390-454					
	$3.57^{+0.06}_{-0.09}$ G	$3.56^{+0.06}_{-0.10}$ G					

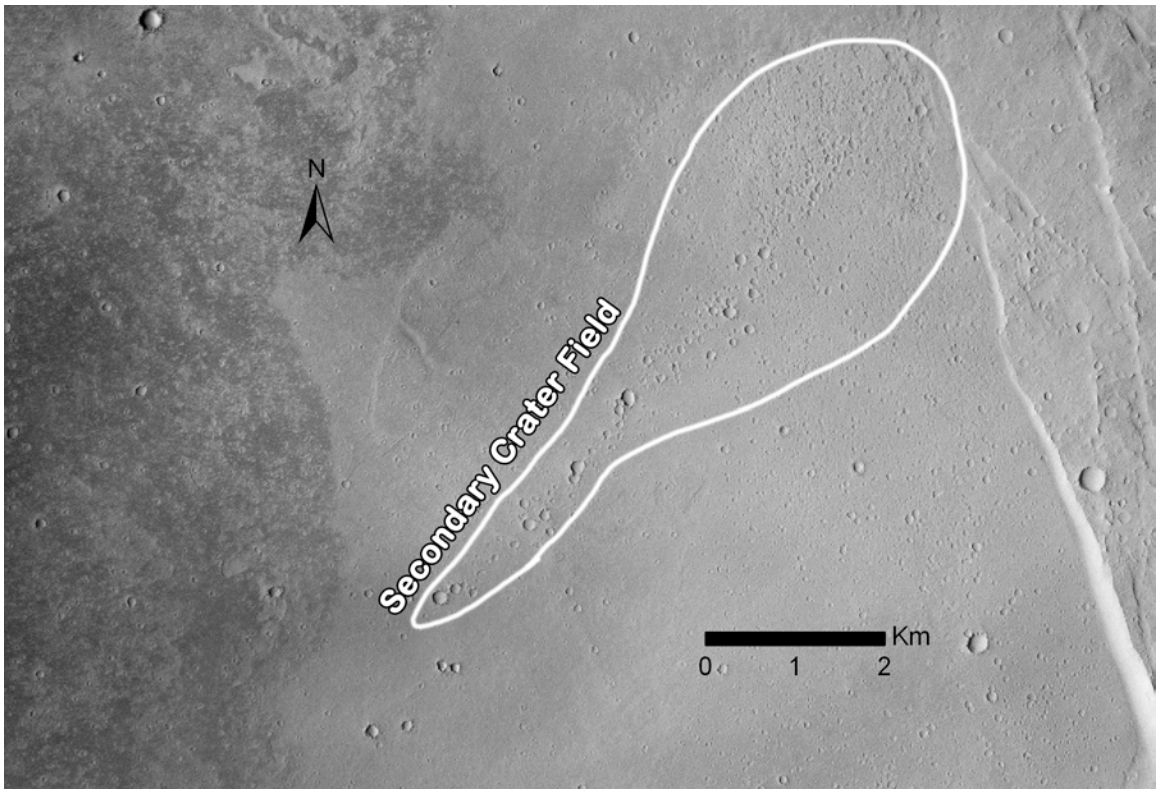

Figure 50: CTX mosaic image of a small section of Arsia Mons' caldera floor. This shows one of the regions containing fields of obvious secondary craters, centered at -119.55° E, -8.77° W, near the eastern edge of the caldera.

summarized by McEwen and Bierhaus (2006). However, we find the onset of secondaries becoming important around 130 m in this case, as indicated by the increasing slope in the SFD from the established isochron. This is far smaller than the ~1 km onset that McEwen and Bierhaus (2006) predicted, and we discuss this further in Section 5.8.

An interesting feature of the Arsia summit caldera is the presence of numerous smaller shield volcanoes and vents that postdate the last main event. These small shields are visible from CTX imagery and MOLA topography and have been recently reported throughout the eastern half of Tharsis by Hauber *et al.* (2009 and references therein). Some dated to approximately 50-100 Ma (Hauber *et al.*, 2010). We also dated one of the vents located at 9.70°S 239.18°E using craters visible in HiRISE (High-Resolution Imaging Science Experiment aboard MRO (McEwen *et al.*, 2007)) image PSP_009343_1700_RED within the Arsia caldera. Our model crater age for

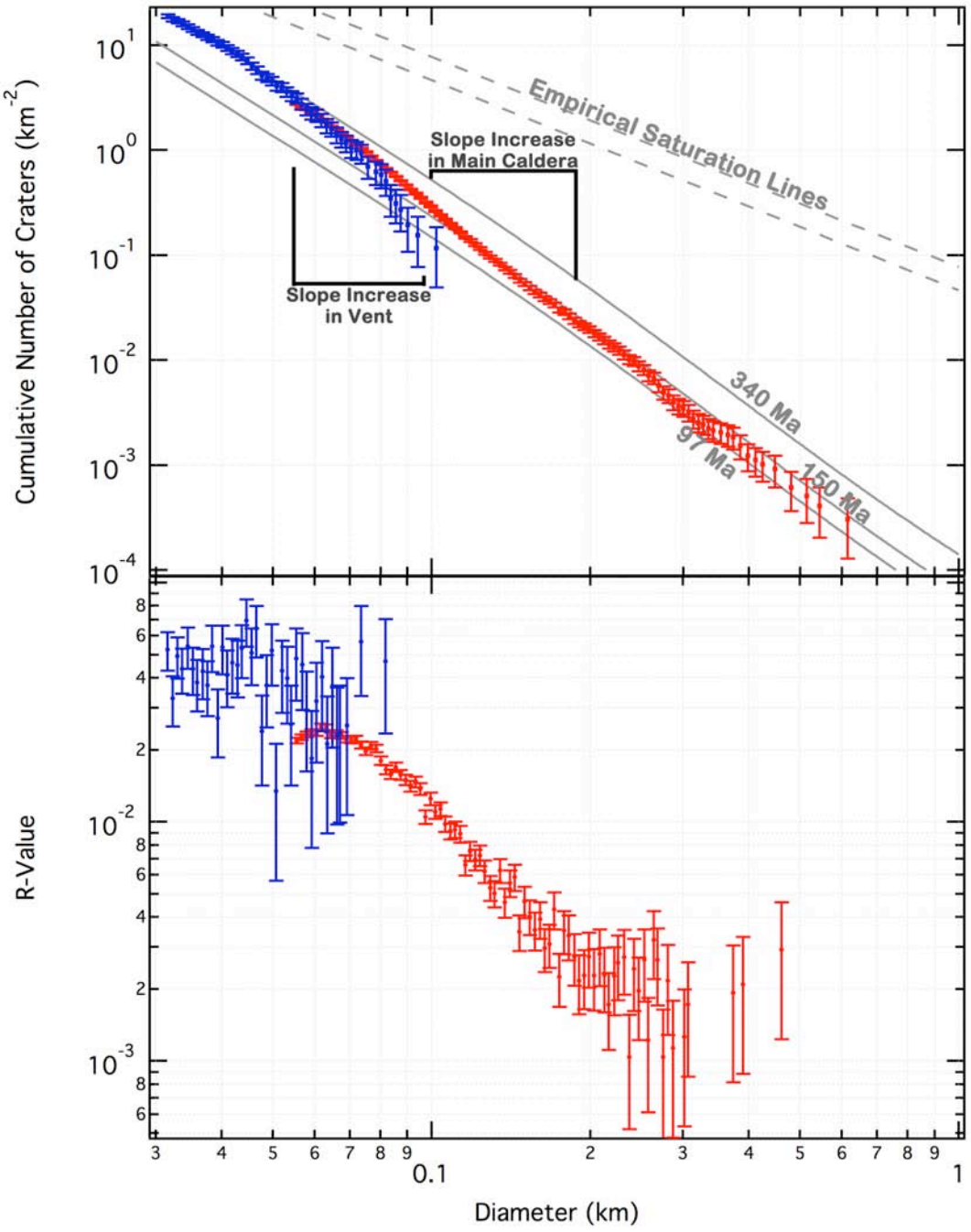

Figure 51: Size-frequency diagram (cumulative, top; R-plot, bottom) illustrating the main caldera of Arsia Mons and the youthful vent that we also dated. The "lower" ages for the two are statistically significant, and we attribute the increase in crater frequency at smaller diameters to be a consequence of secondary cratering (*e.g.*, as illustrated in Fig. **50**) despite them resting on a 350 Ma isochron.

this vent is 97±49 Ma - younger than the overall caldera (Fig. **51**). The reason for the large uncertainties is that we used the largest three size bins - 93-108 m, which had large statistical

uncertainties due to relatively few craters - to date the vent's flows as opposed to the bulk of the SFD. We did this because we noticed a steep increase in slope at smaller diameters of ~50-90 m before the SFD again matched an isochron, which is similar to what we observed in the overall SFD for Arsia's caldera (Fig. **51**). We attribute this enhancement to secondary craters, as discussed above.

5.3.3. Ascraeus Mons

Ascraeus Mons is the northernmost of the three Tharsis Montes, residing at 12°N 255°E. The volcano rises 15 km above the surrounding surface and 18 km above the martian datum surface. It has an average diameter of 350-400 km. The caldera complex of Ascraeus (Fig. **45**c) is characterized by a large, central caldera with an average diameter of ~25 km (total area 508 km^2). It is surrounded by four additional calderas, one each to the northeast, northwest, southeast, and southwest. The southwest caldera (caldera 5 in our mapping) is surrounded by two terraces. Though each terrace was initially thought to be a collapse feature and so should have the same age as each other and the caldera, our crater ages show the upper to be approximately twice as old and statistically distinct from the main floor of caldera 5 for diameters $D < 110$ m ; this was likely missed in previous studies because they were incomplete to the decameter scale. Because the lower terrace and the main caldera 5 had similar ages, we combined them in our final mapping and age determinations. It is still possible these represent collapses of one originally larger caldera, but such an interpretation would need to account for the significantly different ages.

Caldera 1 did not parallel the isochron slopes throughout most of its range, instead having a slope slightly greater than the isochrons (indicating possible contamination by secondary craters) (Fig. **48**c). We were able to fit it between 80-160 meters to the 250 Ma isochron. Caldera 2 was nearly an ideal case, closely matching the 320 Ma isochron throughout its entire extent, 55-225 m. Caldera 3 started on a ~570 Ma isochron at ~300 m diameter craters but it rose to lie on the 1.1 Ga isochron between 67 and 135 meters. Caldera 4 was more ambiguous,

starting at the large diameter (500 m) end around an age of 3.2 Ga, but quickly crossing several billion years of crater density to 730 Ma between 65 and 165 meters. Combined, calderas 5 and 6 have a relatively small area and few craters, but they seem to parallel two distinct isochrons – 320±100 Ma at the larger 120-170 meter range and 230±30 Ma at sizes of 75-90 meters. Finally, the upper terrace, caldera 7, appears to have a younger age at larger crater sizes of 230 Ma, and then an older age of 570 Ma at sizes of 50-80 m. This older age at a larger size is one of three instances (Arsia Mons, this, and Olympus Mons) resulting from probable contamination from undistinguished secondaries. See discussion of Arsia Mons in sections 5.3.2 and 5.8.1.

Our derived crater ages agree with Neukum *et al.* (2004) and Werner (2009) for caldera 4 (the southwestern caldera), for which we estimate the age as 730±60 Ma, Neukum *et al.* (2004) 800 Ma, and Werner (2009) 785 Ma. Within a ±20% uncertainty for the former comparison, these ages are consistent. Otherwise, our ages are consistently older than determined in the other two papers. Caldera 1 is older by a factor of 2.5, caldera 2 a factor of 1.5, and caldera 5 is older by a factor of 2.4; the absolute age differences here are only 100-150 Myr, though. By far, the largest disagreement is caldera 3, the caldera to the northwest. We calculate an age of 1060±50 Ma, while Neukum *et al.* (2004) and Werner (2009) derive an age of approximately 400 Ma. We discuss potential reasons for discrepancies in Section 5.10.

5.3.4. Biblis Tholus

Biblis Tholus is an asymmetric volcano located at 2.5°N 235.5°E. The volcano rises 4 km above the surrounding terrain though the caldera sinks down to a remarkable 5.5 km below the rim. Biblis is a highly asymmetric volcano even after the local topography and likely burying of its eastern flanks are taken into account. Its present-day major axis is 170 km and minor axis is 120 km, and the caldera is located in the eastern third with shallower flanks to the west.

The caldera of Biblis Tholus is somewhat complex, though at first glance it is a simple collapse structure, as shown in Fig. **45**d. The northern walls show evidence of heavy alluvial-

colluvial mass wasting, covering part of the caldera floor and thus confusing crater counts in this region. One of the main features of the caldera is a central collapse feature nearly 10 km across which likely represents the last central vent of primary volcanism for the volcano - a possibility also supported by our derived ages. Topographically, the northern half of the caldera is lower than the southern half, and it also shows textural and graben features not observed in the southern half.

In the SFDs for the calderas of Biblis Tholus, we found one of the most severe cases of resurfacing out of the 20 volcanoes we analyzed (Fig. **48**d). Determining which diameter bins to use to fit isochrons was very difficult and highly subjective. Our method for the main central vent was to use the largest diameter bin that contained 3 or more craters. The resulting age was 480±270 Ma, and we interpret this as a maximum surface age; by "surface age" we are not necessarily indicating formation age, but rather the most recent event to cover it, keeping in mind it sits in a steep topographic low. Calderas 2 and 3 were fit as per Section 5.2.4, which led to model ages $3.20^{+0.19}_{-0.67}$ Ga and 2.10±0.44 Ga, respectively. Statistically, these are the same age, and if one were to choose a different range over which to fit the SFDs, the ages would be closer. Caldera 4 was fit to the two largest diameter size bins that had ≥3 craters, which resulted in a model age of $3.35^{+0.19}_{-1.45}$ Ga. This is also statistically identical to calderas 2 and 3.

If we combine all four calderas into a single surface, we calculate a model age $3.37^{+0.14}_{-0.67}$ Ga when fitting between diameters 500-870 meters. The only comparable research on the caldera of Biblis Tholus that has been published is from Werner (2009), who calculated an age of 3.68 Ga for the entire caldera. This is older than our derived age, though Werner does not provide uncertainties in the published measurements. If we apply a conservative ±10% uncertainty to Werner (2009), then we agree statistically, though we note that Werner's age also includes the volcano's flanks.

5.3.5. Ceraunius Tholus

Ceraunius Tholus is a volcano at 24°N 262.5°E with flanks that are characterized by the

presence of a dense network of fluvial channels arranged in a radial pattern with respect to the volcano's summit, similar to its northern neighbor Uranius Tholus. The structure rises 6.5 km above the surrounding surface and contains three distinct calderas - the upper two elevated about 800 meters above the main central one. The tholus is elliptical, having a major axis ~140 km and minor ~100 km, although the caldera is centrally located, unlike that of the similarly elliptical Biblis Tholus.

We mapped four separate calderas on Ceraunius' summit, as shown in Fig. **45**e. The first is the main collapse caldera. It is uncertain whether the second represents a separate volcanic event based on the mapping, but it has a distinct topography rising above the primary caldera, and its surface roughness is very different. This raised block could be the relic of the volcanic cap broken by the events responsible for the formation of the main caldera. Calderas 3 and 4 are both hemispherical and are to the north of the primary caldera.

Ceraunius Tholus' calderas reveal an archetypal case in interpreting SFDs (Fig. **48**e). Calderas 3 and 4 between diameters ~160-230 m show Hesperian ages of $3.59^{+0.05}_{-0.08}$ Ga for caldera 4 and $3.41^{+0.13}_{-0.62}$ Ga for caldera 3, likely representing distinct eruption events early in Mars' history. We do note that these are statistically distinct, despite the northern margins of calderas 3 and 4 residing along the same arc and having an alternative interpretation that caldera 3 collapsed to a lower elevation than caldera 4 after they formed together; we prefer not to make assumptions about this caldera since its statistical significance could be complicated by small number statistics at the larger diameters we used. However, the interpretation that the two calderas are distinct is bolstered by the fact that caldera 4 lies along ~2-3% of the geometric saturation for diameters 150-300 m; if it is actually saturated, then our derived age is a minimum because further crater accumulation is not possible. At smaller diameters - until about $D < 70$ m - the SFDs are nearly flat, representing a resurfacing event. At smaller diameters, the SFDs again parallel an isochron at nearly identical ages of 590±50 Ma and 510±70 Ma for caldera 4 and 3, respectively.

While calderas 3 and 4 are old, calderas 1 and 2 are much younger. It is possible they

have the same original age and caldera 2 is a deposit within caldera 1 that was placed very soon after activity ceased within caldera 1. We derive a split age of 630±140 Ma for caldera 1 at large diameters 160-250 m and a statistically distinct 470±40 Ma for 100-125 m. Caldera 2 has a model age of 400±70 Ma for diameters 70-110 m. Within the counting statistics, these ages match the age at which calderas 3 and 4 began to re-accumulate craters.

The tholus has several features that suggest calderas 3 and 4 may have held paleolakes that drained into Rahe Crater to the immediate north (Fassett and Head, 2007). Evidence to suggest this includes fluvial drainage channels that emanate from caldera 3 primarily, run down the north face of the tholus after merging into a single channel, and then breach Rahe's wall and terminate in a topographically elevated region of deposits at the mouth of the channel that opens into Rahe crater (Fassett and Head, 2007). The deposits are positioned like a delta, but they are morphologically dissimilar to other identified deltas on the planet (Di Achille and Hynek, 2010).

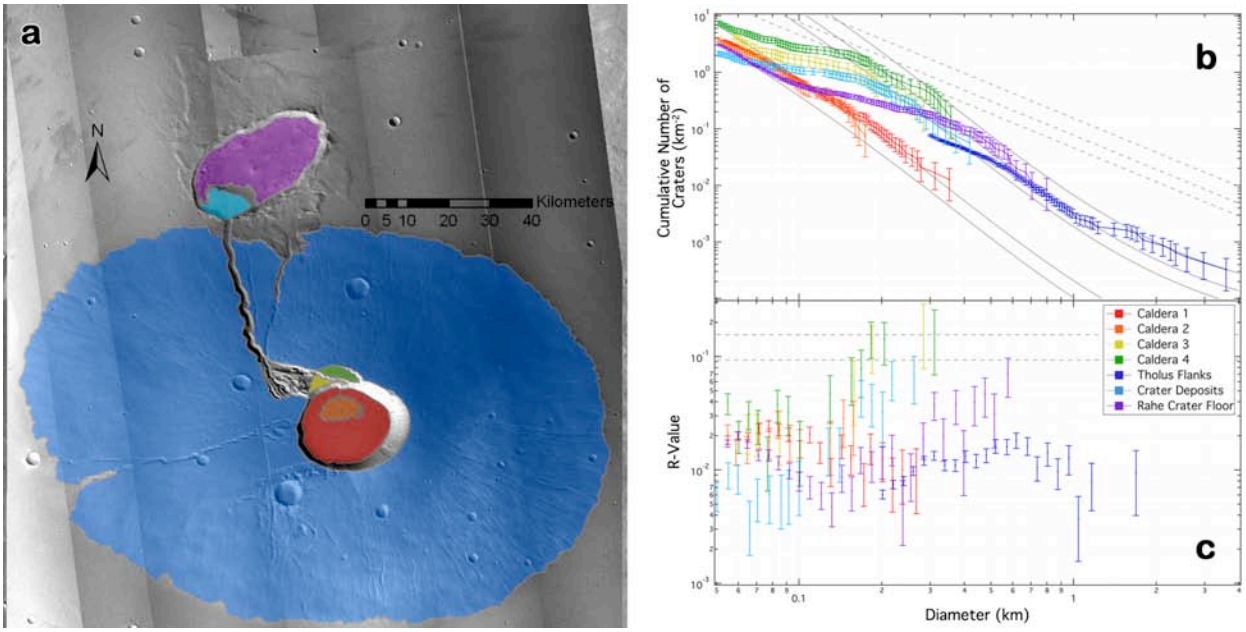

Figure 52: Part (a) shows the geologic mapping and larger context of Ceraunius Tholus, including all mapped regions. Part (b) contains the cumulative SFDs of the four calderas, Rahe Crater, the deposits within the Rahe Crater, and the tholus itself. The channel discussed in the text is not shown in the SFD due to its likely anomalous results that we attribute to billions of years of infilling. Isochrons shown are 0.25, 0.50, 3.4, 3.6, and 3.75 Ga. Due to space considerations, the legend does not contain fitted ages but they are included in the text. Shallower grey lines are 3%, 5%, and 10% geometric saturation. (c) Shows the same as (b) but as an R-plot with coarser $2^{1/8}D$ binning and without the isochrons.

A different plausible interpretation is that they are simple lava deposits, though this would make the paleolake interpretation of Fassett and Head (2007) less likely. However, this would not change the chronology.

We have age-dated the relevant features in support of the chronology of events discussed above - whether the fluvial morphologies are volcanic or aqueous in nature does not change this. We have dated the flanks of Ceraunius by using $1.5 < D < 4$ km craters to $3.75^{+0.06}_{-0.09}$ Ga, though we note that the $0.6 < D < 1$ km range has a well-defined and distinct isochron age of $3.58^{+0.03}_{-0.04}$ Ga (Werner (2009) determined a crater retention age of 3.74 Ga). Both of these are fully consistent with the ages we derived for calderas 3 and 4. We date Rahe Crater to $3.68^{+0.05}_{-0.07}$ Ga, placing it roughly 100-200 Myr older than the surface of calderas 3 and 4, though this is still consistent with our interpretation that we are dating the last volcanic activity from each caldera, and it is also consistent with the older age at larger diameters for the volcano's flanks. The deposits at the base of the channel within Rahe have a model age $3.42^{+0.10}_{-0.32}$ Ga, placing it at statistically the same age as caldera 3 and statistically younger than the crater floor - a good find that helps validate our methods of age dating using small craters over small areas. The narrow channel floor itself was more difficult to date and has a model age of 210±100 Ma. While this is significantly younger, it can be explained by mass wasting within the originally steep channel walls over time even though we only used the floor for crater counts. The floor of Rahe shows the same evidence of erosion as calderas 3 and 4, with its younger age roughly fitting a 260±10 Ma isochron.

In sum, and as illustrated in Fig. **52**, our derived chronology for the Ceraunius Tholus region has most of the volcano built by ~3.75 Ga with Rahe Crater emplaced ~70 Ma later. Caldera 4 was last resurfaced ~3.59 Ga with caldera 3 resurfaced ~180 Ma later. The deposits on the floor of Rahe have an age matching caldera 3's age. The volcano was relatively quiet for the next 3 billion years or it had ongoing but subsequently erased activity, with calderas 1 and 2 showing ages ~400-500 Ma and small-crater resurfacing ages in calderas 3 and 4 just slightly older, ~500-600 Ma.

5.3.6. Jovis Tholus

Jovis Tholus is a volcano centered at 18.5°N 242.5°E. The structure is probably the smallest volcanic tholus on Mars, rising only 2 km above the surrounding surface. It shows a complex collapse structure with the deepest caldera dropping the full 2 km below the highest point. The tholus averages 50 km across. The caldera structure of Jovis is open to interpretation: We mapped out 7 distinct calderas (Fig. **45**f), we later combined calderas 3 and 4. The main caldera 1 empties into the surrounding terrain on its west edge, while 2 through 4 appear to be terraces above it. Calderas 5, 6, and 7 are somewhat distinct, appearing to represent successive stages of volcanism relative to each other, but before the main caldera.

Age dating the different calderas of Jovis was complicated by the small-diameter fall-off seen in the SFDs, often after only the first few larger-diameter bins (Fig. **48**f). The main caldera 1 has the age 2.13±0.38 Ga, by fitting diameters 210-370 m. Calderas 2-6 were less clear, and our estimates range from 400 Ma to 2.78 Ga (see Table **9**). Caldera 7 had a derived crater age of 1.76±0.44 Ga over the 220-320 m diameter range. With the large uncertainties and ill-behaved SFDs, we are hesitant to state these ages with any certainty other than calderas 1, 2, and 7. Overall, caldera 5 does appear to be the youngest based upon the overall cumulative crater density, with the joint 3/4 the second youngest, while caldera 6 is the oldest. Much of the uncertainty is due to the small numbers of craters (as few as 13) found in some of the calderas (see Table **8**).

5.3.7. Olympus Mons

Olympus Mons is aptly named because it is the tallest volcano in the solar system, rising 21 km above Mars' datum and up to 24 km above the surrounding plains. It is the westernmost of the Tharsis volcanoes with its center at 18.5°N, 226°E. The main volcano averages 550 km across, though beyond the high scarps at its present-day margin, material from it extends over 1000 km from the summit. Typically, Olympus Mons has been mapped with five calderas at its summit (*e.g.*, Neukum *et al.*, 2004). Following our liberal mapping, we identified six calderas, splitting one of the middle calderas by following an arcuate ridge, shown in Fig. **45**g.

Nearly all of the SFDs of the calderas on the summit of Olympus Mons represent an interesting case of split ages where the younger age is at larger diameters and the older age is at smaller diameters (Fig. **48**g) (this is one of three cases where we observe this, the other two being Arsia Mons and caldera 7 of Ascraeus Mons). This is likely a feature of secondary cratering combined with erosion and/or incomplete crater identification at small diameters. There is possible evidence for secondary craters in the distribution of craters on the ground, but it is not nearly as conclusive as Arsia Mons' caldera (Fig. **50**).

In general, the ages were fit over diameters ~140-300 m, while the "older ages" (laying on an older isochron) are over ~70-130 m. Because these likely do not represent an actual older age and are the results of secondary crater contamination, we will only quote here the "younger" ages. The figure legend (Fig. **45**g and **48**g) contains both. Caldera 1 dates to 240±70 Ma; caldera 2 140±50 Ma; caldera 3 to 240±40 Ma; caldera 4 260±70 Ma; caldera 5 250±40 Ma. Although workers typically combine calderas 3 and 4 into a single unit, our crater counting statistics point to different ages for each. Finally, caldera 6 has a single age of 140±20 Ma, making it the youngest on Olympus Mons, and it is also the third youngest age that we found (older than Pavonis and Arsia, though all are statistically within each other's uncertainties). We note that over the diameters fit - which was nearly the entire available range - the SFDs were extraordinarily good fits to the isochrons, paralleling them almost exactly with minimal scatter.

Comparable, statistically-identical ages were found by Neukum *et al.* (2004), who found ages that agree with all of our younger ages for every caldera except for caldera 5. For caldera 5, they derived an age of 140 Ma, approximately 60% as old as our younger age for that caldera. Overall, Werner (2009) dated the entire summit caldera complex to 101-215 Ma, which is a reasonable match to Neukum *et al.*'s (2004) average. If we combine all craters from the summit and age-date that, we arrive at an age of 230±30 Ma which is in statistical agreement.

5.3.8. Pavonis Mons

Pavonis Mons is the central of the three Tharsis Montes, situated at 1°N 246.5°E. It rises

9.5 km above the surrounding surface and 14 km above the martian datum. The volcano averages 300-350 km across. Geomorphologic mapping of Pavonis' summit calderas is uncomplicated. There is one large caldera approximately 80-85 km in diameter and another, smaller caldera 30 km across superimposed on its southwest margin (Fig. **45**h). We did not date the two much smaller calderas with a total area 10.9 km^2 located at the northern edge of the main one due to the small area and few craters. One interesting feature of the main caldera is that on its western side it is bounded by a scarp and falls below the surrounding surface, having an obvious rim. On the eastern side, the margin of the caldera is marked by a semicircular convex ridge, rising above the surrounding surface. This is interpreted to be the result of the most recent lava flows overtopping the rim but being viscous enough to maintain a competent flow.

Determining a model age for Pavonis' caldera 1 was straightforward, and we used diameters in the range of 93-200 m to derive an age of 130±20 Ma – tying Arsia as the youngest age of a caldera that we found (Fig. **48**h). Caldera 4 showed more evidence of resurfacing in the down-turn in the SFD for $D < 300$ m. We fit from 300 m to 600 m and derived a model age of 860±170 Ma. The relatively large uncertainty is due to scatter around the isochron at those diameters. Our age for caldera 1 compares reasonably well with Werner (2009), who derived an age of 82 Ma. If we attach a ±20% uncertainty to the quoted age, we nearly agree. Comparison with the older caldera does not agree, where Werner derived an age dating to 367 Ma - less than half our age. In comparing published SFD data and examining crater morphologies, we believe this is due to Werner under-counting the craters in the caldera. This caldera age is one of the largest discrepancies between our work and hers.

5.3.9. Tharsis Tholus

Tharsis Tholus is a small volcano that is the easternmost of the Tharsis edifices, its center located at 13.5°N 269°E. It is relatively small, rising a maximum of 7.5 km above the surrounding surface, with its base averaging approximately 140 km across, though the shape is irregular and does not have a simple footprint. Like Jovis Tholus, the volcano shows significant

signs of collapse with its east-northeastern quarter slumped by over ~3 km, its western fifth similarly collapsed by ~1.5 km, and the deepest caldera dropping approximately 6.5 km below the highest point. Mapping Tharsis Tholus' complex again illustrates our liberal approach, leading to the identification of seven calderas within the summit (Fig. **45**i). Caldera 2 is separated from the first due to the fact it appears to be a newer surface likely as a result of the mass wasting deposits from the western wall. Calderas 3 through 7 are topographically or geographically separated terraces that we cannot obviously link together. However, we did combine calderas 3 and 4 in our final analysis due to their rather small sizes and possible genetic link.

Fitting isochrons to the SFDs for the various calderas was rather difficult as they are nearly flat instead of following the isochron slopes (Fig. **48**i). We attribute the deficit to resurfacing events. We report a few examples and direct the reader to Table **9** for a complete listing: In dating the calderas, we attempted to use the largest few diameter bins for each caldera that approximately paralleled an isochron. Although we provide formal uncertainties per Section 5.2.4, we believe that this is another case where the actual uncertainties are likely larger due to the marked resurfacing evidenced by the SFDs. With those caveats, we fit an age of $2.46^{+0.63}_{-0.75}$ Ga to caldera 1, and $3.24^{+0.17}_{-0.62}$ Ga to caldera 2. Already, geologically we see problems in our age fits because cross-cutting relations indicate caldera 2 overlies 1 as a result of collapse and not volcanism, indicating it should be younger. A possible explanation - besides the uncertainties in the ages actually overlapping - is that caldera 1 collapsed further after 2 formed, erasing many of the craters emplaced on it, and then it began to re-accumulate them. This is somewhat supported in that the largest two bins - craters $D > 600$ m - for caldera 1 indicate an older age than caldera 2. Previous published work for just dating Tharsis Tholus' calderas does not exist, so we cannot turn to those for possible reconciliation.

5.3.10. Ulysses Patera

Ulysses Patera is next to Biblis Tholus, centered at 3°N 238.5°E, and it rises only 1.5 km

above the surrounding surface. The edifice is 95 km across on average. A rather unique feature of this volcano is that the floor drops an impressive 2.5 km below the summit and averages about 1 km below the surrounding surface. The caldera is also one of the largest in diameter relative to the volcano's extent, slightly more than 50% its width.

Mapping the caldera of Ulysses was complicated only by the two relatively large craters superimposed on it with their layered ejecta blankets (Fig. **45**j). The latter were not included in the final mapping and therefore we only considered the region of the caldera not covered by the ejecta. Our analysis (Fig. **48**j) shows some resurfacing at diameters smaller than ~250 m, but the SFD shows no evidence of any contamination by secondaries from the two large craters; this is somewhat expected because we do not anticipate seeing significant secondaries until at least one crater diameter from the rim. We fit an isochron to the caldera that dates it to 1.42±0.30 Ga.

5.3.11. Uranius Mons

Uranius Mons contains the third largest caldera complex on the planet - behind Alba Mons and Arsia Mons - with a caldera complex area of ~6260 km^2. Uranius Mons is located at 26°N 267°E, just east of Uranius Tholus and Ceraunius Tholus. It rises a maximum of 4 km above the surrounding surface, and it averages ~250 km across. The floor drops to only ~200 m above the surrounding surface (~3.8 km below the rim).

Geomorphologic mapping of Uranius Mons was made difficult by the poor data quality of the available CTX imagery (Fig. **45**k). While there is complete CTX coverage of the volcano, just over 50% of the caldera is only covered by very grainy images that have not been re-imaged at the time of this writing (May 2010) and updating (April 2011). This reduced the usable area of Uranius Mons' caldera complex to 3,183 km^2, as reflected in Table **8**. We mapped the region with seven different calderas, the first two segregated by a topographic ridge, and the third and fourth based on textural characteristics. Calderas 5 and 6 are tilted regions raised above the main summit and trending towards the central region of the volcano. The layered ejecta blanket of the large crater embedded in the eastern half was excluded from the final units. Caldera 7 is a

terrace above caldera 5 but below the surrounding rim. We note that, while liberal, this was also a pragmatic approach to mapping similar to Alba Mons, where we did not attempt to trace original caldera margins but instead concentrated on attempting to delineate eruptive events.

Dating Uranius Mons was clear for some calderas and not for others (Fig. **48**k). Of primary interest, calderas 1 and 2, with well constrained model ages of $3.19^{+0.10}_{-0.19}$ Ga and $3.43^{+0.07}_{-0.05}$ Ga, respectively, lie on their respective isochrons with minimal deviation. Caldera 1 shows signs of resurfacing at $D < 150$ m. Caldera 2 shows a possible increase due to secondaries between 250 and 300 m, but below that has significant signs of resurfacing. However, for $D < 60$ m, the SFD changes slope again and appears to nearly parallel a production function. Empirical saturation provides an alternative explanation to resurfacing since the crater population SFD matches 1.4-1.5% of geometric saturation. Using this as an explanation is complicated by the SFD for caldera 6 easily breaching that empirical saturation line. The remaining calderas are more ambiguous, and we list the results in Table **9**.

Werner (2009) also attempted to date the summit caldera complex of Uranius Mons, though Werner dated the entire region as one caldera. The paper's age of 3.7 Ga is older than any of our derived ages, though if we attach a ±15% uncertainty to the estimate we would be in statistical agreement over much of it.

5.3.12. Uranius Tholus

Uranius Tholus is just north of Ceraunius Tholus and west of Uranius Mons; its center is at approximately 26.5°N 262.5°E. It rises 2.5 km above the surrounding plains with an approximate diameter of ~60 km. Its flanks are characterized by several channels radiating from its summit, similar to its southern neighbor, Ceraunius Tholus.

The summit of Uranius Tholus contains two clear nested calderas shown in Fig. **45**l. Their SFDs (Fig. **48**l) show significant evidence of resurfacing at diameters smaller than ~300 m. We date them to statistically identical ages – $3.57^{+0.06}_{-0.09}$ Ga and $3.56^{+0.06}_{-0.10}$ Ga. Due to the closeness in ages, it is likely that the two calderas formed originally from the same eruptive

event, and caldera 1 is a subsequent collapse from the original elevation of caldera 2. The SFD of caldera 1 shows a decrease in slope at diameters smaller than ~300 m, where it is statistically older than caldera 2. This could be due to erosion, but the crater population lies near the 1.4% geometric saturation line so saturation may also play a role. Similarly, caldera 2 shows a decrease in slope that closely matches an empirical saturation of ~1% geometric, and this match is over the 100-300 m diameter range. Attributing the overturn to empirical saturation or to a process that is not volcanic- nor crater-related is not a distinction we can make with this work. Werner (2009) dates both calderas together to be 3.9 Ga, significantly older than this analysis. However, if we attach a conservative 10% uncertainty to the age estimate, then we do statistically agree.

5.4. Syrtis Major

Between Arabia Terra on its west and Isidis Basin on its east, Syrtis Major is a large volcano composed of two main caldera complexes - Meroe Patera to the south and Nili Patera to the north (Figs. **46**a and **46**b). The flows of Syrtis Major roughly date to the Hesperian epoch of Mars, around 3.5 Ga (Tanaka *et al.*, 1988). They overlie Nili Fossae and breach the western rim of Isidis. Syrtis Major has an approximate diameter of 1200 km (~1/3 Tharsis' extent).

The volcanism of Syrtis Major was probably partly explosive, typically characterized by far-reaching flows from the caldera and little topographic difference between caldera floors and their rims. However, the low slopes and long still-visible lava flows emanating from the calderas today indicate that a significant part of it was built effusively. The edifice reaches a maximum elevation of 2 km above Mars' datum. The caldera complex drops to ~500 m above that surface, while the calderas themselves drop an additional 300 m to reside ~200 m above the MOLA datum. This is likely due to a broad collapse into a vast, evacuated magma chamber.

In the next two sub-sections, we derive the ages for Meroe and Nili Paterae (Fig. **49**a and **49**b), and we determine that the surface of Nili Patera post-dates Meroe by up to 1.5 Gyr. We speculate on three possible reasons for this observation. The first is that Nili and Meroe were fed

by a single plume that migrated over time towards the north, shutting off volcanism in Meroe and starting it in Nili. A second possibility is a branching vent fed both Meroe and Nili, and the one under Meroe died out first. A third possible explanation is that there were simply two original vents, the southern one exhausting its magma supply before the northern. It is also possible, although unlikely, that weathering patterns are different over the ~3° distance that separates the two and Nili endured more recent resurfacing than did Meroe.

5.4.1. Meroe Patera

The vent towards the south, Meroe Patera, is centered on 7°N 68.5°E and is more circular than its counterpart to the north. We were very liberal in mapping the caldera, identifying 8 separate events and regions based upon topography and texture. However, after a second look at the mapping and the indications from later-determined ages, we combined both calderas 2/4 and calderas 6/7 into single events for SFD and age-determination purposes.

Even with these combinations, age-dating Meroe's calderas was complicated by the resurfacing and erasure of its smaller craters. Calderas 1 through 4 were relatively easy to date: 1 dates to $2.9^{+0.4}_{-0.8}$ Ga, caldera 2/4 to 2.9±0.5 Ga, and caldera 3 to $3.0^{+0.3}_{-0.7}$ Ga. We note that all of these are statistically identical. Caldera 5 may be as old as 1.4 Gyr based on the largest two diameter bins, but the 230±90 Ma isochron provides the best fit. Calderas 6/7 have a split age, the diameters 500-800 m yielding a 3.8±1 Ga age while diameters 300-400 m show a 3.6±0.1 Ga model age. Caldera 7 spans over 3 Gyr of isochrons, but about half of the bins lie on the 2.0±0.7 Ga isochron with little scatter.

The only comparable work on Meroe's caldera was done by Werner (2009), who found an overall age of 3.73 Ga for the entire caldera complex. Within any reasonable uncertainty on this number (*i.e.*, 5%), we are in statistical agreement.

5.4.2. Nili Patera

Nili Patera, north of Meroe, is a heavily modified caldera that is centered at 9°N 67°E. A significant portion of its southwestern surface is covered by vast, dark dune and ripple fields -

the only such instance in all of the calderas we examined - making mapping somewhat difficult. These aeolian deposits are relatively young and obscure the underlying features, making the determination of their crater ages difficult. We speculate they may be due to weather patterns from the adjacent Isidis Basin (Rafkin and Michaels, 2003).

We initially identified five separate calderas, but we merged calderas 3, 4, and 5 into a single event for purposes of age dating based both upon a re-examination of the contacts and on their individual ages. Following the same techniques as with the other volcanoes, we determined a split model crater age of $3.0^{+0.2}_{-0.5}$ Ga and $3.6^{+0.1}_{-0.2}$ Ga for caldera 1, based on craters ~170-300 m and 350-500 m, respectively. Caldera 2 has an age of 1.6±0.5 Ga, while the combined calderas 3-5 have a model age dating to 2.0±0.3 Ga.

5.5. Elysium Complex

The Elysium region is located near the eastern rim of the giant Utopia Basin and consists of three relatively clustered volcanoes amidst fairly young terrain. The complex's largest, westernmost volcano is eponymously named, while to its northeast lies Hecates Tholus, and to the southeast is Albor Tholus. Farther south lies Apollinaris Mons, though we address that separately in Section 5.6 for reasons made clearer in Section 5.9.

5.5.1. Albor Tholus

Albor Tholus, the southernmost of the three Elysium volcanoes, is centered around 19°N 150.4°E. It rises ~3.8 km above both the surrounding plains and the martian datum. It has a diameter of approximately 165 km. Mapping the summit calderas of Albor seems, at first glance, relatively clear with a smaller, lower elevation caldera to the north, emplaced within a larger caldera (Fig. **46**c). However, to be consistent with the mapping of Neukum *et al.* (2004) and based upon the presence of ridges and surface textures, we segregated the larger caldera into three separate ones.

Resurfacing plagued our age determinations for Albor (Fig. **49**c). We estimate the age of caldera 1 to be 1.50±0.36 Ga based upon the 110-280 m range; at smaller diameters the slope is

shallower, matching ~1% geometric saturation. Caldera 2 has a model age of 940±270 Ma for diameters 175-250 m. Caldera 3 has an age relatively close to the other two, 1.01±0.31 Ga over 125-220 m. Finally, we derive an ancient age for caldera 4 of $3.54^{+0.07}_{-0.13}$ Ga over the diameter range 380-475 m.

Compared with the work of Neukum *et al.* (2004), our model crater ages are fairly different. For caldera 1, their age is 500 Ma, 1/3 ours. We barely statistically agree to within their standard 20% uncertainty with caldera 2, where they derive an age of 600 Ma. Caldera 3 is the same case, though their age is older at 1.6 Ga, barely within the joint uncertainties. Finally, caldera 4 is completely different, where they derive an age of 2.2 Ga, placing it in the Amazonian while our age of $3.54^{+0.07}_{-0.13}$ Ga places the caldera in the Hesperian epoch. This caldera complex represents our largest discrepancy with the work of Neukum *et al.* (2004). In reconciling these, Werner (2009) is not helpful as the entire caldera complex was dated as one, assigning it an age of 1.6 Ga.

5.5.2. Elysium Mons

Elysium Mons is the tallest of the three in this region, and it is the farthest west at 25°N 147°E. The volcano rises to a maximum of 14 km above the martian datum, though it is difficult to estimate where precisely the volcano's base lies due to the very steep ~8.3° slope for ~50 km from the summit that breaks to a shallower ~5.3° for ~100 km from the summit, and then a much shallower, ~0.6° slope that continues for an additional 350-600 km. If we take the maximum extent, then the volcano rises 18 km above the surrounding surface.

The summit of Elysium Mons is capped by a single main caldera (caldera 2) and two ancillary ones (Fig. **46**d). Caldera 1 is fully embedded within caldera 2, and we chose to separate it due to its topographic distinction since it lies below the surrounding surface of caldera 2. This is in marked contrast with our mapping of Alba Mons and Uranius Mons, where we only identified the last eruption episodes due to an inability to distinguish individual historic eruption regions. Caldera 3 for Elysium is a thin crescent-shaped terrace above caldera 2, following it

about 60% around.

When dating the three calderas, we used crater diameters approximately in the range 100-250 m for all three (Fig. **49**d). Caldera 1 had a model crater age of $3.1^{+0.2}_{-0.6}$ Ga, caldera 2 $2.8^{+0.2}_{-0.2}$ Ga, and caldera 3 was $3.2^{+0.2}_{-0.6}$ Ga. We note that these are statistically identical and interpret them as likely being from the same eruptive episode. A possible history for the three is the last eruptive event created a caldera that extended through calderas 2 and 3, and it was at the elevation of caldera 3. Subsequent collapse brought calderas 1 and 2 to the present day elevation of caldera 2, and collapse from possible evacuation of a magma chamber drained support from caldera 1, causing slight subsidence.

Elysium represents an interesting case of empirical saturation of craters. Caldera 1's slope matches an empirical saturation level of 3.5% geometric, while caldera 2's is fully 4.2% geometric saturation at smaller diameters. This represents the highest level we observed of any region we studied in this work. Caldera 3 is roughly 3% of geometric saturation at larger diameters (as large as ~125 m) though it falls below this at $D < 100$ m, likely due to resurfacing and mass wasting since it is a narrow strip no wider than 500 m.

Werner (2009) also age-dated Elysium Mons, though the entire summit was dated as a single caldera. The derived age of 3.49 Ga statistically agrees with our ages if we apply a conservative ±10% uncertainty. In contrast, Pasckert *et al.* (2010) arrived at a much younger 1.48±0.20 Ga for the combined calderas 1 and 2. However, they did not include approximately half of the craters in their analysis. Their argument is that they are likely to be secondary craters (personal communication), though upon morphologic examination we do not see such evidence. One could make a statistical argument to exclude a certain fraction of the total craters counted due to them being probable secondaries, but we do not think one can dismiss regions of the surface from the initial mapping as well as omit craters that are fully within the designated mapping region when they do not display any standard morphologic secondary crater characteristics (Shoemaker, 1962; Oberbeck and Morrison, 1974), such as entrainment in ejecta or clusters. Subtraction of presumed secondaries from a model crater population could be a

reasonable approach, but that was not done in this case.

5.5.3. Hecates Tholus

Hecates Tholus is the northern volcano of the trio that comprise the Elysium complex; it is centered at 32.5°N 150°E. It has a summit that lies ~7 km above the surrounding terrain and an average diameter of ~190 km. Mapping the summit calderas of Hecates was relatively easy (Fig. **46**e). There are four obvious concentric levels of calderas at the summit, though we followed Neukum *et al.* (2004) and subdivided the second-highest into two distinct calderas due to a ridge that lies between them. The total area of the summit calderas is only 66.4 km^2, and we were only able to identify 145 craters over all five calderas from CTX imagery.

This number is woefully inadequate to obtain statistically significant ages (Fig. **49**e), though we performed the exercise for completeness as well as a resolution verification case study. We also compare our ages with Neukum *et al.* (2004) and Werner (2009), though the ages reported are identical so we will only list the comparison once. Caldera 1 was dated based on the two largest bins, ~100 m in diameter, and fits to 200±110 Ma. Compared with an age of 322 Ma from Neukum *et al.* (2004) and Werner (2009), this is a reasonable match. Caldera 2 was fit between 70 and 105 m and we fit an age of 220±80 Ma. This is also in reasonable agreement with Neukum *et al.* and Werner's age of 90 Ma. Using all three diameter bins of caldera 3, we date it to 1.01±0.46 Ga, though this is approximately 3-4 times as old as the 250-300 Ma comparison age. Caldera 4 was the most significant difference. We used our three largest diameter bins, 220-270 m, and derived an age of $3.53^{+0.11}_{-0.57}$ Ga. In contrast, they derived an age of 110 Ma by dating external lava flows in addition to the calderas to derive what they considered statistically more meaningful results. We consider our method of dating only the calderas to be more reliable in this case. Additionally, our SFD for caldera 4 is among the best defined for this region, for it shows a good fit to the 3.53 Ga isochron. Finally, caldera 5 is also not in statistical agreement. We used a range of 185-210 m to fit a model crater age of $2.67^{+0.59}_{-1.00}$ Ga, while they calculate an age of 1.01 Ga. Interestingly, from approximately 90 m to 200 m,

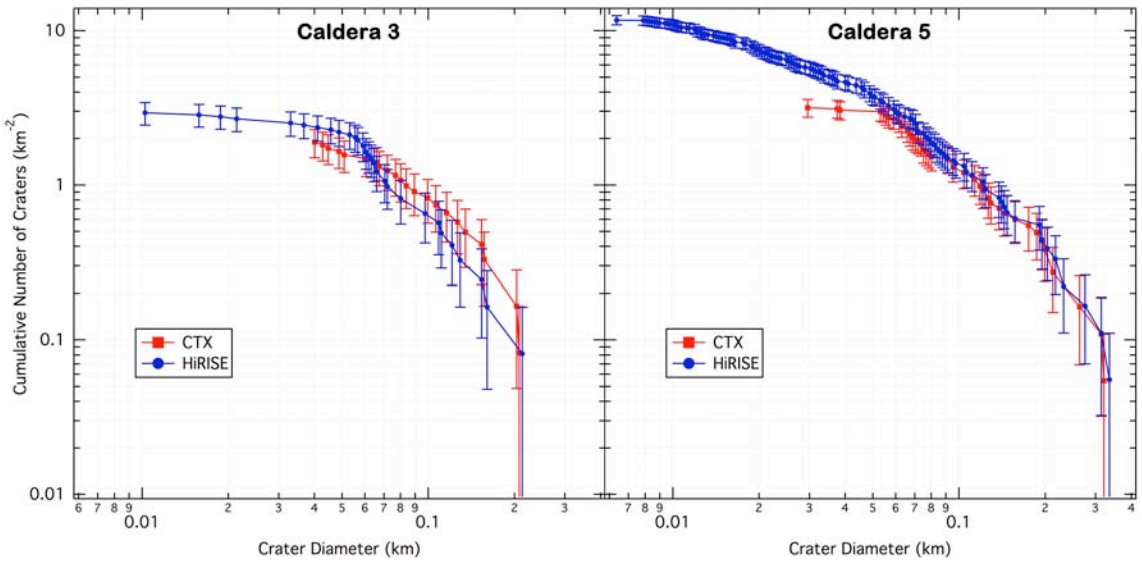

Figure 53: SFD of Hecates Tholus' caldera 3 (a) and 5 (b), showing the comparison for HiRISE-based counts with CTX-based counts. We show these two calderas because they contain the most craters and they had the most complete HiRISE coverage (caldera 3 is 100% and caldera 5 is 98.6% covered). The results show that with independent resolution verification, we are statistically complete to the small diameters that we claim, roughly 50-75 meters.

the crater frequencies for calderas 4 and 5 lie on the 1% geometric saturation line, though we are not convinced that this is the reason for the shallower slopes here.

While Hecates Tholus fails as an overall useful location for our technique of crater-age dating volcanic calderas, it is small enough to serve as a case study for our statistical completeness of craters. We obtained the HiRISE image PSP_005259_2120_RED, which covers ~76% of the summit's calderas. At a resolution of ~25 cm/pix (compared with 10 m/pix for our CTX mosaics) and outlining crater rims at a resolution of 1 vertex every 5 meters (compared with 25 meters for CTX), we performed crater counts independent of the counts we did using CTX images. The results (calderas 3 and 5 shown in Fig. **53**) show that we were statistically complete for craters to diameters ~60-70 m in the CTX data, helping to validate our claim of completeness to those diameters.

5.6. Apollinaris Mons

This volcano, centered at -8.5°N 174.5°E, is the only large, prominent, and isolated volcano on the planet that is visible today. It is southeast of the Elysium complex, and it resides

near the crustal dichotomy boundary. Understanding it, the history of the region, and its eruptive past are important not only to the broader picture of Mars, but also to the interpretation of MER (Mars Exploration Rover) Spirit data since the Gusev Crater in which MER Spirit landed is covered by volcanic material likely from the nearby Apollinaris volcano (*e.g.*, Grant *et al.*, 2004; Morris *et al.*, 2008), though this has been debated (*e.g.*, Lang *et al.*, 2010).

Apollinaris is characterized by a summit that lies ~4.5 km above the surrounding terrain though the main two calderas drop ~1.5 km below this. The volcano has an average diameter of 180 km. Geomorphologic mapping of Apollinaris' summit calderas was a complex undertaking, and it represents perhaps the one instance where we were fairly conservative (Fig. **46**f). A sizeable region of this complex was excluded from the mapping due to its appearance of subsequent non-volcanic modification processes. We still identified 6 separate calderas, though due to their identical SFDs we later combined calderas 4 and 5 into a single unit.

The SFDs of Apollinaris Mons are a classic case, much like those of Ceraunius Tholus' calderas, of a resurfacing event. We observe an expected production function at larger diameters that match a relatively old isochron that likely represents the original crater population post-formation. We then observe a less steep slope in the SFD at intermediate diameters, representing a burial or erasure event that affected craters smaller than a certain size. After that event occurred, crater retention would resume, and we again observe a relatively steep production function slope that matches a younger isochron (Fig. **49**f). For caldera 1, we calculate a model age of $3.57^{+0.03}_{-0.04}$ Ga. We note that the isochron is very clearly matched by the SFD over the range of ~500-800 m, below-which it matches the 1.1% geometric saturation line. Similarly, caldera 2 matches its isochron age of $3.52^{+0.05}_{-0.07}$ Ga over 400-700 m. Caldera 3 is more difficult to interpret. Between 1.08 and 1.53 km, the model crater age is the oldest we found – Noachian, at $3.93^{+0.06}_{-0.10}$. The SFD then goes nearly flat, increasing slowly, until $D < 100$ m, at which point it increases again to a model age that matches the increase in calderas 2, 4/5, and 6, of ~220±20 Ma. The age of the combined calderas 4/5 fits the $3.77^{+0.04}_{-0.06}$ Ga isochron, while finally caldera 6 at larger diameters matches to $3.54^{+0.11}_{-0.52}$ Ga and 220±30 Ma at smaller sizes. Over the brief

range of 400-500 m, caldera 4/5 match 1.4% geometric saturation.

The comparable work done on Apollinaris was by Werner (2009), who lumped our calderas 1 and 2 into a single caldera, and then the rest into another. Werner's age for calderas 1/2 is 3.61 Ga, and the age for the rest is 3.72 Ga. With even the most conservative uncertainty estimate of ±3%, our ages statistically match.

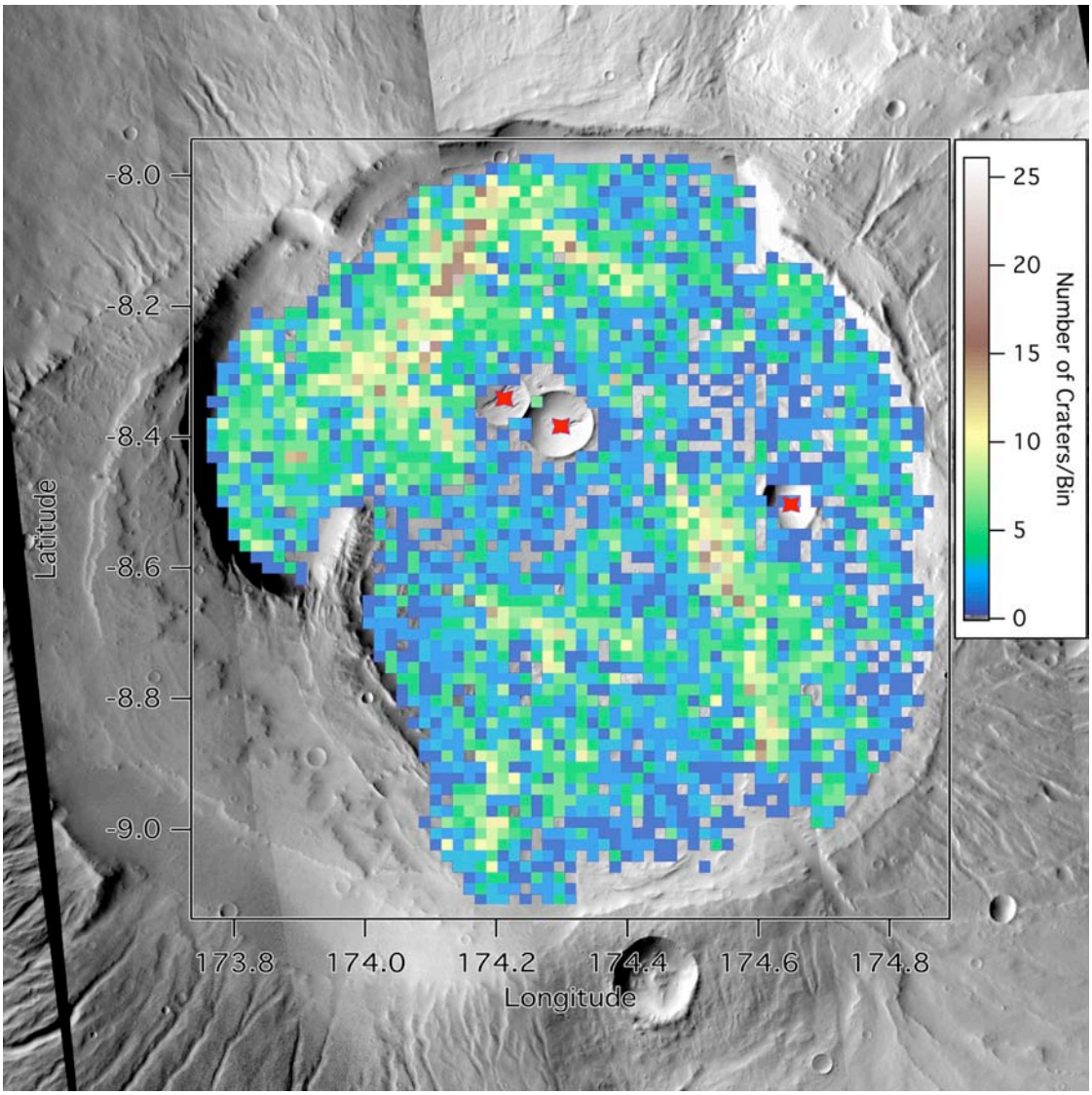

Figure 54: A crater density plot of Apollinaris Mons' two main calderas. The three stars indicate the three largest >1 km superposed craters. Binning is 1x1 km. There are large, statistically significant enhancements of craters surrounding each of these large craters, indicating probable secondary fields. With standard $\sqrt{N}$ Poisson statistics, the general "background" levels of craters in these calderas averages 2-3 ±1-1.5 craters per km^2. Within 2-3 crater diameters of the three large craters, the number of craters increases to 10-27 ±3-5 craters per km^2, a statistically significant enhancement. Bins with 0 craters in it have been made transparent so the underlying base CTX map shows through.

As with a few of the other volcanoes studied herein, Apollinaris Mons is a good case study for exploring the role of secondary craters - both where they are produced and how they affect or do not affect crater size-frequency distributions. Apollinaris Mons contains three relatively large fresh impact craters on its summit – two are in caldera 1 and one is in caldera 2. They are 5.00, 6.14, and 5.23 km in diameter. A region of enhanced cratering surrounds all three that could be indicative of nearby secondary crater fields. The only problem is that they are not morphologically obvious secondaries, unlike on the summit of Arsia Mons. In fact, the only suggestion that there are secondaries present is through a crater latitude/longitude density analysis (Fig. **54**). This figure shows an increase of craters in an arc surrounding about 60% of the pair in caldera 1 and about 40% surrounding the one in caldera 2. These density increases are statistically significant, increasing from a background 0-5 (±0-2) craters per 1x1 km latitude-longitude bin to 15-25 (±4-5) craters per bin. A spatial analysis of the isolated 5.23-km-diameter primary is discussed in detail in Section 4.2.4 and agrees well with other nearby primary crater fields in the text (Robbins and Hynek, 2011d). Similar analysis of the overlapping primary craters was less conclusive and we cannot make a thoroughly convincing case that these northern craters are indeed secondaries from these primary craters. A further way in which at least the eastern secondary craters differ from those of Arsia Mons is we do not observe a statistical increase in the SFD in the caldera. We explore the implications of these further in Section 5.8.

5.7. Northeastern Hellas Basin

Hellas Basin is the third- or fourth-largest impact feature recognized today on Mars (behind Chryse, Utopia Basin, and possibly the basin that formed the entire northern lowlands if it is of impact origin (Andrews-Hanna *et al.*, 2008)). Hellas Basin dates roughly to 4.08 Ga, but it is still younger than all other large basins, save Argyre and Isidis (*e.g.*, Barlow, 1988; Nimmo and Tanaka, 2005). The impact event that formed Hellas must have induced massive melting that could have affected magma pockets around it and severely fractured the crust, acting as a catalyst for a large amount of local volcanism with crustal fractures acting as conduits. We

support this scenario (proposed by *e.g.*, Peterson, 1978; and linked as the "Circum-Hellas Volcanic Province" by Williams *et al.*, 2009) because the only major volcanoes in the southern highlands of the planet surround Hellas: Two to the northeast - Tyrrhena Mons and Hadriaca Mons - and four to the south-southwest - Amphitrites Patera, Malea Patera, Peneus Patera, and Pityusa Patera. Unfortunately, due to a lack of CTX coverage we were only able to analyze Tyrrhena and Hadriaca. As we show below, the oldest model crater ages we found for the calderas is approximately 3.2-3.7 Ga, at least 400 Ma younger than Hellas itself.

5.7.1. Hadriaca Mons

Hadriaca Mons is located within the rim of Hellas, centered around -30°N 93°E. It is characterized by a summit rim height that lies roughly 700 m below the Mars datum and a caldera floor that drops another 400-600 meters. It is difficult to estimate the elevation above the surrounding surface because it resides upon the sloping walls of Hellas Basin, but we very roughly estimate that it rises ~1 km above the surrounding surface. The diameter of the mons averages ~270 km.

Geomorphologic mapping of Hadriaca Mons (Fig. **46**g) was the most difficult and interpretative of the 20 we performed for this study although Apollinaris Mons' mapping was also one of the most difficult and subjective. We identified nine separate regions within the summit of Hadriaca by using a liberal mapping approach mostly based upon topographic relations and bounding ridges throughout. Upon reexamination after crater identification had been completed, we combined calderas 3 and 4, and calderas 6 and 7, for a total of seven regions.

Overall, Hadriaca Mons' SFDs (Fig. **49**g) show evidence of resurfacing, as with most we studied, though it was overall less severe than the worst cases (*e.g.*, Biblis, Jovis, and Tharsis Tholi). Caldera 1 was dated to 3.6±0.1 Ga. Caldera 2 has a model crater age $3.3^{+0.2}_{-1.0}$ Ga. Calderas 3/4 combined have a joint age of 1.8±0.5 Ga, and along with caldera 5 dated to 1.6±0.5 Ga are the youngest. Calderas 6/7 date to $3.6^{+0.1}_{-0.4}$ Ga. Caldera 8 has a split age, where craters ~400-600 m in diameter indicate a model age of $3.6^{+0.1}_{-0.4}$ Ga, while ~200-300 m craters fit an age

of 2.1±0.7 Ga - statistically separate events, and possibly matching the event that formed calderas 3, 4, and 5. A possible interpretation is that if those caldera regions formed in a single, separate volcanic event, lava ~20-30 m thick covered caldera 8, burying craters D < 200-300 m, after which it resumed crater accumulation. Finally, caldera 9 dates to $3.3^{+0.2}_{-0.6}$ Ga.

Comparing our results with others is somewhat subjective due to different mapping styles. Werner (2009) dated the entire caldera to 1.08-3.54 Ga. This easily fits within all of our caldera ages. Williams *et al.* (2007) also age-dated the caldera of Hadriaca. They divided it into two regions, their first caldera corresponding to our caldera 1, and their second roughly corresponding to our calderas 5-8. Our results agree well, where for the first and second they calculated an age of $3.5^{+0.1}_{-0.3}$. Their resurfacing ages are $2.6^{+0.3}_{-0.4}$ Ga and 1.5±0.2 Ga, respectively, which roughly correspond with the ages of our calderas 3-5 and the resurfacing age of caldera 8.

5.7.2. Tyrrhena Mons

Tyrrhena Mons is located farther away from Hellas than Hadriaca, its center at -21.5°N 106.5°E. It is characterized by a summit that lies roughly 3 km above the surrounding terrain with a caldera that drops 500 m below the rim. The diameter of the mons averages ~250 km.

Mapping Tyrrhena's caldera was straightforward. There is only one identifiable unit that continues in an extended channel for 10s of km (Fig. **46**h). We included the center and a few km of the lava channel until it changed directions. We initially opted to see if that directional change could have been evidence for a different floor age, but we then excluded that possibility based on crater statistics and combined it with the main caldera and channel.

Resurfacing events are evident from the SFD in Tyrrhena, and we had to exclude some of the channel near the southern walls due to a marked visible deficit of craters. Fitting between 280 and 525 m, we determined a model crater age of $3.41^{+0.08}_{-0.16}$ Ga (Fig. **49**h). This agrees well with Werner's (2009) age of 3.29 Ga as well as Williams' *et al.* (2008) age of $3.2^{+0.3}_{-1.2}$ Ga.

5.8. Implications for Secondary Cratering and Resurfacing

The issue of secondary craters - relatively small craters that are formed from the ejecta of a primary crater formed by a extra-planetary impactor - was raised as far back as Shoemaker (1965), but it was relegated by the cratering community to a relatively unimportant effect by the 1980s, despite evidence that they may become important on the Moon at diameters smaller than ~1 km (McEwen and Bierhaus, 2006). This has changed in recent years, noticeably in 2005 with separate papers – one discussing mapping of vast, planet-wide fields of secondaries on Europa (Bierhaus *et al.*, 2005), and the other illustrating fields of secondary craters from the Zunil crater on Mars (McEwen *et al.*, 2005). Their work was combined in McEwen and Bierhaus (2006), showing the cratering community that secondary craters were an unresolved and potentially important issue that needs to be taken into account when using craters for age-dating and geologic mapping.

Since then, data returned from the MESSENGER spacecraft has shown that secondary craters on Mercury become important at sizes $D < 10$ km, a potentially significant issue for mercurian crater age dating (*e.g.*, Strom *et al.*, 2008). In their 2006 paper, McEwen and Bierhaus estimated that secondary craters become statistically important on Mars - where the probability that a given crater is a secondary is ≥50% - for $D < 1$ km. As a consequence, our research into dating volcanic calderas where nearly all of our craters are smaller than 1 km provides a test bed for studying the role of secondaries.

One way to determine whether a crater is an "obvious" secondary is that it will be entrained in an elongated clump, where the long axis of the group is oriented radially away from the primary. On Mars, the largest secondary crater is usually only ~2.5-5% the diameter of the primary due to the vastly different impact energy (McEwen and Bierhaus, 2006). They will also usually be shallower than primaries, again due to the lower impact energy. Other classic morphologic features include being generally more elliptical than primary craters due to their lower impact energy, being entrained in other crater ejecta or surrounded by a "herring bone" pattern (*e.g.*, Oberbeck and Morrison, 1974), and/or generally form an annulus of decreasing

crater density with increasing distance from the crater. Unfortunately, that is just for "obvious" secondaries. The crux of what McEwen and Bierhaus showed in their respective and joint papers is that there exists a "background field" of secondary craters that cannot be obviously tied to a primary and cannot be morphologically differentiated as a primary versus secondary crater.

Mapping of secondary fields as well as modeling experiments have shown that the SFD of a field of secondary craters roughly follows a $b \approx -4$ power-law slope (*e.g.*, McEwen and Bierhaus, 2006), rising more steeply towards smaller diameters than a standard production function slope of $b \approx -3$. Of primary interest relative to our results, we do not observe this increase in SFD slope in any of the volcanic calderas that we analyzed, save one (see sections 5.3.2, 5.8.1). The implications for this and possible explanations are discussed below in Section 5.8.3.

Meanwhile, the two main groups who have worked to establish the crater-frequency age of Mars through isochrons generally do not agree that secondary craters are important to factor in separately. The Neukum group (*e.g.*, Neukum *et al.*, 2006, 2007; Neukum 2008; Werner *et al.*, 2009) argues that they do not significantly affect SFDs when craters are chosen judiciously. The Hartmann isochrons (Hartmann, 2005) are assumed to take an average background secondary field into account and are not treated separately. For this reason, in an ideal situation one can assume that the "background field" of secondaries is uniform, exclude obvious secondary craters, and then still include "non-obvious" secondary craters in their SFDs to calculate an accurate age from the established isochrons.

5.8.1. In-Depth Analysis of Arsia Mons

When discussing the age of the vast, 10,000 km^2 caldera of Arsia Mons in Section 5.3.2, we briefly raised the point that Arsia's SFD is the only case where we observed a marked increase in the SFD slope for $D < 110$ m. Arsia's caldera was also unique in that it was the only case where we observed the "obvious" fields of secondary craters (Fig. **50**), and there was no obvious nearby primary from which they may have been formed. The characteristics of these

fields were dissimilar from the fields identified by Popova *et al*. (2007) as originating from breakup of a primary impactor, and this is mostly due to their vast extent and group morphology. They do match the general morphology of launched and fragmented ejecta blocks identified by those authors. We mapped the secondary craters we identified in Arsia by their morphology and clustering, and we observed a general northeast-southwest orientation. We used this in an attempt to find a primary, and the closest sizable (~20 km) candidate was ~850 km to the southwest of the volcano and fully 13.5 km lower in elevation than its summit. A potential smaller, ~10 km crater, is located ~450 southwest of the summit and 11.5 km lower in elevation.

After identifying the fields of secondaries, we created separate SFDs showing the secondaries compared with the rest of the craters in the caldera (Fig. **55**). For $D > 130$ m , both SFDs lie along the ~140 Ma isochron. We attribute this to the fields of secondaries being contaminated by primaries – more detailed modeling would be needed to statistically extract the primaries. At smaller diameters, the secondaries quickly become more numerous and have a steeper slope than the branch of primaries, as theory would predict (*e.g.*, McEwen and Bierhaus, 2006). While the slope of the primaries does increase, it does so less significantly, especially at larger diameters, and we can attribute this to an additional population of background secondaries that were not removed along with the "obvious" fields.

These results have two important implications. First, the background field of secondary craters on Mars is likely to exist, in contrast with Neukum (2008) and Werner *et al.* (2009), and they can exist with no obvious primary crater anywhere near them. The second implication is that, while we observe the SFD enhancement of secondaries, it occurs at a diameter 10% that estimated by McEwen and Bierhaus (2006). While one example does not make a case for the ~100 m diameter being the *maximum* diameter at which secondaries become important (that we observed), it at least raises the issue that there may not be a uniform size dependence across the planet, further complicating the role of secondaries.

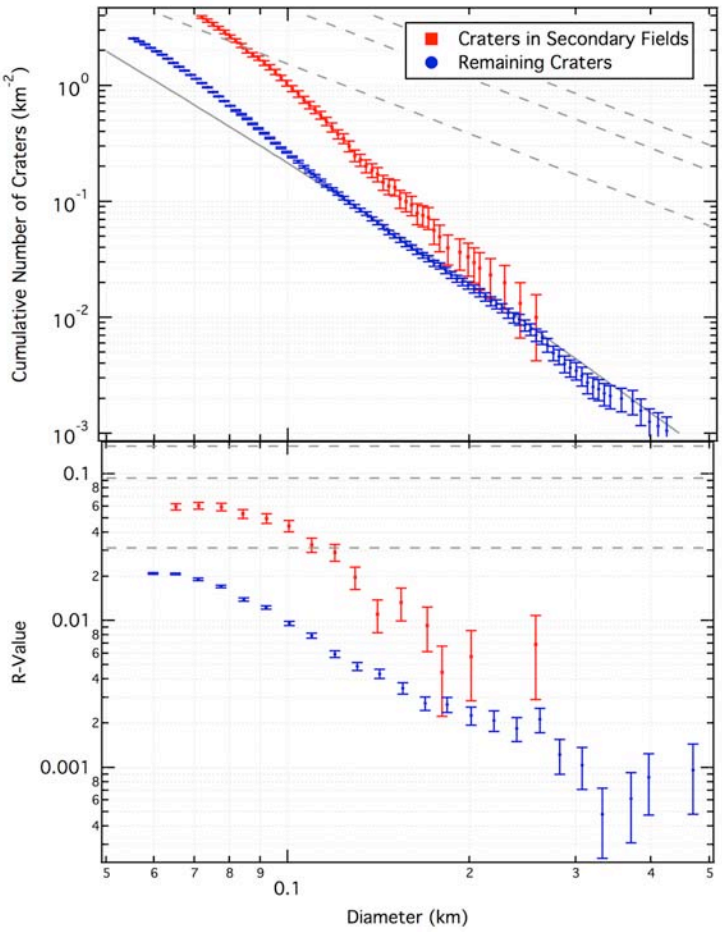

Figure 55: Both - Size-frequency diagram (top, cumulative; bottom, R-plot) for Arsia Mons showing the SFD for assumed secondary fields compared with the remaining craters. Top - For $D > 130$ m, both SFDs lie along the ~130 Ma isochron. We attribute this to the fields of secondaries being contaminated by primaries – more detailed modeling would be needed to statistically extract the primaries. At smaller diameters, the secondaries quickly become more numerous and have a steeper slope than the branch of primaries While the slope of the primaries does increase, it does so less significantly, especially at larger diameters, and we can attribute this to an additional population of background secondaries that were not removed along with the "obvious" fields. Bottom - Same as the top but without isochrons and with coarser $2^{1/8}D$ binning.

5.8.2. In-Depth Analysis of Apollinaris Mons

We discussed the opposite case to Arsia Mons in Section 5.6, Apollinaris Mons. While Arsia's SFD showed an increase of slope attributable to secondaries, Apollinaris did not. Where there were morphologically obvious fields of secondaries in Arsia's caldera, no such fields exist in Apollinaris'. And while there was no obvious nearby primary to form the fields in Arsia, there were three, quite obvious, large primaries that formed nearby secondaries in an annulus about the primary (Fig. **54**).

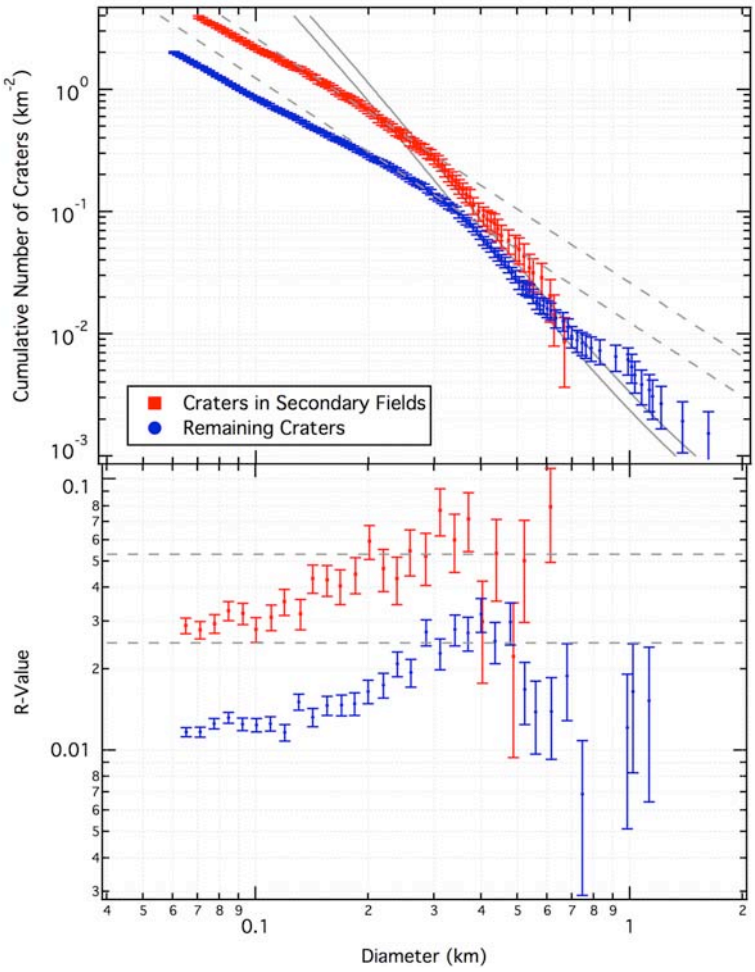

Figure 56: Both - Size-frequency diagram (top, cumulative; bottom, R-plot) for Apollinaris Mons showing the SFD for presumed secondary fields contrasted with the SFD for the other craters mapped within calderas 1 and 2. Top - Steep vertical lines are $b \approx -3.78$ isochrons for this diameter range. Shallower lines are $b = -2$ saturation (upper is 1.7% saturation, lower is 0.8% saturation. As shown, the "background" craters have slopes that are shallower than the isochrons for D > 500 m, matches the isochron for 350 < D < 500 m, matches saturation for 225 < D < 350 m, and then falls below saturation at smaller diameters. The "secondary" region craters have a statistically insignificant steeper slope for 550 < D < 725 m, generally match the slopes of the background craters, and follow empirical saturation over a much larger diameter range, through ~125 m. Bottom - Same as the top but without isochrons and with coarser $2^{1/8}D$ binning.

In an attempt to examine the SFD slope of the secondaries, we isolated the regions of enhanced craters within calderas 1 and 2. We then created SFDs for these and compared them with the rest of the craters in the two calderas, shown in Fig. **56**. The results are inconclusive. The "background" craters have slopes that are shallower than the isochrons for $D > 500$ m, match the isochron for $350 < D < 500$ m, match saturation for $225 < D < 350$ m, and then fall

below saturation at smaller diameters. The "secondary" regions' craters have a statistically insignificant steeper slope for $550 < D < 725$ m, generally match the slopes of the background craters, and follow empirical saturation over a much larger diameter range, through ~125 m. We cannot say for certain from analysis of the SFDs that these regions are dominated by secondaries, though we do maintain this is the likely case based upon the locations of enhanced crater density.

5.8.3. Possible Model Interpretations and Explanations

While McEwen and Bierhaus (2006) estimated that secondaries become important on Mars for $D < 1$ km, it should be apparent from our SFDs that this is at least not the case for the caldera regions that we studied (totals 0.0356% of the global surface area), although the only methods we used to search for secondary craters was visual inspection of the CTX data and hence we were not exhaustive of all methods. One possible way to explain this while still maintaining the $D < 1$ km size as the transition diameter is to suggest that the rate of resurfacing in all these calderas is greater than the production rate of secondary craters. For this to be the case, we can estimate what the resurfacing rate must be as we show in the following:

A 1 km primary crater has a nominal depth of 100 m (10% the diameter) (Melosh, 1989). Secondary craters are shallower, generally by 50%, so a 1 km secondary crater is ideally 50 m deep (Melosh, 1989). From Hartmann and Neukum (2001), the average formation rate of a 1 km primary crater between 1 and 3 Ga was 10^{-3} km^{-2}. If we assume a $b = -3$ power-law slope for the production of craters at Mars (Hartmann, 2005), and we require a minimum of a 20-km primary crater to form a 1 km secondary (McEwen and Bierhaus, 2006), then we would expect a $D = 1$ km secondary crater to form on Mars roughly once every 5 Myr. To then erase that crater would require a minimum erosion rate >10 nm/yr.

This is a fairly rapid rate compared with previous works: From mapping Zunil crater, Preblich *et al.* (2007) estimated a rate ≥80 nm/yr. Golombek *et al.* (2007) estimated a rate of 1.3 nm/yr in the Late Amazonian from the Mars Exploration Rover landing sites, though noted average erosion rates of 0.03 nm/yr in the Gusev Crater floor, 0.02 nm/yr at the Mars Pathfinder

site, and 1 nm/yr at the Viking Lander 1 site. However, they noted higher erosion rates of 1-10 nm/yr since the Hesperian (~3.5 Ga) in Meridiani Planum. This is comparable to rates determined by Hartmann (2003) of 0.05-2 nm/yr for the rate of crater infilling, perhaps the best direct comparison to our suggested rate for this model. In sum, we think it is unlikely that normal erosive processes can account for the lack of a secondary crater branch on our SFDs, considering that not only do we not see the increase due to secondaries (except at Arsia), but we see a more rapid decrease in the SFDs at smaller diameters than expected at most locations.

An alternative model to save the 1 km transition diameter is to argue that volcanic material on the surface undergoes alteration over time that changes the production of secondaries (*e.g.*, as proposed by Hartmann and Barlow (2006)). Since Apollinaris Mons has the oldest surface age of the volcanoes we dated, one may expect that its near-surface material may be well gardened and most similar to the bulk crust of Mars, therefore secondaries would lie closest to primaries on it; one could also argue at least for $D < 250$ m that it is empirically saturated already and the SFD will not reflect additional secondaries (Figs. **49**f, **56**). Conversely, with the Tharsis region having a young surface, we could expect the issues with volcanic terrain producing secondaries to be best reflected there. This is somewhat buoyed by the lack of SFD enhancement attributable to secondaries on the young (1.42±0.30 Ga) Ulysses Patera. However, this model is not supported by the lack of secondaries around the large crater in the middle of caldera 1 in Hadriaca Mons: aged at 3.1±0.1 Ga, this is only ~800 Myr younger than the oldest Apollinaris Mons caldera, and while matching 8‰ geometric saturation, a value this low strains believability as an explanation. More work would need to be done with a Zunil-type crater on volcanic terrain (*e.g.*, somewhere on Tharsis) to determine if this may be a valid explanation.

Instead, we propose a more likely explanation that - at least in our regions of study - secondary craters do not become statistically important on Mars for $D \leq 1$ km but rather at sizes 1-2 orders of magnitude smaller. However, secondaries are still important to consider in crater counting statistics - as evidenced by their presence in Apollinaris but not reflected in its SFD - and our work supports the models that suggest there is a broad background secondary field

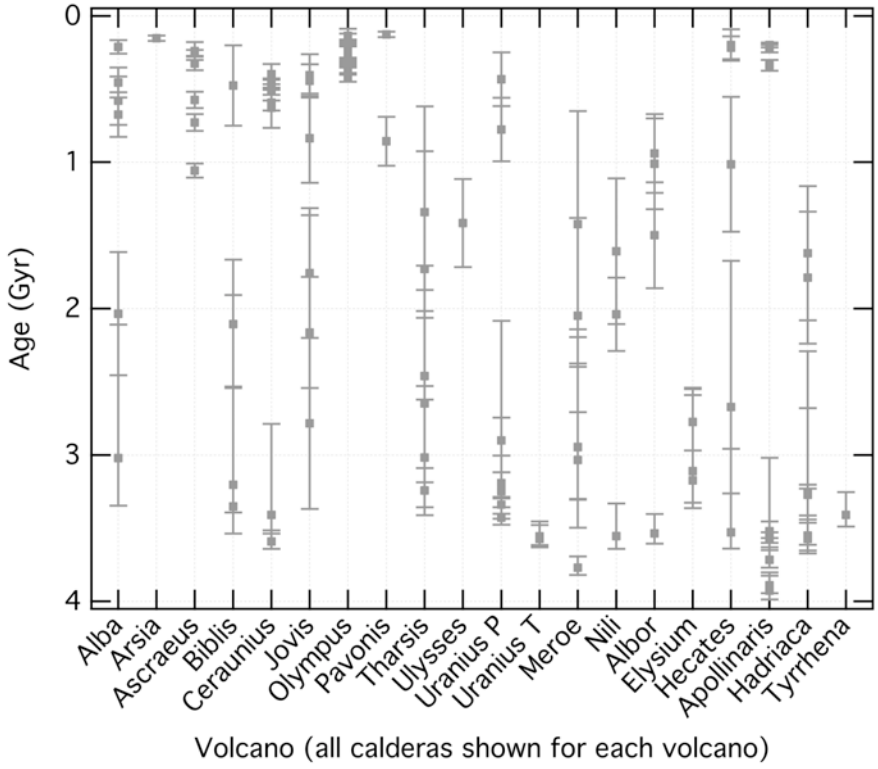

Figure 57: Timeline illustrating the ages discussed in the text and Table **9** for every volcano in this study. Split ages for a single caldera are included in this figure, even though several are likely due to resurfacing processes (*e.g.*, Ceraunius Tholus for calderas 3 and 4).

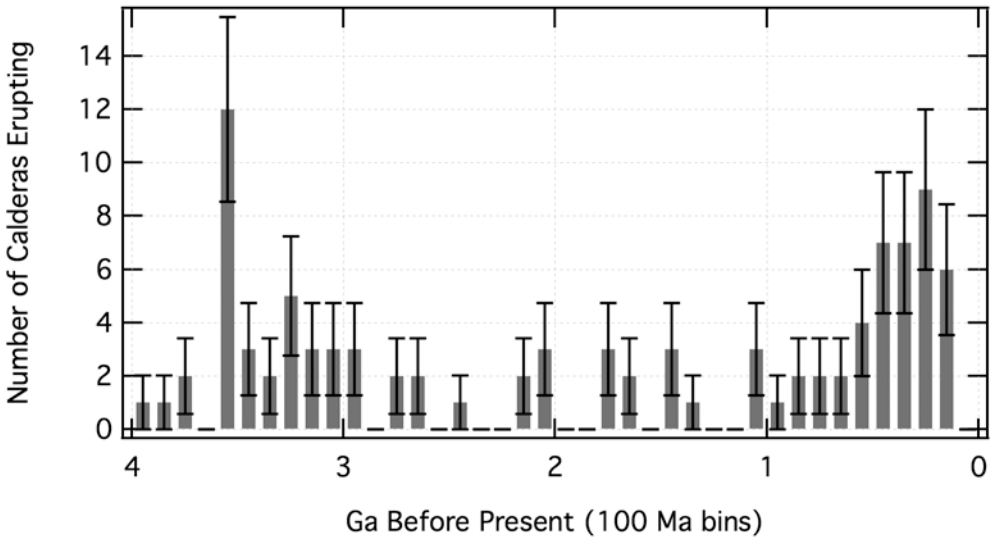

Figure 58: The minimum volcanic history illustrated by the number of calderas as a function of time in 100 Ma-wide bins. Error bars are Poisson $N^{1/2}$ uncertainties. All but the most recent bins should be considered *minimum* caldera numbers because any eruption after another from the same caldera will have its surface reset and be undetectable by this method.

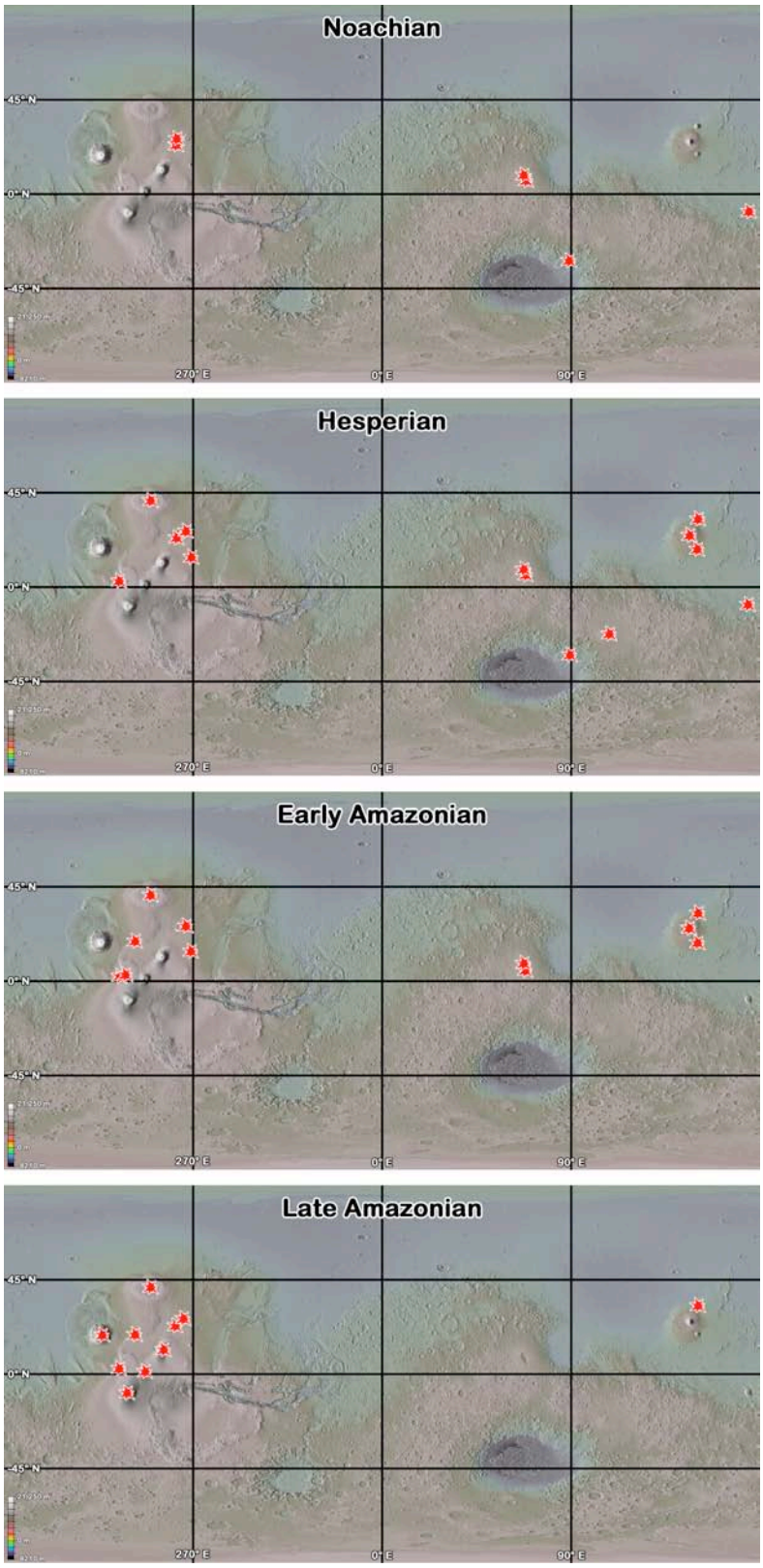

Figure 59: Following the ages in Fig. **56**, we illustrate here roughly the ages of the calderas during the Noachian, Hesperian, Early-Amazonian, and Late-Amazonian. We also provide a movie to illustrate this sequence in online supplemental material.

across Mars, though we question the diameter previously proposed at which it becomes statistically important (*i.e.*, McEwen and Bierhaus, 2006). We think that more studies over a broader area are needed to help answer this ongoing question.

5.9. Implications for the History of Volcanism on Mars

A timeline with all caldera ages discussed in Sections 5.3-5.7 is shown in Fig. **57**, converted into a histogram in Fig. **58**, and we illustrate these over the main epochs of geologic history on Mars in Fig. **59**. We also provide a movie of this sequence in online supplemental material. Before our summary analysis, we reiterate two main constraints on our study. First, we dated the caldera surfaces, therefore our conclusions are limited to the last episodes of volcanism from the summit of each volcano. For example, we fully expect that Arsia Mons is an old volcano, having been built up over several billion years (*e.g.*, Hodges and Moore, 1994 and references therein; Anderson *et al.*, 2001), but its single caldera has a modeled crater age of 130 Ma and so that is the age we report. This also ignores several of the younger vents that surround it. Second, approximately 20% of the calderas we dated were given split ages. Often, we attributed this to resurfacing events, such as Ceraunius Tholus' calderas 3 and 4 (Section 5.3.5). In a few cases, such as Olympus Mons, the older age is at a smaller diameter and this is difficult to explain. However, because we cannot state conclusively a non-volcanic reason for these counterintuitive observations, we have displayed both ages in all cases in Fig. **57**. There have been many previous authors who have derived crater ages in the past (numerous references throughout this paper), and the purpose of our results is to help refine these ages and last episodes of summit volcanism. Finally, in the discussion below, Mars' epochs are based on the times given in Hartmann and Neukum (2001).

Apollinaris Mons shows the oldest caldera ages, dating back to 3.9 Ga. It was also the first volcano to die out, its activity ending around the start of the Hesperian (if we attribute the lone split ages of 200 and 220 Ma for calderas 3 and 6 to non-volcanic resurfacing events). This is in contrast with the nearby Elysium region, where Elysium Mons ceased activity

approximately 3 Ga, but the two nearby tholi (Hecates and Albor) show ages that date from that period to fairly recent. This adds to the case that Apollinaris Mons likely had a different magma source than Elysium, and it should be considered completely separate from that complex.

Moving to the circum-Hellas highlands volcanoes, Tyrrhena Mons shows a complex erosional history, but its last volcanism died out squarely within the Hesperian epoch. This contrasts with the Hadriaca volcano which shows crater ages that span over 2 billion years of martian history, ending around 1.6 Ga. This is also approximately when the Syrtis Major volcanoes ceased large-scale activity. Meroe and Nili Paterae show ages almost as old as Apollinaris, but then sporadic activity though ~1.4 Ga, with the split age of 230 Ma in Meroe's caldera 5 likely due to non-volcanic resurfacing events.

The vast Tharsis region, fully 60% of the volcanoes we studied, shows no obvious trends in ages in terms of latitude/longitude distributions. We note that generally the smallest volcanoes - Biblis, Ceraunius, Tharsis, and Uranius Tholi along with Uranius Mons - show the oldest caldera ages, while it is generally the largest volcanoes - Arsia, Ascraeus, Olympus, and Pavonis Montes - that show the youngest (in agreement with previous works, such as Hodges and Moore (1994) and Werner (2009)). The most notable exception is the vast Alba Mons that shows caldera ages ranging between 3.0 Ga and ~300 Ma. This adds to the uniqueness of Alba Mons that has been recognized before as a transitional volcano between explosive and effusive volcanism (*e.g.*, Raitala, 1989; Ivanov and Head, 2006).

Broadly from our analysis, we can conclude that Mars has had active large-scale volcanism at least until ~100-150 million years ago (constrained by the Arsia, Olympus, and Pavonis Montes). Every volcano we studied was active through the Hesperian epoch, while all except for Tyrrhena Mons and Apollinaris Mons were active through at least the Early Amazonian. Only the Syrtis Major calderas and Apollinaris Mons show ages that date to the Noachian time, indicating that volcanism likely died out rapidly in those areas in early martian history. This is consistent with the evidence for widespread volcanic flooding during the Hesperian that has been identified by other researchers (*e.g.*, Greeley and Spudis, 1981; Head *et*

al., 2002).

We do observe a trend in the ages of the three Tharsis Montes, which are Ascraeus, Pavonis, and Arsia, from north to south (similar to previous findings, *e.g.* Hodges and Moore, 1994, and references therein). Ascraeus' calderas show six distinct ages, ranging in time from approximately 1.1 Ga to 250 Ma. Pavonis' calderas date to 850 Ma and 130 Ma, while Arsia's single caldera dates to ~140 Ma. In short, they all die out roughly within ~100 Myr of each other, while their oldest calderas are successively older northward. This could be simple random chance since there is a sample size of three. Or, a possible explanation is that a branching plume fed all three montes and successively died out southward. This runs contrary to a model proposed by Bleacher *et al.* (2007). They suggest an original mantle upwelling fed Arsia, branched and spread to Pavonis, and continued to migrate northward with the two branches eventually settling under Pavonis and Ascraeus. We suggest effectively the opposite based on our derived ages; clearly, more work needs to be done in this area and one needs to consider both the crater ages of the surface as well as surrounding geomorphologic properties.

Another temporal analysis of this work comes from examining Fig. **58**, the minimum number of calderas erupting as a function of time. This is effectively a histogram of Fig. **57**, but any interpretation must be cautioned by every bin - save perhaps the most recent two or three - are the *minimum* number of calderas erupting because any subsequent activity would erase previous surfaces and hence not be discoverable by our method. This also ignores any flank or field vent volcanism that has been observed elsewhere (*e.g.*, Hartmann, 2005; Hauber *et al.*, 2009, 2010). Within those limitations, there are two primary statistical interpretations about *recent* volcanism, and one about *early* volcanism. First is that summit caldera eruptions on the major volcanoes are still occurring or may still occur. It is unlikely that the lack of eruptions in the most recent bin is simply a stochastic variation. Assuming Poisson statistics for independent volcanic eruption events, the odds of finding 0 events for an average rate of 6 per 100 Ma bin (the 100-200 Ma ago value), would be ~0.25%. It remains possible that activity has subsided in a non-random way, and it may return in the future. The second interpretation is that caldera

eruptions indeed did decline fairly rapidly in the recent geologic past as evidenced by the two most recent non-zero bins dropping to no volcanism in the last 100 Ma. This latter interpretation is supported by the earlier times being lower limits and fits well within the context of the previous discussion. A second interpretation from this figure deals with earlier volcanism. There is a marked increase around the Noachian / Hesperian boundary that may be a real effect and agrees with previous work by Phillips *et al*. (2001) and Head and Wilson (2011).

Finally, we can relate our results to a broad transition from explosive to effusive volcanism, generally attributed to a decreasing near-surface water table (*e.g.*, Mouginis-Mark *et al.*, 1988). Explosive/pyroclastic eruption styles on Earth in silica-poor magmas generally occur when there is a high water content. On Mars, this can be generalized to volatiles in the magma. As the magma rises, the volatiles are under less pressure and can explosively separate from the liquid rock. In contrast, effusive flows lack volatiles and correspond more towards a steadier, less viscous morphology. This will generally produce two identifiable features, the first being that effusive flows will have more competent lavas that have flow-like morphologies emanating from the source, and second is there will generally be a better-defined caldera rim for the effusive type (Wilson and Head, 1994). A large caveat to this analysis stems from our ability to only assess eruption style based on the calderas we mapped. In-depth morphological studies of the entirety of each volcano and related deposits is beyond the scope of this work. For example, below, we classify Hecates Tholus as primarily effusive in style even though numerous previous researchers have noted potential pyroclastic deposits (*e.g.*, Mouginis-Mark *et al.*, 1988). Another example is Olympus Mons, which we also classify as effusive from its calderas, though previous theoretical and observational work has shown it may have a significant component of pyroclastics (*e.g.*, Head and Wilson, 1998a, 1998b; Wilson *et al.* 1998).

From these morphologic predictions and with these caveats in mind, we can classify Apollinaris Mons, Elysium Mons, Syrtis Major, Uranius Tholus, the circum-Hellas vents Hadriaca and Tyrrhena Mons, and some of Alba Mons as primarily explosive. The majority of the Tharsis volcanoes and Elysium tholi show more of an effusive morphology. From Fig. **57**,

we can roughly place that transition at ~3.2-3.5 Ga, around the time of the Hesperian epoch and Hesperian/Amazonian transition. It likely happened at different times for different geographic locations, and more detailed morphologic studies would be needed to characterize this with greater accuracy (*e.g.*, the meticulous study of Alba Mons provided in Ivanov and Head, 2006).

5.10. Discussion and Conclusions

With the notable exception of the systematic study by Werner (2009), all previous work in dating Mars' volcanoes was done by different researchers at different times using disparate imagery data and various isochron chronologies. This creates unknown systematic and non-systematic uncertainties throughout the literature and limits the utility of combining the results to piece together as accurate a timeline of volcanism on the planet as is possible today. The work presented here varies from Werner (2009) by using a different, higher-resolution imagery set (CTX from Mars Reconnaissance Orbiter as opposed to HRSC from Mars Express), and it focuses on dating each individual caldera or terrace within the volcanic caldera complex for 20 major martian volcanoes. In contrast, Werner (2009) bulk-dated many of the calderas and ignored about half of them in favor of age-dating the volcanic edifice and/or surrounding flows. As a consequence, our present study represents the highest-resolution imagery-based crater-model-age-based chronology for the last episodes of volcanism from the summits of all major martian volcanoes (save Amphitrites, Malea, Peneus, and Pityusa Paterae).

In the text, we have compared our results to Neukum *et al.* (2004), Williams *et al.* (2007, 2008), and Werner (2009) where comparisons could be made. Overall, we are in good agreement with Williams *et al.* (2007, 2008), and our ages are generally older than but still mostly comparable with Neukum *et al.* (2004) once statistical uncertainties are taken into account. When comparing with Werner (2009), we make the interesting observation that the published results are identical with Neukum *et al.* (2004) for the volcanoes they both did - in general, younger than ours - but otherwise the rest are split between older and younger. We are within each others' uncertainties more than 50% of the time.

A probable explanation for why our ages are generally older than Neukum *et al.* (2004) is that we are using higher resolution data and hence likely are complete to smaller diameters. This is supported via direct comparisons between our SFDs and those published in both Neukum *et al.* (2004) and Werner (2009). From visual inspection of figures from these papers, they generally appear complete to around the 100-200 m level, while our completeness varies between ~50-75 m. We also note that the often-used $N(1)$, $N(5)$, or similar type of crater age based on a single diameter size is insufficient to obtain an accurate crater model age unless the SFDs are well behaved; as we show in Figs. **48** and **49**, this is rarely the case. It is difficult to know over what range these two sets of authors fit isochrons because that data are not published, and in the earlier paper the figures are not high enough resolution for a meaningful comparison.

We have used our CTX-based crater counts to construct a timeline for the last volcanic activity from each major volcano's calderas (Figs. **57**, **59**, and online supplemental movie). We confirm that Mars has had almost continuous active volcanism throughout its geologic history, with major volcanism ceasing only ~100-150 million years ago, 98% through the planet's history. We note a change from explosive to effusive styles of eruption transitioning at different times across the planet, but generally the transition was made around the Hesperian-Amazonian boundary. We also have shown evidence that volcanism has "shut off" in different locations at different times as Mars' interior has cooled. This started with Apollinaris Mons, continued through the rest of the highlands and Syrtis Major, and ended with the Elysium tholi and the largest of the Tharsis volcanoes.

Besides deriving surface ages to add to the broader picture of Mars' volcanic history, we have used the craters to study implications for the role of secondary craters across the planet. We did not find evidence for a general "background field" of secondaries that becomes statistically important - as determined by an increase in slope of SFDs - for diameters $D \leq 1$ km, contrary to expectations from McEwen and Bierhaus (2006), though this could be due to the relatively isolated regions we examined. We did find evidence that secondaries can occur close to their primaries (Apollinaris Mons) but can be indistinguishable from primaries based on

morphology alone; we also found they may not occur next to larger primaries (such as in Hadriaca and Ulysses Paterae). Conversely, we also confirmed previous results that secondaries can occur very far from a primary crater yet still maintain the classic morphology associated with them (Arsia Mons). These conflicting cases do not have an obvious simple resolution, leaving secondary crater studies still a necessary area of future research.

In an attempt to explain the paucity of secondary craters below 1 km, we used a simple model of crater flux and scaling laws to determine the necessary erosion rate to maintain a SFD, not factoring in that we found SFDs showing evidence of additional heavy erosion. We found an unreasonably rapid requisite erosion rate approximately 10× higher than previous estimates would be necessary to account for this. We also verified using higher resolution imagery for limited locations that we are statistically complete to the crater sizes that we claim, despite the significant decrease in the expected number of craters across several calderas.

Finally, if we assume there are no other young volcanic terrains on Mars that are not associated with a major volcano, ignore the factor of ~2 uncertainty in current isochrons, and take our model crater ages as the actual ages for the volcanoes, we can speculate that most of the Martian meteorites, dating to only a ~few 100 Myr, likely came from the younger flows of the Tharsis Montes. This is in agreement with some other researchers' speculations based on crater ages (*e.g.*, Wood and Ashwal, 1981; Mouginis-Mark *et al*., 1992; Hartmann, 2005), but it disagrees with others based on spectra (*e.g.*, Hamilton *et al.*, 2003), modeling of inferred crystallization versus modification ages (Bouvier *et al.*, 2005), and some interpretations of geologic and petrologic data (McSween, 2002).

Overall, Mars continues to yield more information with higher-resolution imagery, and much can be gleaned from crater studies especially when geologic and geomorphologic context is used in concert. We believe that studies of volcanic calderas with even higher resolution data would not be useful due to the significant resurfacing we observed at the decameter scale in most cases, and that future work should be focused on continuing to map the flanks and studying the characteristics and implications of secondary craters on volcanic terrain.

6. Discussion

Impact craters are important tools for the study of planetary surfaces, processes that affect surfaces, surface ages, properties of planetary crusts or near-surface material, impact physics, and impact flux through time. Specifically for the work presented here, I constructed a new global Martian crater database and analyzed the global and regional crater properties in several of those applications. The database contains a large amount of detailed positional, geometric, and topographic data as well as descriptive interior morphologies, degradation states, and ejecta morphologies and morphometries. These parameters informed the various studies presented here, but they are also generalizable to dozens more that should make this database a useful contribution to the planetary science community for many years.

In proving this database, I explored a large number of previously observed trends. The global distributions of all craters, fresh craters, craters with central peaks, pits, or summit pits, and craters with dunes emplaced were all examined and compared with previous work. The results were comparable and validate this catalog in light of other published results in these areas.

I performed five major analyses of the craters in this database or related work, presented in this thesis. The first deals with the quantification of crater depth-to-diameter ratios, a relationship which is dominated by the collapse process of a crater under gravity but controlled by the strength of the surface. These have been examined previously with coarser data, isolated sub-regions, or other more limited methods. My work is the first to examine this with a global dataset with full morphologic and modification state discriminators. I used the large numbers of craters to examine this relationship of crater depth/Diameter across the entire globe and then by latitude range and terrain type, and mine is the first to compare three different groups of craters in this kind of study – all craters, fresh craters, and the deepest craters. The bulk of the results were incremental updates from previous work in the field and summarized in Table **5**. The three main new results from this examination were that particularly deep craters are found in northern

Chryse basin (in addition to southern Utopia and Isidis which had been known before), the equatorial/polar dichotomy of depth/Diameter ratio is not completely mirrored across the equator but the northern and southern hemispheres display some significant differences (Fig. **28**), and craters at both high latitudes and on just polar terrain are significantly shallower than elsewhere on the planet but increase in depth more rapidly as a function of diameter than the general population. The first new finding is likely explained by lithologic, volcanic, or fine-grained material that can support deeper craters. The second is probably due to differences in crustal and/or ice table thickness. The third finding is explained below in the context of the simple-to-complex crater transition.

The second substantial analysis I conducted with this database was to reexamine the transition between simple and complex craters – simple craters being the classic bowl-shaped type while complex craters form from a larger impact that, because of its size, will experience a broad rebound that creates a flat floor, can undergo collapse circumferential to its rim and show terraces, and/or have an elastic rebound in the center that creates a central peak. Basic cratering physics indicates this is a process significantly dominated by the surface gravity of the object being impacted, but the surface strength has secondary control. Pike (1988) showed this with a finality that has caused people to test his work for the past two decades, revising and refining the basic numbers. In that tradition, this database was used to examine the transition between simple and complex craters based on several different criteria. This is another incremental/revisional result from this database. The final value of ~6.0 km agreed very well with Pike (1988), but it clearly showed there is a terrain dependence of this transition diameter on the planet wherein polar craters had a significantly larger transition diameter (Figs. **31**, **32**). This new result, in the context of the crater depth/Diameter values, led to my proposal of a formation mechanism for these shallow yet large simple high latitude / polar craters: A crater forming in a volatile-rich surface with vaporize nearby and melt them farther away, weakening the crust so that it cannot support a deep crater cavity nor form typical complex crater characteristics.

The third and fourth major results from this database both deal with secondary craters

because of the significant application of crater counting to age-dating surfaces. The basic assumption of age dating is that older surfaces will have a higher density of craters. This assumption requires that (a) cratering be stochastic with time but occur at a predictable rate on average, and (b) cratering be independent with location on the surface such that any given area is as likely as another to be impacted and form a crater. The process of secondary craters belies these: Secondary craters form when large, cohesive ejecta blocks from a primary impact event are launched with sufficient energy to form more craters when they land. Secondary crater formation at this basic level is well understood in theory, but significant observational and experimental work in characterizing secondary craters is lacking. Observations of the distribution of the secondary crater population relative to the primary and the size-frequency distribution of these is an ongoing topic of crater studies: No unified model yet exists that can adequately predict the size distribution of secondary craters from any given primary nor the geographic distribution of where to expect these enigmatic craters. To this end, the global database was used to study two different types of secondary craters – distant clusters and nearby fields.

The former is the third main study discussed in this thesis. In Robbins and Hynek (2011a) (Section 4.1, this thesis), I showed that a single large impact crater on Mars - Lyot Crater - can produce $>10^4$ secondary craters $D \geq 1$ km and emplace clusters of them over 5000 km from the primary – 25% of the way across the planet. While this has been known to happen on the Moon (*e.g.*, Wilhelms *et al.*, 1978) which has a smaller diameter and lower surface gravity, showing this was possible under a larger gravity field had not yet been accomplished. The only previous in-depth case study on Mars examined Zunil Crater (*e.g.*, Preblich *et al*., 2007) and its distribution is dissimilar to Lyot's. More case studies of distant secondary crater fields are needed in order to develop any model to explain their characteristics. My findings for Lyot show that even if these secondary craters were not from Lyot and their properties are not typical of distant secondary crater clusters, one cannot assume they are "safe" from secondary crater contamination even if there is no large primary crater for hundreds or even thousands of

kilometers, even if they are using only kilometer-scale craters. This has the potential to significantly affect geologic mapping, stratigraphic relationships, and any age-dating work via crater counting.

The fourth main analysis examined secondary craters, as well, where I studied 24 primary craters' nearby secondary crater fields in Robbins and Hynek (2011d) (Section 4.2, this thesis). I used the database in the first-of-its-kind global, uniform study of the statistical distribution and properties of secondary crater fields near to their primary crater. The results (Table **7**) showed a general variation between different fields though there were a few generalizable trends and properties. The trends suggest the diameter and geographic distributions of secondary craters relative to their primary crater may be dependent upon terrain type, in support of previous work by Hartmann and Barlow (2006). At a practical level, the work showed that nearby secondary craters have a predictable distribution of where they are on the planet's surface and hence one may be able to account for them by automated means without characterizing every crater as either a primary or secondary. This can speed the modeling of surface ages and estimates of primary crater populations, for it was found to be valid for crater diameters ranging from 5 to 220 km. An extension of this is that particularly large craters - such as Holden Crater with $D \approx 150$ km - will have a secondary crater field that affects a large region of the planet's surface (>3% in Holden's case) and these secondary craters contaminate the crater statistics at diameters larger than 1 km.

With this in mind, the final work in this thesis addressed the age-old application of craters to date surfaces via the additional identification of order 10^5 small craters within major volcanic calderas on the planet to reconstruct the "last gasps" of major summit volcanism for Mars. This was also an incremental result, revising some numbers appearing recently in the literature (mainly Neukum *et al*., 2004, and Werner, 2009), but in a more uniform application of *just* age-dating the last eruptive events from the Martian volcanic calderas: Mars has 24 primary shield volcanoes, and the calderas of 20 were geologically mapped and high-resolution imagery allowed the identification of craters as small as a few 10s of meters in diameter (the remaining

four lack adequate high-resolution coverage). While relative age dating was done at a basic level to show which calderas were older than others, the frequency of craters was compared with established isochrons from the literature (Neukum *et al.*, 2001) to estimate model ages for the surfaces. This chronology system was chosen because it was used in all of our comparisons with ages in the published literature. These were reconstructed into a timeline for each volcano (Fig. **57**) and then combined to give an overview of the major eruptive timeline from each volcanic summit over Mars' history (Fig. **59**). The results agree with previous work that argue for early, widespread volcanism across the planet that steadily became more localized until the most recent eruptive events from the youngest calderas occurred approximately 100-150 million years ago from the large Tharsis montes.

The work throughout this thesis and their applications show a sample of the wide range of studies that can be done with craters, but they can be simplified back to the fundamentals: (1) Craters show that terrains on planets have different properties and (2) different ages, and (3) they can be used to refine our models and understanding of the physics that governs the impact process. Bringing the application closer to home in terms of planetary hazards, knowing more about craters can impact our survival because they inform the population and frequency of extraplanetary impactors. The scaling laws derived from observations, models, and experiments allow for an informed assessment of risk from an approaching bolide. From a military standpoint, understanding craters formed by bombs and missiles is the same as that from an extraplanetary impactor and, historically, those on the forefront of studying craters were employed by the U.S. Department of Defense (*i.e.*, Eugene Shoemaker and David Roddy) and studied bomb detonation sites. Beyond this, though, studying impact craters furthers our knowledge of planetary surface properties under different regimes and criteria, whereby a greater understanding of their characteristics under different environments and circumstances constrains our knowledge of how they form, what they inform us about the surface, and other questions of basic science intrigue.

References

Alzate, N., Barlow, N.G., 2011. Central pit craters on Ganymede. Icarus 211, pp. 1274-1283. doi: 10.1016/j.icarus.2010.10.015.

Anderson, R.C., Dohm, J.M., Golombek, M.P., Haldemann, A.F.C., Franklin, B.J., Tanaka, K.L., Lias, J., Peer, B., 2001. Primary centers and secondary concentrations of tectonic activity through time in the western hemisphere of Mars. J. Geophys. Res. 106, E9, pp. 20,563-20,585.

Andrews-Hanna, J.C., Zuber, M.T., Banerdt, W.B., 2008. The Borealis Basin and the origin of the Martian crustal dichotomy. Nature 453, pp. 1212-1215. doi: 10.1038/nature07011.

Arvidson, R., and 11 colleagues, 1979. Standard techniques for presentation and analysis of crater size-frequency data. Icarus 37, pp. 467-474.

Arvidson, R.E., Coradini, M., Carusi, A., Coradini, A., Fulchignoni, M., Federico, C., Funiciello, R., Salomone, M., 1976. Latitudinal variation of wind erosion of crater ejecta deposits on Mars. Icarus 27, pp. 503-516. doi: 10.1016/0019-1035(76)90166-4.

Baldwin, R.B., 1949. The Face of the Moon. University of Chicago Press: Chicago.

Banks, M.E., Byrne, S., Galla, K., McEwen, A.S., Bray, V.J., Dundas, C.M., Fishbaugh, K.E., Herkenhoff, K.E., Murray, B.C., 2010. Crater population and resurfacing of the Martian north polar layered deposits. J. Geophys. Res. 115, E08006. doi: 10.1029/2009JE003523.

Barlow, N.G., 1988. Crater size-frequency distributions and a revised Martian relative chronology. Icarus 75, pp. 285-305. doi: 10.1016/0019-1035(88)90006-1.

Barlow, N.G., 1995. The degradation of impact craters in Maja Valles in Arabia, Mars. J. Geophys. Res. 100, E11, pp. 23,307-23,316. doi: 10.1029/95JE02492.

Barlow, N.G., 2003. Revision of the "Catalog of Large Martian Impact Craters." Int. Conf. on Mars, Abstract #3073.

Barlow, N.G., 2004. Martian subsurface volatile concentrations as a function of time: Clues from layered ejecta craters. Geophys. Res. Lett. 31, L05703. doi: 10.1029/2003GL019075.

Barlow, N.G., 2005. A review of Martian impact crater ejecta structures and their implications for target properties. in Kenkmann, T., Hörz, F., Deutsch, A., eds. Large meteorite impacts III: Geological Society of America Special paper 384, pp. 433-442.

Barlow, N.G., 2006. Impact craters in the northern hemisphere of Mars: Layered ejecta and central pit characteristics. Meteor. & Planet. Sci. 41, 10, pp. 1425-1436. doi: 10.1111/j.1945-5100.2006.tb00427.x.

Barlow, N.G., 2010. Central pit, central peak, and elliptical craters in the Martian northern hemisphere: New results from the revised Catalog of Large Martian Impact Craters. Lunar Planet. Sci. Conf. XLI, Abstract #1065.

Barlow, N.G., 2011. Constraints on the proposed formation models for Martian central pit craters. Lunar Planet. Sci. Conf. XLII, Abstract #1149.

Barlow, N.G., Boyce, J.M., Costard, F.M., Craddock, R.A., Garvin, J.B., Sakimoto, S.E.H.,

Kuzmin, R.O., Roddy, D.J., Soderblom, L.A., 2000. Standardizing the nomenclature of Martian impact crater ejecta morphologies. J. Geophys. Res. 105, E11, pp. 26,733-26,738. doi: 10.1029/2000JE001258.

Barlow, N.G., Bradley, T.L., 1990. Martian impact craters: Correlations of ejecta and interior morphologies with diameter, latitude, and terrain. Icarus, 87, pp. 156-179.

Barlow, N.G., Perez, C.B., 2003. Martian impact crater ejecta morphologies as indicators of the distribution of subsurface volatiles. J. Geophys. Res. 108, E8. doi: 10.1029/2002JE002036.

Barnouin-Jha, O.S., Schultz, P.H., 1998. Lobateness of impact ejecta deposits from atmospheric interactions. J. Geophys. Res. 103, E11, pp. 25,739-25,756. doi: 10.1029/98JE002025.

Berman, D.C., Hartmann, W.K., 2002. Recent fluvial, volcanic, and tectonic activity on the Cerberus Plains of Mars. Icarus 159, pp. 1-17. doi: 10.1006/icar.2002.6920.

Bevington, P.R., Robinson, D.K., 2003. Data Reduction and Error Analysis for the Physical Sciences, 3rd ed. McGraw-Hill Higher Education, New York. ISBN 0-07-247227-8.

Bierhaus, E.B., Chapman, C.R., Merline, W.J., 2005. Secondary craters on Europa and implications for cratered surfaces. Nature Letters 437, pp. 1125-1127. doi:10.1038/nature04069.

Blasius, K.R., 1976. The record of impact cratering on the great volcanic shields of the Tharsis region of Mars. Icarus 29, pp. 343-361. doi: 10.1016/0019-1035(76)90138-X.

Blasius, K.R., Cutts, J.A., 1980. Global patterns of primary crater ejecta morphology on Mars. in Report of the Planetary Geology Program 1980, NASA Tech. Memo. 82385, pp. 147-149.

Bleacher, J.E., Greeley, R., Williams, D.A., Cave, S.R., Neukum, G., 2007. Trends in the effusive style at the Tharsis Montes, Mars, and implications for the development of the Tharsis Province. J. Geophys. Res. 112, E09005, pp. 1-15. doi: 10.1029/2006JE002873.

Bouvier, A., Blichert-Toft, J., Vervoort, J.D., Albarède, F., 2005. The age of SNC meteorites and the antiquity of the Martian surface. Earth & Plan. Sci. Lett. 240, pp. 221-233. doi: 10.1016/j.epsl.2005.09.007.

Boyce, J.M., Barlow, N.G., Mouginis-Mark, P., Stewart, S., 2010. Rampart craters on Ganymede: Their implications for fluidized ejecta emplacement. Meteor. & Planet. Sci. 45, 4, pp. 638-661. doi: 10.1111.j.1945-5100.2010.01044.x.

Boyce, J.M., Garbeil, H., 2007. Geometric relationships of pristine Martian complex impact craters, and their implications to Mars geologic history. Geo. Res. Lett. 34, L16201. doi: 10.1029/2007GL029731.

Boyce, J.M., Mouginis-Mark, P., Garbeil, H, 2005. Ancient oceans in the northern lowlands of Mars: Evidence from impact crater depth/diameter relationships. J. Geophys. Res. 110, E03008. doi 10.1029/2004JE002328.

Boyce, J.M., Mouginis-Mark, P., Garbeil, H, Tornabene, L.L., 2006. Deep impact craters in the Isidis and southwestern Utopia Planitia regions of Mars: High target material strength as a possible cause. Geo. Res. Lett. 33, L06202. doi: 10.1029/2005GL024462.

Boynton, W.V., and 24 colleagues, 2002. Distribution of hydrogen in the near surface of Mars: Evidence for subsurface ice deposits. Science 297, pp. 81-85, doi:

10.1126/science.1073722.

Bray, V.J., Collins, G.S., Morgan, J.V., 2006. Numerical modeling of impact cratering on the Moon and icy satellites. Lunar Planet Sci. Conf. XXXVII, Abstract #1175.

Byrne, S. and 17 colleagues, 2009. Distribution of mid-latitude ground ice on Mars from new impact craters. Science 325, pp. 1674-1676. doi: 10.1126/science.1175307.

Carr, M.H., Crumpler, L.S., Cutts, J.A., Greeley, R., Guest, J.E., Masursky, H., 1977. Martian impact craters and emplacement of ejecta by surface flow. J. Geophys. Res 82, 28, pp. 4055-4065. doi: 10.1029/JS082i028p04055.

Cattermole, P., Reid, C., 1984. The summit calderas of Alba Patera, Mars. Lunar Planet. Sci. XV. 15, pp. 142-143.

Chapman, C.R., Jones, K.L., 1977. Cratering and obliteration history of Mars. Ann. Rev. Earth Planet. Sci. 5, pp. 515-540.

Chapman, C.R., Haefner, R.R., 1967. A critique of methods for analysis of the diameter-frequency relation for craters with special application to the Moon. J. Geophys. Res. 72, 2, pp. 549-557. doi: 10.1029/JZ072i002p00549.

Chapman, C.R., Merline, W.J., Thomas, P.C., Joseph, J., Cheng, A.F., Izenberg, N., 2002. Impact history of Eros: Craters and boulders. Icarus 155, pp. 104-118. doi: 10.1006/icar.2001.6744.

Christensen, P.R., 2003. Formation of recent Martian gullies through melting of extensive water-rich snow deposits. Nature 422, pp. 45-48. doi: 10.1038/nature01436.

Christensen, P.R., and 25 colleagues, 2001. Mars Global Surveyor Thermal Emission Spectrometer experiment: Investigation description and surface science results. J. Geo. Res. 106, E10, pp. 23,823-23,871. doi: 10.1029/2000JE001370.

Christensen, P.R., and 10 colleagues, 2004. The Thermal Emission Imaging System (THEMIS) for the Mars 2001 Odyssey Mission. SSRv, 110:1, pp. 85-130. doi: 10.1023/B:SPAC.0000021008.16305.94.

Cintala, M.J., 1977. Martian fresh crater morphology and morphometry - a pre-Viking review. in Roddy, D.J., Pepin, R.O., Merrill, R.B., eds. Impact and Explosion Cratering, Pergamon Press: New York, pp. 575-591.

Clifford, S.M., 1993. A model for the hydrologic and climatic behavior of water on Mars. J. Geophys. Res. 98, E6, pp. 10,973,11016. doi: 10.1029/93JE00225.

Costard, F.M., 1989. The spatial distribution of the volatiles in the Martian hydrolithosphere. Earth, Moon, & Plan. 45, pp. 265-290.

Craddock, R.A., Howard, A.D., 2002. The case for rainfall on a warm, wet early Mars. J. Geophys. Res. 107, E11, 5111. doi: 10.1029/2001JE001505.

Craddock, R.A., Maxwell, T.A., 1993. Geomorphic evolution of the Martian highlands through ancient fluvial processes. J. Geophys. Res. 98, E2, pp. 3453-3468. doi: 10.1029/92JE02508.

Craddock, R.A., Maxwell, T.A., Howard, A.D., 1997. Crater morphometry and modification in the Sinus Sabaeus and Margaritifer Sinus regions of Mars. J. Geophys. Res. 102, E6, pp. 13,321-13,340. doi: 10.1029/97JE01084.

Croft, S.K., 1981. On the origin of pit craters. Lunar Planet. Sci. Conf. 88, pp. 196-198.

Daubar, I.J., McEwen, A.S., Byrne, S., Dundas, C.M., Kennedy, M., Ivanov, B.A., 2010. The current Martian cratering rate. Lunar Planet. Sci. Conf., Abstract #1978.

Daubar, I.J., McEwen, A.S., Byrne, S., Dundas, C.M., Keske, A.L., Amaya, G.L., Kennedy, M., Robinson, M.S., 2011. New craters on Mars and the Moon. Lunar Planet. Sci. Conf., Abstract #2232.

Davis, P.A., Soderblom, L.A., 1984. Modeling crater topography and albedo from monoscopic Viking Orbiter images: 1. Methodology. J. Geophys. Res. 89, B11, pp. 9449-9457. doi: 10.1029/JB089iB11p09449.

Dence, M.R., 1968. Shock Metamorphosis of Natural Materials, pp. 169.

Di Achille, G., Hynek, B.M., 2010. Deltas and valley networks on Mars: Implications for a global hydrosphere. Chapter 8 in Cabrol and Grin, eds., 2010. Lakes on Mars. Elsevier Publishing. ISBN/9780444528544.

Dickson, J.L., Fassett, C.I., Head J.W., 2009. Amazonian-aged fluvial valley systems in a climatic microenvironment on Mars: Melting of ice deposits on the interior of Lyot Crater. Geophys. Res. Lett. 36, L08201. doi: 10.1029/2009GL037472.

Fassett, C.I., Head III, J.W., 2007. Valley formation on martian volcanoes in the Hesperian: Evidence for melting of summit snowpack, caldera lake formation, drainage and erosion on Ceraunius Tholus. Icarus 189, pp. 118-135. doi:10.1016/j.icarus.2006.12.021.

Fenton, L.K., Hayward, R.K., 2010. Southern high latitude dune fields on Mars: Morphology, aeolian inactivity, and climate change. Geomorphology 121, pp. 98-121. doi: 10.1016/geomorph.2009.11.006.

Frey, H.V., 2006. Impact constraints on, and a chronology for, major events in early Mars history. J. Geophys. Res. 111, E08S91. doi: 10.1029/2005JE002449.

Frey, H.V., 2008. Ages of very large impact basins on Mars: Implications for the late heavy bombardment in the inner solar system. Geophys. Res. Lett. 35, L13203. doi: 10.1029/2008GL033515.

Galilei, G., 1610. Sidereus Nuncius. Venice: Italy, pp. 1-29.

Garvin, J.B., Sakimoto, S.E.H., Frawley, J.J., 2000. North Polar Region craterforms on Mars: Geometric characteristics from the Mars Orbiter Laser Altimeter. Icarus 144, pp. 329-352. doi: 10.1006/icar.1999.6298.

Garvin, J.B., Sakimoto, S.E.H., Frawley, J.J., 2003. Craters on Mars: Geometric properties from gridded MOLA topography. Int. Conf. on Mars, Abstract #3277.

Gault, D.E., Wedekind, J.A., 1978. Experimental studies of oblique impact. Proc. Lunar Planet. Sci. Conf. 9, pp. 3843-3875.

Gilbert, G.K., 1893. The Moon's face. A study of the origin of its features. Bull. Phil. Soc. Wash. 12:241-292.

Golombek, M.P., and 10 colleagues, 2006. Erosion rates at the Mars Exploration Rover landing sites and long-term climate change on Mars. J. Geophys. Res. 111, E12S10, pp. 1-14. doi: 10.1029/2006JE002754.

Golombek, M.P. and 10 coauthors, 2007. Climate change on Mars from erosion rates at the Mars Exploration Rover landing sites. 7th Int. Conf. on Mars 7, Abstract #3034.

Golombek, M., and 14 colleagues, 2010. Landing sites under consideration for Mars Science

Laboratory. Lunar Plan. Sci. Conf. XLI, Abstract #2407.

Gomes, R., Levison, H.F., Tsiganis, K., Morbidelli, A., 2005. Origin of the cataclysmic Late Heavy Bombardment period of the terrestrial planets. Nature Letters 435, pp. 466-469. doi: 10.1038/nature03676.

Grant, J.A., and 23 coauthors, 2004. Surficial deposits at Gusev Crater along Spirit Rover traverses. Science 305, pp. 807-810. doi: 10.1126/science.1099849.

Grant, J.A., Irwin III, R.P., Grotzinger, J.P., Milliken, R.E., Tornabene, L.L., McEwen, A.S., Weitz, C.M., Squyres, S.W., Glotch, T.D., Thomson, B.J., 2008. HiRISE imaging of impact megabreccia and sub-meter aqueous strata in Holden Crater, Mars. Geology 36, 3, pp. 195-198. doi: 10.1130/G24340A.1.

Grant, J.A., Schultz, P.H., 1990. Gradational epochs on Mars: Evidence from west-northwest of Isidis Basin and Electris. Icarus 84, pp. 166-195.

Grant, J.A., Schultz, P.H., 1993. Degradation of selected Terrestrial and Martian impact craters. J. Geophys. Res. 98, E6, pp. 11,025-11,042. doi: 10.1029/93JE00121.

Greeley, R., Fink, J.H., Gault, D.E., Guest, J.H., 1982. Experimental simulation of impact cratering on icy satellites. in Morrison, D., ed. Satellites of Jupiter. University of Arizona Press: Tucson, pp. 340-378.

Greeley, R., Guest, J.E., 1987. Geologic map of the eastern equatorial region of Mars. USGS Misc. Inv. Series Map I-1802-B.

Greeley, R., Lancaster, N., Steven, L., Peter, T., 1992. Martian aeolian processes, sediments, and features. in Kieffer, H.H., Jakosky, B.M., Snyder, C.W., Matthews, M.S., eds. Mars. pp. 730-766. ISBN 978-0816512577.

Greeley, R., Skypeck, A., Pollack, J.B., 1993. Martian aeolian features and deposits: Comparisons with general circulation model results. J. Geophys. Res. 98, E2, pp. 3183-3196. doi: 10.1029/92JE02580.

Greeley, R., Spudis, P.D., 1981. Volcanism on Mars. Rev. of Geophys. 19, pp. 13-41.

Gwinner, K., Scholten, F., Preusker, F., Elgner, S., Roatsch, T., Spiegel, M., Schmidt, R., Oberst, J., Jaumann, R., Heipke, C., 2010. Topography of Mars from global mapping by HRSC high-resolution digital terrain models and orthoimages: Characteristics and performance. Earth & Plan. Sci. Lett. 294, pp. 506-519. doi: 10.1016/j.epsl.2009.11.007.

Haberle, R.M., Murphy, J.R., Schaeffer, J., 2003. Orbital change experiments with a Mars general circulation model. Icarus 161, pp. 66-89. doi: 10.1016/S0019-1035(02)00017-9.

Hamilton, V.E., Christensen, P.R., McSween, Jr., H.Y., Bandfield, J.L., 2003. Searching for the source regions of Martian meteorites using MGS TES: Integrating Martian meteorites into the global distribution of igneous materials on Mars. Meteorit. & Planet. Sci. 38, pp. 871-885.

Hare, T.M., Skinner, J.A., Tanaka, K.L., Fortezzo, C.M., Bleamaster, L.F., Sucharski, R.M., 2009. GIS-based planetary geologic maps: Recommendations for improved preparation, review, and publication. Lunar Planet. Sci. XL, Abstract #2538.

Hartmann, W.K., 2003. Measurement of Martian erosion / obliteration rates from crater populations. AGU, pp. 7354.

Hartmann, W.K., 2005. Martian cratering 8: Isochron refinement and the chronology of Mars.

Icarus 174, pp. 294-320. doi: 10.1016/j.icarus.2004.11.023.

Hartmann, W.K., 2007. Martian cratering 9: Toward resolution of the controversy about small craters. Icarus Note 189, pp. 274-278. doi: 10.1016/j.icarus.2007.02.011.

Hartmann, W.K., Barlow, N., 2006. Nature of the Martian uplands: Effect on the Martian meteorite age distribution and secondary cratering. Meteorit. & Planet. Sci. 41, pp. 1453-1467.

Hartmann, W.K., Cruikshank, D.P., Degewij, J., Capps, R.W., 1981. Surface materials on unusual planetary object Chiron. Icarus 47, pp. 333-341. doi: 10.10160019-1035(81)90181-0.

Hartmann, W.K., Neukum, G., 2001. Cratering chronology and the evolution of Mars. Space Sci. Rev. 96, pp. 165-194.

Hauber, E., Bleacher, J., Gwinner, K., Williams, D., Greeley, R., 2009. The topography and morphology of low shields and associated landforms of plains volcanism in the Tharsis region of Mars. J. Volcan. and Geo. Res. 185, pp. 69-95. doi: 10.1016/j.volgeores.2009.04.015.

Hauber, E., Brož, P., Jagert, F., 2010. Plains volcanism on Mars: Ages and rheology of lavas. Lunar Planet. Sci. XLI, Abstract #1298.

Hayward, R.K., Mullins, K.F., Fenton, L.K., Hare, T.M., Titus, T.N., Bourke, M.C., Colaprete, A., Christensen, P.R., 2007. Mars Global Digital Dune Database and initial science results. J. Geophys. Res. 112, E11007. doi: 10.1029/2007JE002943.

Hayward, R.K., Fenton, L.K., Tanaka, K.L., Mullins, K.F., Titus, T.N., Bourke, M.C., Hare, T.M., Christensen, P.R., 2008. Mars Global Digital Dune Database: Distribution in north polar region and comparison to equatorial region. Lunar Planet Sci. Conf. XXXIX, Abstract, #1208.

Head, J.W., Kreslavsky, M.A., Pratt, S., 2002. Northern lowlands of Mars: Evidence for widespread volcanic flooding and tectonic deformation in the Hesperian Period. J. Geophys. Res.-Planets 107, pp. 5003. doi: 10.1029/2000JE001445.

Head, J.W., Wilson, L., 1998a. Tharsis Montes as composite volcanoes?: 1. The role of expolsive volcanism in edifice construction and implications for the volatile contents of edifice-forming magmas. Lunar Planet. Sci. XXIX, Abstract #1127.

Head, J.W., Wilson, L., 1998b. Tharsis Montes as composite volcanoes?: 3. Lines of evidence for explosive volcanism in edifice construction. Lunar Planet. Sci. Conf. XXIX, Abstract #1124.

Head, J.W., Wilson, L., 2011. The Noachian-Hesperian transition on Mars: Geological evidence for a punctuated phase of global volcanism as a key driver in climate change and atmospheric evolution. Lunar Planet. Sci. Conf. XLII, Abstract #1214.

Heiken, G.H., Vaniman, D.T., French, B.M., 1991. Lunar sourcebook - A user's guide to the Moon. ISBN 0521334446.

Herkenhoff, K.E., Plaut, J.J., 2000. Surface ages and resurfacing rates of the polar layered deposits on Mars. Icarus 144, pp. 243-253. doi: 10.1006/icar.1999.6287.

Hodges, C.A., Moore, J.J., 1994. Atlas of volcanic landforms on Mars. Washington: U.S. G.P.O.

Hoefen, T.M., Clark, R.N., Banfield, J.L., Smith, M.D., Pearl, J.C., Christensen, P.R., 2003. Discovery of olivine in the Nili Fossae region of Mars. Science 203, pp. 627-630. doi: 10.1126/science.1089647.

Horner, V.M., Greeley, R., 1987. Effects of elevation and ridged plains thicknesses on Martian crater ejecta morphology. Proc. Lunar Planet. Sci. Conf, p. 2, XVII. J. Geophys. Res. 92, B4, pp. E561-E569. doi: 10.1029/JB092iB04p0E561.

Hynek, B.M., Philips, R.J., Arvidson, R.E., 2003. Explosive volcanism in the Tharsis region: Global evidence in the Martian geologic record. J. Geophys. Res. 108, E9, 5111, doi: 10.1029/2003JE00262.

Ivanov, B.A., 2001. Mars/Moon cratering rate ratio estimates. Chronology and Evolution of Mars 96, pp. 87-104.

Ivanov, M.A., Head, J.W., 2006. Alba Patera, Mars: Topography, structure, and evolution of a unique late Hesperian-early Amazonian shield volcano. J. Geophys. Res. 111, E09003, pp. 1-31. doi: 10.1029/2005JE002469.

Johansen, L.A., 1979. The latitude dependence of Martian splash cratering and its relationship to water. in Reports of the Planetary Geological Program 1978-1979, NASA Tech. Memo. 80339, pp. 123-125.

Kargel, J.S., 1986. Morphologic variations of Martian rampart crater ejecta and their dependencies and implications. Lunar Planet. Sci. Conf. XVII, pp. 410-411.

Kirchoff, M.R., Sherman, K.M., Chapman, C.R., 2011. Reevaluation of Lunar impactor population evolution: Preliminary results from crater distributions on diverse terrains. Lunar and Planet. Sci. Conf. XLII, Abstract #2702.

Komatsu, G., Ori, G.G., Di Lorenzo, S., Rossi, A.P., Neukum, G., 2007. Combinations of processes responsible for Martian impact crater "layered ejecta structures" emplacement. J. Geophys. Res. 112, E06005. doi: 10.1029/2006JE002787.

Kreslavsky, M., 2008. Young populations of small impact craters on Mars as observed in HiRISE images. Fall AGU, B1361.

Kuiper, G.P., 1960. Photographic Lunar Atlas. University of Chicago Press: Chicago.

Lang, N.P., McSween, H.Y., Tornabene, L.L., Hardgrove, C.J., Christensen, P.R., 2010. Re-examining the relationship between Apollinaris Patera and the basalts of the Gusev crater plains, Mars. J. Geophys. Res.-Planets 115, E14. doi: 10.1029/2009JE003397.

Lapen, T.J., Righter, M., Brandon, A.D., Debaille, V., Beard, B.L., Shafer, J.T., Peslier, A.H., 2010. A younger age for ALH84001 and its geochemical link to Shergottite sources on Mars. Science 328, pp. 347-351. doi: 10.1126/science.1185395.

Levison, H.F., Dones, L., Champan, C.R., Stern, S.A., Duncan, M.J., Zahnle, K., 2001. Could the Lunar "Late Heavy Bombardment" have been triggered by the formation of Uranus and Neptune? Icarus 151, 2, pp. 286-306. doi: 10.1006/icar.2001.6608.

Lissauer, J.J., Squyers, S.W., Hartmann, W.K., 1988. Bombardment history of the Saturn system. J. Geophys. Res. 93, pp. 13,776-13,804. doi: 10.1029/JB093iB11p13776.

Lucchitta, B.K., 1977. Crater clusters and light mantle at the Apollo 17 site; A result of secondary impacts from Tycho. Icarus 30, pp. 80-96, doi: 10.1016/0019-1035(77)90123-3.

Malin, M.C., Dzurisin, D., 1977. Landform degradation on Mercury, the Moon, and Mars - Evidence from crater depth/diameter relationships. J. Geophys. Res. 82, 2, pp. 376-388. doi: 10.1029/JB082i002p00376.

Malin, M.C., Edgett, K.S., 2000. Evidence for recent groundwater seepage and surface runoff on Mars. Science 288, pp. 2330-2335. doi: 10.1126/science.288.5475.2330.

Malin, M.C., Edgett, K.S., Posiolova, L.V., McColley, S.M., Noe Dobrea, E.Z., 2006. Present-day impact cratering rate and contemporary gully activity on Mars. Science 314, pp. 1573-1577. doi: 10.1126/science.1135156.

Malin, M.C., and 13 colleagues, 2007. Context Camera investigation on board the Mars Reconnaissance Orbiter. J. Geophys. Res. 112, E5. doi: 10.1029/2006JE002808.

Mandelbrot, B., 1967. How long is the coast of Britain? Statistical self-similarity and fractional dimension. Science 156, pp. 636-639.

McCauley, J.F., 1973. Mariner 9 evidence for wind erosion in the equatorial and mid-latitude regions of Mars. J. Geophys. Res. 78, 20, pp. 4123-4137. doi: 10.1029/JB078i020p04123.

McEwen, A.S., Bierhaus, E.B., 2006. The importance of secondary cratering to age constraints on planetary surfaces. Annu. Rev. Earth Planet. Sci. 34, pp. 535-567. doi: 10.1146/annurev.earth.34.031405.125018.

McEwen, A.S., Preblich, B.S., Turtle, E.P., Artemieva, N.A., Golombek, M.P., Hurst, M., Kirk, R.L., Burr, D.M., Christensen, P.R., 2005. The rayed crater Zunil and interpretations of small impact craters on Mars. Icarus 176, pp. 351-381. doi: 10.1016/j.icarus.2005.02.009.

McEwen, A.S., and 14 colleagues, 2007. Mars Reconnaissance Orbiter's High Resolution Imaging Science Experiment (HiRISE). J. Geophys. Res. 112:E5. doi: 10.1029/2005JE002605.

McGill, G.E., Squyres, S.W., 1991. Origin of the Martian crustal dichotomy - Evaluating hypotheses. Icarus 93, pp. 386-393. doi: 10.1016/0019-1035(91)90221-E.

McKinnon, W.B., Melosh, H.J., 1980. Evolution of planetary lithospheres: Evidence from multiringed structures on Ganymede and Callisto. Icarus 44, pp. 454-471. doi: 10.1016/0019-1035(80)90037-8.

McSween, Jr., H.Y., 2002. The rocks of Mars, from far and near. Meteor. Planet. Sci. 37, pp. 7-25.

Mellon, M.T., Jakosky, B.M., 1995. The distribution and behavior of Martian ground ice during past and present epochs. J. Geophys. Res. 100, E6, pp. 11,781-11,799. doi: 10.1029/95JE01027.

Melosh, H.J., 1989. Impact cratering: A geologic process. Oxford University Press: New York.

Moore, J.M., Howard, A.D., 2005. Large alluvial fans on Mars. J. Geophys. Res. 110, E04005. doi: 10.1029/2004JE002352.

Morris, R.V., and 16 colleagues, 2008. Iron mineralogy and aqueous alteration from Husband Hill through Home Plate at Gusev Crater, Mars: Results from the Mössbauer instrument on the Spirit Mars Exploration Rover. J. Geophys. Res.-Planets 113:E12. doi: 10.1029/2008JE003201.

Mouginis-Mark, P.J., 1979. Martian fluidized crater morphology: Variations with crater size, latitude, altitude, and target material. J. Geophys. Res., 84, B14, pp. 8011-8022. doi: 10.1029/JB084iB14p08011.

Mouginis-Mark, P.J., Garbeil, H., Boyce, J.M., Ui, S.E.C., Baloga, S.M., 2004. Geometry of Martian impact craters: First results from an interactive software package. J. Gephys. Res. 109, E08006. doi: 10.1029/2003JE002147.

Mouginis-Mark, P.J., Hayashi, J.N., 1993. Shallow and deep fresh impact craters in Hesperia Planum, Mars. Earth, Moon, & Plan. 61, pp. 1-20.

Mouginis-Mark, P.J., McCoy, T.J., Taylor, G.J., Keil, K., 1992. Martian parent craters for the SNC meteorites. J. Geophys. Res. 97, E6, pp. 10,213-10,225. doi: 10.1029/92JE00612.

Mouginis-Mark, P.J., Wilson, L., Zibelman, J.R., 1988. Polygenic eruptions on Alba Patera, Mars. Bull. of Volcan. 50, pp. 361-379. doi: 10.1007/BF01050636.

Muhleman, D.O., Butler, B.J., Grossman, A.W., Slade, M.A., 1991. Radar images of Mars. Science 253, pp. 1508-1513. doi: 10.1126/science.253.5027.1508.

Mutch, P., Woronow, A., 1980. Martian rampart and pedestal craters' ejecta-emplacement: Coprates Quadrangle. Icarus 41, pp. 259-268. doi: 10.1016/0019-1035(80)90009-3.

Neukum, G., 2008. The lunar and Martian cratering records and chronologies. Lunar Planet. Sci. XXXIX, Abstract #2509.

Neukum, G., and 11 colleagues, 2004. Recent and episodic volcanic and glacial activity on Mars revealed by the High Resolution Stereo Camera. Nature 432, pp. 971-979.

Neukum, G., and 12 colleagues, 2007. Episodicity in the geological evolution of Mars: Resurfacing events and ages from cratering analysis of image data and correlation with radiometric ages of Martian meteorites. Int. Conf. on Mars 7, Abstract #3015.

Neukum, G., Hiller, K., 1981. Martian ages. J. Geophys. Res. 86, pp. 3097-3121. doi: 10.1029/JB086iB04p03097.

Neukum, G., Hiller, K., Henkel, J., Bodechtel, J., 1979. Surface ages of Martian shield volcanoes and channels. Lunar Planet. Sci. X, pp. 907-909.

Neukum, G., Ivanov, B.A., and Hartmann, W.K., 2001. Cratering records in the inner solar system in relation to the lunar reference system. Chronology and Evolution of Mars 96, pp. 55-86.

Neukum, G., Jaumann, R., 2004. HRSC: The High Resolution Stereo Camera of Mars Express. in Wilson, A., Chicarro, A., eds. ESA Special Publications 1240, pp. 17-35.

Neukum, G., Werner, S.C., Ivanov, B.A., 2006. The characteristics of the impact crater production size-frequency distributions on the solar system planetary bodies, their relationships to asteroidal and cometary impacts, and the question of secondary-cratering contributions. Planetary Chronology Workshop, Abstract #6005.

Neumann, G.A., Abshire, J.B., Aharonson, O., Garvin, J.B., Sun, X., and Zuber, M.T., 2003a. Mars Orbiter Laser Altimeter pulse width measurements and footprint-scale roughness. Geophys. Res. Lett., 30, 11, pp. 1561. doi: 10.1029/2003GL017048.

Neumann, G.A., Lemoine, F.G., Smith, D.E., Zuber, M.T., 2003b. The Mars Orbiter Laser Altimeter archive: Final precision experiment data record release and status of radiometry. Lunar Planet. Sci. XXXIV, Abstract #1978.

Nimmo, F., Tanaka, K., 2005. Early crustal evolution of Mars. Annu. Rev. Earth Planet. Sci. 33, pp. 133-161. doi: 10.1146/annurev.earth.33.092203.122637.

Nyquist, L.E., Bogard, D.D., Shih, C.-Y., Greshake, A., Stöffler, D., Eugster, O., 2001. Ages and geologic histories of the Martian meteorites. Chron. and Evo. of Mars 96, pp. 105-164.

Oberbeck, V.R., Morrison, R.H., 1974. Laboratory simulation of the herringbone pattern associated with lunar secondary crater chains. Moon 9, pp. 415-455. doi: 10.1007/BF00562581.

Ong, L., Berger, A.J., Melosh, H.J., 2011. Characterization of a Corinto Crater ray on Mars. Lunar Planet. Sci. Conf., Abstract #1552.

Ostrach, L.R., Robinson, M.S., Denevi, B.W., Thomas, P.C., 2011. Effects of incidence angle on crater counting observations. Lunar Planet. Sci. Conf. XLII, Abstract #1202.

Pasckert, J.H., Hiesinger, H., Reiss, D., 2010. Rheology and age of lava flows on Elysium Mons, Mars. Lunar Planet. Sci. XLI, Abstract #1903.

Passey, Q.R., Shoemaker, E.M., 1982. Craters and basins on Ganymede and Callisto - Morphological indicators of crustal evolution. in Morrison, D., ed. Satellites of Jupiter. University of Arizona Press: Tucson, pp. 379-434.

Peterson, J.E., 1978. Volcanism in the Noachis-Hellas region of Mars, 2. Proc. Lunar. Sci. Conf. 9, pp. 3411-3432.

Phillips, R.J., and 10 colleagues, 2001. Ancient geodynamics and global-scale hydrology on Mars. Science 291, pp. 2587-2591. doi: 10.1126/science.1058701.

Pike, R.J., 1976. Crater dimensions from Apollo data and supplemental sources. Moon 15, pp. 463-477. doi: 10.1007/BF00562253.

Pike, R.J., 1977. Apparent depth/apparent diameter relation for lunar craters. Proc. Lunar. Sci. Conf. 8, pp. 3427-3436.

Pike, R.J., 1980. Formation of complex impact craters: Evidence from Mars and other planets. Icarus 43, pp. 1-19. doi: 10.1016/0019-1035(80)90083-4.

Pike, R.J., 1988. Geomorphology of impact craters on Mercury. pp. 165-273. Chapter 8 in Vilas, F., Chapman, C.R., and Matthews, M.S., eds., 1988. Mercury. University of Arizona Press. ISBN 0-8165-1085-7.

Plescia, J.B., 1994. Geology of the small Tharsis volcanoes: Jovis Tholus, Ulysses Patera, Biblis Patera, Mars. Icarus 111, pp. 246-269. doi: 10.1006/icar.1994.1144.

Plescia, J.B., Saunders, R.S., 1979. The chronology of the Martian volcanoes. Proc. Lunar. Sci. Conf. 10, pp. 2841-2859.

Popova, O.P., Hartmann, W.K., Nemtchinov, I.V., Richardson, D.C., Berman, D.C., 2007. Crater clusters on Mars: Shedding light on Martian ejecta launch conditions. Icarus 190, pp. 50-73. doi: 10.1016/j.icarus.2007.02.022.

Preblich, B.S., McEwen, A.S., Studer, D.M., 2007. Mapping rays and secondary craters from the martian crater Zunil. J. Geophys. Res. 112:E05006, pp. 1-18. doi: 10.1029/2006JE002817.

Putzig, N.E., Mellon, M.T., 2007. Apparent thermal inertia and the surface heterogeneity of Mars. Icarus 191, pp. 68-94. doi: 10.1016/j.icarus.2007.05.013.

Quaide, W.L., Gault, D.E., Schmidt, R.A., 1965. Gravitative effects on lunar impact structures. Annals of the New York Academy of Sci. 123, pp. 563-572.

Rafkin, S.C.R., Michaels, T.I., 2003. Meteorological predictions for 2003 Mars Exploration Rover high-priority landing sites. J. Geophys. Res. 108, E12, pp. 1-23. doi: 10.1029/2002JE002027.

Raitala, J., 1989. Development of the Alba Patera volcano on Mars. Adv. Space Res. 9, 6, pp. (6)143-(6)146.

Robbins, S.J., Di Achille, G., Hynek, B.M., 2011. The volcanic history of Mars: High-resolution crater-based studies of the calderas of twenty volcanoes. Icarus, 211, pp. 1179-1203. doi: 10.1016/j.icarus.2010.11.012.

Robbins, S.J., Hynek, B.M., 2010. Progress towards a new global catalog of Martian craters and layered ejecta properties, complete to 1.5 km. Lunar Plan. Sci. Conf. XLI, Abstract #2257.

Robbins, S.J., Hynek, B.M., 2011a. Distant secondary craters from Lyot crater, Mars, and implications for the surface ages of planetary bodies. Geo. Res. Lett. 38, L05201. doi: 10.1029/2010GL046450.

Robbins, S.J., Hynek, B.M., 2011b. A new global database of Mars impact craters to 1 km: 1. Database creation, properties, and parameters. In prep.

Robbins, S.J., Hynek, B.M., 2011c. A new global database of Mars impact craters to 1 km: 2. Global and regional properties and variations, and their implications to surface properties and gravity scaling. In prep.

Robbins, S.J., Hynek, B.M., 2011d. Secondary crater fields from 24 large primary craters on Mars: Insights into nearby secondary crater production. J. Geophys. Res., submitted. doi: 10.1029/2011JG003820.

Roberts, G.P., Crawford, I.A., Peacock, D., Vetterlein, J., Parfitt, E., Bishop, L., 2007. Possible evidence for on-going volcanism on Mars as suggested by thin, elliptical sheets of low-albedo particulate material around pits and fissures close to Cerberus Fossae. Earth, Moon, & Plan. 101, pp. 1-16. doi: 10.1007/s11038-007-9140-z.

Roddy, D.J., Isabell, N.R., Mardock, C.L., Hare, T.M., Wyatt, M.B., Soderblom, L.M., Boyce, J.M., 1998. 1: Martian impact craters, ejecta blankets, and related morphologic features: Computer digital inventory in Arc/Info and Arcview format. Lunar. Planet. Sci. XXIX, Abstract #1874.

Salamunićcar, G., Lončarić, S., Pina, P., Bandeira, L., Saraiva, J., 2011. MA130301GT catalogue of Martian impact craters and advanced evaluation of crater detection algorithms using diverse topography and image datasets. Planet. & Space Sci. 59, pp. 111-131. doi: 10.1016/j.pss.2010.11.003.

Schimerman, L.A. ed., 1973. The Lunar cartographic dossier. Series NASA-CR 1464000.

Schultz, P.H., 1992. Atmospheric effects on ejecta emplacement. J. Geophys. Res. 97, E7, pp. 11,623-11,662.

Schultz, P.H., Gault, D.E., 1979. Atmospheric effects on Martian ejecta emplacement. J. Geophys. Res. 84, B13, pp. 7669-7687.

Schultz, P.H., Lutz, A.B., 1988. Polar wandering of Mars. Icarus 73, pp. 91-141. doi:

10.1016/0019-1035(88)90087-5.

Scott, D.H., Tanaka, K.L., 1986. Geologic map of the western equatorial region of Mars. USGS Mic. Inv. Ser. Map I-1802-A.

Searls, M.L., Phillips, R.J., 2007. Tectonics of Utopia Basin, Mars: Results from finite element loading models. Lunar. Planet. Sci. Conf. XXXVIII, Abstract #1965.

Shoemaker, E.M., 1962. Interpretation of lunar craters. In Physics and Astronomy of the Moon, ed. Z. Kopal, pp. 283-359. New York: Academic.

Shoemaker, E.M., 1965. Preliminary analysis of the fine structure of the lunar surface in Mare Cognitum. JPL Tech. Report No. 32-700. In The Nature of the Lunar Surface, ed. W.N. Heiss, D.R., Menzel, J.A. O'Keefe, pp. 23-77. Baltimore: Johns Hopkins Press.

Schultz, P.H., Singer, J., 1980. A comparison of secondary craters on the Moon, Mercury, and Mars. Proc. Lunar Planet. Sci. Conf. 11, pp. 2243-2259.

Scott, D.H., Tanaka, K.L., 1986. Geologic map of the western equatorial region of Mars. USGS Misc. Inv. Series Map I-1802-A.

Senft, L.E., Stewart, S.T., 2008. Impact crater formation in icy layered terrains on Mars. Meteor. & Planet. Sci. 43, 12, pp. 1993-2013. doi: 10.1111/j.1945-5100.2008.tb00657.x.

Skinner, J.A., Jr., Nava, R.A., 2011. Using large crater clusters to identify potential source craters on Mars: Technical methods and science applications. Lunar Planet. Sci. Conf. XLII, Abstract #2502.

Sladoje, N., and J. Žinić, 1997. Ellipses estimation from their digitization. Discrete Geometry for Computer Imagery in Lecture Notes in Computer Science, 1347, pp. 187-198, doi: 10.1007/BFb004840.

Smith, D.E., and 23 colleagues, 2001. Mars Orbiter Laser Altimeter: Experiment summary after the first year of global mapping on Mars. J. Geophys. Res. 106, pp. 23,689-23,722. doi: 10.1029/2000JE001364.

Smith, P.H., and 35 colleagues, 2009. H_2O at the Phoenix Landing Site. Science 325, pp. 58-61. doi: 10.1126/science.1172339.

Soderblom, L.A., Condit, C.D., West, R.A., Herman, B.M., Kreidler, T.J., 1974. Martian planetwide crater distributions: Implications for geologic history and surface processes. Icarus 22, pp. 239-263. doi: 10.1016/0019-1035(74)90175-4.

Soderblom, L.A., Kreidler, T.J., Masubsky, H., 1973. Latitudinal distribution of a debris mantle on the Martian surface. J. Geophys. Res. 78, 20, pp. 4117-4122. doi: 10.1029/JB078i020p04117.

Solomon, S.C., and 16 colleagues, 2005. New perspectives on ancient Mars. Science 307, pp. 1214-1220. doi: 10.1126/science.1101812.

Spudis, P.D., Guest, J.E., 1988. Stratigraphy and geologic history of Mercury. pp. 118-164. Chapter 7 in Vilas, F., Chapman, C.R., and Matthews, M.S., eds., 1988. Mercury. University of Arizona Press. ISBN 0-8165-1085-7.

Šrámek, O., Zhong, S., 2010. Long-wavelength stagnant lid convection with hemispheric variation in lithospheric thickness: Link between Martian crustal dichotomy and Tharsis? J. Geophys. Res. 115, E09010. doi: 10.1029/2010JE003597.

Stepinski, T.F., Mendenhall, M.P., Bue, B.D., 2009. Machine cataloging of impact craters on

Mars. Icarus 203, pp. 77-87. doi: 10.1016/j.icarus.2009.04.026.

Stewart, S.T., Valiant, G.J., 2006. Martian subsurface properties and crater formation processes inferred from fresh impact crater geometries. Meteor. & Planet. Sci. 41, 10, pp. 1509-1537.

Strom, R.G., Chapman, C.R., Merline, W.J., Solomon, S.C., Head, J.W., 2008. Mercury cratering record viewed from MESSENGER's first flyby. Science 321, pp. 79-81. doi: 10.1126/science.1159317.

Strom, R.G., Croft, S.K., Barlow, N.G., 1992. The Martian impact cratering record. in Kieffer, H.H., Jakosky, B.M., Snyder, C.W., Matthews, M.S., eds. Mars. pp. 383-423. ISBN 978-0816512577.

Tanaka, K.L., 1982. A new time-saving crater-count technique, with application to narrow features. pp. 123-125. in Holt, H.E. ed. Planetary Geology and Geophysics Program Report, NASA Technical Memo., NASA TM-85127.

Tanaka, K.L., 1986. The stratigraphy of Mars. J. Geophys. Res. 91, E139-E158. doi: 10.1029/JB09liB13p0E139.

Tanaka, K.L., Fortezzo, C.M., Dohm, J.M., Irwin III, R.P., Skinner, Jr., J.R., Hare, T.M., Platz, T., Robbins, S.J., 2011. Completing the New Global Geologic Map of Mars. Lunar Plan. Sci. Conf. XLII, Abstract #2265.

Tanaka, K.L., Hare, T.M., Skinner, J.A., 2005. Geologic map of the northern plains of Mars. US Geol. Surv. Misc. Invest. Ser. Map, I-2888.

Tanaka, K.L., Isabell, N.K., Scott, D.H., Greeley, R., Guest, J.E., 1988. The resurfacing history of Mars: A synthesis of digitized, Viking-based geology. Proc. Lunar. Sci. Conf. 18, pp. 665-678.

Tanaka, K.L., Skinner, J.A., Crumpler, L.S., Dohm, J.M., 2009. Assessment of planetary Geomorphologic mapping techniques for Mars using terrestrial analogs: The SP Mountain area of the San Francisco Volcanic Field, Arizona. Planet. and Space Sci. 57, pp. 510-532. doi: 10.1016/j.pss.2008.06.012.

Thomson, B.J., Head III, J.W., 2001. Utopia Basin, Mars: Characterization of topography and morphology and assessment of the origin and evolution of basin internal structure. J. Geophys. Res. 106, pp. 1-22. doi: 10.1029/2000JE001355.

Tornabene, L.L., McEwen, A.S., Caudill, C., Osinski, G.R., Wray, J.J., Marzo, G.A., Mustard, J.F., Skok, J.R., Grant, J.A., and Mattson, S., 2010. A crater-exposed bedrock database for Mars with applications for determining the composition and structure of the upper crust. Lunar Planet. Sci. XXXIX, Abstract #1737.

Vincenty, T., 1975. Direct and inverse solutions of geodesics on the ellipsoid with application of nested equations. Survey Review, XXIII(176), pp. 88-93.

Werner, S.C., 2008. The early Martian evolution - Constraints from basin formation ages. Icarus 195, pp. 45-60. doi: 10.1016/j.icarus.2007.12.008.

Werner, S.C., 2009. The global Martian volcanic evolutionary history. Icarus 201, pp. 44-68. doi: 10.1016/j.icarus.2008.12.019.

Werner, S.C. Ivanov, B.A., Neukum, G., 2009. Theoretical analysis of secondary cratering on Mars and an image-based study on the Cerberus Plains. Icarus 200, pp. 406-417. doi:

10.1016/j.icarus.2008.10.011.

Wilcox, B.B., Robinson, M.S., Thomas, P.C., Hawke, B.R., 2005. Constraints on the depth and variability of the Lunar regolith. Meteor. & Planet. Sci. 40, 5, pp. 695-710. doi: 10.1111/j.1945-5100.2005.tb00974.x.

Wilhelms, D.E., El-Baz, F., 1977. Geologic Map of the East Side of the Moon. USGS Misc. Inv. Series Map I-948.

Wilhelms, D.E., Oberbeck, V.R., Aggarwal, H.R., 1978. Size-frequency distributions of primary and secondary lunar impact craters. Lunar Plan. Sci. Conf. Proceedings, pp. 3735-3762.

Williams, D.A., Greeley, R., Zuschneid, W., Werner, S.C., Neukum, G., Crown, D.A., Gregg, T.K.P., Gwinner, K., Raitala, J., 2007. Hadriaca Patera: Insights into its volcanic history from Mars Express High Resolution Stereo Camera. J. Geophys. Res. 122, E10004, pp. 1-18. doi: 10.1029/2007JE002924.

Williams, D.A., Greeley, R., Werner, S.C., Michael, G., Crown, D.A., Neukum, G., Raitala, J., 2008. Tyrrhena Patera: Geologic history derived from Mars Express High Resolution Stereo Camera. J. Geophys. Res. 113:E11005, pp. 1-14. doi: 10.1029/2008JE003104.

Williams, D.A., and 15 colleagues, 2009. The Circum-Hellas Volcanic Province, Mars: Overview. Plan. & Space Sci. 57, pp. 895-916. doi: 10.1016/j.pss.2008.08.010.

Wilson, L., Head III, J.W., 1994. Mars: Review and analysis of volcanic eruption theory and relationships to observed landforms. Rev. Geophys. 32, pp. 221-263.

Wilson, L., Head, J.W., Mitchell, K.L., 1998. Tharsis Montes as composite volcanoes?: 2. Lines of evidence for explosive volcanism in far-field deposits. Lunar Planet. Sci. XXIX, Abstract #1125.

Wood, C.A., Andersson, L., 1978. Lunar crater morphometry: New data. Proc. Lunar Planet. Sci. Conf. 9, pp. 1267-1269.

Wood, C.A., Ashwal, L.D., 1982. SNC meteorites: Igneous rocks from Mars? Proc. Lunar Planet. Sci. Conf. 12, pp. 1359-1375.

Wood, C.A., Head, J.W., Cintala, M.J., 1978. Interior morphology of fresh Martian craters: The effects of target characteristics. Proc. Lunar Planet. Sci. Conf. 9, pp. 3691-3709.

Woronow, A., Mutch, P., 1980. On the origin of Martian pedestal, lobate, and multilobate ejecta deposits. Lunar Planet. Sci. Conf. XI, pp. 1282-1284.

Zhong, S.. 2009. Migration of Tharsis volcanism on Mars caused by differential rotation of the lithosphere. Nat-Geosci 2, pp. 19-23. doi: 10.1038/ngeo392.

Zuber, M.T., Smith, D.E., Solomon, S.C., Muhleman, D.O., Head, J.W., Garvin, J.B., Abshire, J.B., and Bufton, J.L., 1992. The Mars Observer laser altimeter investigation. J. Geo. Rev. 97, pp. 7781-7797.

Zwolak, J.W., Boggs, P.T., Watson, L.T., 2004. ODRPACK95: A weighted orthogonal distance regression code with bound constraints. Technical Report TR-04-31, Computer Science, Virginia Tech.

Appendix A - Columns in the Database and Brief Descriptions

This Appendix lists all columns present in the released database as well as a brief description. Text `in fixed-width font` is the column name as it appears in the database. For brevity and since many columns effectively have the same description, items [in square brackets] are multiple instances of the prefix or suffix with the text in square brackets as the variable. For example, `LATITUDE_CIRCLE_[IMAGE, TOPOG]` indicates that there are two columns in the database, one named `LATITUDE_CIRCLE_IMAGE` and the other `LATITUDE_CIRCLE_TOPOG`.

`CRATER_ID` Crater ID for internal use, based upon the region of the planet (1/16ths), the "pass" under which the crater was identified, and the order in which it was identified.

`LATITUDE_CIRCLE_[IMAGE, TOPOG]` Latitude from the derived center of a non-linear least-squares circle fit to the vertices selected to manually identify the crater rim. Units are decimal degrees North.

`LONGITUDE_CIRCLE_[IMAGE, TOPOG]` Longitude from the derived center of a non-linear least-squares circle fit to the vertices selected to manually identify the crater rim. Units are decimal degrees East.

`LATITUDE_CIRCLE_SD_[IMAGE, TOPOG]` Uncertainty in the derived crater center from the non-linear least-squares circle fit.

`LONGITUDE_CIRCLE_SD_[IMAGE, TOPOG]` Uncertainty in the derived crater center from the non-linear least-squares circle fit.

`LATITUDE_ELLIPSE_[IMAGE, TOPOG]` Latitude from the derived center of a non-linear least-squares ellipse fit to the vertices selected to manually identify the crater rim. Units are decimal degrees North.

`LONGITUDE_ELLIPSE_[IMAGE, TOPOG]` Longitude from the derived center of a non-linear

least-squares ellipse fit to the vertices selected to manually identify the crater rim. Units are decimal degrees East.

`DIAM_CIRCLE_[IMAGE, TOPOG]` Diameter from a non-linear least-squares circle fit to the vertices selected to manually identify the crater rim. Units are km.

`DIAM_CIRCLE_SD_[IMAGE, TOPOG]` Uncertainty in the derived crater diameter from the non-linear least-squares circle fit.

`DIAM_ELLIPSE_MAJOR_[IMAGE, TOPOG]` Major axis of a non-linear least-squares ellipse fit to the vertices selected to manually identify the crater rim. Units are km.

`DIAM_ELLIPSE_MINOR_[IMAGE, TOPOG]` Minor axis of a non-linear least-squares ellipse fit to the vertices selected to manually identify the crater rim. Units are km.

`DIAM_ELLIPSE_ECCEN_[IMAGE, TOPOG]` Eccentricity of the non-linear least-squares ellipse fit, defined as $e = \sqrt{1 - b^2/a^2}$.

`DIAM_ELLIPSE_ECCEN_[IMAGE, TOPOG]` Ellipticity of the non-linear least-squares ellipse fit, defined as $\varepsilon = a/b$.

`DIAM_ELLIPSE_ANGLE_[IMAGE, TOPOG]` Tilt angle of the non-linear least-squares ellipse fit. Units are degrees between ±90° where 0° has the major axis aligned along a line of latitude, and positive values are counter-clockwise.

`DEPTH_RIM_TOPOG` Average elevation of each of the manually determined *N* points along the crater rim. Points are selected as relative topographic highs under the assumption they are the least eroded so most original points along the rim. Units are km.

`DEPTH_RIM_SD_TOPOG` The standard deviation from the mean of the *N* points along the rim.

`DEPTH_SURFACE_TOPOG` Average elevation of each of the manually determined *N* points outside of the crater rim and any visible ejecta blanket. This is notoriously difficult to estimate due to ejecta blankets from the crater of interest and other

craters, as well as other complicating topologic features. Units are km.

DEPTH_SURFACE_SD_TOPOG The standard deviation from the mean of the *N* points along the rim.

DEPTH_FLOOR_TOPOG Average elevation of each of the manually determined *N* points inside the crater floor. Points were chosen as the lowest elevation that did not include visible embedded craters. Units are km.

DEPTH_FLOOR_SD_TOPOG The standard deviation from the mean of the *N* points along the rim.

DEPTH_RIMFLOOR_TOPOG Defined as DEPTH_RIM_TOPOG - DEPTH_FLOOR_TOPOG

DEPTH_RIMHEIGHT_TOPOG Defined as DEPTH_RIM_TOPOG - DEPTH_SURFACE_TOPOG

DEPTH_SURFFLOOR_TOPOG Defined as DEPTH_SURFACE_TOPOG - DEPTH_FLOOR_TOPOG

PTS_USED_RIM_[IMAGE, TOPOG] Number of *N* points manually selected around the crater rim to identify the crater.

PTS_USED_SURFACE Number of *N* points manually selected around the crater's surface for the topographic analysis.

PTS_USED_FLOOR Number of *N* points manually selected within the crater's floor for the topographic analysis

PTS_USED_LAYER_1 Number of *N* points manually selected along the perimeter of the inner-most (or only) layer of the crater's ejecta. Note that this was done with THEMIS Daytime IR mosaics.

PTS_USED_LAYER_[2, 3, 4, 5] Number of *N* points manually selected along the perimeter of each successively outer crater layer (or blank if the crater does not have those lobes).

NUMBER_LAYERS The maximum number of cohesive layers in any azimuthal direction that could be reliably identified.

MORPHOLOGY_CRATER_1 Basic morphology of the crater interior (following Barlow and Bradley, 1990); examples are illustrated in Appendix C.

MORPHOLOGY_CRATER_2 Notes features of interest through or on the crater wall.

MORPHOLOGY_CRATER_3 Notes features of interest on the crater floor.

MORPHOLOGY_EJECTA_1 Ejecta morphology classified following Barlow *et al.*, 2000; examples are illustrated in Appendix D. If there are multiple values, separated by a "/", then the order is the inner-most ejecta through the outer-most, or the top-most through the bottom-most.

MORPHOLOGY_EJECTA_2 The morphology of the layers(s) itself/themselves. This column further describes the ejecta/layer morphology to help differentiate. This classification system is unique to this work. Examples are illustrated in Appendix D.

MORPHOLOGY_EJECTA_3 Overall texture and/or shape of some of the layer(s)/ejecta that are generally unique and deserve separate morphological classification. Examples are illustrated in Appendix D.

MORPHOLOGY_EJECTA_COMMENTS Notes or comments about the ejecta or possible ejecta if it was ambiguous.

DEGRADATION_STATE An integer 1-4 that describes how fresh or degraded a crater is. Values are defined in Section 2.4.4.

SECONDARY Subjective indication of whether or not the identified crater is a secondary. If this column has a value, it is a subjective certainty with values defined in Section 2.4.5.

CONFIDENCE_IMPACT_CRATER In some cases, a partial circular depression was identified as a crater, but we are not certain it is a crater. This column is a subjective certainty from 1-4 that the crater is really a crater (1 would be not very confident, 2 is equal chance it may or may not be, 3 is that it very likely is an impact crater, and 4 would be a definite crater).

LAYER_[1, 2, 3, 4, 5]_PERIMETER Perimeter of the manually determined *N*-dimensional irregular polygon of the layer. Units are km.

LAYER_[1, 2, 3, 4, 5]_AREA Area of the manually determined *N*-dimensional irregular polygon of the layer. This is with the area within the crater's rim removed. Units are km^2.

LAYER_[1, 2, 3, 4, 5]_LOBATENESS Abbreviated as Γ. Gives a measure of the lobateness (Bridges and Barlow, 1989). Defined as [perimeter of ejecta] / SQRT(4·π·[area of ejecta]), which is effectively the percent difference of the perimeter of the flow vs. the perimeter of a perfect circle with the equivalent flow area. Unitless.

Note 1: The area of the crater itself IS included in this calculation.

Note 2: In this calculation, local spherical effects were NOT taken into account.

LAYER_[1, 2, 3, 4, 5]_EJECTARADIUS_EQUIV The radius to which the crater's ejecta would extent if it were a circle with the same area as LAYER_[1, 2, 3, 4, 5]_AREA.

LAYER_[1, 2, 3, 4, 5]_EJECTARADIUS_RELATIVE The relative radius to which the crater's ejecta would extent if it were a circle with the same area as LOBE_[1, 2, 3, 4, 5]_AREA. Calculated by:

LAYER_[1,2,3,4,5]_EJECTARADIUS_EQUIV / DIAMETER_CIRCLE_IMAGE.

CRATER_NAME Drawn from the USGS's online Gazetteer of Planetary Nomenclature, maintained by Jennifer Blue (http://planetarynames.wr.usgs.gov/).

Appendix B - Discussion of Ellipse Fit Algorithm

Ellipse fitting in Cartesian coordinates with an arbitrary tilt is notoriously unstable and prone to rapidly approaching zero or infinity, as discussed in Section 2.2.2 of the text. In NLLS fits, the partial derivative of each parameter in the fit function is used. The equation of an ellipse in Cartesian coordinates with an arbitrary tilt (Eq. 8) is much more complex than a circle:

$$y = \frac{\begin{array}{l}-2b^2\left(x_0 - x\cos(\theta)\right)\sin(\theta) + 2a^2\cos(\theta)\left(y_0 - x\sin(\theta)\right) \pm \\ \sqrt{2a^2b^2\left(\begin{array}{l}a^2 + b^2 - x_0^2 - y_0^2 - 2x^2 + \left(a^2 - b^2 - x_0^2 + y_0^2\right)\cos(2\theta) \\ +4y_0\sin(\theta) + 4x_0\cos(\theta)\left(x - y_0\sin(\theta)\right)\end{array}\right)}\end{array}}{2\left(a^2\cos^2(\theta) + b^2\sin^2(\theta)\right)} \tag{8}$$

where a is the semi-major axis, b is the semi-minor axis, x_0 is the center longitude and y_0 the center latitude, and θ is the tilt of the ellipse's major axis. This fit is unstable because of the partial derivatives (Eq. 9):

$$\begin{aligned}
\frac{\partial x_0}{\partial y} &= \frac{-2\left(-x_0 + x\cos(\theta) - y\sin(\theta)\right)}{a^2} \\
\frac{\partial y_0}{\partial y} &= \frac{-2\left(-y_0 + y\cos(\theta) + x\sin(\theta)\right)}{b^2} \\
\frac{\partial a}{\partial y} &= \frac{-2\left(-x_0 + x\cos(\theta) - y\sin(\theta)\right)^2}{a^3} \\
\frac{\partial b}{\partial y} &= \frac{-2\left(-y_0 + y\cos(\theta) + x\sin(\theta)\right)^2}{b^3} \\
\frac{\partial \theta}{\partial y} &= \frac{2\left(-y_0 + y\cos(\theta) + x\sin(\theta)\right)\left(x\cos(\theta) - y\sin(\theta)\right)}{b^2} \\
&\quad + \frac{2\left(-x_0 + x\cos(\theta) - y\sin(\theta)\right)\left(-x\sin(\theta) - y\cos(\theta)\right)}{a^2}
\end{aligned} \tag{9}$$

The derivatives are sensitive to the inverse-square and -cube of the semi-major and -minor axes. If a or b become small, the fit will rapidly approach infinity; if they become large, the fit will approach 0. Consequently, multiple safeguards were in place to checks of each parameter were

performed during every iteration of the fit in order to guard against bad results; these are illustrated in Figure **60**.

An intelligent guessing of the major and minor axes was employed at the start of the fit by taking the average of the maximum minus the minimum of the crater's longitudinal (x) and latitudinal (y) extents. These were multiplied by a random number drawn from a Gaussian distribution with $\mu = 1.0$ and $\sigma = 0.25$ and saved as the initial guesses for the major and minor axes. The tilt angle initial guess was drawn from a uniform distribution between $\pm\pi$. All five fit parameters were monitored throughout each iteration of the fit to increase the chances of the algorithm locking onto a realistic fit: The center latitude and longitude (from the center of mass of the points) were checked so if they became unreasonably large (1000 was the threshold) they would be re-set to 0.01. The major and minor axes were also monitored so if they became unreasonably large, they would be re-set to the diameter that the circle-fit found, multiplied by another random number as described above. The tilt angle was monitored so that if $|\theta| > \pi$, it was re-set to 0.001.

In addition to these safeguards, the ellipse fit was re-done for *every* crater a *minimum* of three times and a maximum of five. The algorithm required the NLLS fit to converge on the *same* fit values for all five parameters three times to a tolerance of 10^{-6}. If this did not happen the first three times the crater was fit, the algorithm would attempt to fit it up to twice more. If by the fifth fit, there were not three identical matches, then the algorithm would record that the fit did not converge for that crater, leaving the values blank. Finally, the algorithm required that the major and minor axes be within 35% of the circle-fit's diameter, otherwise it was rejected. This was chosen to, by definition, exclude fits with an ellipticity $\gtrsim 2.0$ (of which there are less than a dozen on Mars that are $\varepsilon > 2.0$).

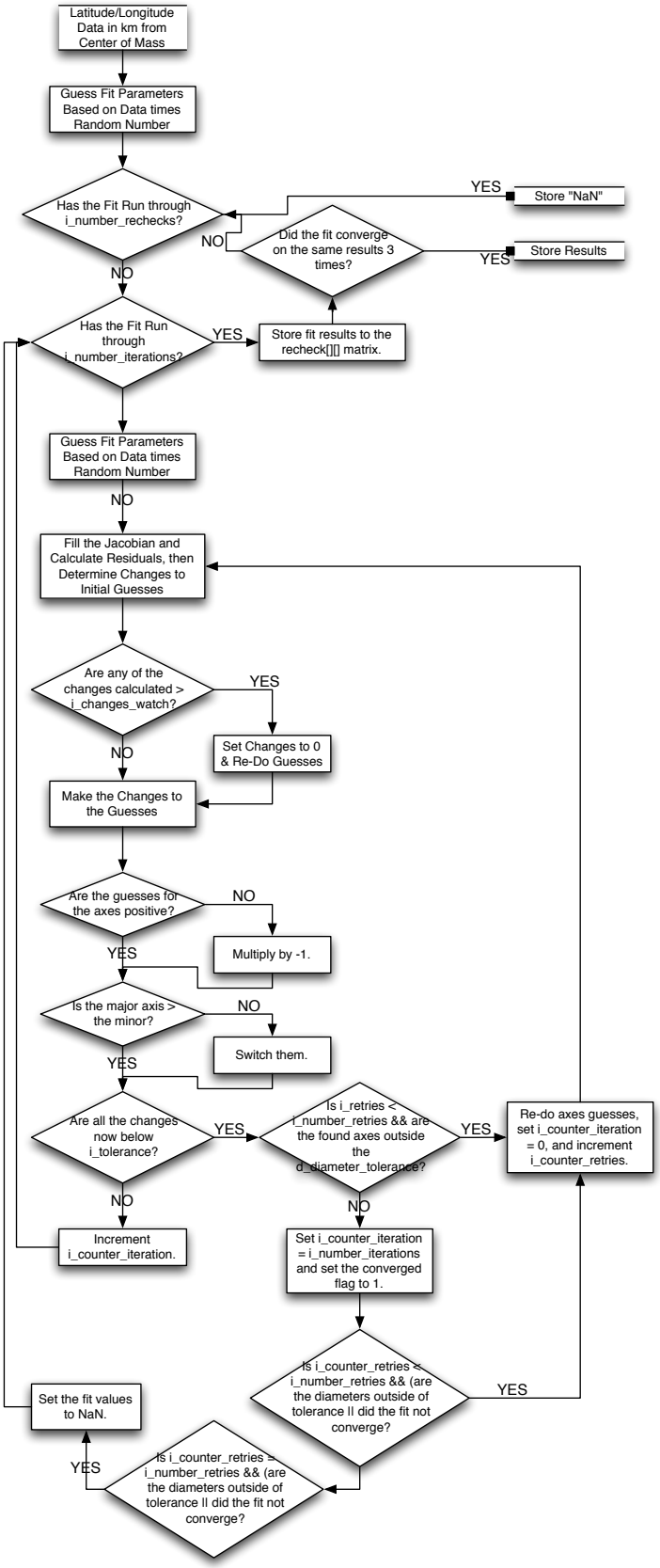

Figure 60: Flow chart illustrating the algorithm to monitor the ellipse fit and verify convergence.

Appendix C - Archetypal Examples of All Crater Interior Morphologies

This Appendix contains archetypical examples of several of the crater interior morphologies that are included in this database. In some cases, a single image is used to display multiple morphologies as described in the figure captions.

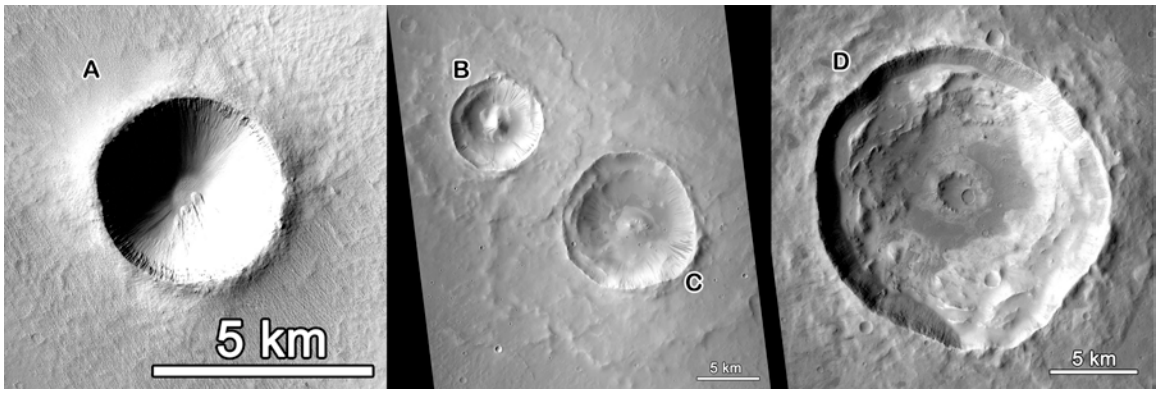

Figure 61: Basic crater morphologies used in the first morphology column; scale bar is 5 km in all examples. Imagery is from CTX (Malin *et al*., 2007). (A) is a basic simple crater with some "slump deposits" along the southeast side (CTX image P19_008619_1840_XI_04N152W). (B) is a complex, central peak crater, while (C) is a complex summit pit crater; both have terraced walls (CTX image B02_010379_1846_XN_04N325W). (D) is a larger complex crater with a central pit and wall terraces; it also has some "slump deposits" from the walls onto the floor of the crater (CTX image B02_010554_1869_XN_06N063W).

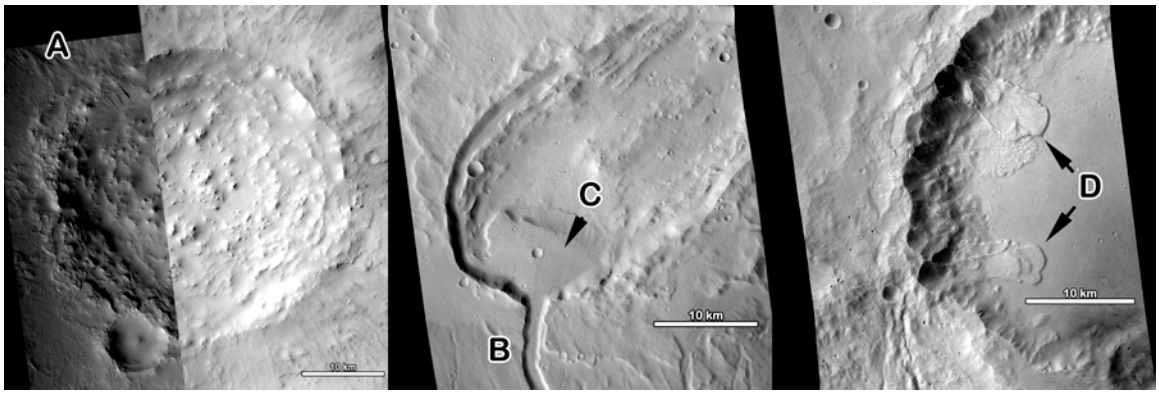

Figure 62: Select floor and wall morphologies; scale bar is 10 km in all examples. Imagery is from CTX (Malin *et al*., 2007). (A) is a crater floor with heavy deposits ("floor deposits" in the third column) that would have a first morphology column label of CpxUnc (complex, unclassifiable) (CTX mosaic from P07_003799_1961_XN_16N311W and P19_008282_1982_XN_18N311W). An example of a channel breaching the crater wall is (B) and (C) is "valley deposits" on the crater floor of Rahe Crater (CTX image B04_011399_2045_XN_24MN097). (D) shows an example of "landslide deposits" (CTX image G02_018952_1919_XI_11N021W).

Appendix D - Archetypal Examples of All Crater Ejecta Morphologies

This Appendix contains archetypal examples of the crater ejecta morphologies that are included in this database. Multiple examples of each type from the first two ejecta morphology columns are included (first column is basic type from Barlow *et al*., 2000; second column describes the texture and shape of the ejecta). Simple radial ejecta is not shown.

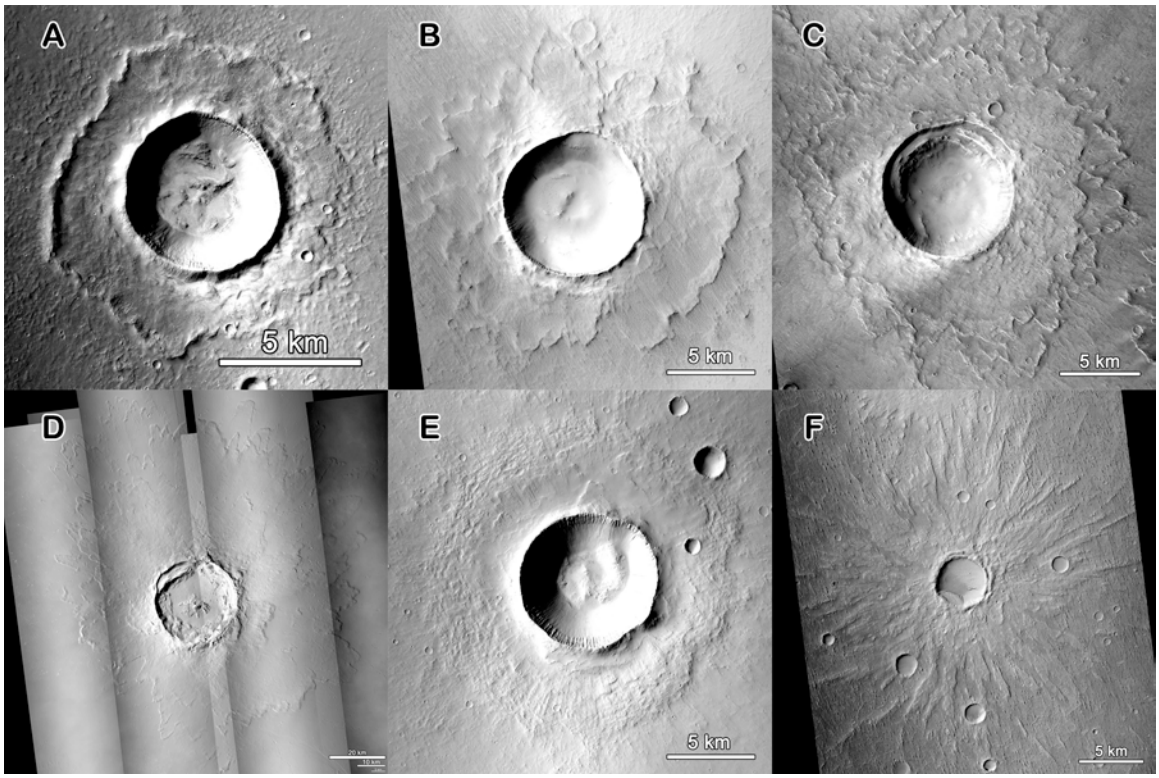

Figure 63: Select ejecta morphologies; scale bar is 5 km in all cases except (D), where the largest bar is 20 km. (A) is an example of the SLERC type in the first morphology column and HuSL (hummocky, short lobes) for the second (CTX image P21_009439_1850_XN_05N221W). (B) is an SLERS, SmSL (smooth, short lobes) (CTX image P19_008619_1840_XI_04N152W). (C) is a DLERS, HuSL type (CTX image B03_010694_1868_XI_06N285W). (D) is the MLERS, HuBL type (CTX mosaic from many images). (E) is an example of the "Pin-Cushion" morphology (also SLEPC, Hu) which, at the higher CTX resolution, has a strong radial ejecta component overlying the cohesive layer (CTX image P21_009381_2010_XN_21N080W). (F) is a good example of the SLEPS, HuSp type (CTX image P17_007606_1808_XI_00N210W).

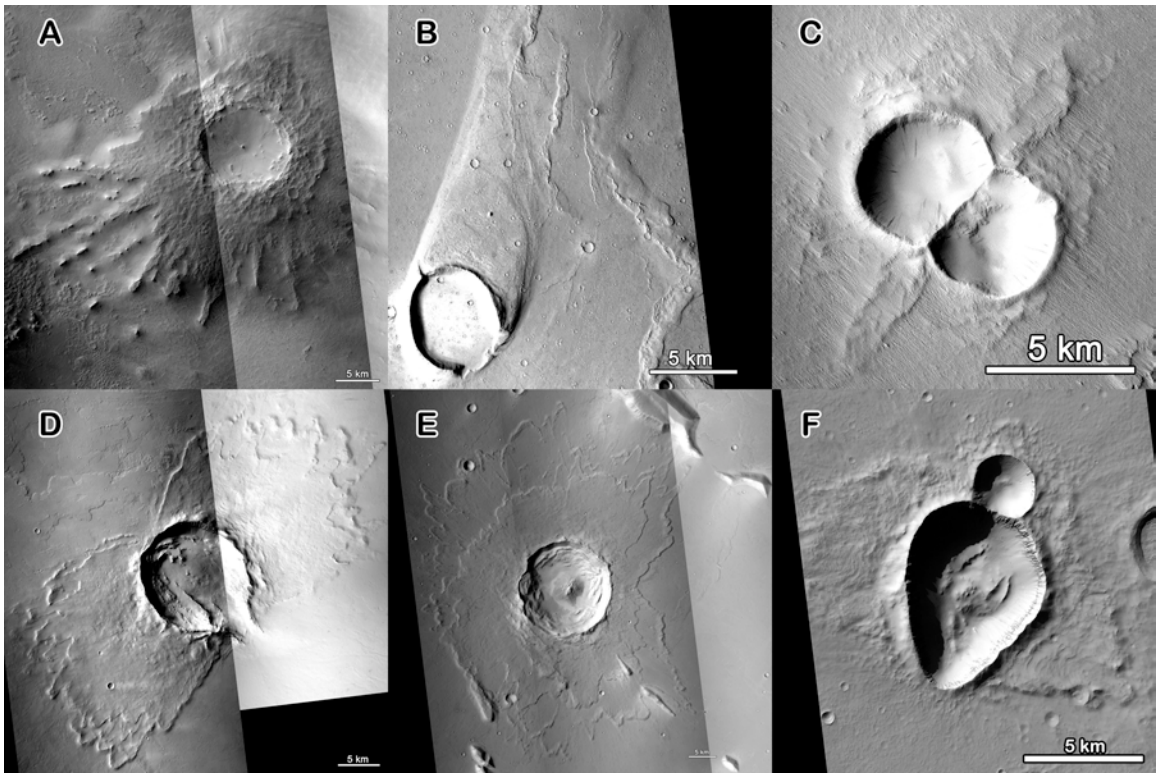

Figure 64: Select ejecta morphologies; scale bar is 5 km in all examples. (A) is both an SLEPd (pedestal crater), an example of the HuSp (hummocky, splash) type, and "Splash" in the third ejecta morphology column (CTX mosaic from P13_005942_1816_XI_01N135W, P21_009304_1806_XN_00N136W, P22_009515_1806_XI_00N136W.IMG). While not actually ejecta, "Sandbar" was indicated in the third ejecta morphology column for craters such as (B) (CTX image P03_002392_1948_XN_14N058W). (C) is the bumblebee ejecta type from a binary impact (CTX image P15_006971_1842_XN_04N151W). (D) is a DLERS, SmBL type with "Butterfly" in the third ejecta morphology column (CTX mosaic from P12_005874_1916_XN_11N080W and P20_008880_1915_XN_11N080W). (E) is the "pseudo-butterfly" type (also DLERS, SmBL) because, while it has the zone of avoidance to the east and some of the larger ejecta mobility immediately beyond the zone of avoidance, it continues around to the west as the normal DLE ejecta type and does not come back to the crater rim as with (D) (CTX mosaic from P02_001962_1967_XN_16N199W, P13_006142_1964_XN_16N198W, P20_008792_1980_XN_18N199W). (F) is an example of the "Rectangular" type which, while likely a progression from "Butterfly," has a ~180° zone of avoidance at the ends of the major axis. (CTX image B18_016578_1475_XI_32S359W).